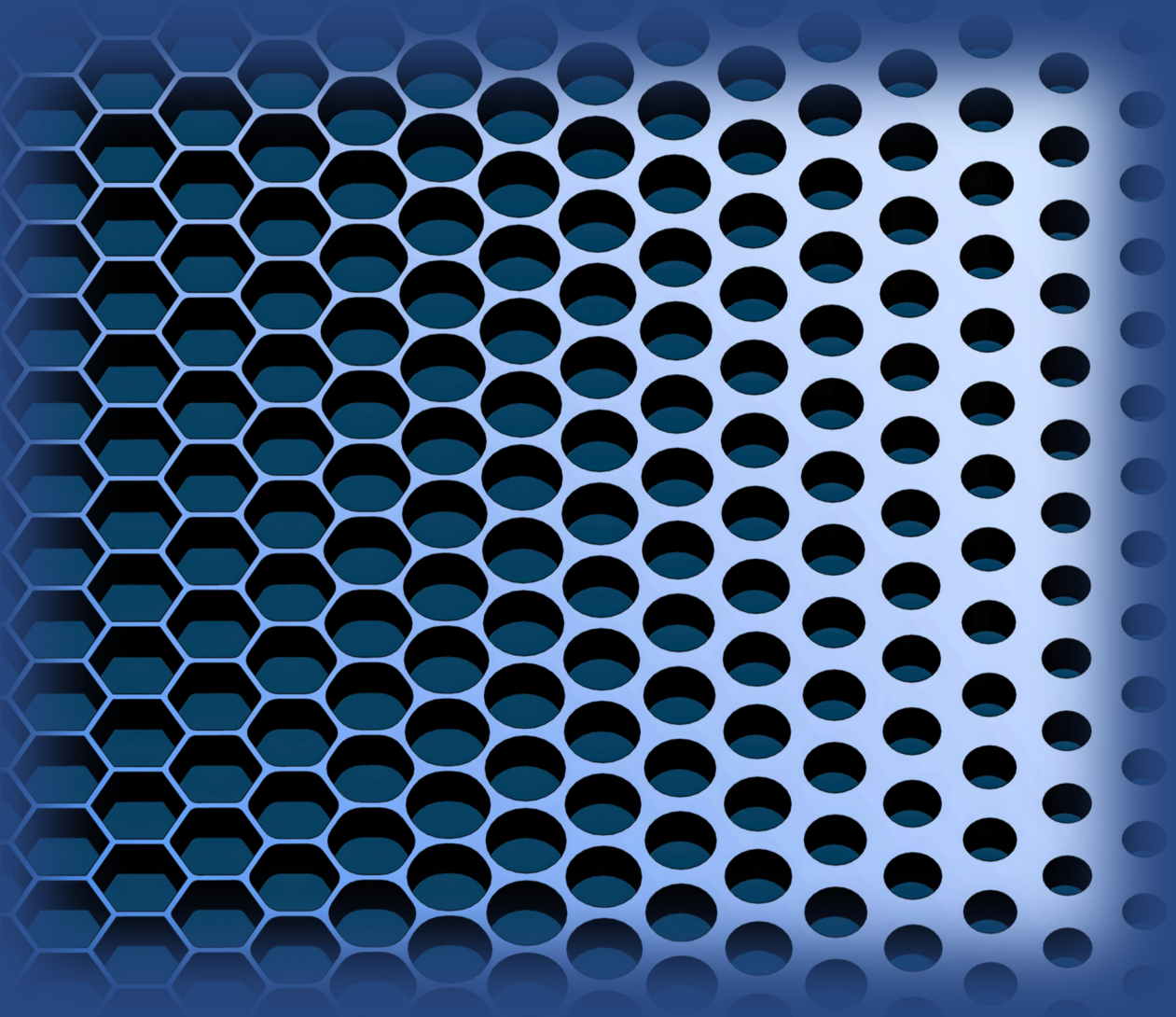


# Designer materials on demand:

Honeycomb semiconductors  
by lithographic design

---





**Designer materials on demand:  
Honeycomb semiconductors by lithographic design**

PhD thesis, Universiteit Utrecht

Christiaan Post, April 2021

The cover was designed by Kees Post

Printed by: Gildeprint

ISBN: 978-94-6419-191-2

# **Designer materials on demand: Honeycomb semiconductors by lithographic design**

Ontwerpmaterialen op aanvraag:  
Honingraat halfgeleiders volgens lithografisch ontwerp

(met een samenvatting in het Nederlands)

## **Proefschrift**

ter verkrijging van de graad van doctor aan de Universiteit Utrecht op gezag van de rector magnificus, prof.dr. H.R.B.M. Kummeling, ingevolge het besluit van het college voor promoties in het openbaar te verdedigen op woensdag 19 mei 2021 des middags te 2.15 uur

door

**Lambert Christiaan Post**

geboren op 6 februari 1991  
te Hilversum

**Promotor:** Prof. dr. D. Vanmaekelbergh

Dit proefschrift werd mede mogelijk gemaakt met financiële steun van de Nederlandse Organisatie voor Wetenschappelijk Onderzoek (NWO-programma TOPPUNT).

# Contents

	<b>Page</b>
<b>I Introduction</b>	<b>1</b>
<b>II Understanding honeycomb semiconductors: Theoretical background</b>	<b>7</b>
II.1 Solid-state physics . . . . .	8
II.2 Graphene . . . . .	14
II.3 Honeycomb semiconductors . . . . .	19
II.4 Fabrication of honeycomb semiconductors . . . . .	23
II.5 Scanning tunneling microscopy and spectroscopy . . . . .	30
<b>III Designing honeycomb semiconductors: The muffin-tin model</b>	<b>43</b>
III.1 Introduction . . . . .	44
III.2 Design of a honeycomb semiconductor . . . . .	45
III.3 Optimization of a honeycomb semiconductor . . . . .	47
III.4 Experimental comparison tool: the numerical muffin-tin model . . .	54
III.5 Conclusions and outlook . . . . .	56
Supplementary information . . . . .	57
<b>IV Realizing honeycomb semiconductors: A lithographic route towards nanoperforated InGaAs quantum wells</b>	<b>77</b>
IV.1 Introduction . . . . .	78
IV.2 Fabrication of a honeycomb semiconductor . . . . .	79
IV.3 Statistical analysis . . . . .	83
IV.4 Radial distribution function . . . . .	86
IV.5 Conclusion and outlook . . . . .	89
Supplementary information . . . . .	93
<b>V Investigating honeycomb semiconductors: Structural and electronic investigation of an engineered InGaAs honeycomb semiconductor</b>	<b>111</b>
V.1 Introduction . . . . .	112

---

V.2	Engineering of a Dirac-type band structure by lithographic design . . . . .	113
V.3	Electronic characterization of the honeycomb semiconductor . . . . .	115
V.4	Conclusions and outlook . . . . .	119
	Supplementary information . . . . .	121
<b>VI</b>	<b>Investigation of the electronic effects of geometric disorder in a honeycomb semiconductor: from a local defect to a glassy system</b>	<b>137</b>
VI.1	Introduction . . . . .	138
VI.2	Investigation of the electronic effects of a single local distortion of the honeycomb lattice . . . . .	140
VI.3	Fully disordered antidot lattices: a glassy version of the honeycomb semiconductor . . . . .	143
VI.4	Disordered tight-binding model . . . . .	148
VI.5	Conclusions and outlook . . . . .	151
	Supplementary information . . . . .	153
<b>VII</b>	<b>Application of honeycomb semiconductors: Outlook &amp; future prospects</b>	<b>163</b>
VII.1	Process optimization . . . . .	164
VII.2	Transport measurements . . . . .	166
VII.3	Beyond InGaAs-based honeycomb semiconductors . . . . .	168
<b>VIII</b>	<b>Samenvatting in het Nederlands</b>	<b>177</b>
	<b>Acknowledgements</b>	<b>187</b>
	<b>Publications and conference contributions</b>	<b>193</b>
	<b>About the author</b>	<b>195</b>

---

# Chapter



---

## Introduction

It has always been the dream of the scientific world to design and construct materials with full control over the electrical, mechanical and other relevant properties. In the ideal case, individual atoms are manipulated and arranged one by one to fabricate designer materials, creating an endless playground of different materials with specific properties for specific applications. Quantum simulators can help us with the understanding of these designer materials. Quantum simulators are systems which can be tuned in composition and geometry at the nanoscale, they are used to investigate less tunable and controllable materials [1]. Individual, manipulatable building blocks can be used to design quantum simulators. These simulators include cold-atom systems [2,3], photonic systems [4–8], trapped ion systems [9–11] or acoustic systems [12]. To mimic electronic systems, electronic quantum simulators can be designed which allow to investigate all fundamental properties of the electrons, such as spin, charge and orbital degree of freedom. For this purpose, scanning tunneling microscopy (STM) is an ideal platform and tool: it allows to observe individual atoms [13], and these individual atoms can also be manipulated and positioned with atomic precision [14]. When the electronic quantum simulator is designed, the electronic properties can be directly accessed using the conducting tip of a STM. Various quantum systems have already been designed and investigated using this tool, starting from 'simple' quantum systems such as artificial atoms [15], quantum corrals [16] and honeycomb lattices [17] towards more complex systems such as Lieb lattices [18, 19], Kagome lattices [20, 21], Su-Schrieffer-Heeger (SSH) chains and squares [22] and kekulé lattices [23]. Even the dimensionality [24] of the confined electron gas can be modulated using the correct design.

In this thesis, the honeycomb geometry is selected as a suitable system, since it has a simple graphene-type lattice and can provide a Dirac-type electronic band structure similar or different from that of graphene. A Dirac band structure means that the conduction band contains one or more Dirac cones, where the energy of the charge

carrier is linear with momentum, and that a  $p$ -orbital flat band emerges if the  $s$ - and  $p$ -orbitals are sufficiently separated. Honeycomb physics have already been studied in various types of quantum simulators using optical traps [25–27], ultra-cold atoms [28] and molecules [17]. Electronically, the properties of graphene originate from the honeycomb symmetry itself and do not depend on the composition [29]. This means that they can be implemented in other types of materials such as semiconductor materials [30]. This could result in a geometric semiconductor with properties such as the band gap that depend on the material, but conduction- and valence band structures determined by the honeycomb geometry. One of the first real materials with a honeycomb symmetry was built using semiconductor nanocrystals, which can form long-scale honeycomb superlattices [31–33]. The electronic properties can be tuned and optimized by changing the dimensions of the honeycomb lattice and composition of the semiconductor material. Such materials will be called honeycomb semiconductors: two-dimensional semiconductor materials with an embedded honeycomb nanogeometry.

In this thesis, a different approach will be used to realize honeycomb semiconductors, namely a top-down approach. In 2009, Gibertini *et al.* [34] proposed to design a honeycomb semiconductor using lithography, a process used in the microfabrication to create patterns in thin semiconductor films. Theoretical models already show that a Dirac-type electronic structure can be obtained in honeycomb semiconductors by lithographic design [35]. First efforts to fabricate a lithographic designed honeycomb semiconductor have already been performed. In 2015, Scarabelli *et al.* [36] fabricated arrays of Au nanodisks with a honeycomb unit cell of 50 nm periodicity onto a modulation-doped GaAs/Al<sub>0.1</sub>Ga<sub>0.9</sub>As quantum well using electron beam lithography, forming an attractive potential for the electrons in the semiconductor quantum well. By using resonant inelastic light scattering [37] and transport measurements [38], first measurements of the electron states were performed, showing only faint features due to the large unit cell size of the honeycomb nanogeometry. Upon changing the design from honeycomb attractive pillars to triangular repulsive pores [39], no clear improvements were established. Although this research showed the possibility to design honeycomb semiconductors with tunable properties such as electron density, doping and symmetry in size, the signatures of Dirac physics were faint and indirect.

The honeycomb semiconductor lattice needs several improvements to make the Dirac cones wider in energy and thus more robust. First, the dimension of the honeycomb unit cell needs to be reduced to reveal Dirac electrons with a measurable band width in standard cryogenic conditions. This can be achieved by pushing the limits of the electron beam lithography technique towards lower unit cell sizes [30]. In parallel, alternative patterning technologies such as block copolymer lithography can be considered. Second, different III-V semiconductor compounds can be considered. For example, InGaAs based quantum well heterostructures can be fabricated using well-established routes [40], leading to electron gases with high carrier mobilities. On top of that, the low effective mass of InGaAs (compared with GaAs) enhances the confinement effects of the charge carriers, improving the band width of the Dirac cone. Finally, the quality of the honeycomb geometry is essential to achieve a robust Dirac-type electronic band structure.

---

Adequate semiconductor compounds and improved patterning will enable us to implement Dirac physics in real semiconductor materials, which will open the way to apply this in real electronic devices fabricated by the semiconductor industry. On top of that, this technique also enables us to explore also other symmetries [41] and other semiconductor materials, truly giving full control over the electronic properties of a designer material.

## Outline of this thesis

The aim of this research to create and measure Dirac-like electronic physics in real semiconductor materials with potential direct applications in electronic devices. This will be achieved by a work-flow to design, realize and characterize InGaAs based two-dimensional semiconductors with a honeycomb nanogeometry. By first modelling and designing the desired honeycomb systems, the electronic structure can be investigated and optimized by changing the lattice parameters. The fabrication process will not only consist of steps which are already well mastered in the semiconductor industry, but also on the optimization of the lithography and etching process by exploring the limits of reducing the unit cell size. For this reason, different lithography and etching techniques will be considered. The local electronic structure of the designed honeycomb semiconductors can be directly accessed by using scanning tunneling microscopy. Finally, the effect of lattice disorder onto the electronic properties will be investigated theoretically and experimentally.

The thesis is structured as follows:

**Chapter II** will introduce methodologies and concepts which are used to understand the research described in this thesis. First, the general properties of bulk and two-dimensional semiconductors are described. Using a simplified tight-binding model, the rich electronic structure of graphene can be outlined and understood providing a first introduction to a Dirac-type electronic band structure. Using both the muffin-tin model to solve the Schrödinger equation and tight-binding theory, the electronic properties of two-dimensional honeycomb semiconductors are predicted. Furthermore, this chapter will also be used to discuss the general procedure to fabricate honeycomb semiconductors, including the tools and machines used during the technological process. Finally, scanning tunneling microscopy (STM) is explained which will be the main characterization tool for these materials.

**Chapter III** presents two different muffin-tin models which can describe the electronic structure of a designed honeycomb semiconductor. First, an analytical muffin-tin model is used to calculate the band structure of a generic honeycomb semiconductor. By changing the parameters of the lattice, the electronic properties can be tuned and optimized, which can be made more realistic by adding additional physics to the calculation. Finally, a numerical approach to the muffin-tin model is used to calculate the local density of states which can be used as a direct comparison tool for experimental scanning tunneling spectroscopy.

**Chapter IV** describes the work-flow to fabricate a honeycomb semiconductor using electron beam lithography. Starting with a p-type grown InGaAs quantum well, electron beam lithography is performed onto a thin resist layer on top of the QW, which will be used as a mask to etch a triangular antidot pattern inside the quantum well. The structure of the honeycomb semiconductor is intensively analysed using various techniques, characterizing the sample not only from above but also inside the pores. Using a particle detection script, disorder in the antidot lattice is studied.

**Chapter V** presents the measured electronic structure of a honeycomb semiconductor based on an InGaAs compound using scanning tunnelling microscopy. First, the honeycomb semiconductor is fabricated using block copolymer lithography using similar work-flow techniques as described in Chapter IV. We show the presence of Dirac-like features marked by a robust flat band with strong density of states on high-symmetry points of the honeycomb lattice. The analysis is supported by the theoretical models described in Chapter III.

**Chapter VI** investigates the effects of geometric disorder in the honeycomb lattice onto the electronic properties of the honeycomb semiconductor. Different types of disorder are identified, investigated experimentally and compared with theory. We discuss the robustness of the Dirac physics in these samples, showing that the flat band can survive the energy fluctuations present due to lattice disorder.

**Chapter VII** presents the future prospects of this research. First, optimization steps towards the fabrication process of the honeycomb semiconductor are proposed. Second, a possible design for an electronic honeycomb semiconductor device is present. Finally, the endless possibilities towards new symmetries, materials and designs are discussed.

---

## References

- [1] T. H. Johnson, S. R. Clark, and D. Jaksch, “What is a quantum simulator?,” *EPJ Quantum Technology*, vol. 1, p. 10, dec 2014.
- [2] I. Bloch, J. Dalibard, and S. Nascimbène, “Quantum simulations with ultracold quantum gases,” *Nature Physics*, vol. 8, no. 4, pp. 267–276, 2012.
- [3] D. Jaksch and P. Zoller, “The cold atom Hubbard toolbox,” *Annals of Physics*, vol. 315, pp. 52–79, jan 2005.
- [4] D. G. Angelakis, M. F. Santos, and S. Bose, “Photon-blockade-induced Mott transitions and XY spin models in coupled cavity arrays,” *Physical Review A*, vol. 76, p. 031805, sep 2007.
- [5] J. Cho, D. G. Angelakis, and S. Bose, “Fractional Quantum Hall State in Coupled Cavities,” *Physical Review Letters*, vol. 101, p. 246809, dec 2008.
- [6] A. Peruzzo, M. Lobino, J. C. F. Matthews, N. Matsuda, A. Politi, K. Poulios, X.-Q. Zhou, Y. Lahini, N. Ismail, K. Wörhoff, Y. Bromberg, Y. Silberberg, M. G. Thompson, and J. L. O’Brien, “Quantum Walks of Correlated Photons,” *Science*, vol. 329, pp. 1500–1503, sep 2010.
- [7] A. Aspuru-Guzik and P. Walther, “Photonic quantum simulators,” *Nature Physics*, vol. 8, pp. 285–291, apr 2012.
- [8] I. Bloch, J. Dalibard, and W. Zwerger, “Many-body physics with ultracold gases,” *Reviews of Modern Physics*, vol. 80, pp. 885–964, jul 2008.
- [9] D. Porras and J. I. Cirac, “Effective Quantum Spin Systems with Trapped Ions,” *Physical Review Letters*, vol. 92, p. 207901, may 2004.
- [10] K. Kim, M.-S. Chang, S. Korenblit, R. Islam, E. E. Edwards, J. K. Freericks, G.-D. Lin, L.-M. Duan, and C. Monroe, “Quantum simulation of frustrated Ising spins with trapped ions,” *Nature*, vol. 465, pp. 590–593, jun 2010.
- [11] B. P. Lanyon, C. Hempel, D. Nigg, M. Müller, R. Gerritsma, F. Zähringer, P. Schindler, J. T. Barreiro, M. Rambach, G. Kirchmair, M. Hennrich, P. Zoller, R. Blatt, and C. F. Roos, “Universal Digital Quantum Simulation with Trapped Ions,” *Science*, vol. 334, pp. 57–61, oct 2011.
- [12] M. J. Schuetz, J. Knörzer, G. Giedke, L. M. Vandersypen, M. D. Lukin, and J. I. Cirac, “Acoustic traps and lattices for electrons in semiconductors,” *Physical Review X*, vol. 7, no. 4, pp. 1–24, 2017.
- [13] G. Binnig, H. Rohrer, C. Gerber, and E. Weibel, “Surface Studies by Scanning Tunneling Microscopy,” *Physical review letters*, vol. 49, no. 1, pp. 57–61, 1982.
- [14] D. M. Eigler and E. K. Schweizer, “Positioning single atoms with a scanning tunnelling microscope,” *Nature*, vol. 344, pp. 524–526, apr 1990.
- [15] M. F. Crommie, C. P. Lutz, and D. M. Eigler, “Confinement of Electrons to Quantum Corrals on a Metal Surface,” *Science*, vol. 262, pp. 218–220, oct 1993.
- [16] V. D. Pham, K. Kanisawa, and S. Fölsch, “Quantum Rings Engineered by Atom Manipulation,” *Physical Review Letters*, vol. 123, p. 066801, aug 2019.
- [17] K. K. Gomes, W. Mar, W. Ko, F. Guinea, and H. C. Manoharan, “Designer Dirac fermions and topological phases in molecular graphene,” *Nature*, vol. 483, pp. 306–310, mar 2012.
- [18] M. R. Slot, T. S. Gardenier, P. H. Jacobse, G. C. P. van Miert, S. N. Kempkes, S. J. M. Zevenhuizen, C. M. Smith, D. Vanmaekelbergh, and I. Swart, “Experimental realization and characterization of an electronic Lieb lattice,” *Nature Physics*, vol. 13, pp. 672–676, jul 2017.
- [19] M. R. Slot, S. N. Kempkes, E. J. Knol, W. M. Van Weerdenburg, J. J. Van Den Broeke, D. Wegner, D. Vanmaekelbergh, A. A. Khajetoorians, C. Morais Smith, and I. Swart, “P-Band Engineering in Artificial Electronic Lattices,” *Physical Review X*, vol. 9, no. 1, p. 11009, 2019.
- [20] S. N. Kempkes, M. R. Slot, J. J. van den Broeke, P. Capiod, W. A. Benalcazar, D. Vanmaekelbergh, D. Bercioux, I. Swart, and C. Morais Smith, “Robust zero-energy modes in an electronic higher-order topological insulator,” *Nature Materials*, vol. 18, no. 12, pp. 1292–1297, 2019.
- [21] S. Paavilainen, M. Ropo, J. Nieminen, J. Akola, and E. Räsänen, “Coexisting Honeycomb and Kagome Characteristics in the Electronic Band Structure of Molecular Graphene,” *Nano Letters*, vol. 16, pp. 3519–3523, jun 2016.

- 
- [22] R. Drost, T. Ojanen, A. Harju, and P. Liljeroth, "Topological states in engineered atomic lattices," *Nature Physics*, 2017.
- [23] S. E. Freeney, J. J. Van Den Broeke, A. J. Harsveld Van Der Veen, I. Swart, and C. Morais Smith, "Edge-Dependent Topology in Kekulé Lattices," *Physical Review Letters*, vol. 124, no. 23, pp. 1–5, 2020.
- [24] S. N. Kempkes, M. R. Slot, S. E. Freeney, S. J. Zevenhuizen, D. Vanmaekelbergh, I. Swart, and C. M. Smith, "Design and characterization of electrons in a fractal geometry," *Nature Physics*, vol. 15, no. 2, pp. 127–131, 2019.
- [25] T. Uehlinger, G. Jotzu, M. Messer, D. Greif, W. Hofstetter, U. Bissbort, and T. Esslinger, "Artificial Graphene with Tunable Interactions," *Physical Review Letters*, vol. 111, p. 185307, oct 2013.
- [26] L. Tarruell, D. Greif, T. Uehlinger, G. Jotzu, and T. Esslinger, "Creating, moving and merging Dirac points with a Fermi gas in a tunable honeycomb lattice," *Nature*, vol. 483, no. 7389, pp. 302–305, 2012.
- [27] B. Wunsch, F. Guinea, and F. Sols, "Dirac-point engineering and topological phase transitions in honeycomb optical lattices," *New Journal of Physics*, vol. 10, p. 103027, oct 2008.
- [28] P. Soltan-Panahi, J. Struck, P. Hauke, A. Bick, W. Plenkers, G. Meineke, C. Becker, P. Windpassinger, M. Lewenstein, and K. Sengstock, "Multi-component quantum gases in spin-dependent hexagonal lattices," *Nat Phys*, vol. 7, no. 5, pp. 434–440, 2011.
- [29] L.-H. Wu and X. Hu, "Topological Properties of Electrons in Honeycomb Lattice with Detuned Hopping Energy," *Scientific Reports*, vol. 6, p. 24347, jul 2016.
- [30] M. Polini, F. Guinea, M. Lewenstein, H. C. Manoharan, and V. Pellegrini, "Artificial honeycomb lattices for electrons, atoms and photons," *Nature Nanotechnology*, vol. 8, pp. 625–633, sep 2013.
- [31] M. P. Boneschanscher, W. H. Evers, J. J. Geuchies, T. Altantzis, B. Goris, F. T. Rabouw, S. A. P. van Rossum, H. S. J. van der Zant, L. D. A. Siebbeles, G. Van Tendeloo, I. Swart, J. Hilhorst, A. V. Petukhov, S. Bals, and D. Vanmaekelbergh, "Long-range orientation and atomic attachment of nanocrystals in 2D honeycomb superlattices," *Science*, vol. 344, pp. 1377–1380, jun 2014.
- [32] C. Delerue, "From semiconductor nanocrystals to artificial solids with dimensionality below two," *Phys. Chem. Chem. Phys.*, vol. 16, no. 47, pp. 25734–25740, 2014.
- [33] E. Kalesaki, C. Delerue, C. Morais Smith, W. Beugeling, G. Allan, and D. Vanmaekelbergh, "Dirac Cones, Topological Edge States, and Nontrivial Flat Bands in Two-Dimensional Semiconductors with a Honeycomb Nanogeometry," *Physical Review X*, vol. 4, p. 011010, jan 2014.
- [34] M. Gibertini, A. Singha, V. Pellegrini, M. Polini, G. Vignale, A. Pinczuk, L. N. Pfeiffer, and K. W. West, "Engineering artificial graphene in a two-dimensional electron gas," *Physical Review B - Condensed Matter and Materials Physics*, vol. 79, no. 24, pp. 8–11, 2009.
- [35] L. Nádvořník, M. Orlita, N. A. Goncharuk, L. Smrčka, V. Novák, V. Jurka, K. Hruška, Z. Výborný, Z. R. Wasilewski, M. Potemski, and K. Výborný, "From laterally modulated two-dimensional electron gas towards artificial graphene," *New Journal of Physics*, vol. 14, p. 053002, may 2012.
- [36] D. Scarabelli, S. Wang, A. Pinczuk, S. J. Wind, Y. Y. Kuznetsova, L. N. Pfeiffer, K. West, G. C. Gardner, M. J. Manfra, and V. Pellegrini, "Fabrication of artificial graphene in a GaAs quantum heterostructure," *Journal of Vacuum Science and Technology B, Nanotechnology and Microelectronics: Materials, Processing, Measurement, and Phenomena*, vol. 33, p. 06FG03, nov 2015.
- [37] S. Wang, D. Scarabelli, L. Du, Y. Y. Kuznetsova, L. N. Pfeiffer, K. W. West, G. C. Gardner, M. J. Manfra, V. Pellegrini, S. J. Wind, and A. Pinczuk, "Observation of Dirac bands in artificial graphene in small-period nanopatterned GaAs quantum wells," *Nature Nanotechnology*, vol. 13, pp. 29–33, jan 2018.
- [38] G. De Simoni, A. Singha, M. Gibertini, B. Karmakar, M. Polini, V. Piazza, L. N. Pfeiffer, K. W. West, F. Beltram, and V. Pellegrini, "Delocalized-localized transition in a semiconductor two-dimensional honeycomb lattice," *Applied Physics Letters*, vol. 97, p. 132113, sep 2010.
- [39] L. Du, S. Wang, D. Scarabelli, L. N. Pfeiffer, K. W. West, S. Fallahi, G. C. Gardner, M. J. Manfra, V. Pellegrini, S. J. Wind, and A. Pinczuk, "Emerging many-body effects in semiconductor artificial graphene with low disorder," *Nature Communications*, vol. 9, p. 3299, dec 2018.
- [40] X. Wallart, B. Pinsard, and F. Mollot, "High-mobility InGaAs/InAlAs pseudomorphic heterostructures on InP (001)," *Journal of Applied Physics*, vol. 97, no. 10, pp. 13851116–1590080, 2005.
- [41] A. Tadjine, G. Allan, and C. Delerue, "From lattice Hamiltonians to tunable band structures by lithographic design," *Physical Review B*, vol. 94, p. 075441, aug 2016.
-

# Chapter II

---

## Understanding honeycomb semiconductors: Theoretical background

**Based on:**

*This chapter was written for this thesis*

**This chapter provides the theoretical background to understand the electronic properties of honeycomb semiconductors, and discusses the design, realization and characterization performed in this research. The general physics of solids and bulk semiconductors will be explained first before switching towards two-dimensional semiconductor materials without the honeycomb symmetry. The effects of a honeycomb geometry onto the electronic structure of a semiconductor material can be understood by performing a simple tight-binding calculation on a well-known material with a honeycomb symmetry: graphene. By implementing Dirac physics in two-dimensional semiconductors, the electronic structure of both systems can be combined. In the second part of this chapter, the design and characterization tools for the fabrication process of honeycomb semiconductors are discussed in more detail: Molecular beam epitaxy (MBE) is used for the growth of the thin semiconductor quantum well (QW). The honeycomb symmetry is fabricated by etching a triangular lattice of pores into the thin semiconductor layer. The pores are manufactured using nanolithography, creating a patterned mask onto the semiconductor device via various fabrication steps. Using multiple chemical wet etching and dry etching techniques, the mask is etched directly into the semiconductor material. Finally, we explain how the electronic band structure can be investigated with scanning tunneling microscopy and spectroscopy.**

### II.1 Solid-state physics

Generally, the materials used in this research are semiconductors. For a better understanding of what these class of solids are, a natural starting point for the thesis is to explain the electronic differences between different type of solids.

#### Electronic structure of solids

Solids can be classified electronically by their ability to conduct charge carriers. The electronic band structure describes the range of allowed energy states that electrons can occupy within a solid. Single atoms have individual energy levels. Increasing the total number of atoms in the material, all the allowed energy states form a continuous band as indicated in Fig. II.1A. The electrons will fill up the available states starting at the lowest available energy state up to the Fermi level, which the maximum energy level where all energy states in the solid are filled with electrons. Only electrons with higher energy can be added to the solid, i.e. when applying a voltage to the system, which will increase the Fermi level of the solid.

A solid is called a metal when the Fermi level lies directly within an electronic band, meaning that electrons can freely move throughout the metal (Fig. II.1A) when a small bias voltage is applied, conducting electricity throughout the solid. In thermodynamic equilibrium, the Fermi-Dirac distribution tells us the likelihood that an energy state  $E$

is filled with an electron [1]:

$$f(E) = \frac{1}{1 + e^{(E-E_F)/k_B T}} \quad (\text{II.1})$$

where  $E_F$  is the Fermi energy,  $k_B$  the Boltzmann constant and  $T$  the temperature of the solid. When the temperature of the solid increases, electrons can occupy states above the Fermi-level, also creating empty states below the Fermi-level, for instance important for the heat capacity. The conduction in a metal is a more collective phenomenon, as an electric field results in a smaller momentum change of all occupied states.

Although bands are continuous for bulk materials, gaps can still occur between bands which are essentially energy ranges without any energy states. These gaps are called band gaps. When the Fermi level of a solid lies directly within a band gap, electrons cannot move freely through the solid when a small voltage is applied, as there are no states available. When the band gap of a solid is insurmountable large, the solid is called an insulator (Fig. II.1A).

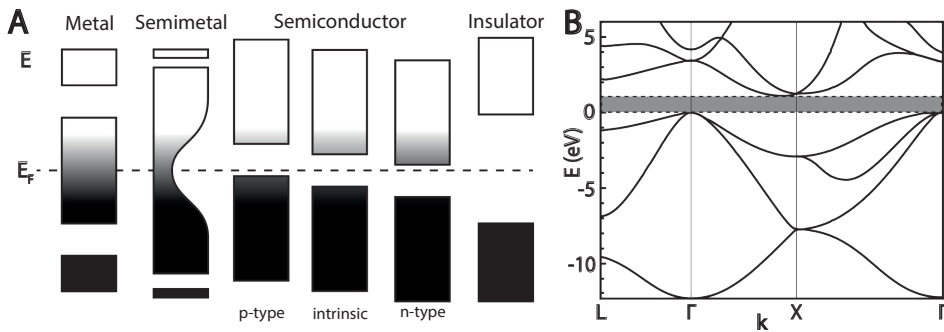


**Figure II.1: Electronic properties of various solids.** (A) Schematic view of the valence and conduction band for various solids, ranging from metals to insulators. Black indicates that the band is filled with electrons, and white shows the empty electron states. The Fermi level ( $E_F$ ) is indicated by the dashed line. (B) Band structure of bulk silicon, which is a typical semiconductor [2]. The band gap between the valence band and the conduction band is indicated in grey.

For a semiconductor, the Fermi level lies within the band gap, but the band gap is relatively small. This means that the material can be easily changed from non-conductive to conductive by shifting the Fermi level to a higher or lower level. This can be performed by adding impurities (dopants) to the semiconductor or by applying an electric field or light to the material. For these reasons, semiconductors are widely used in electronic circuits for amplification, switching and energy conversion. In case of doping of Si, for instance, a small amount of pentavalent or trivalent material is added to the semiconductor, which will add or remove one electron per impurity atom. When electrons are added to a semiconductor, the solid is called a n-type semiconductor, the Fermi level is shifted upwards. When electrons are removed from the semiconductor,

electron vacancies (called holes) are created in the valence band, and the semiconductor becomes p-type; the Fermi level is lowered to just above the valence band edge.

An important example of a semiconductor is silicon (Si). Looking at the band structure of silicon (Fig. II.1B), a small indirect band gap of 1.12 eV is present. Hence, pure silicon is an effective insulator at room temperature. Silicon can easily be doped with a pnictogen (P, As, Sb), introducing one electron per dopant in the solid and shifting the Fermi level. Similarly, a p-type semiconductor can be created from silicon by doping the material with element from group 3 (B, Al, Ga). Due to this versatility of silicon and good surface passivation by silicon oxide, it is widely used in the semiconductor industry.

The semiconductors used in this research are so-called III-V semiconductors, which consist of elements from groups III (B, Al, Ga, In) and V (N, P, As, Sb) in the periodic table. III-V semiconductors have a much lower effective electron mass compared to Si, increasing the confinement effects inside the solid, which is important to obtain robust Dirac-type band structures. The elements from the III-V group are also much heavier compared with Si, adding new interesting physics to the material due to spin-orbit coupling [3].

### From bulk towards two-dimensional semiconductors

In bulk semiconductors and metals, electrons near the minima of the conduction band can be described using the free electron model. When ignoring electron-electron and electron-ion interactions are neglected, the energy of the electrons is given by:

$$E = \frac{\hbar^2 k^2}{2m_e^*} = \frac{\hbar^2}{2m_e^*} (k_x^2 + k_y^2 + k_z^2) \quad (\text{II.2})$$

where  $k$  is the wave vector (proportional to the momentum) of the electron in all three dimensions and  $m_e^*$  is the effective mass of the electron.

When reducing the dimensionality of a semiconductor to a two-dimensional system, the energy states of the electrons in the semiconductor layer will discretize due to the confinement effect in the  $z$ -direction. The discretized energy states can be calculated using the Schrödinger equation, which will yield the following expression for the electron energy [4]:

$$E_n^{2D} = \frac{\hbar^2 k_x^2}{2m_e^*} + \frac{\hbar^2 k_y^2}{2m_e^*} + \frac{\hbar^2 n^2 \pi^2}{2m_e^* D^2} \quad (\text{II.3})$$

where  $D$  is the thickness of the two-dimensional semiconductor layer, and  $n$  are integers ( $n \in \mathbb{Z}$ ). Here, we assume that the two-dimensional electron gas (2DEG) is confined between two high potential barriers, trapping the electron gas in the thin semiconductor layer. In the  $z$ -direction, the energy has become independent of the wave vector, and only discrete values  $E_n$  are allowed:

$$E_n = \frac{\hbar^2 n^2 \pi^2}{2m_e^* D^2} \quad (\text{II.4})$$

while in the  $x$ - $y$  plane the electron energies are still quasi-continuous. Using this expression, the total density of states (DOS) of a two-dimensional quantum well with thickness  $D$  can be calculated. Implementing Eq. (II.3) into the general DOS formula of a bulk semiconductor will yield [5]:

$$g(E) = \frac{\sqrt{2}m_e^{*3/2}}{\pi^2\hbar^3} \sqrt{E} = \frac{m_e^*}{\pi\hbar^2} \frac{n}{D} \quad (\text{II.5})$$

which is equal to the DOS of a pure two-dimensional system multiplied with  $n/D$ :  $g(E) = g_2(E) * n/D$ . This means that in each step of the quantum number  $n$ , a value of  $g_2(E)/D$  is added to the DOS of a semiconductor quantum well. The DOS is plotted and presented in Fig. II.3D.

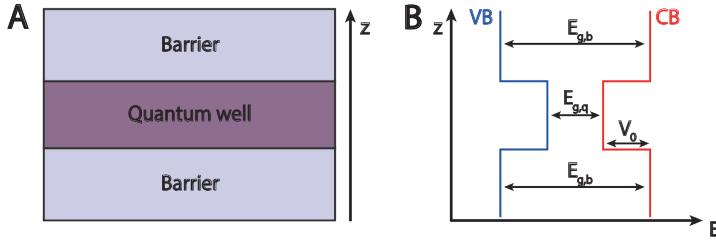


**Figure II.2: Schematic representation of a semiconductor quantum well.** (A) Schematic presentation of a semiconductor quantum well confined between two barrier materials. (B) Representation of the energy diagram of a typical grown quantum well showing the valence bands and conduction bands of the heterostructure. The band gap of the semiconductor quantum well is indicated by  $E_{g,q}$ , the band gap of the two semiconductor barriers is indicated by  $E_{g,b}$ . The depth of the potential well where the 2DEG is confined is indicated by  $V_0$ .

Thin layers of III-V semiconductors can be grown on top of each other with atomically sharp boundaries, allowing to tune the electronic structure of the grown structure almost endlessly due to the variation in band gaps and possibility to dope the heterostructure [6, 7]. A 2DEG can be obtained by growing a semiconductor quantum well layer between two barrier layers (Fig. II.2A), where the band gap of the quantum well layer  $E_{g,Q}$  is lower than the band gap of the barrier material  $E_{g,B}$  (Fig. II.2B). This will confine the charge carriers in the semiconductor quantum well layer by creating a discontinuity in the conduction band (CB) and valence band (VB), presuming that the Fermi level for both the quantum well as the barrier material is the same. The 2DEG will be confined in the conduction band and can be modelled by a potential well with a potential height of  $V_0$ , which depends on the discontinuity of the conduction bands (Fig. II.2B).

For a better understanding of the electronic structure of a 2DEG in a semiconductor heterostructure, the Schrödinger equation can be solved for a potential well with a finite height  $V_0$ . The problem is separated into three areas with three different poten-

## II Understanding honeycomb semiconductors: Theoretical background

---

tials (Fig. II.3A):

$$V(z) = \begin{cases} II : V(z) = V_0 & -\infty < z < -D/2 \\ I : V(z) = 0 & -D/2 < z < D/2 \\ III : V(z) = V_0 & D/2 < z < \infty \end{cases}$$

Inside the well (area I) along the  $z$ -direction, the potential is zero, and the Schrödinger equation can be written as:

$$-\frac{\hbar^2}{2m_e^*} \frac{d^2\psi_I(z)}{dz^2} = E\psi_I(z) \quad (\text{II.6})$$

where  $\psi_I(z)$  is the wave function of the electrons inside the box. The wave function can be solved, yielding the following result:

$$\psi_I(z) = Ae^{ikz} + A'e^{-ikz} \quad (\text{II.7})$$

where the wave number  $k$  is written as  $k^2 \equiv 2m_e^*E/\hbar^2$ , and  $A$  and  $A'$  are complex numbers.

Outside the potential well (region II and III), the potential  $V(z)$  is  $V_0$ . To ensure that the 2DEG is confined in the potential, the assumption is made that the energy of the 2DEG is smaller than the height of the potential barrier. When solving the Schrödinger equation in both regions, the electron wave functions will yield decaying functions:

$$\psi_{II}(z) = Be^{-\alpha z} + B'e^{\alpha z} \quad (\text{II.8})$$

$$\psi_{III}(z) = Ce^{-\alpha z} + C'e^{\alpha z} \quad (\text{II.9})$$

where  $\alpha$  is defined as  $\alpha^2 \equiv 2m_e^*(V_0 - E)/\hbar^2$ .

To find the specific solution for this problem, boundary conditions can be applied to the edges of the regions, since the electron wave functions must be continuous and differentiable at the edges of the potential well:

$$\begin{aligned} \psi_{II}(-D/2) &= \psi_I(-D/2) & \psi_I(D/2) &= \psi_{III}(D/2) \\ \frac{d\psi_{II}}{dz}(-D/2) &= \frac{d\psi_I}{dz}(-D/2) & \frac{d\psi_I}{dz}(D/2) &= \frac{d\psi_{III}}{dz}(D/2) \end{aligned}$$

By applying these boundary conditions, the complex constants  $A, A', B, B', C$  and  $C'$  can be calculated. After some math, the solutions can have two sorts of solutions: symmetric and antisymmetric solutions.

$$\alpha = k \tan(kD/2) \quad \text{Symmetric case} \quad (\text{II.10})$$

$$\alpha = -k \cot(kD/2) \quad \text{Antisymmetric case} \quad (\text{II.11})$$

Recall that both  $\alpha$  and  $k$  are dependent of the electron energy, meaning that the energy of the 2DEG can be calculated with these equations. Also note that  $\alpha$  is written as a function of the FWQ thickness  $D$ , meaning that the solutions will alter when the thickness is changed.

---

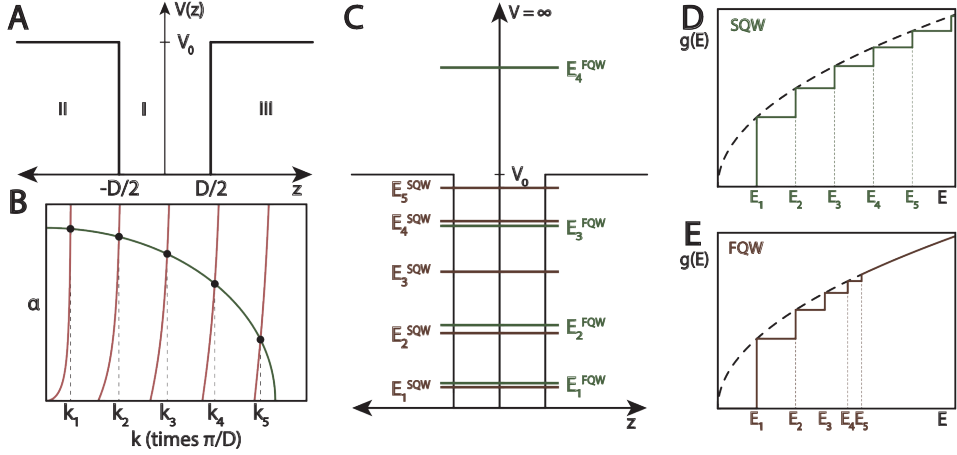


**Figure II.3: Electronic structure of a semiconductor quantum well.** (A) Schematic overview of the finite potential well problem. The height of the potential in areas II and III is  $V_0$ , and the thickness of the well is  $D$ . (B) Solutions to the bound states of a finite potential well. (C) Comparison between the energy states of the infinite potential well (green) and finite potential well problem (brown). (D-E) Comparison between the density of states of the electrons in the infinite potential well (SQW, green) and finite potential well (FQW, brown). Notice that in the finite potential well, the energy of the electrons is no longer inversely proportional to the thickness of the QW, and that the electrons behave similar as for a three-dimensional material when the energy is higher than the potential barrier [5].

These solutions cannot be solved analytically but graphically by plotting the obtained solutions and a quarter circle  $\gamma^2 = \alpha^2 + k^2 = \frac{2m_e^* V_0}{\hbar^2}$ , which is presented in Fig. II.3B. The intersections of the solutions and the quarter circle give discrete values for  $k_n$ . These discrete value can be inserted back in Eq. (II.5) to find the DOS for a finite quantum well (FQW):

$$g^{FQW}(E) = \frac{m_e^* k_n}{\pi \hbar^2 \pi} \quad (\text{II.12})$$

Note that  $k_n$  is dependent on the quantum well thickness  $D$ . Now that we have found the DOS of a finite quantum well, we can look at the differences between the density of states of the FQW and infinite quantum well (SQW) case, which can be viewed in Fig. II.3D& E. Main difference between the two cases is that the DOS at high energies of the FQW is equal to the DOS of a bulk semiconductor, while for the SQW case the step behaviour remain in the DOS. Also, the energy difference between the steps is no longer linear, but are getting more close to each other upon increasing the energy of the electrons. This can also be observed when plotting the energy states of the FQW and the SQW in one plot (Fig. II.3C). Experimentally, this has already been observed for various quantum well heterostructures by performing differential conductance spectroscopy [8, 9].

## II.2 Graphene

Now that the electronic structure of a two-dimensional semiconductor is explained, the focus will switch towards two-dimensional materials with a honeycomb symmetry. The most well-known material with this geometry is graphene. Graphene is a material consisting of an atomically flat layer of carbon atoms arranged in a honeycomb structure. First, it was studied to understand the structural and electronic properties of graphite [10–12], consisting of a stapling of graphene layers [13, 14]. A major breakthrough was achieved when Andre Geim and Kostya Novoselov extracted single-atom-thick crystallite sheets of carbon from bulk graphite, using the ‘scotch tape technique’ [15, 16]. More papers about graphene appeared presenting mostly experimental work, confirming the predicted exotic electronic structure of graphene [17–19]. These electronic properties can be derived using a tight-binding model which will be discussed in this section. First, the geometric structure of graphene needs to be discussed, which will be used in the tight-binding model.

The geometric structure of graphene is presented in Fig. II.4A. The carbon atoms are packed in a hexagonal pattern, which can be described by translating lattice points of the using the formula  $\mathbf{R} = n_1 \mathbf{a}_1 + n_2 \mathbf{a}_2$ , where  $n_1$  and  $n_2$  are whole integers (Fig. II.4A). For a honeycomb lattice, the lattice points  $\mathbf{a}_1$  and  $\mathbf{a}_2$  can be written as:

$$\mathbf{a}_1 = \frac{a}{2}(3, \sqrt{3}), \quad \text{and} \quad \mathbf{a}_2 = \frac{a}{2}(3, -\sqrt{3}), \quad (\text{II.13})$$

where  $a \approx 1.42\text{\AA}$  is the distance between two carbon bonds. To effectively describe the electronic structure of a solid, the reciprocal lattice needs to be defined. The reciprocal lattice vectors of a honeycomb lattice, which span the reciprocal unit cell (Fig. II.4B), are given by:

$$\mathbf{b}_1 = \frac{2\pi}{\sqrt{3}a}(1, \sqrt{3}), \quad \text{and} \quad \mathbf{b}_2 = \frac{2\pi}{\sqrt{3}a}(1, -\sqrt{3}), \quad (\text{II.14})$$

The area within the solid hexagon is the Brillouin zone of the honeycomb lattice, which is the primitive unit cell of graphene in reciprocal space. High symmetry points  $K$ ,  $M$  and  $\Gamma$  of the Brillouin zone are indicated in the figure. The Brillouin zone and the defined high symmetry points are very useful to describe the electronic structure of graphene.

In graphene, each atom has three  $\sigma$ -bonds with neighboring atoms and one  $\pi$ -bond which is oriented out of plane. The  $\sigma$ -bonds of the carbon atom are very stable due to the overlap of the  $s$ -,  $p_x$ - and  $p_y$ -orbitals, resulting in an  $sp^2$  hybridized system. The remaining  $p_z$ -orbital makes one  $\pi$ -bond. These  $\pi$ -bonds hybridize together to form noninteracting  $\pi$ - and  $\pi^*$ -bonds [20], leading to graphene’s geometric and electronic properties. Although the  $\sigma$ -bonds are very stable, graphene is unstable when the dimensions are smaller than 20 nm [21].

A tight-binding model can be used for a detailed description of the electronic structure of graphene. In this model, the electrons are described by trial wave functions constructed from the orbital wave function which reflects the symmetry of the underlying

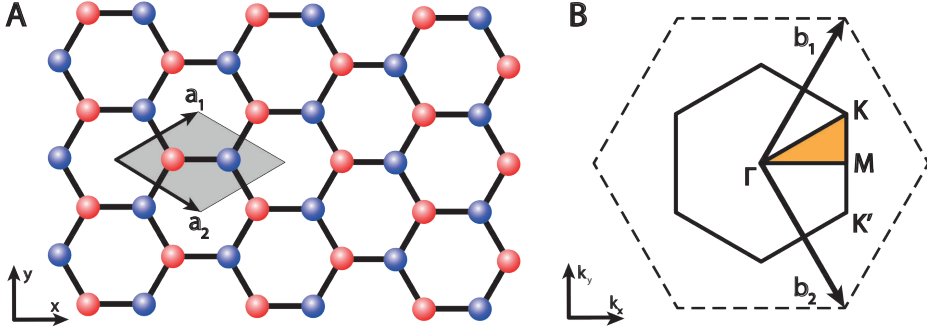


**Figure II.4: Geometric structure of graphene.** (A) The honeycomb structure of graphene in real space. The lattice points of graphene are denoted by  $\mathbf{a}_1$  and  $\mathbf{a}_2$ , and span the unit cell for graphene, indicated by grey. The different atom sites inside the unit cell are denoted in red and blue. (B) The structure of graphene in reciprocal space. The six reciprocal points form the first Brillouin zone of graphene. The reciprocal unit cell contains two different K points (K and K'). The middle of the Brillouin zone is denoted by  $\Gamma$ .

lattice. For graphene, which has two different atoms per unit cell (A and B), the trial wave function  $\Psi_{\mathbf{k}}$  can be written as a sum of two different orbital wave functions  $\psi_{\mathbf{k}}^A$  and  $\psi_{\mathbf{k}}^B$ :

$$\Psi_{\mathbf{k}}(\mathbf{r}) = a_{\mathbf{k}}\psi_{\mathbf{k}}^A + b_{\mathbf{k}}\psi_{\mathbf{k}}^B \quad (\text{II.15})$$

where  $a_{\mathbf{k}}$  and  $b_{\mathbf{k}}$  are complex. Now we can assume that  $\psi_{\mathbf{k}}^A$  and  $\psi_{\mathbf{k}}^B$  are Bloch functions, meaning that the wave functions are composed of a plane wave modulated by a periodic function [22]:

$$\psi_{\mathbf{k}}^j(\mathbf{r}) = \sum_{\mathbf{R}} e^{i\mathbf{k}\cdot\mathbf{R}} \phi^j(\mathbf{r} + \boldsymbol{\delta}_j - \mathbf{R}) \quad (\text{II.16})$$

where  $j$  labels the atoms on the two sublattices (A or B),  $\boldsymbol{\delta}_j$  is a vector which connects the sites of the Bravais lattice with the site of the atom and  $\mathbf{R}$  is a translation vector.

Now that we have a general description of the trial electron wave function  $\Psi_{\mathbf{k}}$ , the Schrödinger equation can be written down to calculate the electronic structure:

$$\begin{aligned} \hat{H}\Psi_{\mathbf{k}} &= E_{\mathbf{k}}\Psi_{\mathbf{k}} \\ \hat{H}(a_{\mathbf{k}}\psi_{\mathbf{k}}^A + b_{\mathbf{k}}\psi_{\mathbf{k}}^B) &= E_{\mathbf{k}}(a_{\mathbf{k}}\psi_{\mathbf{k}}^A + b_{\mathbf{k}}\psi_{\mathbf{k}}^B) \end{aligned} \quad (\text{II.17})$$

where  $E_{\mathbf{k}}$  are the corresponding eigenvalues of the trial wave function, which are the allowed energies of the system.  $\hat{H}$  is the Hamiltonian operator, accounting for the kinetic and potential energy of the electrons. The expectation value of the Hamiltonian operator will yield the total energy of the system, which can be calculated by integrating the following expression over the entire space:

$$\langle E \rangle = \langle \Psi_{\mathbf{k}}^*(\mathbf{r}) \hat{H} \Psi_{\mathbf{k}}(\mathbf{r}) \rangle \quad (\text{II.18})$$

$$= \int_{\text{space}} \Psi_{\mathbf{k}}^*(\mathbf{r}) \hat{H} \Psi_{\mathbf{k}}(\mathbf{r}) d\mathbf{r} \quad (\text{II.19})$$

## II Understanding honeycomb semiconductors: Theoretical background

---

This equation can be obtained by multiplying the Schrödinger equation with the complex conjugate of the wave function  $\Psi_{\mathbf{k}}^*(\mathbf{r})$  on the left side, and taking the integral over the total equation. This equation can be written out in a general matrix format:

$$(a_{\mathbf{k}}^*, b_{\mathbf{k}}^*)\mathbf{H} \begin{pmatrix} a_{\mathbf{k}} \\ b_{\mathbf{k}} \end{pmatrix} = E_{\mathbf{k}}(a_{\mathbf{k}}^*, b_{\mathbf{k}}^*)\mathbf{S} \begin{pmatrix} a_{\mathbf{k}} \\ b_{\mathbf{k}} \end{pmatrix} \quad (\text{II.20})$$

where  $\mathbf{H}$  and  $\mathbf{S}$  are both matrices, called the Hamiltonian matrix and overlap matrix respectively. They are defined as:

$$\mathbf{H} \equiv \begin{pmatrix} H_{AA} & H_{AB} \\ H_{BA} & H_{BB} \end{pmatrix} = \mathbf{H}^*$$

$$\mathbf{S} \equiv \begin{pmatrix} S_{AA} & S_{AB} \\ S_{BA} & S_{BB} \end{pmatrix} = \mathbf{S}^*$$

All the individual matrix elements of  $\mathbf{H}$  and  $\mathbf{S}$  are defined as:

$$H_{i,j} = \int \psi_{\mathbf{k}}^i(\mathbf{r}) \hat{H} \psi_{\mathbf{k}}^j(\mathbf{r}) d\mathbf{r}$$

$$S_{i,j} = \int \psi_{\mathbf{k}}^i(\mathbf{r}) \psi_{\mathbf{k}}^j(\mathbf{r}) d\mathbf{r}$$

which are complex values independent of position. Although these values are not known yet, assumptions can be made to simplify both matrices, which can be used to find a general expression for the energy of the system. First we note that the on-site energy on atom A and atom B are equal:  $H_{AA} = H_{BB}$ , and that the interaction between atom A and B are equal:  $H_{AB} = H_{BA}$ . We assume that the atomic wave functions are normalized, meaning that  $S_{AA}$  and  $S_{BB}$  will both yield one.

Now that the Schrödinger equation has been simplified, we can calculate the energies of the system by obtaining the eigenvalues from the Schrödinger equation. This can be performed by calculating the determinant of the following matrix:

$$\det[\mathbf{H} - E(\mathbf{k})\mathbf{S}] = 0 \quad (\text{II.21})$$

Using the same convention as in Ref. [23], the obtained eigenvalues from the Schrödinger equation can be expressed as:

$$E_{\pm}(\mathbf{k}) = \frac{-(-2E_0 + E_1) \pm \sqrt{(-2E_0 + E_1)^2 - 4E_2E_3}}{2E_3} \quad (\text{II.22})$$

where  $E_0$ ,  $E_1$ ,  $E_2$  and  $E_3$  are defined as followed:

$$E_0 = H_{AA} \qquad E_1 = S_{AB}H_{AB}^* + H_{AB}S_{AB}^*$$

$$E_2 = H_{AA}^2 - H_{AB}H_{AB}^* \qquad E_3 = 1 - S_{AB}S_{AB}^*$$

Now that we have found the general form of the allowed energies  $E_{\pm}(\mathbf{k})$ , the individual components need to be calculated. The on-site matrix element  $H_{AA}$  can be calculated

---

by using Bloch's theorem on the atomic wave functions (Eq. (II.16)), and plugging this into Eq. (II.2). It can be shown that this can be reduced to a constant value  $\epsilon_{2p}$ :

$$H_{AA} = \frac{1}{N} \sum_{\mathbf{R}_A} \sum_{\mathbf{R}_{A'}} e^{i\mathbf{k}(\mathbf{R}_{A'} - \mathbf{R}_A)} \langle \phi_A(\mathbf{r} - \mathbf{R}_A) | \hat{H} | \phi_A(\mathbf{r} - \mathbf{R}_{A'}) \rangle \quad (\text{II.23})$$

$$= \frac{1}{N} \sum_{\mathbf{R}_A} \langle \phi_A(\mathbf{r} - \mathbf{R}_A) | \hat{H} | \phi_A(\mathbf{r} - \mathbf{R}_A) \rangle = \epsilon_{2p} \quad (\text{II.24})$$

where  $N$  is the total number of unit cells in the crystal,  $\mathbf{R}_A$  and  $\mathbf{R}_{A'}$  are the positions of atom  $A$  and  $A'$  respectively, and  $\phi_A$  is the atomic Bloch wave function of the  $p_z$  orbital. A real value for  $\epsilon_{2p}$  can be obtained by fitting the calculated band structure to experimental data.

$H_{AB}$  is a bit more complicated to calculate, but an approximation can be made by to take only nearest-neighbors interactions into account, which will simplify the problem. When looking at site  $A$  of the unit cell in the honeycomb lattice, three  $B$  sites can be recognized as nearest-neighbors (Fig. II.4A). Therefore, the off-diagonal element  $H_{AB}$  can be expressed using the following equation:

$$H_{AB} = \frac{1}{N} \sum_{\mathbf{R}_A} \sum_{\mathbf{R}_B} e^{i\mathbf{k}(\mathbf{R}_B - \mathbf{R}_A)} \langle \phi_A(\mathbf{r} - \mathbf{R}_A) | \hat{H} | \phi_B(\mathbf{r} - \mathbf{R}_B) \rangle \quad (\text{II.25})$$

$$= \gamma_0 (e^{i\mathbf{k} \cdot \mathbf{R}_{11}} + e^{i\mathbf{k} \cdot \mathbf{R}_{12}} + e^{i\mathbf{k} \cdot \mathbf{R}_{13}}) \quad (\text{II.26})$$

where  $\mathbf{R}_{11}$ ,  $\mathbf{R}_{12}$  and  $\mathbf{R}_{13}$  are the nearest neighbor distances between atom  $A$  and atom  $B$ , and  $\gamma_0 = \langle \phi_A(\mathbf{r} - \mathbf{R}_A) | \hat{H} | \phi_B(\mathbf{r} - \mathbf{R}_B) \rangle$  is a constant value. A similar expression can be found when we calculate the overlap matrix  $S_{AB}$ :

$$S_{AB} = s_0 (e^{i\mathbf{k} \cdot \mathbf{R}_{11}} + e^{i\mathbf{k} \cdot \mathbf{R}_{12}} + e^{i\mathbf{k} \cdot \mathbf{R}_{13}}) \quad (\text{II.27})$$

where  $s_0$  is denoted as  $\langle \phi_A(\mathbf{r} - \mathbf{R}_A) | \phi_B(\mathbf{r} - \mathbf{R}_A - \mathbf{R}_{1i}) \rangle$ .

Using these values and substituting them in Eq. (II.22), the energy  $E_{\pm}(\mathbf{k})$  can be expressed in terms of  $\epsilon_{2p}$ ,  $\gamma_0$ ,  $s_0$  and some function  $f(\mathbf{k})$  [10, 23, 24]:

$$E_{\pm}(\mathbf{k}) = \frac{\epsilon_{2p} \mp \gamma_0 \sqrt{3 + f(\mathbf{k})}}{1 \mp s_0 \sqrt{3 + f(\mathbf{k})}} \quad (\text{II.28})$$

where  $f(\mathbf{k})$  is defined as:

$$f(\mathbf{k}) = 2 \cos(\mathbf{k} \cdot \mathbf{a}_1) + 2 \cos(\mathbf{k} \cdot \mathbf{a}_2) + 2 \cos(\mathbf{k} \cdot (\mathbf{a}_1 - \mathbf{a}_2)) \quad (\text{II.29})$$

$$= 2 \cos(\sqrt{3} k_y a) + 4 \cos\left(\frac{3}{2} k_x a\right) \cos\left(\frac{\sqrt{3}}{2} k_y a\right) \quad (\text{II.30})$$

The values  $\epsilon_{2p}$ ,  $\gamma_0$  and  $s_0$  can be experimentally determined by fitting the result to experimental or first-principle data. Since there are two energy solutions depending on  $\mathbf{k}$ , two electronic bands can be plotted. The obtained band structure is presented in a two-dimensional representation along the high symmetry points of the reciprocal

## II Understanding honeycomb semiconductors: Theoretical background

lattice (Fig. II.5A), where the two bands in red are the calculated bands from the simplified tight-binding approach. The other bands in the band structure are calculated using a full potential linearized plane wave method (FP-LAPW) [25–27].

Since the position of the Fermi level is at  $E = 0\text{eV}$ , graphene itself does not have a band gap. The two gapless bands touch each other at the symmetry point  $\mathbf{K} = \frac{2\pi}{3\sqrt{3}a}(\sqrt{3}, 1)$ . The interesting electronic structure of graphene can be explained by zooming in on both bands at the  $\mathbf{K}$  point, and by plotting both band in an three-dimensional representation, which can be viewed in Fig. II.5B. Around the  $\mathbf{K}$  points, the bands are conical shaped and called Dirac cones, and the points where the bands touch each other are called Dirac points, which describe some unusual electron properties.

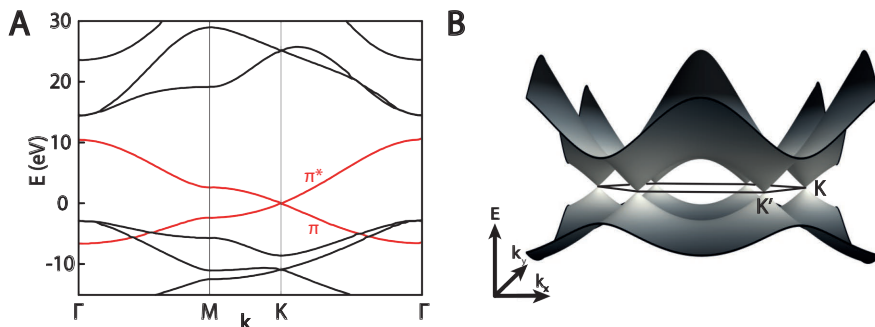


**Figure II.5: Electronic properties of graphene.** (A) The band structure of graphene obtained using a full potential linearized plane wave method (FP-LAPW). The two bands indicated in red are the  $\pi$  and  $\pi^*$  bands, which are equal to the calculated bands from the TB method. (B) The band structure of graphene in three-dimensional representation, showing the Dirac cones at the  $\mathbf{K}$  and  $\mathbf{K}'$  points.

When zooming in on the Dirac cone near the Dirac point, a linear relation between the energy and the momentum of the electrons is found. This can also be calculated by using a Taylor expansion on Eq. (II.28) near the Dirac point, using the definition  $\mathbf{q} \equiv \mathbf{k} + \mathbf{K}$  and presuming  $|\mathbf{q}| \ll |\mathbf{K}|$ :

$$E_{\pm} \approx \pm \hbar v_F |\mathbf{q}| \quad (\text{II.31})$$

where  $v_F = \sqrt{3}\gamma_0 a / 2\hbar$  is called the Fermi velocity [24, 28, 29]. This equation is fundamentally different from the energy dispersion relation for massive particles in bulk crystals, where the energy dispersion is quadratic with the electron wave vector:  $E(k) = \hbar^2 k^2 / 2m_e^*$ . For graphene, around the  $\mathbf{K}$  point the energy dispersion is linear with the electron wave vector, similar as the energy dispersion for relativistic particles:  $E(k) = \hbar c k$ . This means that the charge carriers near the  $K$  points of the Brillouin zone can be treated as relativistic, massless particles with velocity  $v_F$ . The Fermi velocity of the electrons in graphene yield  $v_F \approx 10^6\text{m/s}$ , which is only 300 times lower than the speed of light.

The existence of Dirac carriers in graphene leads to its interesting properties. One

of its most interesting properties is the half-integer quantum Hall effect, where only half-integer values are allowed in the Hall conductivity  $\sigma_{xy}$  [30–32], which is directly observed in the oscillations of the conductivity at low temperature and high magnetic fields [17, 18]:

$$\sigma_{xy} = \frac{2N-1}{2} \left( \frac{4e^2}{h} \right) \quad (\text{II.32})$$

where  $N \in \mathbb{Z}$ . This is fundamentally different from other conventional two-dimensional materials, where the conductivity is also discrete but follows whole integer values ( $\sigma_{xy} = N(\frac{4e^2}{h})$ ).

Besides the specific half-integer quantum Hall effect, graphene also shows both a tremendous electrical and thermal conductivity [15, 33, 34]. Another surprisingly effect is that graphene has a non-zero conductivity, even when there is a negligible amount of charge carriers present in the graphene [35]. It is also independent of temperature beneath 100 K.

After the discovery of graphene, other materials with potential Dirac physics got strong interest from the community, for instance monolayer sheets consisting of silicium and germanium atoms [36]. Calculations based on density functional theory [37] show that silicene and germanene are also semimetallic and have Dirac cones in the band structure, similar as for graphene. These two-dimensional materials have a buckled honeycomb symmetry, which adds spin-orbit coupling to the electronic lattice, opening up the bands at the Dirac points [38]. Although the growth of these materials is already intensively studied [39–41], there is a debate whether Dirac physics can be measured in these class of materials. Absence of Dirac physics in honeycomb lattice will occur if there is a large coupling between the two-dimensional material and the substrate, or if there is symmetry breaking in the lattice [42–44]. Extensive research is conducted in this field of research, since artificially opening the gap using electric fields [45] could lead to new interesting physical phenomena such as topological insulators [46] and the quantum anomalous Hall effect [47]. Other examples of carbon-like materials which are under a lot of attention are graphynes and other types of carbon [48–51] and boron allotropes [52]. However, the tight-binding model only presumed quantum mechanical interaction between neighbour atoms in the honeycomb geometry without any restrictions on the material type specifically. Therefore, designing Dirac physics in any two-dimensional conducting material is theoretically possible [53].

## II.3 Honeycomb semiconductors

Honeycomb semiconductors are two-dimensional semiconductor crystals with a honeycomb nanogeometry, potentially holding Dirac physics [54]. By fine-tuning the parameters defining the honeycomb lattice, hybridization between the  $s$ - and  $p$ -orbitals can be avoided. The resulting orbital degree of freedom result in  $s$ - $s$  and  $p$ - $p$  interactions, and thus Dirac physics very different from that in graphene. A novel feature that emerges besides the Dirac cone, is a  $p$ -orbital flat band.

Designing these materials is important not only for fundamental physics, but also for

the semiconductor industry. The fabrication of semiconductor devices is already well-mastered, and constitutes, therefore, an ideal platform to add Dirac physics to the device. Calculations have already shown the possibility to combine Dirac physics with the properties of a two-dimensional semiconductor in a semiconductor device [55].

Before we treat semiconductor devices, we first discuss electronic simulations of the honeycomb lattice. Artificial honeycomb lattices can be prepared atom-by-atom in an STM, and the electronic density of states can be measured *in-situ*. In 2012, Gomes *et al.* [56] designed and prepared a honeycomb lattice by arranging carbon mono-oxide (CO) molecules on a Cu(111) surface using scanning tunneling microscopy (STM). By creating a triangular formation of the CO molecules, the two-dimensional electron gas which is trapped in the surface state of the Cu(111) is forced into a honeycomb pattern, since the CO molecules act as repulsive barriers. A Dirac cone is observed in the differential conductance spectra, showing that these quantum simulators are an ideal candidate to study new physics. They also show that they can tune the electronic properties of the system, by for example changing the lattice parameters. Small gaps can be added by rearranging CO molecules, a pseudo-magnetic field up to  $B = 60$  T can be generated and the position of the Fermi level can be altered by increasing or decreasing the lattice constant, making it possible to build artificial p-n junctions on the atomic scale. Also new physics can be measured in these types of system: the presence of the zeroth Landau level was clearly observed, which is not possible to measure in natural graphene due to the larger energy scale [18,57]. In our group, we were able to optimize the investigated honeycomb lattices using double-ringed CO rosettes as scatters, separating the *s*-orbital and *p*-orbital bands from each other such that a *p*-orbital flat-band emerges besides the Dirac cone [58].

Now, we return to the case of honeycomb semiconductors which should finally result in stable electronic materials in a device, which needs extra steps with respect to the quantum simulators discussed above. A first method to fabricate honeycomb semiconductors is by oriented attachment of II-VI semiconductor nanocrystals into honeycomb superlattices. In this bottom-up approach, monodisperse quantum dots are fabricated using well-known synthesis procedures [59], and attached to each other by slowly evaporating the solvent under nitrogen atmosphere. By changing the process conditions, different type of structures can be formed ranging from linear structures to honeycomb structures. The oriented attachment is performed using PbSe quantum dots, honeycomb semiconductors of other compounds can be obtained from the PbSe structure by performing cation-exchange [60, 61] after the attachment process. Looking at the attachment in more detail, it shows that the quantum dots attach on the {100} facets [60, 62], and form a silicene-type honeycomb lattice [63]. Long-range transport measurements on two-dimensional square superstructures have shown the possibilities for these class of semiconductor devices [64], although improvements in the formation process are desired due to structural defects in the lattice and the small size of the crystalline domains [65, 66].

Theoretical modelling has demonstrated the interest and feasibility of honeycomb semiconductors. Kalesaki *et al.* [67] showed that in the case of CdSe semiconductors with

a honeycomb geometry, Dirac cones appear in the conduction band at two different energies, which are separated by a non trivial flat band. The lowest Dirac conduction band ( $s$ -like bands) can be compared with the  $\pi - \pi^*$  band of graphene, but the higher bands have no counterpart in graphene. These high-order bands ( $p$ -like bands) show a dispersive Dirac cone at the K-point and two flat-bands above and below the Dirac cone [68, 69].  $s$ - $p$  hybridization destroys the single-orbital bands including the interesting flat band when the coupling between the atomic sites is too large. Other types of symmetries are also investigated [70], which could be used to implement other interesting physical phenomena such as topological states [71].

## Nanopatterning III-V semiconductors

The ideal concept would be to design and construct honeycomb semiconductors using a method which is well-mastered in semiconductor industry. III-V Semiconductor QWs have already obtained a central place in opto-electronics and advanced logics. By using a top-down approach, these two-dimensional semiconductors can be patterned by means of nanolithography.

Such a lithographic design has several advantages: first, it can be applied to families of well-established semiconductor materials with low effective carrier mass and very high electron mobilities, such as several III-V semiconductors [72]. Secondly, by performing nanoporation using lithography, the size of the honeycomb unit cell can be altered in an independent way. This allows for a precise tuning of the electronic band structure. Lastly, the lithographic procedures can be directly applied to semiconductor quantum wells incorporated in classic transistor devices, allowing for direct investigation of the band structure and transport properties of the honeycomb semiconductor with a controllable position of the Fermi-level.

First efforts to design honeycomb semiconductors using nanolithography on III-V semiconductors were already performed. In previous works, a modulation-doped GaAs heterostructure subjected to a lateral attractive potential with honeycomb geometry was proposed [73–76]. Experiments revealed interesting many-body effects but direct evidence for massless Dirac fermions (MDFs) remains elusive because the width of the Dirac band was too small ( $\ll 0.1$  meV) due to the relatively large lattice constant ( $> 100$  nm) [77]. Recently, S. Wang *et al* realized a honeycomb semiconductor in a nanopatterned GaAs quantum well with a lattice constant of 50 nm. Resonant inelastic light-scattering spectra revealed some features of Dirac type bands [78]. However, it was reported that the lattice parameter of the honeycomb semiconductor based on GaAs heterostructures should be as low as 20 nm to directly observe MDFs in standard cryogenic conditions [54]. As a result, nanofabrication techniques should be pushed to their ultimate limit in terms of resolution.

We found that it is more effective to etch a triangular antidot lattice inside the QW instead of using attractive potential barriers. By creating a triangular antidot lattice directly in the semiconductor layer, a honeycomb semiconductor will be formed by the remainder of the semiconductor quantum well. Using this approach, the lattice

## II Understanding honeycomb semiconductors: Theoretical background

constant of the honeycomb unit cell can be decreased by a factor  $\sqrt{3}$  compared with previous results, which will increase the width of the Dirac band [79].

The width of the Dirac cone is not only dependent on the lattice constant of the honeycomb lattice, but also on the effective mass of the charge carriers in the employed semiconductor material. When lowering the effective mass of the semiconductor material, the effects of the lateral confinement are enhanced, resulting in a broader Dirac cone. Calculations from Tadjine *et al.* show that the energy range of the Dirac cone can extend over tens of meV in honeycomb semiconductors with a reasonable size of lattice parameters in InAs heterostructures [80]. In-based semiconductor materials are therefore more promising candidates as 2DEG channel materials for realizing Dirac semiconductors compared to GaAs, which was used in previous research. For instance, InGaAs with a relatively low electron effective mass ( $0.041m_0$  for  $\text{In}_{0.53}\text{Ga}_{0.47}\text{As}$  lattice-matched to InP), can be grown by molecular beam epitaxy (MBE) on InP barrier substrates using well-established routes, leading to 2DEG with high carrier mobility [81–84].

The general design for the honeycomb semiconductor obtained from a triangular antidot lattice presented in Fig. II.6A, from a top view and a side view perspective. The III-V semiconductor quantum well is nanoporated with pores forming a triangular antidot lattice with a pore-to-pore distance  $D$  and pore size  $d$ . The remaining semiconductor crystal can be considered as a two-dimensional semiconductor with a honeycomb geometry; the inequivalent lattice sites are indicated with red and blue spheres.

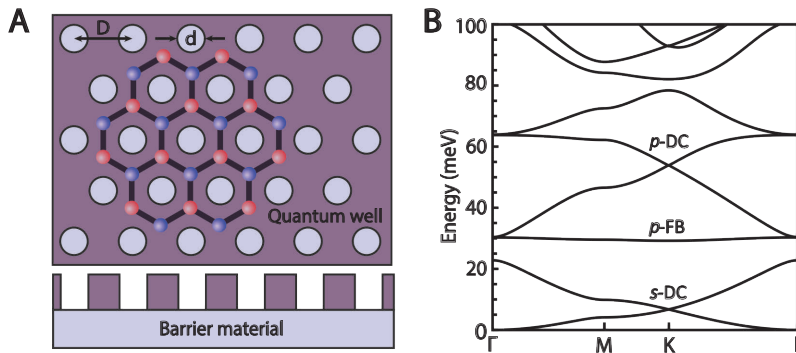


**Figure II.6: Electronic structure of a nanoporated InGaAs QW.** (A) Schematic top view and side view of the triangular etched III-V semiconductor quantum well, with a barrier material placed beneath to confine the electrons. The critical parameters for these lattices is the distance  $d$  between two adjacent pores, and the diameter  $D$  of the pores. (B) A typical band structure of a nanoporated InGaAs QW with lattice parameters  $D = 40$  nm and  $d = 24$  nm. The calculation is performed using a muffin-tin model, assuming a two-dimensional free electron gas at the bottom of the conduction band.

A calculated band structure of a nanoporated InGaAs quantum well with lattice parameters  $D = 40$  nm and  $d = 24$  nm is presented in Fig. II.6B, showing the lowest conduction bands of the honeycomb lattice [85]. The two lowest bands form a  $s$ -type

Dirac cone (*s*-type DC) at the K point. Looking at higher bands, a *p*-like flat band (*p*-type FB) and a second DC are obtained. Aside from the energy range, similar results are obtained in the tight-binding calculations on the heavy-element CdSe superlattices using a different calculation. Since this multi-orbital behaviour is absent in natural graphene, it would be very interesting to not only measure the first Dirac cone, but also higher orbital bands.

Multiple challenges need to be overcome in order to fabricate honeycomb semiconductors using nanolithography. The electrons need to be confined in the quantum well layer, while minimizing defects in the semiconductor material during the growth, lithography and etching process which can drastically alter the local electronic properties of the electrons. The pores in the nanoporated semiconductor need to be preferably fully cylindrical in order to obtain a true two-dimensional honeycomb semiconductor. Another important factor which is usually not considered is the quality of the build-in honeycomb symmetry etched in the QW. Positional disorder in the antidot lattice can greatly affect the symmetry in the lattice, perturbing the Dirac cone and providing mass to the carriers [86]. The fabrication of high quality antidot triangular lattices is essential for the observation of Dirac physics in these samples. It is therefore relevant to fully understand the complete fabrication process.

## II.4 Fabrication of honeycomb semiconductors

To fabricate a honeycomb semiconductor using nanolithography, a complete roadmap needs to be designed using various process steps. A general technological roadmap of the proposed fabrication method can be viewed in Fig. II.7. The main techniques will be discussed further in this chapter, but a general overlook of the whole process will be presented here.

In Fig. II.7A, the III-V semiconductor heterostructure is grown to assure that a two-dimensional electron gas is obtained. In this step, a thin layer of high-quality semiconductor material is grown on top of a semiconductor barrier material using molecular beam epitaxy (MBE). Most important is to pick a barrier material where the conduction band is higher in energy, which will confine the electron gas in the thin III-V semiconductor layer, obtaining a semiconductor quantum well (QW). With this technique, it is also possible to dope the barrier material or QW material by adding dopants during the growth process such that a gas of conduction electrons is present under equilibrium, rising the Fermi level of the heterostructure. On top of the QW layer, a thin layer of SiO<sub>2</sub> is grown to protect the QW layer from oxidation during the fabrication process.

After the growth of the semiconductor heterostructure, nanolithography can be performed onto the heterostructure. To start this process, a layer of organic resist is spin coated on top of the sample (Fig. II.7B). This organic layer will be exposed during the lithography process, changing the solubility of the exposed resist. For this research, a triangular pattern is exposed to the resist which can be viewed in Fig. II.7C. After the lithography process, the exposed parts of the resist can be removed by placing the sample in a chemical bath. This part of the process is called wet etching (Fig. II.7D). The

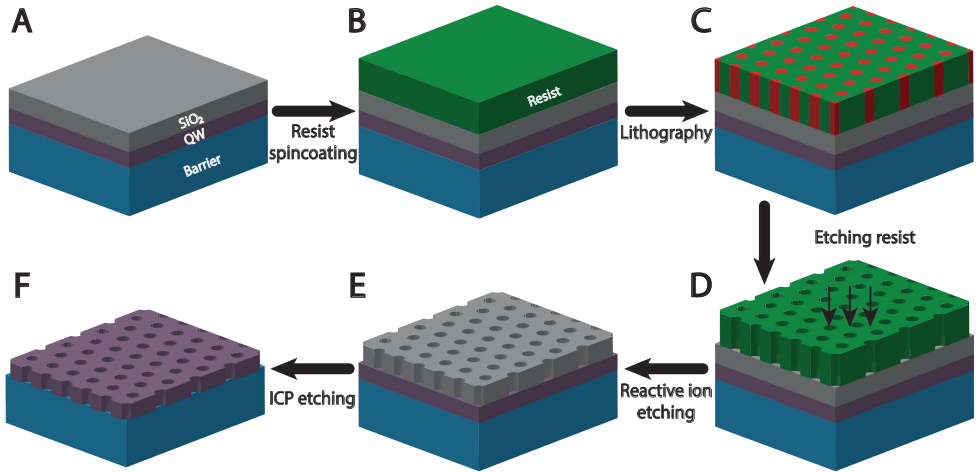


**Figure II.7: General fabrication process towards nanoporated III-V semiconductors.** (A) Growth of the III-V semiconductor heterostructure using molecular beam epitaxy. (B) Organic resist is spin coated on top of the semiconductor heterostructure. (C) Lithography process, where part of the organic resist is exposed (red), while another part is unexposed (green). (D) Exposed resist is etched using a wet etching process, forming a mask on top of the semiconductor heterostructure. (E-F) The pattern is etched into the protective SiO<sub>2</sub> layer (E) and heterostructure (F) using different dry etching processes.

etched resist layer will act as a mask to transfer the triangular pattern initially into the SiO<sub>2</sub> layer, followed by an etching process to transfer the pattern into the underlying semiconductor layer (Fig. II.7E-F). Dry etching is performed by bombarding the etched resist layer with a mixtures of atoms or molecules inside a reactive ion etching chamber.

Although the principles are simple, many steps are involved during the total fabrication process using various instruments. Each step will be discussed in more detail for a better understanding of each fabrication procedure.

## Molecular beam epitaxy

High-quality semiconductor thin films can be grown using molecular beam epitaxy (MBE). This is a thin-film deposition method for growing epitaxially single elements onto a wafer. The method was developed in the late 1970s in the Bell Telephone lab by Alfred Y. Cho and J.R. Arthur [87]. Nowadays, it is commonly used to fabricate diodes and MOSFETs (metal-oxide-semiconductor field-effect transistors). MOSFETs are generally used to switch electronic signals, and therefore form the basis of modern electronics.

A schematic view of the MBE chamber can be viewed in Fig II.8A. From effusion cells, various materials can be heated such as III-V semiconductors, II-VI semiconductors and silicides until the material sublimates. The cells are directed towards the wafer,

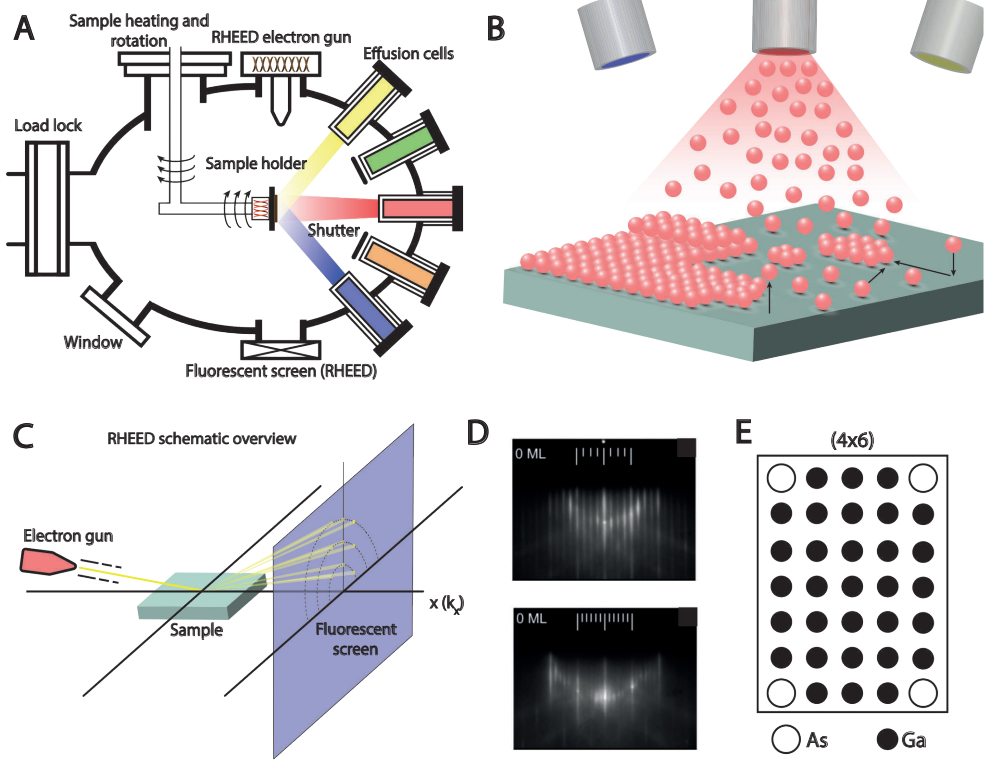


**Figure II.8: Molecular beam epitaxy.** (A) Schematic view of the vacuum chamber of a MBE. (B) Schematic view of the deposition of atoms onto the surface. (C) Schematic overview of the RHEED setup. (D) An example of a RHEED pattern of the growth of GaAs along the  $[110]$  (top image) and  $[\bar{1}10]$  (bottom image) direction. (E) Schematic view of the  $(4 \times 6)$  surface reconstruction of GaAs. Adapted from [88, 89].

and the gaseous material condenses onto the wafer (Fig. II.8B). The mean free path of an atom inside the chamber will go up to 1 km due to the low pressure inside the chamber ( $10^{-11}$  mbar), meaning that no collisions will take place with other particles when it travels to the surface of the wafer. This will result in a high quality film with low impurities from other gases in the chamber. The number of impurities  $\phi$  is linear with the pressure, and it is therefore essential to work in ultra high vacuum, as can be understood from the Hertz-Knudsen equation [90, 91]:

$$\phi = \frac{P}{\sqrt{2\pi M k_B T}} \quad (\text{II.33})$$

where  $P$  is the pressure of the impurity element,  $M$  is the molar mass of the impurity,  $k_B$  is the Boltzmann constant and  $T$  is the temperature.

When the atoms arrive onto the wafer, they react with the wafer or other condensed atoms, forming a crystalline layer of material. The deposition rate onto the wafer can be controlled at a sub-monolayer level by changing the temperature of the sources and

opening or closing the shutter of the effusion cells. Diffusion and desorption of the substrate can be controlled using sample heating. Sample heating can also be used to introduce dopants to the film, enabling to create n-type or p-type semiconductor films.

The surface quality of the grown quantum well is usually monitored *in situ* using high-energy electron diffraction (RHEED). An electron gun targets electrons onto the surface of the wafer during the growth, which reflects onto a fluorescent screen. By following the pattern, the surface reconstruction of the film can be measured, and the growth kinetics of the sample can be observed. This technique can also observe removal of contaminants from the substrate surface, and to determine the stoichiometry. A schematic overview of this technique is presented in Fig. II.8C. In Fig. II.8D-E, a typical line pattern is presented of a GaAs wafer during the MBE growth. A four line pattern can be observed in the top image, while in the bottom image a six line pattern can be viewed when observing from a different angle. Combining both patterns, a (4×6) surface reconstruction can be extracted from both images. During the growth, the surface reconstruction will naturally change of the grown film. The challenge in this technique is to control mono layer growth with high lateral uniformity while retaining the structural quality and epitaxial match between layers.

### Nanolithography

Originally, lithography is a method of printing text and figures using immiscible oil and water phases, and was invented in 1796 by a German author Senefelder, who used it to publish theatrical works. Nanolithography refers specifically to patterns smaller than 100 nm, which are lithographically obtained. It is a technique which is often applied in the fabrication of semiconductor devices. A large number of different nanolithography techniques exist or are being developed. The most well-known technique is photolithography, which uses photons to transfer a geometric pattern to a photosensitive material (photoresist) [92]. Other techniques are for example nanoimprint lithography [93], X-ray lithography [94,95] and scanning probe lithography [96,97].

The two lithography techniques used during this research are electron-beam lithography (EBL) and block copolymer lithography (BCP). Both techniques will be discussed in more detail.

#### Electron-beam lithography

Electron-beam lithography is a writing technique where a focused beam of electrons writes a pattern in an organic resist [98]. The beam size is very small compared with photolithography, which enables to create smaller structures. Thus, this technique is ideal for small scale production of electronic devices. Electron-beam lithography is not conventionally used in large scale production due to the long duration of writing large-scale patterns. This can be easily understood when calculating the time  $t$  to write an area  $A$ , which is dependent on the electron beam dose  $D$  and beam current  $I$ :

$$D \cdot A = t \cdot I \tag{II.34}$$

For example, to write a total exposure area of  $1\text{ cm}^2$  using a typical dose of  $10^{-3}\text{ C/cm}^2$  and a beam current of  $10^{-9}\text{ A}$ , the minimum writing time would be  $10^6$  seconds, which is about 12 days. Therefore, optimization of EBL writing time by using different scanning techniques [99, 100] or different shaped electron beams [101, 102] is a leading research field in the lithography community.

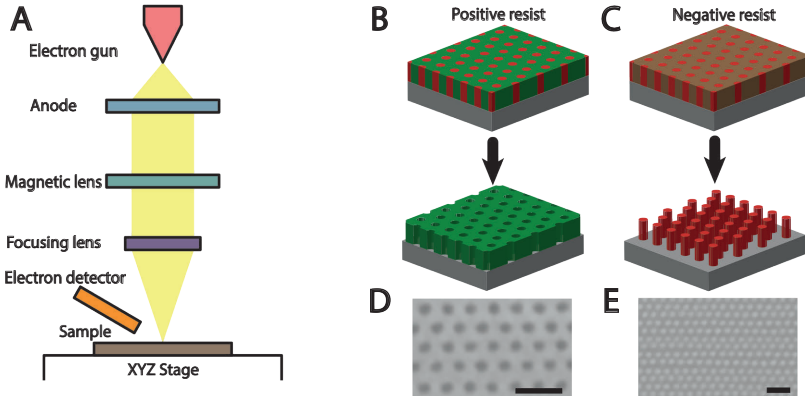


**Figure II.9: Electron-beam lithography.** (A) Schematic overview of an electron-beam lithography machine setup. (B-C) Development of a positive resist and a negative resist. The result shows that pores and pillars respectively are obtained. (D) SEM image of a developed PMMA resist on top of a GaAs substrate. Scalebar denotes 100 nm. (E) SEM image of a developed HSQ resist on top of a GaAs/SiO<sub>2</sub> substrate. Scalebar denotes 100 nm.

A schematic setup of a typical electron-beam lithography column inside the machine can be viewed in Fig II.9A. Electrons are generated from an electron source and accelerated to the anode with a typical acceleration voltage of 100 kV. Different lenses are used to focus the electron into a bundle with a certain size and shape. The beam is accelerated towards the resist of the sample, which is sensitive to high-energy electrons. The chamber of the EBL is kept under vacuum ( $10^{-6}$  mbar) to limit collisions of electrons with other elements in the chamber, keeping the electron bundle uniform in shape and energy. When the primary electrons hit the resist, chemical bonds are formed or destroyed, changing the chemical composition of the exposed resist, and therefore the solubility. For a positive resist, the exposed resist will be removed when rinsing the sample with an appropriate solvent, creating an organic mask on top of the sample (Fig. II.9B). The most widely used positive resist is polymethyl methacrylate (PMMA), which is a high-resolution resist with low sensitivity [103–105]. Another widely used resist is hydrogen silsesquioxane (HSQ), which is a negative resist [106–109] (Fig. II.9C). Here, the unexposed resist is removed during the wet etching step, leaving the exposed resist onto the wafer. When printing a similar pattern, organic pillars in a triangular symmetry are obtained onto the wafer in stead of pores. The difference between the two types of resist can also be observed in Fig. II.9D-E when printing pores in a triangular symmetry. In the first scanning electron microscope (SEM) image, dark spots can be observed, which are holes inside the organic mask. The second image shows bright spots, which are organic pillars on top of the wafer.

Although it depends on more factors, the resolution in this technique is mainly limited due to the proximity effect [110]. This effect occurs when two patterned areas merge together if the areas are too small or are too close to each other. The cause of this effect is due to inelastic scattering of the primary electrons from the incident beam line onto the resist or substrate, changing the direction of the primary electrons. When the primary electrons hit the atomic electrons of the resist, secondary electrons can be produced. These electrons can also generate lower energy electrons, which can result in an electron cascade throughout the resist. The secondary electrons can transfer to other patterned areas, resulting in disordered patterns. The proximity effect is already intensively studied [111–114], and various correction procedures have been proposed to limit this effect by applying different electron beam doses depending on the geometry of the pattern [115]. In addition, the use of high-energy electron beams will also reduce the proximity effect [116].

### Block copolymer lithography

Another lithography technique used in this research is block copolymer (BCP) lithography. In this technique, block copolymers are used to obtain long-range self-assembled morphologies, which can be etched to obtain nano patterns with large length scales and low costs. A block copolymer are two or more monomers which have been polymerized in long chains and form subunits of homopolymers (Fig. II.10A). They are generally fabricated using various polymerization techniques. A thin layer of the polymer mixture can be spin coated on top of the sample, similar as any other resist for electron-beam lithography or photo lithography. Upon annealing the wafer with the polymer mixture, various self-assembled morphologies can be obtained. By performing plasma etching, one of the polymers can be removed, and the remaining polymer layer can be used as a mask to etch the obtained pattern into the semiconductor wafer. The process scheme is presented in Fig. II.10B.

Various self-assembled microphases can be obtained, including lamellae (L), gyroid networks (G), hexagonally close-packed cylinders (H) and spheres (S) [119]. The type of morphology can be controlled by changing the degree of polymerization ( $N$ ), the Flory-Huggins parameter, which is the interaction between the different polymers ( $\chi_{AB}$ ) and the relative volume fraction of each block ( $f_A, f_B$ ) [120]. A phase diagram can be constructed (Fig. II.10C), showing how different microphases can be acquired by varying  $f = f_A/f_B$ ,  $\chi_{AB}$  and  $N$ . The different Flory-Huggins parameters between polymers can be predicted by extensive computer simulations [121]. The resolution of the morphology can be controlled by varying  $N$  and  $\chi_{AB}$ , since the domain length  $L_0$  scale with  $\chi_{AB}^{1/6} N^{2/3}$  [122]. This means that when increasing the Flory-Huggins parameter and decreasing the polymerization length  $N$ , the same microphase can be obtained while increasing the resolution of the domain. Feature sizes with lattice spacings of 7 nm have already been reported [123].

By optimizing the plasma etching procedure, the quality of the domains can be enhanced [124] and ordered, high-quality nanopatterns can be obtained with much lower periodicities compared to EBL [125]. The nanopatterns can be transferred into the

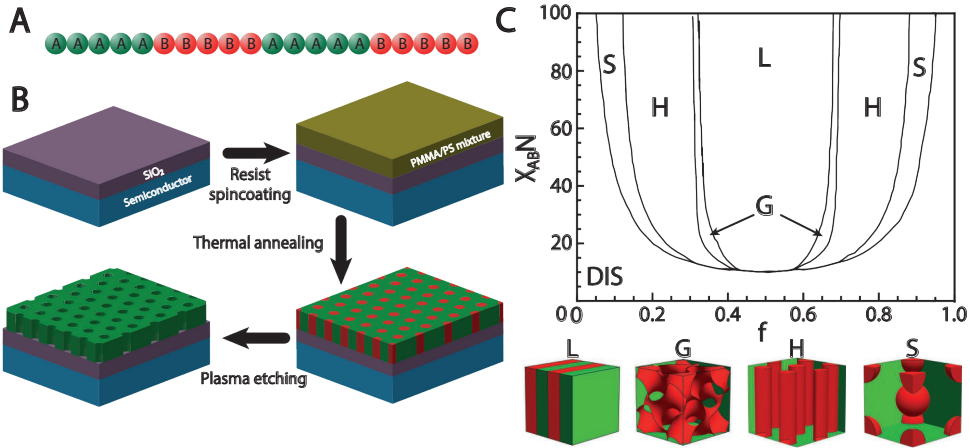


**Figure II.10: Block copolymer lithography.** (A) Schematic view of a block copolymer, consisting of two different polymers which are attached in a block formation. (B) Schematic overview of the block copolymer lithography process. (C) Phase diagram showing how to obtain different microphases in a polymer mixture by changing the volume fraction of the polymers, the interaction and the chain length. Adapted from [117, 118].

semiconductor wafer using similar techniques as in conventional lithography [126], which can be used to further etch down the sample or grow other structures on top of the etched wafer such as quantum dots [127] or nanowires [128]. Extensive studies have already shown the possibility to create long-range, defect free systems [129, 130], which opens up a new route towards ultra-high density systems.

## Dry etching techniques

The last part in the fabrication process will be etching the mask with the obtained pattern into the semiconductor layers. This will be performed using various dry etching steps. Dry etching refers to removal of material by bombarding ions onto the wafer. It is widely used in the semiconductor industry due to the ability to etch very small features with high anisotropic etch profiles patterns, and the etching parameters are easy to control. Dry etching can be performed by both physical bombardment or by chemical reaction between the ions and the semiconductor layer.

The dry etching step mostly used in this research is reactive ion etching (RIE), which is a plasma dry etching step where ions are created from a gas and are launched directly to the sample by using an electromagnetic field under low pressures. This will uniformly remove material from the wafer by using both physical removal and chemical reaction. Various settings control the etching rates and the profiles of the etched layers: the temperature of the surface of the wafer, the flow rate of the used gas (scm), the chamber pressure and the RF power. Depending on the material that needs to be patterned, different gases can be used. For example, sulfur hexafluoride ( $\text{SF}_6$ ) is commonly used to etch silicon-based materials. Many standard procedures are already provided to accurately etch different materials [131–134]. Lastly, this technique can

also be used in more gentle etching steps to remove residual resist from the wafer, for instance by employing an oxygen plasma.

When a more controlled etching procedure is desired for high-quality etching profiles at low dimensions, inductively coupled plasma (ICP)-RIE can be deployed. In this process, similar techniques are used compared with regular RIE, but the ion density and ion energy can be decoupled from each other, enabling more flexibility during the etching process. By wrapping a coil around the plasma in the RIE chamber, further ionization of the plasma can be achieved, creating more or less ions by varying the ICP-power over the coils. This will result in a higher quality etching profiles than for standard RIE. Similar gases can be used as in regular RIE to etch different materials. ICP-RIE etching using a boron trichloride ( $\text{BCl}_3$ ) based plasma already showed promising results on III-V semiconductors such as InGaAs [133, 135]. Therefore, this plasma is used in this research to etch the triangular pattern into the III-V semiconductor quantum well layer.

### II.5 Scanning tunneling microscopy and spectroscopy

Scanning tunneling microscopy (STM) is a technique to image surfaces on the atomic scale while spectroscopy is used to determine the local electronic properties by measuring the local density of states (LDOS). This technique was invented by Rohrer and Binnig in 1981 [136, 137], who measured a  $7 \times 7$  surface reconstruction of a Si(111) crystal on the atomic scale [138]. The possibilities of STM does not only extend to measuring the surface accurately or probe the local electronic attributes, but it also extends to the manipulation of atoms [139] which could be used to form electronic lattices [140] and chemical identification of molecules and atoms using their magnetic [141–143], vibrational [144] or optical [145] properties. In order to achieve image resolution on the order to the atomic scale, measurements are normally performed under ultra high vacuum (UHV) with a typical pressure  $p = 10^{-11}$  mbar, and cryogenic conditions ( $T = 4.1$  K). To better understand the technique and physics behind scanning tunneling microscopy and spectroscopy, a concise background will be presented below.

#### Surface imaging

STM uses the concept of quantum tunneling, meaning that electrons tunnel through a small vacuum gap from an atomically sharp tip to a surface when a bias voltage is applied between the tip and the sample (Fig. II.11A). The distance between the end of the tip and the surface is about 0.5 to 1 nm. The tunneling current  $I$  depends on the bias  $V$ , and increases exponentially with decreasing tip-sample distance  $d$ . With an electric driven piezo, the tip is manoeuvred over the surface of the sample. When using constant-current mode, a feedback loop is applied to keep the tunneling current constant, changing the height of the tip with values  $\Delta z$ , which are used to construct a height map of the measured surface. Not only will this mode produce high-resolution topography images of the surface, but this mode will also prevent damage to the tip due to the proximity of the tip and surface.

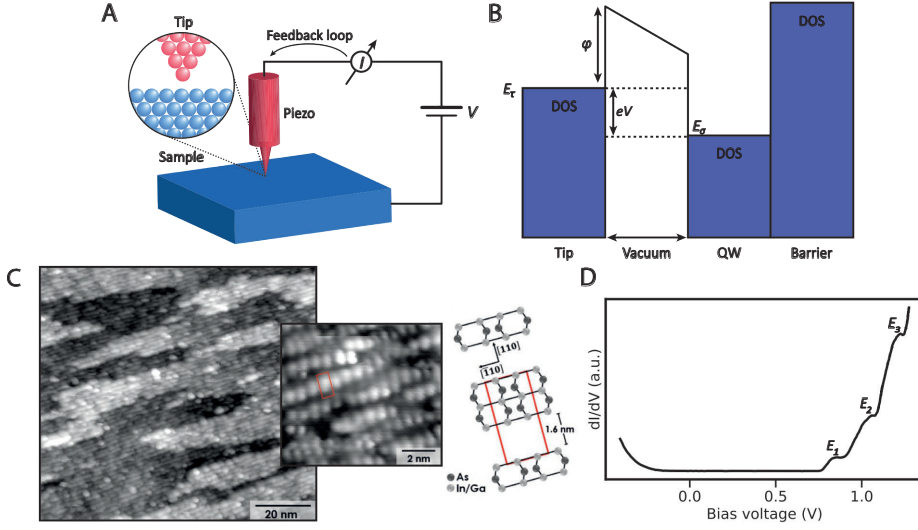


**Figure II.11: Scanning tunneling microscopy.** (A) Schematic overview of the STM principles in constant-current mode. (B) Energy landscape of the tip/vacuum/quantum well sample present on a barrier materials. (C) High-resolution STM image of a MBE grown  $\text{In}_{0.53}\text{Ga}_{0.47}\text{As}(001)$  QW. A zoom-in on the surface shows a  $(2 \times 4)$  surface reconstruction, which is schematically presented besides the STM scan. Imaging parameters:  $I = 10$  pA,  $V = 1.8$  V for both STM images. (D) Differential conductance spectrum acquired above an MBE grown  $\text{In}_{0.53}\text{Ga}_{0.47}\text{As}/\text{InP}$  heterostructure. Clear steps can be observed in the conduction band at 0.8 V, 1.0 V and 1.2 V indicated by  $E_1$ ,  $E_2$  and  $E_3$  respectively, showing the step-like behaviour of the local density of states. Feedback parameters:  $V = 1.3$  V,  $I = 400$  pA. Both the STM images and the differential conductance spectrum are adapted from [9].

To describe the tunneling of the electrons more accurately, time dependent perturbation theory can be used, as originally proposed by Bardeen. The tunneling current can be written using Fermi's golden rule:

$$I = \frac{2\pi e}{\hbar} \sum_{\tau, \sigma} f(E_{\tau}) [1 - f(E_{\sigma} + eV)] |M|^2 \delta(E_{\tau} - E_{\sigma}) \quad (\text{II.35})$$

where  $M$  is the tunneling matrix, which describes the coupling between the sample and the tip,  $\delta$  is the Dirac delta function,  $f(E)$  is the Fermi distribution and  $E_{\tau}$  and  $E_{\sigma}$  are the energies corresponding the states  $\tau$  of the tip and  $\sigma$  of the sample respectively [146, 147]. When using Fermi's golden rule, a couple of assumptions were taken into account: electron tunneling is approximated as a one-particle process, meaning that interactions between electrons are neglected, which is a good approximation in the low tunneling regime. Secondly, coupled electronic states between sample and tip are disregarded, which is valid if the distance between tip and sample is large enough ( $> 0.4$  nm). Lastly, the electrons tunnel elastically from the tip to the sample, meaning that there is no energy loss in this process.

The tunneling matrix  $M_{mn}$  derived from the tunneling current can be expressed using

## II Understanding honeycomb semiconductors: Theoretical background

---

the wave function from the state  $m$  in the tip  $\phi_m^T$  and states  $n$  in the sample  $\phi_n^S$ :

$$M_{mn} = \frac{\hbar^2}{2m} \int \left[ \phi_n^S \nabla \phi_m^{T*} - \phi_m^{T*} \nabla \phi_n^S \right] \cdot d\mathbf{S} \quad (\text{II.36})$$

meaning that the current between the tip and sample is not only dependent on the wave function of the sample, but also on the wave function of the tip [148]. A general approximation which can be made is the assumption that the end of the tip is perfectly spherical, which would lead to a symmetrical  $s$  orbital wave function from the end of the tip. Coupling from the bulk of the tip can be neglected, since the distance between bulk states and sample states is much larger. This will significantly simplify the tunneling matrix  $M_{mn}$ , showing the exponential dependence between the tunneling current and the distance between the sample and the tip  $d$  when a bias voltage  $eV$  is applied which is smaller than the work function  $\phi$  [149]:

$$I \propto \int_{E_F}^{E_F+eV} \rho_T(E-eV) \rho_S(E) \exp\left(-2d \frac{\sqrt{2m\phi}}{\hbar}\right) dE \quad (\text{II.37})$$

where  $\rho_T$  and  $\rho_S$  are the energy-dependent density of states (DOS) of the tip and sample respectively. We obtain indeed that the current is exponentially dependent on the distance  $d$  between tip and sample. A schematic representation of the electron tunneling is illustrated in Fig. II.11B. Now that the tunneling current is expressed as a function of the density of states of the sample, we can define the local density of states (LDOS) at vector position  $\mathbf{x}_0$ , which is proportional to the total DOS of the sample.

$$\rho_S(E, \mathbf{x}_0) \propto \rho_S \exp\left(-2d \frac{\sqrt{2m\phi}}{\hbar}\right) \quad (\text{II.38})$$

This equation is only for a good approximation for coupled  $s$  orbitals between the sample and the tip, and when a spherical, point-like tip at the center of curvature  $\mathbf{x}_0$  is assumed. This will finally yield an equation where the variation in the tunneling current is proportional to the local density of states of the sample:

$$I \propto \int_{E_F}^{E_F+eV} \rho_T(E-eV) \rho_S(E, \mathbf{x}_0) dE \quad (\text{II.39})$$

The exponential dependence of the tunneling current on the tip-sample distance gives the opportunity to create atomically precise image with high resolution. A typical STM image of  $\text{In}_{0.53}\text{Ga}_{0.47}\text{As}(001)$  QW grown by MBE is presented in Fig. II.11C, adapted from [9]. Individual atomic terraces can be identified, and a  $(2 \times 4)$  surface reconstruction can be observed, giving direct information how the atoms are arranged near the surface of the quantum well.

### Differential conductance measurements

The local electronic properties of a conducting material can be investigated by measuring the local density of states using the scanning tunneling microscope. The local

density of states of the sample can be accessed due to the linear relation between the differential conductance  $dI/dV$  and  $\rho_S$ . This can be easily obtained by taking the derivative of Eq. (II.5):

$$\frac{dI}{dV}(V) \propto \rho_T \cdot \rho_S(E_F + eV, \mathbf{x}_0) \quad (\text{II.40})$$

The DOS of the tip  $\rho_T$  is assumed to be constant at different energies and different positions of the tip onto the sample, meaning that the differential conductance is directly related to the local electronic structure of the sample.

The differential conductance can be obtained using a modulation technique. A bias modulation is superimposed to the bias voltage applied between the tip and the sample using a lock-in amplifier with a modulation frequency  $\omega_{\text{mod}}$ .

$$V = V_0 + V_{\text{mod}} \cos(\omega_{\text{mod}} t) \quad (\text{II.41})$$

The modulation in the bias voltage will automatically introduce a small modulation to the tunneling current  $I(V)$ . For small oscillations around a bias voltage  $V_0$ , a Taylor expansion can be used to approximate  $I(V)$ :

$$I(V) = I(V_0) + \left. \frac{dI}{dV} \right|_{V_0} (V - V_0) + \dots \quad (\text{II.42})$$

Here, only the zeroth and first order terms are taken into account, which is a good approximation for small oscillations ( $V - V_0$ ). The modulated bias voltage can be implemented in this equation, yielding:

$$\begin{aligned} I(V) &= I(V_0) + \left. \frac{dI}{dV} \right|_{V_0} V_{\text{mod}} \cos(\omega_{\text{mod}} t) \\ &= I(V_0) + I_{\text{mod}} \cos(\omega_{\text{mod}} t) \end{aligned}$$

showing that the differential conductance can be measured using the modulation in the current, providing direct access to the local electronic structure of the sample.

A typical differential-conductance spectrum of an InGaAs/InP heterostructure can be viewed in Fig. II.11D, adapted from [9]. A bias voltage  $V$  of 1.3 V is applied, and swept down to -0.4 V, before increasing back to 1.3 V. In the spectrum, a valence band between -0.25 V and -0.4 V and a conduction band between 0.8 V and 1.3 V is observed, separated by a clear band gap of 0.9 V. In the conduction band, three steps (indicated by  $E_1$ ,  $E_2$  and  $E_3$  respectively) are visible in the spectrum, which can be assigned to the electronic structure of a two-dimensional semiconductor material. Differences between theoretical spectra and experimental spectra can be explained by defects in the quantum well or tip induced band bending [9, 150]. Further increase of the bias voltage will result in leaking of electrons to the InP barrier material, losing the two-dimensional characteristics in the electronic structure, and obtaining the electronic structure of a bulk semiconductor.

## Broadening

Although differential conductance spectroscopy is a powerful tool to measure the electronic properties of a material, various sources of broadening have to be taken into

---

account. First, the intrinsic lifetime  $\tau$  of the electrons in a III-V semiconductor quantum well state need to be taken into account. A straightforward calculation shows that the intrinsic lifetime of an electron trapped in a two-dimensional semiconductor layer can extend to tens of nanoseconds [9, 151, 152] without any nanoporation, which is mainly determined by electron-electron and electron-phonon interactions. Following the uncertainty principle, this translates to a Lorentzian broadening of  $\Gamma = \hbar/\tau = 0.00065$  meV, which is very low compared with the experimental measured energy width. The long lifetime of the electrons also allow for large coherence lengths, i.e. the average propagation distance of an electron before it collides with other particles. Since the coherence length is typical larger than the unit cell size of the lattice, Dirac physics can be observed in these materials. However, this is only the case for a perfect two-dimensional electron gas. Since electrons can easily be scattered into bulk states by defects in the material such as step edges or dopants, the electron lifetime will be much lower. More importantly, the Bloch wave functions will scatter with the disordered potential barriers in the periodic honeycomb landscape, which will drastically increase the energy broadening of the electrons confined to the honeycomb symmetry.

Differential conductance spectroscopy on the nanoporated honeycomb semiconductor exhibit an energy broadening of approximately  $\Gamma = 5 - 8$  meV, which can mainly be assigned due to scattering via the disordered potential barriers. Compared with artificial lattices on the more widely used Cu(111) surface, this value is much lower, allowing us to perform scanning tunneling spectroscopy on lattices with larger unit cells [153]. Since the bandwidth of Dirac features in the desired unit cell size are in the order of 10 meV or higher, no major loss of resolution is expected when performing differential conductance measurements on a honeycomb semiconductor.

Another source of broadening originates from modulation of the bias voltage, which is in the order of  $\Delta E_{\text{rms}} \approx 1.22V_{\text{rms}} = 6.2$  mV when a typical bias modulation of  $V_{\text{rms}} = 5$  mV is used. Also thermal broadening could potentially play a role, but can be neglected since the thermal broadening  $\Delta E_{th}$  is much smaller compared with other sources of broadening ( $\Delta E_{th} \approx 5.4k_B T = 0.65$  mV at liquid helium temperatures [154]).

---

## References

- [1] C. Kittel, *Introduction to Solid State Physics*. Wiley, 8 ed., 2004.
- [2] J. R. Chelikowsky and M. L. Cohen, “Electronic structure of silicon,” *Physical Review B*, vol. 10, no. 12, pp. 5095–5107, 1974.
- [3] M. Gmitra and J. Fabian, “First-principles studies of orbital and spin-orbit properties of GaAs, GaSb, InAs, and InSb zinc-blende and wurtzite semiconductors,” *Physical Review B*, vol. 94, p. 165202, oct 2016.
- [4] H. Hook, J R, Hall, *Solid State Physics*. second ed., 1991.
- [5] M. Prairie and R. Kolbas, “A general derivation of the density of states function for quantum wells and superlattices,” *Superlattices and Microstructures*, vol. 7, pp. 269–277, jan 1990.
- [6] F. CAPASSO, “Band-Gap Engineering: From Physics and Materials to New Semiconductor Devices,” *Science*, vol. 235, pp. 172–176, jan 1987.
- [7] Z. I. Alferov, “Nobel lecture: The double heterostructure concept and its applications in physics, electronics, and technology,” *International Journal of Modern Physics B*, vol. 16, pp. 647–675, feb 2002.
- [8] S. Perraud, K. Kanisawa, Z. Z. Wang, and T. Fujisawa, “Imaging the percolation of localized states in a multisubband two-dimensional electronic system subject to a disorder potential,” *Physical Review B - Condensed Matter and Materials Physics*, vol. 76, no. 19, p. 195333, 2007.
- [9] N. A. Franchina Vergel, A. Tadjine, V. Notot, M. Mohr, A. Kouassi N’Guissan, C. Coinon, M. Berthe, L. Biadala, K. K. Sossoe, M. M. Dzagli, J.-C. Girard, G. Rodary, L. Desplanque, R. Berndt, D. Stievenard, X. Wallart, C. Delerue, and B. Grandidier, “Influence of doping level and surface states in tunneling spectroscopy of an  $\text{In}_{0.53}\text{Ga}_{0.47}\text{As}$  quantum well grown on p-type doped  $\text{InP}(001)$ ,” *Physical Review Materials*, vol. 3, p. 094604, sep 2019.
- [10] P. R. Wallace, “The Band Theory of Graphite,” *Physical Review*, vol. 71, pp. 622–634, may 1947.
- [11] J. W. McClure, “Diamagnetism of Graphite,” *Physical Review*, vol. 104, pp. 666–671, nov 1956.
- [12] D. P. DiVincenzo and E. J. Mele, “Self-consistent effective-mass theory for intralayer screening in graphite intercalation compounds,” *Physical Review B*, vol. 29, pp. 1685–1694, feb 1984.
- [13] G. Ruess and F. Vogt, “Hochstlammellarer Kohlenstoff aus Graphitoxhydroxyd.,” *Monatshfte fur Chemie*, vol. 78, no. 3-4, pp. 222–242, 1948.
- [14] C. Oshima and A. Nagashima, “Ultra-thin epitaxial films of graphite and hexagonal boron nitride on solid surfaces,” *Journal of Physics: Condensed Matter*, vol. 9, pp. 1–20, jan 1997.
- [15] A. K. Geim and K. Novoselov, “The rise of graphene,” *Nature Mater.*, vol. 6, no. 3, pp. 183–191, 2007.
- [16] K. Novoselov, A. Geim, S. Morozov, D. Jiang, Y. Zhang, S. Dubonos, I. Grigorieva, and A. Firsov, “Electric Field Effect in Atomically Thin Carbon Films,” *Science*, vol. 306, no. 666, pp. 666–669, 2004.
- [17] K. S. Novoselov, A. K. Geim, S. V. Morozov, D. Jiang, M. I. Katsnelson, I. V. Grigorieva, S. V. Dubonos, and A. A. Firsov, “Two-dimensional gas of massless Dirac fermions in graphene,” *Nature*, vol. 438, no. 7065, pp. 197–200, 2005.
- [18] K. I. Bolotin, F. Ghahari, M. D. Shulman, H. L. Stormer, and P. Kim, “Observation of the fractional quantum Hall effect in graphene,” *Nature*, vol. 462, pp. 196–199, nov 2009.
- [19] X. Du, I. Skachko, F. Duerr, A. Luican, and E. Y. Andrei, “Fractional quantum Hall effect and insulating phase of Dirac electrons in graphene,” *Nature*, vol. 462, pp. 192–195, nov 2009.
- [20] P. Avouris, *Physics of Graphene*. NanoScience and Technology, Cham: Springer International Publishing, 2014.
- [21] O. A. Shenderova, V. V. Zhirnov, and D. W. Brenner, “Carbon Nanostructures,” *Critical Reviews in Solid State and Materials Sciences*, vol. 27, pp. 227–356, jul 2002.
- [22] F. Bloch, “Über die Quantenmechanik der Elektronen in Kristallgittern,” *Zeitschrift für physik*, vol. 52, no. 7, pp. 555–600, 1929.
- [23] S. Reich, J. Maultzsch, C. Thomsen, and P. Ordejón, “Tight-binding description of graphene,” *Physical Review B*, vol. 66, p. 035412, jul 2002.

- 
- [24] A. H. Castro Neto, F. Guinea, N. M. R. Peres, K. S. Novoselov, and A. K. Geim, "The electronic properties of graphene," *Reviews of Modern Physics*, vol. 81, pp. 109–162, jan 2009.
- [25] E. Kogan and V. U. Nazarov, "Symmetry classification of energy bands in graphene," *Physical Review B*, vol. 85, p. 115418, mar 2012.
- [26] V. M. Silkin, J. Zhao, F. Guinea, E. V. Chulkov, P. M. Echenique, and H. Petek, "Image potential states in graphene," *Physical Review B*, vol. 80, p. 121408, sep 2009.
- [27] V. N. Popov and L. Henrard, "Comparative study of the optical properties of single-walled carbon nanotubes within orthogonal and nonorthogonal tight-binding models," *Physical Review B*, vol. 70, p. 115407, sep 2004.
- [28] F. Bonaccorso, Z. Sun, T. Hasan, and A. C. Ferrari, "Graphene photonics and optoelectronics," *Nature Photonics*, vol. 4, pp. 611–622, sep 2010.
- [29] D. R. Cooper, B. D'Anjou, N. Ghattamaneni, B. Harack, M. Hilke, A. Horth, N. Majlis, M. Massicotte, L. Vandsburger, E. Whiteway, and V. Yu, "Experimental Review of Graphene," *ISRN Condensed Matter Physics*, vol. 2012, pp. 1–56, 2012.
- [30] S. Fujita and A. Suzuki, "Theory of the Half-integer Quantum Hall Effect in Graphene," *International Journal of Theoretical Physics*, vol. 55, no. 11, pp. 4830–4840, 2016.
- [31] V. P. Gusynin, S. G. Sharapov, and J. P. Carbotte, "AC conductivity of graphene: From tight-binding model to  $2 + 1$ -dimensional quantum electrodynamics," 2007.
- [32] V. P. Gusynin and S. G. Sharapov, "Magnetic oscillations in planar systems with the Dirac-like spectrum of quasiparticle excitations. II. Transport properties," *Physical Review B*, vol. 71, p. 125124, mar 2005.
- [33] A. A. Balandin, S. Ghosh, W. Bao, I. Calizo, D. Teweldebrhan, F. Miao, and C. N. Lau, "Superior Thermal Conductivity of Single-Layer Graphene," *Nano Letters*, vol. 8, pp. 902–907, mar 2008.
- [34] W. Cai, A. L. Moore, Y. Zhu, X. Li, S. Chen, L. Shi, and R. S. Ruoff, "Thermal Transport in Suspended and Supported Monolayer Graphene Grown by Chemical Vapor Deposition," *Nano Letters*, vol. 10, pp. 1645–1651, may 2010.
- [35] G. L. Klimchitskaya, V. M. Mostepanenko, and V. M. Petrov, "Conductivity of graphene in the framework of Dirac model: Interplay between nonzero mass gap and chemical potential," *Physical Review B*, vol. 96, p. 235432, dec 2017.
- [36] J. Wang, S. Deng, Z. Liu, and Z. Liu, "The rare two-dimensional materials with Dirac cones," *National Science Review*, vol. 2, pp. 22–39, mar 2015.
- [37] S. Cahangirov, M. Topsakal, E. Aktürk, H. Şahin, and S. Ciraci, "Two- and One-Dimensional Honeycomb Structures of Silicon and Germanium," *Physical Review Letters*, vol. 102, p. 236804, jun 2009.
- [38] C. C. Liu, W. Feng, and Y. Yao, "Quantum spin Hall effect in silicene and two-dimensional germanium," *Physical Review Letters*, vol. 107, no. 7, pp. 1–4, 2011.
- [39] P. Vogt, P. De Padova, C. Quaresima, J. Avila, E. Frantzeskakis, M. C. Asensio, A. Resta, B. Ealet, and G. Le Lay, "Silicene: Compelling experimental evidence for graphenelike two-dimensional silicon," *Physical Review Letters*, vol. 108, no. 15, pp. 1–5, 2012.
- [40] A. Fleurence, R. Friedlein, T. Ozaki, H. Kawai, Y. Wang, and Y. Yamada-Takamura, "Experimental evidence for epitaxial silicene on diboride thin films," *Physical Review Letters*, vol. 108, no. 24, pp. 1–5, 2012.
- [41] D. Chiappe, E. Scalise, E. Cinquanta, C. Grazianetti, B. Van Den Broek, M. Fanciulli, M. Houssa, and A. Molle, "Two-dimensional Si nanosheets with local hexagonal structure on a MoS<sub>2</sub> surface," *Advanced Materials*, vol. 26, no. 13, pp. 2096–2101, 2014.
- [42] S. Cahangirov, M. Audiffred, P. Tang, A. Iacomino, W. Duan, G. Merino, and A. Rubio, "Electronic structure of silicene on Ag(111): Strong hybridization effects," *Physical Review B - Condensed Matter and Materials Physics*, vol. 88, no. 3, pp. 1–6, 2013.
- [43] Z. X. Guo, S. Furuya, J. I. Iwata, and A. Oshiyama, "Absence and presence of Dirac electrons in silicene on substrates," *Physical Review B - Condensed Matter and Materials Physics*, vol. 87, no. 23, pp. 1–10, 2013.
-

- 
- [44] L. Chen, C.-C. Liu, B. Feng, X. He, P. Cheng, Z. Ding, S. Meng, Y. Yao, and K. Wu, "Evidence for Dirac Fermions in a Honeycomb Lattice Based on Silicon," *Physical Review Letters*, vol. 109, p. 056804, aug 2012.
- [45] N. D. Drummond, V. Zólyomi, and V. I. Fal'ko, "Electrically tunable band gap in silicene," *Physical Review B - Condensed Matter and Materials Physics*, vol. 85, no. 7, pp. 1–7, 2012.
- [46] M. Ezawa, "A topological insulator and helical zero mode in silicene under an inhomogeneous electric field," *New Journal of Physics*, vol. 14, p. 033003, mar 2012.
- [47] M. Ezawa, "Valley-polarized metals and quantum anomalous hall effect in silicene," *Physical Review Letters*, vol. 109, no. 5, pp. 1–5, 2012.
- [48] H. Huang, W. Duan, and Z. Liu, "The existence/absence of Dirac cones in graphynes," *New Journal of Physics*, vol. 15, p. 023004, feb 2013.
- [49] B. G. Kim and H. J. Choi, "Graphyne: Hexagonal network of carbon with versatile Dirac cones," *Physical Review B - Condensed Matter and Materials Physics*, vol. 86, no. 11, pp. 1–5, 2012.
- [50] D. Malko, C. Neiss, F. Viñes, and A. Görling, "Competition for Graphene: Graphynes with Direction-Dependent Dirac Cones," *Physical Review Letters*, vol. 108, p. 086804, feb 2012.
- [51] G. Wang, M. Si, A. Kumar, and R. Pandey, "Strain engineering of Dirac cones in graphyne," *Applied Physics Letters*, vol. 104, p. 213107, may 2014.
- [52] X.-F. Zhou, X. Dong, A. R. Oganov, Q. Zhu, Y. Tian, and H.-T. Wang, "Semimetallic Two-Dimensional Boron Allotrope with Massless Dirac Fermions," *Physical Review Letters*, vol. 112, p. 085502, feb 2014.
- [53] K. Asano and C. Hotta, "Designing Dirac points in two-dimensional lattices," *Physical Review B*, vol. 83, p. 245125, jun 2011.
- [54] M. Polini, F. Guinea, M. Lewenstein, H. C. Manoharan, and V. Pellegrini, "Artificial honeycomb lattices for electrons, atoms and photons," *Nature Nanotechnology*, vol. 8, pp. 625–633, sep 2013.
- [55] M. Weinberg, C. Staarmann, C. Ölschläger, J. Simonet, and K. Sengstock, "Breaking inversion symmetry in a state-dependent honeycomb lattice: artificial graphene with tunable band gap," *2D Materials*, vol. 3, p. 024005, apr 2016.
- [56] K. K. Gomes, W. Mar, W. Ko, F. Guinea, and H. C. Manoharan, "Designer Dirac fermions and topological phases in molecular graphene," *Nature*, vol. 483, pp. 306–310, mar 2012.
- [57] N. Levy, S. A. Burke, K. L. Meaker, M. Panlasigui, A. Zettl, F. Guinea, A. H. C. Neto, and M. F. Crommie, "Strain-Induced Pseudo-Magnetic Fields Greater Than 300 Tesla in Graphene Nanobubbles," *Science*, vol. 329, pp. 544–547, jul 2010.
- [58] T. S. Gardenier, J. J. van den Broeke, J. R. Moes, I. Swart, C. Delerue, M. R. Slot, C. M. Smith, and D. Vanmaekelbergh, "p Orbital Flat Band and Dirac Cone in the Electronic Honeycomb Lattice," *ACS Nano*, p. acsnano.0c05747, oct 2020.
- [59] W. H. Evers, B. Goris, S. Bals, M. Casavola, J. de Graaf, R. van Roij, M. Dijkstra, and D. Vanmaekelbergh, "Low-Dimensional Semiconductor Superlattices Formed by Geometric Control over Nanocrystal Attachment," *Nano Letters*, vol. 13, pp. 2317–2323, jun 2013.
- [60] M. P. Boneschanscher, W. H. Evers, J. J. Geuchies, T. Altantzis, B. Goris, F. T. Rabouw, S. A. P. van Rossum, H. S. J. van der Zant, L. D. A. Siebbeles, G. Van Tendeloo, I. Swart, J. Hilhorst, A. V. Petukhov, S. Bals, and D. Vanmaekelbergh, "Long-range orientation and atomic attachment of nanocrystals in 2D honeycomb superlattices," *Science*, vol. 344, pp. 1377–1380, jun 2014.
- [61] C. van Overbeek, J. L. Peters, S. A. P. van Rossum, M. Smits, M. A. van Huis, and D. Vanmaekelbergh, "Interfacial Self-Assembly and Oriented Attachment in the Family of PbX (X = S, Se, Te) Nanocrystals," *The Journal of Physical Chemistry C*, vol. 122, pp. 12464–12473, jun 2018.
- [62] J. J. Geuchies, C. van Overbeek, W. H. Evers, B. Goris, A. de Backer, A. P. Gantapara, F. T. Rabouw, J. Hilhorst, J. L. Peters, O. Konovalov, A. V. Petukhov, M. Dijkstra, L. D. A. Siebbeles, S. van Aert, S. Bals, and D. Vanmaekelbergh, "In situ study of the formation mechanism of two-dimensional superlattices from PbSe nanocrystals," *Nature Materials*, vol. 15, pp. 1248–1254, dec 2016.
- [63] J. L. Peters, T. Altantzis, I. Lobato, M. A. Jazi, C. Van Overbeek, S. Bals, D. Vanmaekelbergh, and S. B. Sinai, "Mono- and Multilayer Silicene-Type Honeycomb Lattices by Oriented Attachment of PbSe Nanocrystals: Synthesis, Structural Characterization, and Analysis of the Disorder," *Chemistry of Materials*, vol. 30, no. 14, pp. 4831–4837, 2018.
-

- 
- [64] M. Alimoradi Jazi, V. A. Janssen, W. H. Evers, A. Tadjine, C. Delerue, L. D. Siebbeles, H. S. Van Der Zant, A. J. Houtepen, and D. Vanmaekelbergh, "Transport Properties of a Two-Dimensional PbSe Square Superstructure in an Electrolyte-Gated Transistor," *Nano Letters*, vol. 17, no. 9, pp. 5238–5243, 2017.
- [65] B. H. Savitzky, R. Hovden, K. Whitham, J. Yang, F. Wise, T. Hanrath, and L. F. Kourkoutis, "Propagation of Structural Disorder in Epitaxially Connected Quantum Dot Solids from Atomic to Micron Scale," *Nano Letters*, vol. 16, pp. 5714–5718, sep 2016.
- [66] K. Whitham, J. Yang, B. H. Savitzky, L. F. Kourkoutis, F. Wise, and T. Hanrath, "Charge transport and localization in atomically coherent quantum dot solids," *Nature Materials*, vol. 15, pp. 557–563, may 2016.
- [67] E. Kalesaki, C. Delerue, C. Morais Smith, W. Beugeling, G. Allan, and D. Vanmaekelbergh, "Dirac Cones, Topological Edge States, and Nontrivial Flat Bands in Two-Dimensional Semiconductors with a Honeycomb Nanogeometry," *Physical Review X*, vol. 4, p. 011010, jan 2014.
- [68] C. Delerue and D. Vanmaekelbergh, "Electronic band structure of zinc blende CdSe and rock salt PbSe semiconductors with silicene-type honeycomb geometry," *2D Materials*, vol. 2, p. 034008, jun 2015.
- [69] C. Delerue, "From semiconductor nanocrystals to artificial solids with dimensionality below two," *Phys. Chem. Chem. Phys.*, vol. 16, no. 47, pp. 25734–25740, 2014.
- [70] A. Tadjine and C. Delerue, "Colloidal nanocrystals as LEGO® bricks for building electronic band structure models," *Physical Chemistry Chemical Physics*, vol. 20, no. 12, pp. 8177–8184, 2018.
- [71] W. Beugeling, E. Kalesaki, C. Delerue, Y.-M. Niquet, D. Vanmaekelbergh, and C. M. Smith, "Topological states in multi-orbital HgTe honeycomb lattices," *Nature Communications*, vol. 6, p. 6316, dec 2015.
- [72] J. A. del Alamo, "Nanometre-scale electronics with III–V compound semiconductors," *Nature*, vol. 479, pp. 317–323, nov 2011.
- [73] M. Gibertini, A. Singha, V. Pellegrini, M. Polini, G. Vignale, A. Pinczuk, L. N. Pfeiffer, and K. W. West, "Engineering artificial graphene in a two-dimensional electron gas," *Physical Review B*, vol. 79, p. 241406, jun 2009.
- [74] C.-H. Park and S. G. Louie, "Making Massless Dirac Fermions from a Patterned Two-Dimensional Electron Gas," *Nano Letters*, vol. 9, pp. 1793–1797, may 2009.
- [75] L. Nádorník, M. Orlita, N. A. Goncharuk, L. Smrčka, V. Novák, V. Jurka, K. Hruška, Z. Výborný, Z. R. Wasilewski, M. Potemski, and K. Výborný, "From laterally modulated two-dimensional electron gas towards artificial graphene," *New Journal of Physics*, vol. 14, p. 053002, may 2012.
- [76] G. De Simoni, A. Singha, M. Gibertini, B. Karmakar, M. Polini, V. Piazza, L. N. Pfeiffer, K. W. West, F. Beltram, and V. Pellegrini, "Delocalized-localized transition in a semiconductor two-dimensional honeycomb lattice," *Applied Physics Letters*, vol. 97, p. 132113, sep 2010.
- [77] A. Singha, M. Gibertini, B. Karmakar, S. Yuan, M. Polini, G. Vignale, M. I. Katsnelson, A. Pinczuk, L. N. Pfeiffer, K. W. West, and V. Pellegrini, "Two-Dimensional Mott-Hubbard Electrons in an Artificial Honeycomb Lattice," *Science*, vol. 332, pp. 1176–1179, jun 2011.
- [78] S. Wang, D. Scarabelli, L. Du, Y. Y. Kuznetsova, L. N. Pfeiffer, K. W. West, G. C. Gardner, M. J. Manfra, V. Pellegrini, S. J. Wind, and A. Pinczuk, "Observation of Dirac bands in artificial graphene in small-period nanopatterned GaAs quantum wells," *Nature Nanotechnology*, vol. 13, pp. 29–33, jan 2018.
- [79] L. Du, S. Wang, D. Scarabelli, L. N. Pfeiffer, K. W. West, S. Fallahi, G. C. Gardner, M. J. Manfra, V. Pellegrini, S. J. Wind, and A. Pinczuk, "Emerging many-body effects in semiconductor artificial graphene with low disorder," *Nature Communications*, vol. 9, p. 3299, dec 2018.
- [80] A. Tadjine, G. Allan, and C. Delerue, "From lattice Hamiltonians to tunable band structures by lithographic design," *Physical Review B*, vol. 94, p. 075441, aug 2016.
- [81] N. A. Yuzeeva, A. V. Sorokoumova, R. A. Lunin, L. N. Oveshnikov, G. B. Galiev, E. A. Klimov, D. V. Lavruchin, and V. A. Kulbachinskii, "Electron Mobilities and Effective Masses in InGaAs/InAlAs HEMT Structures with High In Content," *Journal of Low Temperature Physics*, vol. 185, pp. 701–706, dec 2016.
- [82] X. Wallart, B. Pinsard, and F. Mollot, "High-mobility InGaAs/InAlAs pseudomorphic heterostructures on InP (001)," *Journal of Applied Physics*, vol. 97, p. 053706, mar 2005.
-

- 
- [83] J. Millunchick, A. Riposan, B. Dall, C. Pearson, and B. Orr, "Surface reconstructions of InGaAs layers," in *2003 International Symposium on Compound Semiconductors*, pp. 43–44, IEEE, 2003.
- [84] H. Li, J. Wu, Z. Wang, J. Liang, B. Xu, C. Jiang, Q. Gong, F. Liu, and W. Zhou, "Growth and characterization of InGaAs/InAlAs/InP high-electron-mobility transistor structures towards high channel conductivity," *Journal of Crystal Growth*, vol. 186, pp. 309–314, mar 1998.
- [85] L. C. Post, T. Xu, N. A. Franchina Vergel, A. Tadjine, Y. Lambert, F. Vaurette, D. Yarekha, L. Desplanque, D. Stiévenard, X. Wallart, B. Grandidier, C. Delerue, and D. Vanmaekelbergh, "Triangular nanoporation and band engineering of InGaAs quantum wells: a lithographic route toward Dirac cones in III–V semiconductors," *Nanotechnology*, vol. 30, p. 155301, apr 2019.
- [86] C. Flindt, N. A. Mortensen, and A.-P. Jauho, "Quantum Computing via Defect States in Two-Dimensional Antidot Lattices," *Nano Letters*, vol. 5, pp. 2515–2518, dec 2005.
- [87] A. Cho and J. Arthur, "Molecular beam epitaxy," *Progress in Solid State Chemistry*, vol. 10, pp. 157–191, jan 1975.
- [88] T. W. Pi, H. Y. Lin, Y. T. Liu, T. D. Lin, G. K. Wertheim, J. Kwo, and M. Hong, "Atom-to-atom interactions for atomic layer deposition of trimethylaluminum on Ga-rich GaAs (001)- $4 \times 6$  and As-rich GaAs(001)- $2 \times 4$  surfaces: A synchrotron radiation photoemission study," *Nanoscale Research Letters*, vol. 8, no. 1, pp. 1–7, 2013.
- [89] C. W. Burrows, S. A. Hatfield, F. Bastiman, and G. R. Bell, "Interaction of Mn with GaAs and InSb: Incorporation, surface reconstruction and nano-cluster formation," *Journal of Physics Condensed Matter*, vol. 26, no. 39, 2014.
- [90] K. W. Kolasinski, *Surface Science*. Chichester, UK: John Wiley & Sons, Ltd, apr 2012.
- [91] R. Hołyst, M. Litniewski, and D. Jakubczyk, "A molecular dynamics test of the Hertz-Knudsen equation for evaporating liquids," *Soft Matter*, vol. 11, no. 36, pp. 7201–7206, 2015.
- [92] C. G. Willson, R. R. Dammel, and A. Reiser, "Photoresist materials: a historical perspective," in *Optical Microlithography X* (G. E. Fuller, ed.), vol. 3051, p. 28, jul 1997.
- [93] S. Y. Chou, P. R. Krauss, and P. J. Renstrom, "Imprint Lithography with 25-Nanometer Resolution," *Science*, vol. 272, pp. 85–87, apr 1996.
- [94] A. R. Neureuther, "Microlithography with Soft X Rays," in *Synchrotron Radiation Research*, pp. 223–275, Boston, MA: Springer US, 1980.
- [95] Y. Vladimírsky, A. Bourdillon, O. Vladimírsky, W. Jiang, and Q. Leonard, "Demagnification in proximity X-ray lithography and extensibility to 25 nm by optimizing Fresnel diffraction," *Journal of Physics D: Applied Physics*, vol. 32, no. 22, 1999.
- [96] R. Garcia, A. W. Knoll, and E. Riedo, "Advanced scanning probe lithography," *Nature Nanotechnology*, vol. 9, pp. 577–587, aug 2014.
- [97] R. V. Martínez, N. S. Losilla, J. Martínez, Y. Huttel, and R. Garcia, "Patterning polymeric structures with 2 nm resolution at 3 nm half pitch in ambient conditions," *Nano Letters*, vol. 7, no. 7, pp. 1846–1850, 2007.
- [98] A. N. Broers, W. W. Molzen, J. J. Cuomo, and N. D. Wittels, "Electron-beam fabrication of 80-Å metal structures," *Applied Physics Letters*, vol. 29, pp. 596–598, nov 1976.
- [99] J. Trasobares, F. Vaurette, M. François, H. Romijn, J.-L. Codron, D. Vuillaume, D. Théron, and N. Clément, "High speed e-beam lithography for gold nanoarray fabrication and use in nanotechnology," *Beilstein Journal of Nanotechnology*, vol. 5, pp. 1918–1925, oct 2014.
- [100] V. Lacatena, M. Haras, J.-F. Robillard, S. Monfray, T. Skotnicki, and E. Dubois, "Phononic engineering of silicon using "dots on the fly" e-beam lithography and plasma etching," *Microelectronic Engineering*, vol. 121, pp. 131–134, jun 2014.
- [101] H. C. Pfeiffer, "New imaging and deflection concept for probe-forming microfabrication systems," *Journal of Vacuum Science and Technology*, vol. 12, pp. 1170–1173, nov 1975.
- [102] N. Saitou, S. Ozasa, T. Komoda, G. Tatsuno, and Y. Uno, "Variably shaped electron beam lithography system, EB55: II Electron optics," *Journal of Vacuum Science and Technology*, vol. 19, pp. 1087–1093, nov 1981.
-

- 
- [103] V. M. Bermudez, "Low-energy electron-beam effects on poly(methyl methacrylate) resist films," *Journal of Vacuum Science and Technology B: Microelectronics and Nanometer Structures*, vol. 17, no. 6, p. 2512, 1999.
- [104] N. Arjmandi, L. Lagae, and G. Borghs, "Enhanced resolution of poly(methyl methacrylate) electron resist by thermal processing," *Journal of Vacuum Science and Technology B: Microelectronics and Nanometer Structures*, vol. 27, no. 4, pp. 1915–1918, 2009.
- [105] D. R. S. Cumming, S. Thoms, S. P. Beaumont, and J. M. R. Weaver, "Fabrication of 3 nm wires using 100 keV electron beam lithography and poly(methyl methacrylate) resist," *Applied Physics Letters*, vol. 68, pp. 322–324, jan 1996.
- [106] A. Grigorescu, M. van der Krogt, C. Hagen, and P. Kruit, "10nm lines and spaces written in HSQ, using electron beam lithography," *Microelectronic Engineering*, vol. 84, pp. 822–824, may 2007.
- [107] H. Yang, A. Jin, Q. Luo, J. Li, C. Gu, and Z. Cui, "Electron beam lithography of HSQ/PMMA bilayer resists for negative tone lift-off process," *Microelectronic Engineering*, vol. 85, pp. 814–817, may 2008.
- [108] J. K. W. Yang, B. Cord, H. Duan, K. K. Berggren, J. Klingfus, S.-W. Nam, K.-B. Kim, and M. J. Rooks, "Understanding of hydrogen silsesquioxane electron resist for sub-5-nm-half-pitch lithography," *Journal of Vacuum Science and Technology B: Microelectronics and Nanometer Structures*, vol. 27, no. 6, p. 2622, 2009.
- [109] A. S. Gangnaik, Y. M. Georgiev, and J. D. Holmes, "New Generation Electron Beam Resists: A Review," *Chemistry of Materials*, vol. 29, pp. 1898–1917, mar 2017.
- [110] S. Okazaki, "High resolution optical lithography or high throughput electron beam lithography: The technical struggle from the micro to the nano-fabrication evolution," *Microelectronic Engineering*, vol. 133, pp. 23–35, feb 2015.
- [111] V. R. Manfrinato, J. Wen, L. Zhang, Y. Yang, R. G. Hobbs, B. Baker, D. Su, D. Zakharov, N. J. Zaluzec, D. J. Miller, E. A. Stach, and K. K. Berggren, "Determining the Resolution Limits of Electron-Beam Lithography: Direct Measurement of the Point-Spread Function," *Nano Letters*, vol. 14, pp. 4406–4412, aug 2014.
- [112] V. R. Manfrinato, A. Stein, L. Zhang, C.-Y. Nam, K. G. Yager, E. A. Stach, and C. T. Black, "Aberration-Corrected Electron Beam Lithography at the One Nanometer Length Scale," *Nano Letters*, vol. 17, pp. 4562–4567, aug 2017.
- [113] J. Zhou and X. Yang, "Monte Carlo simulation of process parameters in electron beam lithography for thick resist patterning," *Journal of Vacuum Science and Technology B: Microelectronics and Nanometer Structures*, vol. 24, no. 3, p. 1202, 2006.
- [114] M. Rommel, K. E. Hoffmann, T. Reindl, J. Weis, N. Unal, and U. Hofmann, "Benchmark test of Monte-Carlo simulation for high resolution electron beam lithography," *Microelectronic Engineering*, vol. 98, pp. 202–205, oct 2012.
- [115] T. R. Groves, "Efficiency of electron-beam proximity effect correction," *Journal of Vacuum Science and Technology B: Microelectronics and Nanometer Structures*, vol. 11, no. 6, p. 2746, 1993.
- [116] A. Broers, A. Hoole, and J. Ryan, "Electron beam lithography—Resolution limits," *Microelectronic Engineering*, vol. 32, pp. 131–142, sep 1996.
- [117] R. A. Segalman, "Patterning with block copolymer thin films," *Materials Science and Engineering: R: Reports*, vol. 48, pp. 191–226, feb 2005.
- [118] F. S. Bates and G. H. Fredrickson, "Block Copolymers—Designer Soft Materials," *Physics Today*, vol. 52, pp. 32–38, feb 1999.
- [119] L. Leibler, "Theory of Microphase Separation in Block Copolymers," *Macromolecules*, vol. 13, pp. 1602–1617, nov 1980.
- [120] C. M. Bates, M. J. Maher, D. W. Janes, C. J. Ellison, and C. G. Willson, "Block Copolymer Lithography," *Macromolecules*, vol. 47, pp. 2–12, jan 2014.
- [121] A. Chremos, A. Nikoubashman, and A. Z. Panagiotopoulos, "Flory-Huggins parameter  $\chi$ , from binary mixtures of Lennard-Jones particles to block copolymer melts," *The Journal of Chemical Physics*, vol. 140, p. 054909, feb 2014.
-

- 
- [122] M. W. Matsen and F. S. Bates, "Block copolymer microstructures in the intermediate-segregation regime," *The Journal of Chemical Physics*, vol. 106, pp. 2436–2448, feb 1997.
- [123] S. Park, D. H. Lee, J. Xu, B. Kim, S. W. Hong, U. Jeong, T. Xu, and T. P. Russell, "Macroscopic 10-Terabit-per-Square-Inch Arrays from Block Copolymers with Lateral Order," *Science*, vol. 323, pp. 1030–1033, feb 2009.
- [124] R. Tiron, A. Gharbi, M. Argoud, X. Chevalier, J. Belledent, P. Pimenta Barros, C. Navarro, G. Cunge, S. Barnola, L. Pain, M. Asai, and C. Pieczulewski, "The potential of block copolymer's directed self-assembly for contact hole shrink and contact multiplication," p. 868012, mar 2013.
- [125] R. Segalman, H. Yokoyama, and E. Kramer, "Graphoepitaxy of Spherical Domain Block Copolymer Films," *Advanced Materials*, vol. 13, pp. 1152–1155, aug 2001.
- [126] K. W. Guarini, C. T. Black, K. R. Milkove, and R. L. Sandstrom, "Nanoscale patterning using self-assembled polymers for semiconductor applications," *Journal of Vacuum Science and Technology B: Microelectronics and Nanometer Structures*, vol. 19, no. 6, p. 2784, 2001.
- [127] M. Park, P. M. Chaikin, R. A. Register, and D. H. Adamson, "Large area dense nanoscale patterning of arbitrary surfaces," *Applied Physics Letters*, vol. 791, no. 10, pp. 2784–1128, 2001.
- [128] T. Thurn-Albrecht, J. Schotter, G. A. Kastle, N. Emley, T. Shibauchi, L. Krusin-Elbaum, K. Guarini, C. T. Black, M. T. Tuominen, and T. P. Russell, "Ultrahigh-Density Nanowire Arrays Grown in Self-Assembled Diblock Copolymer Templates," *Science*, vol. 290, pp. 2126–2129, dec 2000.
- [129] A. Stein, G. Wright, K. G. Yager, G. S. Doerk, and C. T. Black, "Selective directed self-assembly of coexisting morphologies using block copolymer blends," *Nature Communications*, vol. 7, p. 12366, nov 2016.
- [130] K. Aissou, J. Shaver, G. Fleury, G. Pécastaings, C. Brochon, C. Navarro, S. Grauby, J.-M. Rampnoux, S. Dilhaire, and G. Hadziioannou, "Nanoscale Block Copolymer Ordering Induced by Visible Interferometric Micropatterning: A Route towards Large Scale Block Copolymer 2D Crystals," *Advanced Materials*, vol. 25, pp. 213–217, jan 2013.
- [131] A. Clawson, "Guide to references on III–V semiconductor chemical etching," *Materials Science and Engineering: R: Reports*, vol. 31, pp. 1–438, jan 2001.
- [132] S. K. K. Kwon, K. H. K. Kwon, B. W. K. Kim, J. M. P. Park, S. W. Y. Yoo, K. S. P. Park, and Y. K. Kyu, "Characterization of Via Etching in CHF<sub>3</sub>/CF<sub>4</sub> Magnetically Enhanced Reactive Ion Etching Using Neural Networks," *ETRI Journal*, vol. 24, pp. 211–220, jun 2002.
- [133] T. Maeda, H. Cho, J. Hong, and S. J. Pearton, "New plasma chemistries for etching III–V compound semiconductors: B13 and BBr<sub>3</sub>," *Journal of Electronic Materials*, vol. 28, pp. 118–123, feb 1999.
- [134] H. Tamura and H. Kurihara, "GaAs and GaAlAs Reactive Ion Etching in BCl<sub>3</sub>-Cl<sub>2</sub> Mixture," *Japanese Journal of Applied Physics*, vol. 23, pp. L731–L733, sep 1984.
- [135] T. Maeda, J. Lee, R. Shul, J. Han, J. Hong, E. Lambers, S. Pearton, C. Abernathy, and W. Hobson, "Inductively coupled plasma etching of III–V semiconductors in BCl<sub>3</sub>-based chemistries," *Applied Surface Science*, vol. 143, pp. 174–182, apr 1999.
- [136] G. Binnig, H. Rohrer, C. Gerber, and E. Weibel, "Surface Studies by Scanning Tunneling Microscopy," *Physical Review Letters*, vol. 49, pp. 57–61, jul 1982.
- [137] G. Binnig, H. Rohrer, C. Gerber, and E. Weibel, "Tunneling through a controllable vacuum gap," *Applied Physics Letters*, vol. 40, no. 2, pp. 178–180, 1982.
- [138] G. Binnig, H. Rohrer, C. Gerber, and E. Weibel, "7 × 7 Reconstruction on Si(111) Resolved in Real Space," *Physical Review Letters*, vol. 50, pp. 120–123, jan 1983.
- [139] D. M. Eigler and E. K. Schweizer, "Positioning single atoms with a scanning tunnelling microscope," *Nature*, vol. 344, pp. 524–526, apr 1990.
- [140] H. C. Manoharan, C. P. Lutz, and D. M. Eigler, "Quantum mirages formed by coherent projection of electronic structure," *Nature*, vol. 403, no. 6769, pp. 512–515, 2000.
- [141] A. J. Heinrich, "Single-Atom Spin-Flip Spectroscopy," *Science*, vol. 306, pp. 466–469, oct 2004.
- [142] C. F. Hirjibehedin, C. P. Lutz, and A. J. Heinrich, "Spin coupling in engineered atomic structures," *Science*, vol. 312, no. 5776, pp. 1021–1024, 2006.
-

- 
- [143] A. A. Khajetoorians, S. Lounis, B. Chilian, A. T. Costa, L. Zhou, D. L. Mills, J. Wiebe, and R. Wiesendanger, "Itinerant nature of atom-magnetization excitation by tunneling electrons," *Physical Review Letters*, vol. 106, no. 3, pp. 6–9, 2011.
- [144] B. C. Stipe, M. A. Rezaei, and W. Ho, "Inducing and viewing the rotational motion of a single molecule," *Science*, vol. 279, no. 5358, pp. 1907–1909, 1998.
- [145] S. W. Wu, N. Ogawa, and W. Ho, "Atomic-scale coupling of photons to single-molecule junctions," *Science*, vol. 312, no. 5778, pp. 1362–1365, 2006.
- [146] J. Tersoff and D. R. Hamann, "Theory of the scanning tunneling microscope," *Physical Review B*, vol. 31, no. 2, pp. 805–813, 1985.
- [147] J. Tersoff and D. R. Hamann, "Theory and Application for the Scanning Tunneling Microscope," *Physical Review Letters*, vol. 50, pp. 1998–2001, jun 1983.
- [148] J. Bardeen, "Tunnelling from a Many-Particle Point of View," *Physical Review Letters*, vol. 6, pp. 57–59, jan 1961.
- [149] N. D. Lang, "Spectroscopy of single atoms in the scanning tunneling microscope," *Physical Review B*, vol. 34, no. 8, pp. 5947–5950, 1986.
- [150] K. Suzuki, K. Kanisawa, C. Janer, S. Perraud, K. Takashina, T. Fujisawa, and Y. Hirayama, "Spatial Imaging of Two-Dimensional Electronic States in Semiconductor Quantum Wells," *Physical Review Letters*, vol. 98, p. 136802, mar 2007.
- [151] C. H. Henry, R. A. Logan, F. R. Merritt, and C. G. Bethea, "Radiative and nonradiative lifetimes in n-type and p-type 1.6  $\mu\text{m}$  InGaAs," *Electronics Letters*, vol. 20, no. 9, pp. 358–359, 1984.
- [152] U. Cebulla, G. Bacher, A. Forchel, G. Mayer, and W. T. Tsang, "Excitonic lifetimes in thin  $\text{In}_x\text{Ga}_{1-x}\text{As}/\text{InP}$  quantum wells," *Physical Review B*, vol. 39, pp. 6257–6259, mar 1989.
- [153] M. R. Slot, T. S. Gardenier, P. H. Jacobse, G. C. P. van Miert, S. N. Kempkes, S. J. M. Zevenhuizen, C. M. Smith, D. Vanmaekelbergh, and I. Swart, "Experimental realization and characterization of an electronic Lieb lattice," *Nature Physics*, vol. 13, pp. 672–676, apr 2017.
- [154] J. Klein, A. Léger, M. Belin, D. Défourneau, and M. J. L. Sangster, "Inelastic-Electron-Tunneling Spectroscopy of Metal-Insulator-Metal Junctions," *Physical Review B*, vol. 7, pp. 2336–2348, mar 1973.

# Chapter III

---

## Designing honeycomb semiconductors: The muffin-tin model

**Partially based on:**

L.C. Post, T. Xu, N.A. Franchina Vergel, A. Tadjine, Y. Lambert, F. Vaurette, D. Yarekha, L. Desplanque, D. Stiévenard, X. Wallart, B. Grandidier, C. Delerue, D. Vanmaekelbergh

**Triangular nanoperforation and band engineering of InGaAs quantum wells:  
a lithographic route toward Dirac cones in III-V semiconductors**

*Nanotechnology* **30**, 15 (155301) 2019

**The electronic structure of an electron gas in a two-dimensional semiconductor can be altered by an external potential landscape which forces electrons to move in different nanogeometries. In the case of a honeycomb nanogeometry created by a triangular lattice of electron repelling barriers [1–3], a Dirac-type band structure with massless fermions is expected. Here, the electronic properties of a designed honeycomb semiconductor are theoretically investigated using a muffin-tin model. This model gives the opportunity to investigate the effects on the band structure by varying the lattice and material parameters of the honeycomb semiconductors to realistic values obtained using different lithographic techniques [4–6]. This can be used to optimize the honeycomb semiconductor, e.g. to increase the energy width of the Dirac cone in order to obtain separate *s*-orbital and *p*-orbital Dirac bands, unlike the case of graphene. Using a numerical approach to this model, the electronic properties of the honeycomb semiconductor can be determined locally, providing us with a tool to compare the theoretical model with experimental differential conductance measurements.**

### III.1 Introduction

The muffin-tin model is a two-dimensional (2D) description of the electronic structure of a free electron gas subjected to barriers with a certain potential height [7]. By purposely positioning potential barriers in certain lattices, electrons can therefore be forced to move in certain lattice symmetries.

The electrons inside the conduction band of the two-dimensional semiconductor quantum well can be treated as a two-dimensional free electron gas with an effective mass  $m_e^*$ . The energy states and wave functions of the two-dimensional free electron gas can be calculated using the Schrödinger equation, showing a step-like behaviour in the density of states. When placing cylindrical potential barriers with height  $V_0$  and diameter  $d$  into the two-dimensional electron gas, the energies and states of the electrons will change. The general time-independent Schrödinger equation can be written using a spherical coordinate system:

$$\mathbf{H}\psi_n(\mathbf{r}) = E_n\psi_n(\mathbf{r}) \quad (\text{III.1})$$

which can be written out as:

$$\left[ -\frac{\hbar^2}{2m_e^*} \nabla_{\mathbf{r}}^2 + \sum_i V(\mathbf{r} - \mathbf{R}_i) \right] \psi_n(\mathbf{r}) = E_n\psi_n(\mathbf{r}) \quad (\text{III.2})$$

where  $\mathbf{R}_i$  are the Bravais lattice vectors of the potential barriers in real space forming the lattice,  $i$  is the index number of barrier potentials,  $\psi_n$  are  $n$  linear coupled wave functions of the electrons and  $E_n$  are  $n$  number of eigenvalue energies states of the electrons. For cylindrical potential barriers with height  $V_0$  and diameter  $d$ ,  $V(\mathbf{r} - \mathbf{R}_i)$  can be defined as:

$$V(\mathbf{r} - \mathbf{R}_i) = \begin{cases} V_0 & : |\mathbf{r} - \mathbf{R}_i| \leq d/2 \\ 0 & : |\mathbf{r} - \mathbf{R}_i| > d/2 \end{cases} \quad (\text{III.3})$$

meaning that when  $\mathbf{r}-\mathbf{R}_i$  is smaller than/or equal to the radius of the potential barrier, the potential energy has a value of  $V_0$ .

In this chapter, two different approaches to the muffin-tin model will be explored. When a periodic honeycomb lattice is considered, the muffin-tin model can be solved analytically using Bloch's theorem [5, 8]. This theorem allows us to solve the Schrödinger equation analytically, meaning that the band structure along the high symmetry points of the Brillouin zone can be calculated with a low calculation time and high precision. By changing the lattice and material parameters, the electronic structure of the modelled system can be altered to our liking, and additional effects onto the electronic structure can be considered such as the confinement in the  $z$ -direction and the non-parabolicity behaviour of III-V semiconductors. This will be further investigated by calculating the total density of states (DOS) of the first Brillouin zone.

For a better subscription of the local electronic structure of the honeycomb semiconductor, a numerical muffin-tin model is used to solve the Schrödinger equation on individual grid points of the total lattice, obtaining the local density of states (LDOS). This result can be directly compared to the results of differential conductance spectroscopy from scanning tunneling microscopy (STM) experiments. Therefore, the numerical muffin-tin model gives us a tool to compare theoretical and experimental work. This model can also be used to simulate differential conductance maps by plotting locally the absolute values of the solved wave functions, which is a more convenient tool to observe Dirac physics over the entire lattice. Since the simulated lattice is finite-sized, direct effects of the locality on the electronic structure can be investigated.

## III.2 Design of a honeycomb semiconductor

To obtain an electronic honeycomb semiconductor (Fig. III.1A), the potential barriers have to be positioned in a triangular arrangement (Fig. III.1B). In this configuration, the free electrons moving through the two-dimensional plane scatter from the repulsive potential barriers into a honeycomb nanogeometry. Looking from the side view (Fig. III.1B), the potential barriers have a repulsive potential  $V_0$ , while outside the barrier the potential is zero ( $V = 0$ ). Other lattice parameters for the muffin-tin model are the size of the honeycomb unit cell which can be altered by changing the distance  $D$  between the potential barriers. The diameter of the barriers  $d$  can also be varied to better define the honeycomb symmetry. Lastly, the effective mass  $m_e^*$  of the electrons will also affect the solved energies, which is solely dependent on the semiconductor material. The mathematical background on the analytical muffin-tin model can be found in the supplementary information (SI).

Performing the muffin-tin calculation, the energy states are plotted at individual reciprocal point  $(k_x, k_y)$ , and a three-dimensional plot of the electronic band structure can be obtained. When plotting the two lowest conduction bands, six Dirac cones are observed where the bands touch each other (Fig. III.1C). At these points, the energy scales linearly with the wave number  $\mathbf{k}$ , obtaining conical shaped bands. The six-fold symmetry is visible in Fig. III.1D, where a contour plot of the lowest conduction band

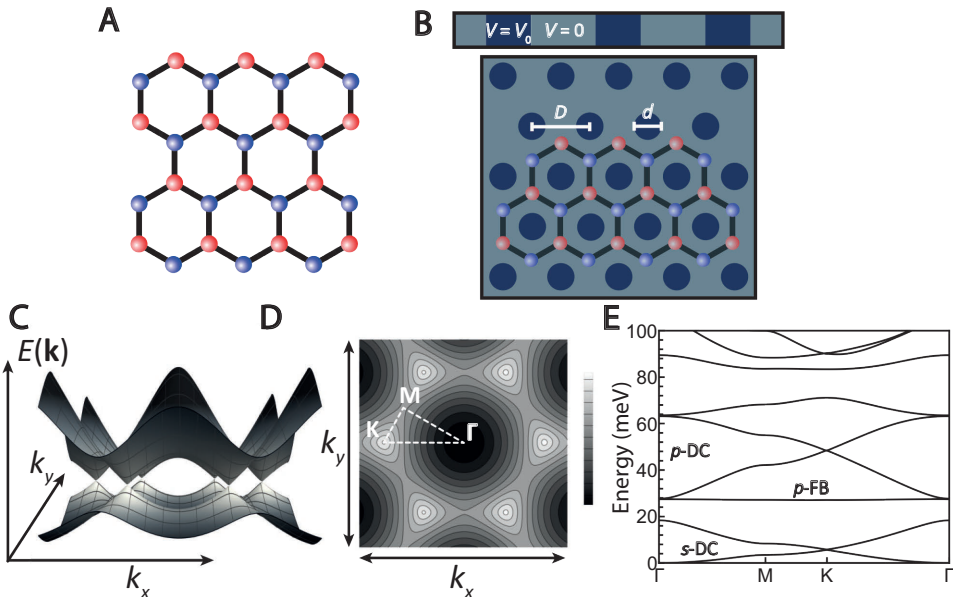


**Figure III.1: Electronic structure of a two-dimensional electron gas with a honeycomb nanogeometry.** (A) Schematic view of the honeycomb nanogeometry. (B) Top and side view of the described muffin-tin model. By placing the potential barriers in a triangular lattice, the free electron gas will move into a honeycomb nanogeometry. (C) Three-dimensional band structure of the honeycomb lattice ( $D = 40$  nm,  $d = 24$  nm,  $V_0 = 1$  eV), only showing the first two bands. An effective mass of  $m_e^* \approx 0.041m_e$  is used, which is a typical value for a III-V semiconductor such as InGaAs [9]. (D) Two-dimensional contourplot of the lowest energy conduction band in  $k_x, k_y$  space. High symmetry points K, M and  $\Gamma$  are indicated in the plot. High intensity is visible at the K points of the Brillouin zone, indicating the presence of the Dirac cone. (E) Band structure of the described model along the high symmetry lines of the Brillouin zone, showing a  $s$ -type Dirac cone ( $s$ -DC), a  $p$ -type flat band ( $p$ -FB) and a  $p$ -type Dirac cone ( $p$ -DC).

is presented. An increase of intensity at the edges of the first Brillouin zone is observed where the Dirac cones are located. Since the lattice is symmetrical, it is more common to plot the energy versus the wavevector in a two-dimensional plot, following the high-symmetry lines of the first Brillouin zone  $\Gamma \rightarrow K \rightarrow M \rightarrow \Gamma$  of the honeycomb lattice, which is indicated in Fig. III.1D. The band structure along these symmetry points is presented in Fig. III.1E. Since the muffin-tin is a single particle model, the energy reference of the conduction band starts at 0 meV. The lowest two bands of the band structure are similar bands as presented in Fig. III.1C, showing similar dispersion as the  $\pi$ - and  $\pi^*$ -bands in graphene [10]. Comparing the muffin-tin model with a tight-binding model, both bands can be treated as coupled  $s$ -orbitals of the honeycomb lattice sites. Therefore, the Dirac cones formed by these  $s$ -like orbital bands are called  $s$ -type Dirac cones ( $s$ -DC).

Furthermore, at higher energy directly above the  $s$ -like Dirac cone, four bands with interesting features are observed. These bands originate from coupling between in-

plane  $p$ -orbitals of the on-site electrons, where two  $p$ -bands form a Dirac cone ( $p$ -DC) and two  $p$ -bands form flat bands above and below the Dirac cone ( $p$ -FB). These two dispersionless flat bands are formed due to destructive interference of the electron hopping. This can be solely assigned to the honeycomb nanogeometry [11], but is not naturally found in graphene due to  $s - p_x - p_y$  hybridization. These bands are however already observed in other electronic and photonic honeycomb lattices [12, 13]. The flat band can give rise to new physical phenomena such as fractional quantum Hall states [14–16]. Also, superconductive pairing of electrons in a flat band is of high scientific interest [17].

These results show the effectiveness of the muffin-tin model for the honeycomb lattice. Further investigation of the lattice parameters on the electronic structure can now be performed.

### III.3 Optimization of a honeycomb semiconductor

By tuning the parameters of the honeycomb lattice, well separated  $s$ - and  $p$ -orbitals can be obtained with well-defined Dirac cones and flat bands. First, the effects on the band structure for varying potential barrier heights is investigated (Fig. III.2). When the potential is completely removed ( $V_0 = 0$  meV), an empty lattice is obtained in a two-dimensional material, and parabolic bands folded in the reciprocal space are observed. For all calculations, the conduction band starts at 0 meV as a reference energy. Upon applying a small potential height to the barriers, the model shows that bands are starting to split, and a non-isolated Dirac cone is formed at the K point in the two lowest  $s$ -like bands. Since the trigonal potential landscape of the honeycomb lattice and the quantum confinement is weak, other possible electronic states are still near the Dirac cone, meaning that the Dirac cone is not fully isolated yet. Looking at higher band, the bands are still parabolic and folded into each other. When further increasing the potential of the barriers, bands are splitting in different regions and clear gaps between bands are formed. The two  $s$ -orbital bands are separated from the four  $p$ -orbital bands at sufficient high potential height. At  $V_0 = 100$  meV, the two  $s$ -orbital bands form an isolated Dirac cone at the K-points, while at  $V_0 = 1000$  meV, the four  $p$ -orbital bands form a dispersionless flat band, a Dirac cone, and a second flat band above the Dirac cone. Increasing the potential has therefore a direct effect on the emergence of Dirac physics in the system. This has also been observed in other models [18, 19]. Upon further increasing the potential height, higher orbital bands are affected, while the lower  $s$ - and  $p$ -orbital bands remain constant.

The energy width of the Dirac cones can be altered by changing the size of the unit cell, i.e. the distance between the lattice sites of the honeycomb lattice. This is verified by performing muffin-tin calculations with varying distances between barriers of the triangular lattice (Fig. III.3A-D). To correctly compare different unit cell sizes with each other, the ratio  $d/D$  is kept constant for all lattices, meaning that the diameter of the potential barriers varies linearly with the unit cell size. For unit sizes with a pore-to-pore distance of 80 nm, the width of the energy bands is very small (Fig. III.3A),

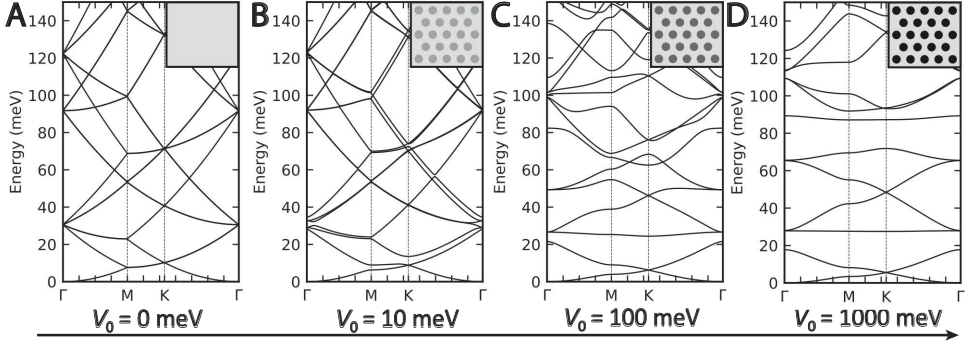


**Figure III.2: Electronic structure of the triangular antidot lattice versus the potential height.** (A–D) Band structure calculations for a triangular antidot lattice. Lattice parameters:  $D = 40$  nm,  $d = 24$  nm. The height of the barrier potentials is increased from 0 meV (A), 10 meV (B), 100 meV (C) to 1000 meV (D).

since many bands are visible in the same energy range. Decreasing the size of the unit cell will increase the energy range of the bands quadratically, enhancing the energy width of the  $s$ - and  $p$ -orbital Dirac cone.

To be able to measure the electronic structure experimentally, a certain energy width is needed to overcome various sources of broadening, meaning that a certain dimension of the honeycomb unit cell is needed. This can be expressed as the effective energy width  $E_{\text{DC}}$  of the  $s$ -DC, which is the energy distance between the two M points of the  $s$ -like Dirac cone, indicated in Fig. III.3D.

For large unit cells ( $D = 80$  nm), the effective energy width  $E_{\text{DC}}$  of the  $s$ -DC is only 1 meV, which will be too difficult to measure directly. However, it was reported that the lattice parameters of triangular antidot lattices based on GaAs should be as low as 35 nm to directly observe massless Dirac fermions in standard cryogenic conditions [20]. Since the energy width is inversely proportional to the effective carrier mass, InGaAs-based heterostructures will enhance the energy width due to a lower effective carrier mass compared with GaAs. Therefore, triangular lattices of 40 nm and below are needed in order to measure the modelled electron properties in InGaAs-based heterostructures. As a result, nanofabrication techniques such as lithography should be pushed to their ultimate limit in terms of resolution [4, 6].

Finally, changing the diameter of the barriers will also affect the electronic structure (Fig. III.3(E–H)). For small pore sizes, the honeycomb lattice is not well defined and an electronic structure of a nearly empty lattice is obtained, resulting in parabolic, non-separated bands. Increasing the diameter of the potential barriers will result in a better defined honeycomb lattice, improving the definition of the lattice sites coupled in the honeycomb geometry. Splitting is observed between the bottom two  $s$ -bands and the four  $p$ -bands above the  $s$ -bands. For  $d = 26$  nm, there is a system of two  $s$ -orbital bands with a Dirac cone at K, followed by four  $p$ -orbital bands: a flat band, a  $p$ -orbital Dirac cone and a second flat band. No hybridization between the  $s$ - and  $p$ -bands is

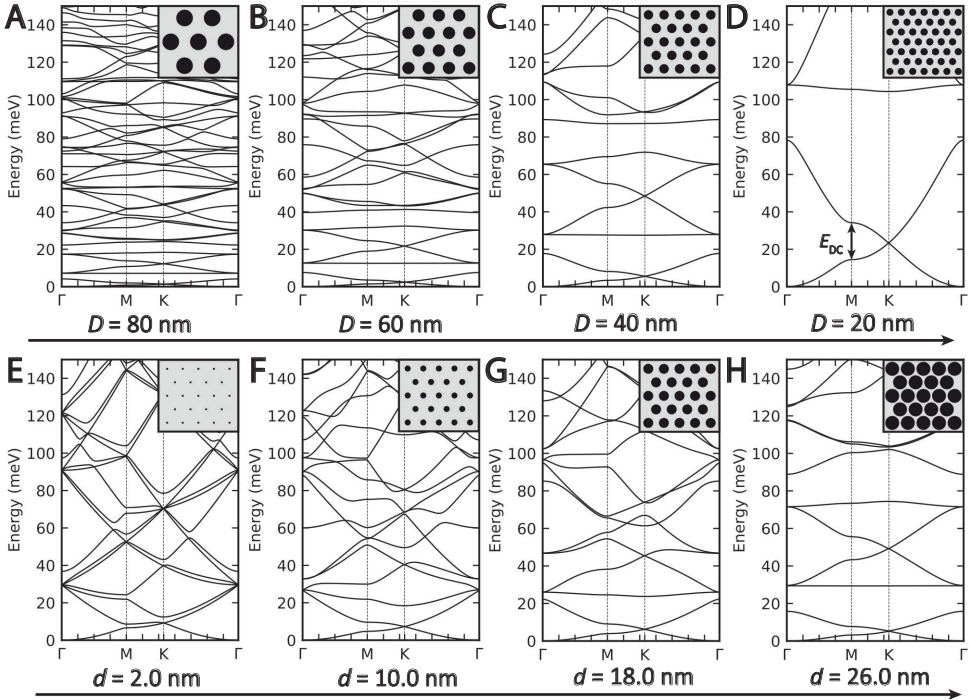


**Figure III.3: Electronic structure of the triangular antidot lattice versus the lattice parameters.** (A-D) Band structure calculations with a constant pore radius ratio of 0.3, a potential barrier of 1000 meV and a periodicity  $D = 80$  nm, 60 nm, 40 nm and 20 nm. The width of the  $s$ -type Dirac cone can be expressed by the energy distance between the two  $s$ -bands at the M point, indicated by  $E_{DC}$  in (D). (E-H) Band structure calculation with a periodicity of  $D = 40$  nm, a potential barrier of 1000 meV and a pore diameter  $d' = 4.0$  nm, 10.0 nm, 18.0 nm and 26.0 nm.

observed, making this system an ideal candidate to study orbital degrees of freedom in the honeycomb geometry. Tight-binding calculations on similar patterned systems by lithographic design show similar results [1, 21]. The obtained band structures also show excellent agreement with theoretical work on other types of honeycomb semiconductor systems, such as honeycomb superstructures by oriented attachment of PbSe and CdSe quantum dots [18, 19, 22] and artificial electronic lattices on Cu(111) using CO molecules [23, 24].

As an ideal, we wish to achieve a semiconductor with well-defined and separated  $s$ -orbital and  $p$ -orbital bands. This can be achieved by fine-tuning the lattice parameters of the triangular lattice of potential barriers. The width of the Dirac cone is not only dependent on the lattice constant of the honeycomb lattice, but also on the effective mass of the charge carriers in the employed semiconductor material [25]. When lowering the effective mass  $m_e^*$  of the semiconductor material, the effects of the lateral confinement are enhanced, resulting in a broader Dirac cone. Calculations from Tadjine *et al.* show that the energy range of the Dirac cone can extend over tens of meV in InAs-based

heterostructures [21]. For all calculations, an effective mass  $m_e^* = 0.041 m_e$  was taken into account, which is the effective mass of electrons in an InGaAs semiconductor [9].

## Towards lithographic designed honeycomb semiconductors

Designing and optimization of the honeycomb semiconductor has been performed using an ideal two-dimensional model. By applying some adaptations, more realistic systems designed by lithography can be investigated.

### Potential barrier shape

First, two differently shaped potential barriers will be considered: the conical potential barrier and the inverted harmonic oscillator barrier, illustrated in Fig. III.4A-B. Both models could give a more realistic electronic structure, since the shape of the electron-repelling barriers will not be perfectly cylindrical in lithographic patterned semiconductors. Using the Kronig-Penney model, it is already displayed that potential barriers with different shapes can change the electronic properties of a material [26, 27].

In the linear model, the potential term in the Schrödinger equation can be defined as:

$$V(\mathbf{r} - \mathbf{R}_i) = \begin{cases} V_0 & 0 < |\mathbf{r} - \mathbf{R}_i| \leq d'/2 \\ \frac{2V_0}{d}(d/2 - \mathbf{r}) & d'/2 < |\mathbf{r} - \mathbf{R}_i| \leq d/2 \\ 0 & |\mathbf{r} - \mathbf{R}_i| > d/2 \end{cases} \quad (\text{III.4})$$

where  $d'$  is defined as the diameter of the barrier at the bottom of the gap, as indicated in Fig. III.4A. When  $d' = 0 \text{ nm}$ , perfect conical potential barriers are obtained. When  $d' = d$ , it will result in cylindrical potential barriers similar as in the previous case.

For the inverted harmonic oscillator, the potential term in the Schrödinger equation can be written as (Fig. III.4B):

$$V(\mathbf{r} - \mathbf{R}_i) = \begin{cases} -\frac{4V_0}{d}((d/2)^2 - \mathbf{r}^2) & : |\mathbf{r} - \mathbf{R}_i| \leq d/2 \\ 0 & : |\mathbf{r} - \mathbf{R}_i| > d/2 \end{cases} \quad (\text{III.5})$$

In both models, the Schrödinger equation can be solved analytically using Bloch's theorem, assuming a periodic triangular antidot lattice. The mathematical background can be found in the SI.

Placing the differently shaped potential barriers in the triangular lattice, the band structures can be calculated and compared with the ideal case (Fig. III.4(C-E)). Looking at the lower bands, no large differences are observed comparing the conical shaped barriers and the inverted harmonic oscillator barriers with the cylindrical barriers. The shape of the  $s$ -type Dirac cone remains the same, and is well separated from the  $p$ -states with a dispersionless flat band. Looking at higher order bands, the bands become more dispersive, and there is more mixing of the bands. This can be explained

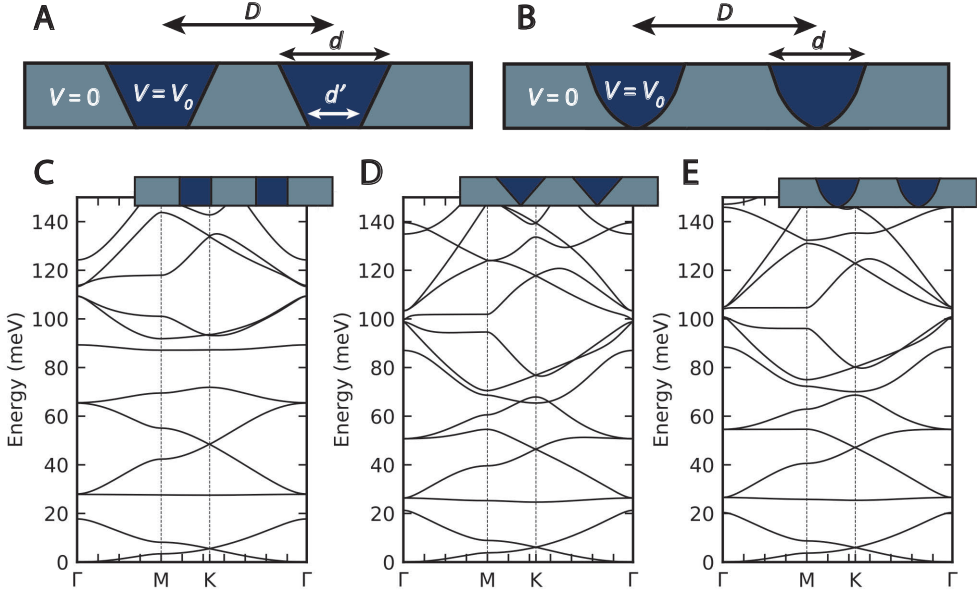


**Figure III.4: Linear and inverted harmonic potential barrier.** (A-B) Schematic side view of the conical potential barrier and inverted harmonic oscillator barrier.  $D$  is the distance between the barriers,  $d$  is the diameter of on the top of the barriers and  $d'$  is the diameter on the bottom of the barrier for the linear case. (C-E) Band structure for the cylindrical potential barrier (C), the linear potential barrier (D) and inverted harmonic oscillator barrier (E). For all calculations,  $D = 40$  nm,  $d = 24$  nm,  $V_0 = 100$  meV. For the linear calculation,  $d' = 0$  nm, meaning that fully conical shaped potential barriers are obtained.

by the fact that the electrons are less confined in the honeycomb symmetry due to the differently shaped barriers. Since the focus will be mainly on the  $s$ -bands and  $p$ -bands of the band structure, higher bands are further ignored in this research, and cylindrical shaped potential barriers will be used in further muffin-tin calculations.

## Vertical confinement

Next, a third dimension can be added to the calculation, since previous calculations were performed on a pure two-dimensional system. In reality, the electron gas will be confined in a semiconductor quantum well with a certain thickness  $t$  along the  $z$ -direction, adding confinement along the  $z$ -dimension. Since the potential barriers add only confinement effects along the  $x$ - $y$  direction, both problems are completely separable when solving the Schrödinger equation. Considering the infinite square well model, the problem in the  $z$ -direction can be solved analytically and the well-known discrete energy are obtained:

$$E_n^z = \frac{\hbar^2}{2m_e^*} \left( \frac{n\pi}{t} \right)^2 \quad (\text{III.6})$$

where  $n = 1, 2, 3, \dots$  is an integer number. To show the effect of the addition of the  $z$ -dimension, density of states (DOS) calculations are performed onto a InGaAs quantum

### III Designing honeycomb semiconductors: The muffin-tin model

well with thickness  $t$  using the muffin-tin model (Fig. III.5A-B). In this calculation, no potential barriers are added to this calculation. Information on the DOS calculation can be found in the SI. The characteristic steps of a confined two-dimensional material are clearly observed in the DOS, indicated by the dashed lines. Increasing the thickness of the quantum well will result in less confinement in the  $z$ -direction, resulting in smaller quantization steps in the DOS.

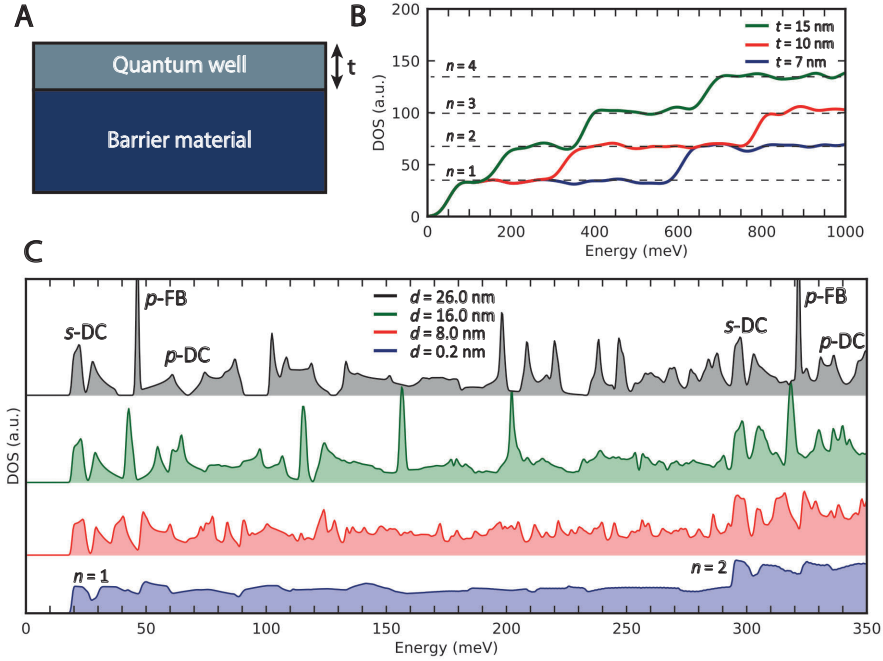


**Figure III.5: Density of states of a honeycomb semiconductor versus a pure quantum well.** (A) Schematic view of the quantum well with thickness  $t$ , confined by a barrier material. (B) Density of states for a pure InGaAs quantum well with a thickness  $t$  of 15 nm (green), 10 nm (red) and 7 nm (blue) calculated with the muffin-tin model. The quantization levels are indicated with dashed lines. (C) Density of states for a 10 nm thick InGaAs QW with a triangular lattice ( $D = 40$  nm) with a superimposed triangular lattice of electron-repulsive potential barrier ( $V_0 = 1.0$  eV) with diameters  $d = 0.2$  nm (blue), 8.0 nm (red), 16.0 nm (green) and 26.0 nm (black). For all the DOS calculation, a broadening parameter  $\Gamma$  of 0.5 meV is applied. The quantization levels for the blue density of states are indicated.

To show the effects of the potential barriers in a honeycomb lattice with a realistic thickness, the DOS is calculated by modelling a 10 nm thick quantum well with a triangular lattice of potential barriers. The results are presented in Fig. III.5C. Starting at a very small diameter (0.2 nm), the quantization steps due to the confinement in the  $z$ -direction are similar as in Fig. III.5B, with nearly perfect flat quantization steps. When increasing the radius of the lattice, more distinct features are visible: first, two clear peaks with a dip in between are visible at the start of the first quantization step, which can be subscribed to the  $s$ -type Dirac cone at the start of the quantization step.

Upon further increasing the diameter of the pores, a clear peak can be observed directly after the Dirac cone, which originates from the  $p$ -like flat band. Although theoretically this feature is infinitely high, the dispersionless band is observed by a clear peak due to the added broadening effect. Finally, when increasing the pore diameter to 26.0 nm, a second Dirac cone can be observed between 60 and 70 meV, and a second flat band is starting to emerge. The  $s$ -orbitals and  $p$ -orbitals are completely separated without any mixing as can be seen by the absence of states between the  $s$ -bands and  $p$ -bands, similar as in the calculated band structure in the previous section.

When looking at the second quantization step of the 0.1 nm radius triangular lattice around  $E = 300$  meV, similar features are observed compared with the first plateau. Upon increasing the diameter of the electron-repelling barriers, the effect of the  $z$ -quantization step seems to fade away, but similar features compared with the first quantization step are still observed in the region of the second plateau. This can be explained by a repetition of Dirac physics in the second quantization step in the  $z$ -direction, defined by the thickness of the quantum well. Due to in-plane coupling of the orbitals, we observe the separation of solutions for the  $z$ -direction (quantum well thickness) and  $x$ - $y$  direction (triangular lattice). In the current system, it will be difficult to address these repetitive features in experiments due to the small feature sizes and larger energy broadening at higher energy, but will definitely be interesting to investigate experimentally when possible.

## Non-parabolicity effect

In the muffin-tin model, we assumed that the two-dimensional electron gas can be described with the free particle model, where the energy of the electrons has a parabolic dependence on the wavenumber. In reality, it is known that III-V semiconductors such as GaAs, InAs and InGaAs are strongly non-parabolic further away from the band edge [28, 29]. This will lead to an overestimation of the confinement energies in all dimensions.

Several methods can be used to quantify non-parabolicity. Here, a direct approximation is used to correct for the non-parabolicity, which has a low computational cost and shows good agreement with other calculations including non-parabolicity [28]. In the used model, a correction formula will be applied to the calculated energy:

$$E(k) = \frac{1}{2\alpha} \left[ -1 + \sqrt{1 + 4\alpha\gamma(k)} \right] \quad (\text{III.7})$$

where  $\gamma(k) = \hbar^2 k^2 / 2m_e^*$  is the parabolic band dispersion energy, and the value  $\alpha$  is adjustable to the amount of non-parabolicity. For InGaAs,  $\alpha = 1.3 \text{ eV}^{-1}$  when comparing this model with  $sp^3d^5s^*$  tight-binding calculations [30]. The difference on the dispersion relation between the parabolic and non-parabolic model can be viewed in Fig. III.6A, where especially away from the band edge the energy is visible non-parabolic. The implication of the NP model on the DOS for a pure QW can be viewed in Fig. III.6B. The quantization steps for the non-parabolic model are much smaller compared with the parabolic model, especially further away from the band edge. The size of the quan-

tization steps obtained from STS experiments are well-explained when accounting for non-parabolicity [31].

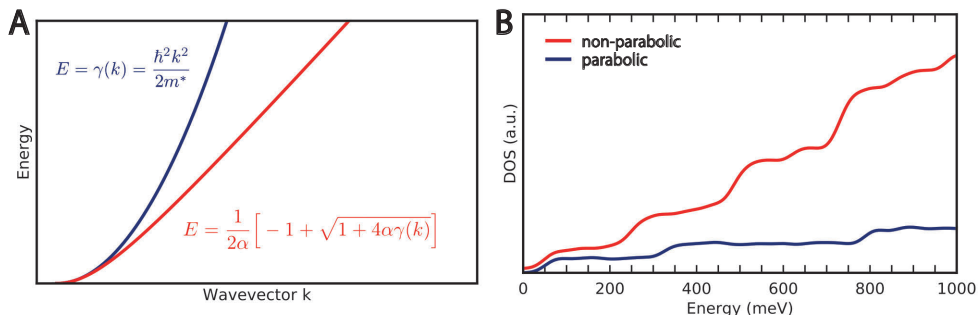


**Figure III.6: Non-parabolic energy dispersion for III-V semiconductors.** (A) Energy dependence versus the wavevector for the free electron model (blue) and the corrected non-parabolic model, showing non-parabolicity away from the band edge. (B) Density of states of 10 nm thick InGaAs QW using the free electron model (blue) and the corrected non-parabolic model.

### III.4 Experimental comparison tool: the numerical muffin-tin model

Using the muffin-tin model including the discussed improvements, a tool is provided to us to compare the experimental differential conductance  $dI/dV$  measured with scanning tunneling microscopy with the theoretical muffin-tin model. The differential conductance  $dI/dV$  is proportional to the local density of states (LDOS), assuming a constant density of states in the tip. From the theoretical side, the LDOS can be calculated using a numerical approach to the muffin-tin model by simulating a finite lattice. The numerical approach also allow us to calculate the electron wave functions, allowing to simulate differential conductance maps for direct comparison with measured differential conductance maps. The numerical muffin-tin model also gives us the opportunity to investigate the effects of disorder in the lattice parameters onto the electronic structure, since non-periodic lattices can be modelled. This will be discussed in Chapter VI.

A schematic view of the simulated lattice is shown in Fig. III.7A. The lattice is divided in smaller grid points, and a total Hamiltonian matrix is calculated using a finite-element method, allowing to obtain the energies and wave functions at individual grid points. The implicitly restarted Arnoldi method is used to find the lowest  $n$  number of eigenvalues and eigenvectors [32] in the Hamiltonian matrix. For all calculations, enough eigenvalues and eigenvectors were calculated to completely present the local density of states (LDOS) in the desired energy range. A more in-depth mathematical background on the method can be found in the SI. The energies can be binned, and the density of states at every grid point can be calculated at different high symmetry

points of the triangular lattice (see Fig. III.7B). In the numerical model, both vertical confinement and non-parabolicity are taken into account similar as in the analytical muffin-tin model.

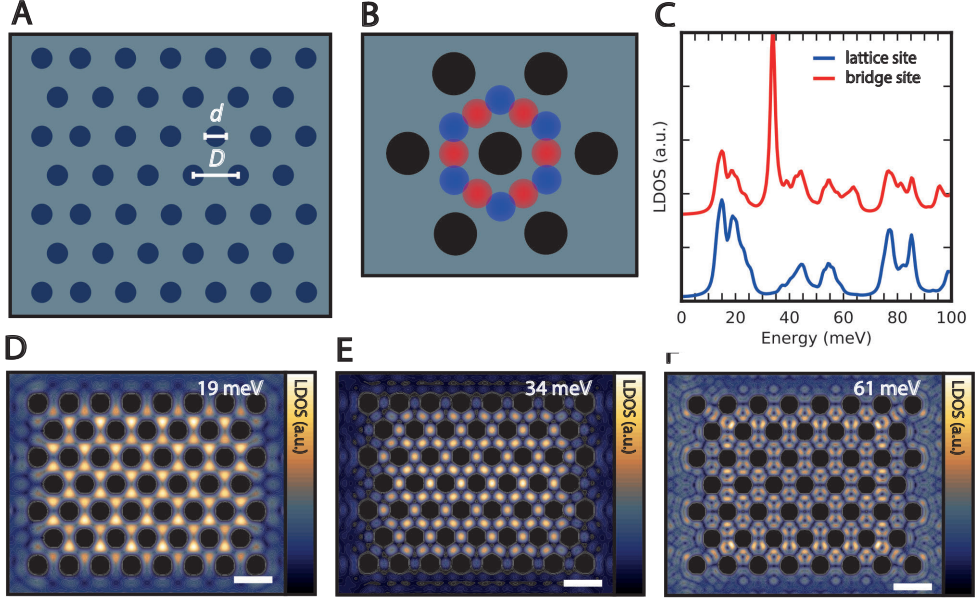


**Figure III.7: Numerical muffin-tin model on the triangular antidot lattice.** (A) Schematic view of the triangular lattice, showing the positions of the calculated LDOS. Lattice parameters are  $D = 40$  nm,  $d = 24$  nm and  $V_0 = 1.0$  eV. (B) Local density of states calculated on the lattice and bridge site of the honeycomb lattice. (C) Simulated differential conductance spectra calculated at the energy of the  $s$ -type Dirac cone,  $p$ -like flatband and higher-order orbitals. For all the LDOS calculations, a broadening  $\Gamma$  of 1.0 meV is used.

Taking a unit cell of the triangular lattice, two different sites of the honeycomb symmetry will be investigated: the lattice site of the honeycomb geometry (blue), and the bridge site (red) located between two lattice sites (see Fig. III.7B). It will be important to measure and understand the local density of states on the lattice sites and bridge positions. The LDOS of both positions are presented in Fig. III.7C for a triangular lattice with electron-repulsive potential barriers ( $D = 40$  nm,  $d = 24$  nm,  $V_0 = 1.0$  eV). Also in the numerical muffin-tin model, the conduction band starts at 0 meV as reference. On both sites, two peaks are observed at  $V = 14$  meV and 20 meV. In between the two peaks, a small dip is visible corresponding to the Dirac point. This double peak corresponds to the LDOS of the  $s$ -orbital Dirac peak. At  $V = 35$  meV, a large peak is visible on the bridge position, but is absent on the lattice site. This peak corresponds to the  $p$ -like flat band. The visibility of the  $p$ -like flat band on the bridge site seems to point to a bonding combination of  $p$ -orbitals with nodes on the lattice sites. This is however not correct:  $p$ -orbitals are orthogonal and their interaction pattern is mismatched with the triangular honeycomb lattice. The exact physics of the electron density patterns

will be described in more detail in the next chapters.

Looking at higher energies, two small peaks at 45 meV and 55 meV can be observed on both the lattice and bridge site, with a small dip in between. This feature can be assigned to the  $p$ -like Dirac point, which also corresponds to the previously calculated band structure.

To support these findings and to investigate the spatial distributions of the electrons onto the lattice, differential conductance maps are numerically calculated at specific energies (see Fig. III.7D-F). Using these maps, the features described in the LDOS can be assigned to the honeycomb symmetry. The first map is calculated around the energy range of the  $s$ -type Dirac cone, showing similar high intensity on both the lattice and bridge site. Looking at the flat band energy, a clear high intensity is visible on the bridge site, confirming the presence of the  $p$ -like flat band. The calculated differential conductance maps are in excellent agreement with experimental maps from the electronic honeycomb lattice build using CO molecules on Cu(111) by Gardenier *et al.* [24], confirming the fidelity of the numerical model and the potential use for comparing simulated maps with experimentally obtained maps.

## III.5 Conclusions and outlook

In this chapter, two methods are presented to calculate the electronic structure of a two-dimensional electron gas superimposed to electron-repelling potential barriers. By placing the barriers in a triangular arrangement, the rich Dirac-type electronic structure of a honeycomb semiconductor is revealed by calculating the band structure and density of states. The electronic properties can be altered and optimized to our liking by changing the lattice parameters of the triangular antidot lattice. Extra effects such as vertical confinement and non-parabolicity away from the band edge can be added to the muffin-tin model, obtaining more realistic results. Finally, the local electronic structure can be calculated by using a numerical approach to the muffin-tin model, which can be directly compared to the results of scanning tunneling experiments, discussed further in this thesis.

# Supplementary information

## Analytical muffin-tin model

The muffin-tin model can be solved analytically using Bloch's theorem, stating that the wave function of an electron in a periodically-repeating environment can be written as [8]:

$$\psi_n(\mathbf{r}) = \sum_{\mathbf{k}} C_{\mathbf{k}} e^{i\mathbf{k}\cdot\mathbf{r}}$$

where  $\mathbf{k}$  is the crystal wave vector and  $C_{\mathbf{k}}$  is a periodic function equal to the periodicity of the crystal. Inserting Bloch theorem into the Schrödinger equation will yield:

$$\sum_{\mathbf{k}} \frac{\hbar^2 \mathbf{k}^2}{2m^*} C_{\mathbf{k}} e^{i\mathbf{k}\cdot\mathbf{r}} + \sum_{\mathbf{k}', \mathbf{G}} C_{\mathbf{k}'} V_{\mathbf{G}} e^{i(\mathbf{k}'+\mathbf{G})\cdot\mathbf{r}} = E \sum_{\mathbf{k}} C_{\mathbf{k}} e^{i\mathbf{k}\cdot\mathbf{r}}$$

Here  $\mathbf{G}$  is a reciprocal lattice vector which can be written in terms of a reciprocal lattice vector basis  $\mathbf{G}_1$  and  $\mathbf{G}_2$ :  $\mathbf{G} = m_1 \mathbf{G}_1 + m_2 \mathbf{G}_2$ ,  $m_1, m_2 \in \mathbb{Z}$ .  $V_{\mathbf{G}}$  is defined as the Fourier transform of the potential  $V(\mathbf{r})$ :

$$V(\mathbf{r}) = \sum_{\mathbf{G}} V_{\mathbf{G}} e^{i\mathbf{G}\cdot\mathbf{r}}$$

Note that the second summation in the equation is written in terms of  $\mathbf{k}'$ . We can set  $\mathbf{k}'$  as  $\mathbf{k} - \mathbf{G}$  and rewrite this equation as:

$$\sum_{\mathbf{k}} e^{i\mathbf{k}\cdot\mathbf{r}} \left[ \left( \frac{\hbar^2 \mathbf{k}^2}{2m_e} - E \right) C_{\mathbf{k}} + \sum_{\mathbf{G}} V_{\mathbf{G}} C_{\mathbf{k}-\mathbf{G}} \right] = 0$$

which only holds when the equation inside the brackets is equal to zero:

$$\left[ \frac{\hbar^2 \mathbf{k}^2}{2m^*} - E \right] C_{\mathbf{k}} + \sum_{\mathbf{G}} V_{\mathbf{G}} C_{\mathbf{k}-\mathbf{G}} = 0$$

This equation can be solved by translating the equation by a reciprocal lattice vector  $\mathbf{G}_i$ :

$$\left[ \frac{\hbar^2}{2m^*} |\mathbf{k} - \mathbf{G}_i|^2 - E \right] C_{\mathbf{k}-\mathbf{G}_i} + \sum_{\mathbf{G}} V_{\mathbf{G}} C_{\mathbf{k}-\mathbf{G}_i-\mathbf{G}} = 0$$

### III Designing honeycomb semiconductors: The muffin-tin model

---

By changing the variables in a way that  $\mathbf{G} = \mathbf{G}_j - \mathbf{G}_i$ , we can write the equation in the final form:

$$\left[ \frac{\hbar^2}{2m^*} |\mathbf{k} - \mathbf{G}_i|^2 - E \right] C_{\mathbf{k}-\mathbf{G}_i} + \sum_{\mathbf{G}_j} V_{\mathbf{G}_j-\mathbf{G}_i} C_{\mathbf{k}-\mathbf{G}_j} = 0$$

Using this formula, the individual elements of a  $n \times n$  Hamiltonian matrix  $\mathbf{H}$  can be calculated using  $n$  number of reciprocal lattice vectors. By calculating the eigenvalues of this matrix,  $n$  number of energy eigenstates  $E_n$  can be calculated. More specific, the individual matrix elements of the Hamiltonian are calculated using the equation:

$$\mathbf{H}_{i,j} = \left[ \frac{\hbar^2}{2m^*} |\mathbf{k} - \mathbf{G}_i|^2 - E \right] \delta_{\mathbf{G}_i, \mathbf{G}_j} + V_{\mathbf{G}_j-\mathbf{G}_i} = 0$$

where  $\delta_{\mathbf{G}_i, \mathbf{G}_j}$  is a delta function which is equal to 1 when  $i = j$  and 0 when  $i \neq j$ . On the diagonal of the Hamiltonian matrix ( $i = j$ ), the potential term  $V_{\mathbf{G}_i-\mathbf{G}_i}$  becomes 0 and only the first term of the equation remains. Looking at the off diagonal elements, only the term  $V_{\mathbf{G}_j-\mathbf{G}_i}$  remains because the delta function in the equation removes the kinetic term of the Schrödinger equation. The Hamiltonian matrix  $\mathbf{H}$  can therefore be constructed in the following form:

$$\mathbf{H} = \begin{pmatrix} \frac{\hbar^2}{2m^*} |\mathbf{k} - \mathbf{G}_1|^2 - E & V_{\mathbf{G}_1-\mathbf{G}_2} & \cdots & V_{\mathbf{G}_1-\mathbf{G}_N} \\ V_{\mathbf{G}_2-\mathbf{G}_1} & \frac{\hbar^2}{2m^*} |\mathbf{k} - \mathbf{G}_2|^2 - E & \cdots & V_{\mathbf{G}_2-\mathbf{G}_N} \\ \vdots & \vdots & \ddots & \vdots \\ V_{\mathbf{G}_N-\mathbf{G}_1} & V_{\mathbf{G}_N-\mathbf{G}_2} & \cdots & \frac{\hbar^2}{2m^*} |\mathbf{k} - \mathbf{G}_N|^2 - E \end{pmatrix}$$

The Fourier coefficients of the potential function  $V(\mathbf{r})$  can be calculated using the following general formula:

$$V_{\mathbf{G}} = \frac{1}{A} \int_{\text{space}} V(\mathbf{r}) e^{-i\mathbf{G}\cdot\mathbf{r}} d^2r$$

where  $A$  is the area of the primitive unit cell. Since the potential outside the barriers is equal to zero, we only have to integrate inside the potential barrier. For cylindrical potential barriers, we only have to integrate over a circle. This will yield the following expression [1, 33, 34]:

$$V_{\mathbf{G}} = \frac{V_0}{A} \int_{\text{circle}} e^{-i\mathbf{G}\cdot\mathbf{r}} d^2r$$

We perform first the integral over the angle component  $\theta$ , which is a standard integral. After this, we are left with only the radial part of the integral:

$$V_{\mathbf{G}} = \frac{2\pi V_0}{A} \int_0^R r J_0(|\mathbf{G}|r) dr$$

where  $J_0$  being the zeroth order cylindrical Bessel function, which is the first solution to the Schrodinger equation for an infinite circular well [35].  $R$  is the radius of

---

the cylindrical potential barrier, which is the bound for the obtained one-dimensional integral. Integrating over  $r$  finally yields [33].

$$V_{\mathbf{G}} = \frac{2\pi R V_0 J_1(|\mathbf{G}|R)}{A|\mathbf{G}|}$$

here,  $J_1$  is the first order cylindrical Bessel function.

Now that we can calculate all the individual matrix components, we can construct total Hamiltonian matrices  $\mathbf{H}$  as a function of the wave vector  $\mathbf{k}$ , and therefore calculate the energy bands at wave vector  $\mathbf{k}$  by calculating the determinant of the Hamiltonian matrix. By following specific wave vectors along the high symmetry points of the lattice, band structure are constructed.

## Finite-size Effects

In the analytical model, a periodic lattice needs to be assumed in order to use Bloch's theorem. The reciprocal lattice represents the Fourier transform of the initial periodic lattice. Upon including more reciprocal lattice vectors, the periodic lattice gets better defined. To investigate the effects of the total number of reciprocal lattice vectors on the electronic structure, band structures of a periodic triangular lattice with different number  $n$  of reciprocal lattice vectors have been calculated and compared with each other. Upon including  $n$  number of reciprocal lattice vectors into the muffin-tin model,  $n \times n$  sized Hamiltonian matrices will be calculated for every  $\mathbf{k}$  point. This means that  $n$  number of energies will be calculated, resulting in  $n$  number of electronic bands in the band structure.

Fig. S1 shows the results for band structure when different number of reciprocal lattice sizes are included. A triangular lattice is assumed with lattice parameters  $D = 40$  nm,  $d = 24$  nm and  $V_0 = 1.0$  eV. In the inset of each band structure, the reciprocal lattice vectors used for that calculation are included. Starting with only four reciprocal lattice vectors (Fig. S1A), the band structure is not stable yet, changing drastically when adding more reciprocal lattice vectors. When adding more lattice vectors, more bands are added to the band structure. Starting from the 64 reciprocal lattice vectors (Fig. S1D), the band structure stabilizes, showing the typical Dirac features in the band structure such as Dirac cones and flat bands. Upon including more reciprocal lattice vectors, the band structure does not change any more in this energy range. Nevertheless, 144 reciprocal lattice vector were used to calculate the band structures in all the analytical muffin-tin models to ensure that the band structure is correctly calculated, which has only a small effect on the calculation time.

## Potential barrier shape

Using the analytical muffin-tin model, the effects of differently shaped potential barrier onto the electronic structure can be considered and calculated. Since the shape of the potential barrier affects the Fourier components of the potential, only the non-diagonal

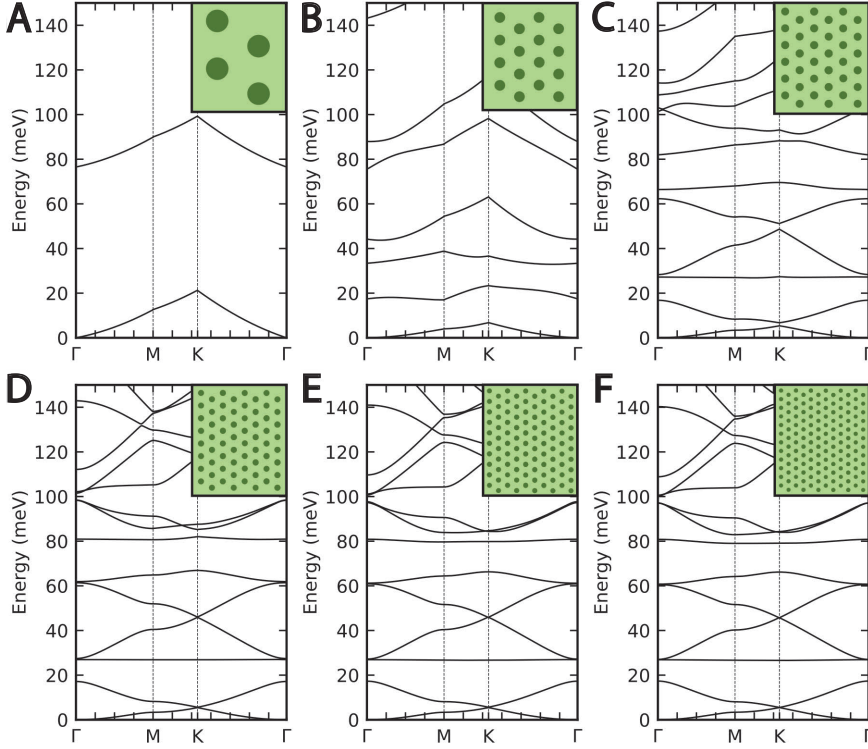


**Figure S1: Finite-size effect on the band structure.** (A-F) Band structures of triangular lattice with size  $2 \times 2$  (A),  $4 \times 4$  (B),  $6 \times 6$  (C),  $8 \times 8$  (D),  $10 \times 10$  (E) and  $12 \times 12$  (F) using the analytical muffin-tin model. The lattice parameters of the triangular lattice are  $D = 40$  nm,  $d = 24$  nm and  $V_0 = 1.0$  eV.

element of the Hamiltonian matrix depend on the potential barrier shape. A schematic view of the discussed potential barrier shapes are presented in Fig. S2, showing the linear potential barrier and the inverse harmonic oscillator barrier.

The Fourier components  $V_{\mathbf{G}}$  of a general potential landscape dependent on the position  $\mathbf{r}$  can be calculated using the formula:

$$V_{\mathbf{G}} = \frac{1}{A} \int_{\text{space}} V(\mathbf{r}) e^{-i\mathbf{G} \cdot \mathbf{r}} d^2r$$

To obtain linear potential barriers with height  $V_0$ , the potential is defined as following:

$$V(\mathbf{r} - \mathbf{R}_i) = \begin{cases} V_0 & 0 < |\mathbf{r} - \mathbf{R}_i| \leq d/2' \\ -\frac{2V_0}{d}(\mathbf{r} - d/2) & d/2' < |\mathbf{r} - \mathbf{R}_i| \leq d/2 \\ 0 & |\mathbf{r} - \mathbf{R}_i| > d/2 \end{cases}$$

where  $d'$  is defined as the diameter of the barrier at the bottom of the gap and  $\mathbf{R}_i$  are the positions of the potential barriers onto the two-dimensional plane. When  $d'$  is 0 nm, a perfect conical potential barrier is obtained, and when  $d' = d$ , we end up

with cylindrical potential barriers as in the previous case. The integral for the Fourier components can be separated into two integral when implementing:

$$V_{\mathbf{G}} = \frac{2\pi V_0}{A} \int_0^{R'} r J_0(|\mathbf{G}|r) dr - \frac{2\pi V_0}{AR} \int_{R'}^R (r-R)r J_0(|\mathbf{G}|r) dr$$

where  $J_0$  is the zeroth order Bessel function. The first integral calculates the Fourier component over a flat potential barrier  $V_0$ , which has the same solution as for the cylindrical model. The second part of the integral is more complicated. By expressing  $R'$  in terms of  $R$  by writing  $R' = \alpha R$ , the solution can be simplified. Solving the second part of the integral will yield the following expression:

$$V_{\mathbf{G}} = \frac{\pi V_0}{A|\mathbf{G}|^2} (\pi J_1(|\mathbf{G}|R)\mathbf{H}_0(|\mathbf{G}|R) + \alpha J_1(|\mathbf{G}|R\alpha)(2|\mathbf{G}|R\alpha - \pi\mathbf{H}_0(|\mathbf{G}|R\alpha)) - \pi J_0(|\mathbf{G}|R)\mathbf{H}_1(|\mathbf{G}|R) + \pi\alpha J_0(|\mathbf{G}|R\alpha)\mathbf{H}_1(|\mathbf{G}|R\alpha))$$

where  $J_1$  is the first order Bessel function and  $\mathbf{H}_0$  and  $\mathbf{H}_1$  are the zeroth and first order Struve functions respectively, which are solutions to the non-homogeneous Bessel's differential equation introduced by Hermann Struve [36].

The inverted harmonic oscillator potential model can be described using the following potential:

$$V(\mathbf{r} - \mathbf{R}_i) = \begin{cases} -\frac{4V_0}{d^2}(\mathbf{r}^2 - (d/2)^2) & : |\mathbf{r} - \mathbf{R}_i| \leq d/2 \\ 0 & : |\mathbf{r} - \mathbf{R}_i| > d/2 \end{cases}$$

The potential barrier will therefore have a parabolic shape. Using this model, the Fourier components can be calculated, which will yield:

$$V_{\mathbf{G}} = -\frac{2\pi V_0}{AR^2} \int_0^R (r^2 - R^2)r J_0(|\mathbf{G}|r) dr$$

and we end up with the following expression for  $V_{\mathbf{G}}$  after solving the integral:

$$V_{\mathbf{G}} = -\frac{4\pi V_0}{A|\mathbf{G}|^2} J_2(|\mathbf{G}|R)$$

where  $J_2$  is the second order Bessel function. Implementing these expressions for  $V_{\mathbf{G}}$  back in the Hamiltonian matrix and calculating the eigenvalues of both systems will obtain the presented band structures in Fig. III.4 .

## Density of states

The density of states (DOS) shows the number of energy states  $D(E)$  available for the electrons at a specific energy  $E$ . The DOS is calculated by taking a grid in reciprocal space and calculate the energy states at every grid point. The modelled grid is framed by the high-symmetry lines  $\Gamma \rightarrow \text{K} \rightarrow \text{M} \rightarrow \Gamma$  of the Brillouin zone, since the modelled grid is symmetrical in all directions. The obtained energies are counted and binned into a histogram:

$$D(E) = \sum_{n,k} \delta(E - E_{n,k})$$

### III Designing honeycomb semiconductors: The muffin-tin model

where  $E_{n,k}$  are the calculated energy states of the system. To create a distribution instead of an histogram, the DOS is smoothed out by replacing the delta function with a Gaussian distribution:

$$D(E) = \sum_{n,k} \frac{\exp^{-(E-E_{n,k})^2/2\sigma^2}}{\sqrt{2\pi\sigma^2}}$$

where  $\sigma$  is a broadening value for the DOS function. To reduce calculation time, all data points which are  $6\sigma$  outside of the center are neglected from the calculation.

To check the consistency of the DOS calculation, a triangular lattice with periodicity of  $D = 40$  nm and diameter of  $d = 24$  nm is calculated for different number of grid points, different energy steps in the DOS histogram and different broadening values  $\sigma$ . The calculated DOS distributions are presented in Fig. S2.

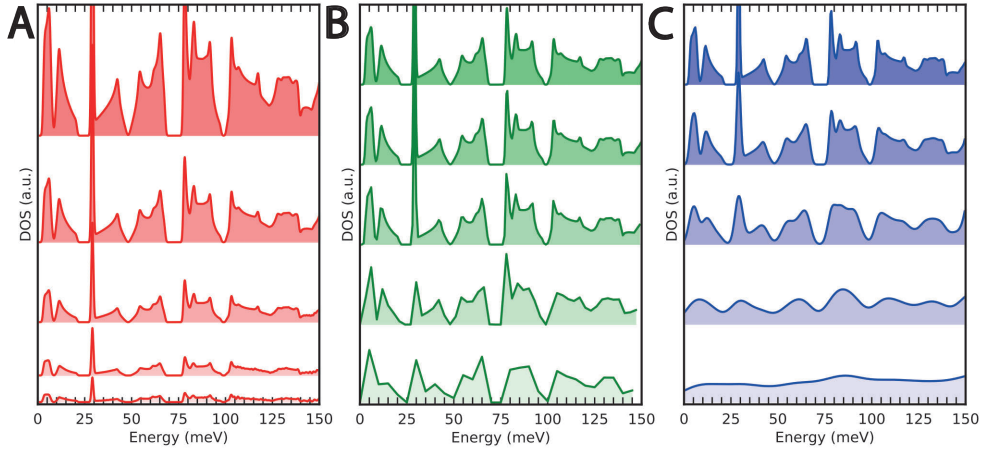


**Figure S2: Density of states consistency.** (A) Density of states calculation with 50, 100, 200, 400 and 800  $k$ -points from the bottom to the top respectively. (B) Density of states calculations with different energy steps. The steps are 5.0 meV, 3.0 meV, 1.0 meV, 0.5 meV and 0.1 meV from bottom to top. (C) Density of states with different amount of broadening. Broadening of 10 meV (bottom), 5.0 meV, 2.0 meV, 1.0 meV and 0.5 meV (top) is used in these calculations.

First, the DOS is calculated where the reciprocal area enclosed by the high symmetry points is divided between 50 grid points (bottom) to 800 grid points (top). For a low number of grid points, the number of states per energy step will be low. Therefore, more fluctuations are expected in the DOS distribution using only 50 grid points. Upon increasing the number of grid points, features will get more distinct. Naturally, more grid points will also mean that the calculation time will increase, limiting the total number of grid points to a certain value. For all the DOS calculations, 400  $k$ -points were used, restraining the calculation time while still obtaining trustful results. Since the number of calculated energies per grid point  $n$  goes linear with the total number of grid points used for the calculation, more grid points are only needed when calculating the DOS at higher energies.

Second, the width of the energy steps in the DOS distribution is varied between 5.0 meV (bottom) and 0.1 meV (top), showed in Fig. S2 in green. Clearly, using a large energy width means less resolution in the DOS, showing no clear features any more such as the  $s$ -type Dirac cone and  $p$ -like flat band. Therefore, an energy step of 0.5 meV is used for all DOS calculations to obtain clear features, since this has only a minor impact on the calculation time.

Lastly, the broadening parameter of the Gaussian distribution is varied between 10 meV (bottom) and 0.5 meV (top), showed in Fig. S2C. For high broadening, all Dirac features are absent, showing a smooth continuous distribution of energies. Decreasing the broadening reveals again the Dirac like properties of the simulated semiconductor. In all the theoretical work, a broadening of 0.5 meV is used to clearly reveal the Dirac cones and flat bands in the DOS. Upon comparing the calculated DOS with experiments, the value of the broadening parameter can be altered to better fit theoretical work with experimental results.

## Numerical muffin-tin model

In a numerical muffin-tin model, the complete simulated potential landscape is divided in discrete data points (Fig. S3A,B). By selectively assign potential values to individual grid points, a lattice of potential barriers can be formed, such as the triangular symmetry forming the honeycomb semiconductor. By transforming the Schrödinger equation into a matrix equation, the energies and wave functions are calculated on each individual grid point numerically, which are used to calculate the local density of states and to create a simulated differential conductance map. To calculate this, the Schrödinger equation needs to be written in some sort of a matrix form:

$$E\psi(\mathbf{r}) = \mathbf{H}\psi(\mathbf{r}) \Rightarrow E \begin{bmatrix} \psi(\mathbf{r}_1) \\ \psi(\mathbf{r}_2) \\ \psi(\mathbf{r}_3) \\ \vdots \\ \psi(\mathbf{r}_N) \end{bmatrix} = \begin{pmatrix} H_{11} & H_{12} & \cdots & H_{1N} \\ H_{21} & H_{22} & \cdots & H_{2N} \\ \vdots & \vdots & \ddots & \vdots \\ H_{N1} & H_{N2} & \cdots & H_{NN} \end{pmatrix} \begin{bmatrix} \psi(\mathbf{r}_1) \\ \psi(\mathbf{r}_2) \\ \psi(\mathbf{r}_3) \\ \vdots \\ \psi(\mathbf{r}_N) \end{bmatrix}$$

where  $H_{mn}$  are the individual terms of the Hamiltonian matrix,  $N$  is the total number of discrete points used for the calculation and  $\psi(\mathbf{r})$  is a column vector, telling the value of the wave function at vector  $\mathbf{r}$ . When the Hamiltonian matrix is calculated, the eigenvalues of the matrix can be evaluated obtaining  $N$  eigenvalues and  $N$  eigenvectors, which can be calculated using the restarted Arnoldi method [32]. By increasing the number of grid points of the numerical muffin-tin calculation, the resolution will increase and more energies and wave functions can be calculated. Naturally, the calculation time will also increase exponentially.

To investigate the exact form of the matrix equation, we need to first recall the form of the Schrödinger equation:

$$\mathbf{H}\psi(\mathbf{r}) = \left[ -\frac{\hbar^2}{2m_e^*} \nabla^2 + V(\mathbf{r} - \mathbf{R}_i) \right] \psi(\mathbf{r}) = E\psi(\mathbf{r})$$

### III Designing honeycomb semiconductors: The muffin-tin model

where  $\mathbf{R}_i$  are the Bravais lattice vectors of the lattice formed by the potential barriers,  $i$  is the index number of barrier potentials,  $N$  is the total number of grid points,  $\psi(\mathbf{r})$  are the value of the wave function at vector  $\mathbf{r}$  and  $E$  is the calculated energy state of the electron.

Since the Schrödinger equation consist of two parts, both parts can individually be written into a matrix form. For simplicity, we start with one-dimensional case, which will be later translated into two dimensions. Looking at the the potential landscape on the simulated grid,  $V(\mathbf{r}-\mathbf{R}_i)$  will be a step-like function, telling us the potential energy at each individual grid point. Since the potential on each grid point does not interact with other neighboring points, the potential matrix  $\mathbf{V}$  can be written as a diagonal matrix where on the diagonal the potential value  $V(\mathbf{x}_i)$  is written of each grid point at vector point  $\mathbf{x}_i$ :

$$\mathbf{V} = \begin{pmatrix} V(\mathbf{x}_1) & 0 & \cdots & \cdots & \cdots & 0 \\ 0 & V(\mathbf{x}_2) & 0 & \cdots & \cdots & 0 \\ \vdots & 0 & \ddots & & & \vdots \\ \vdots & \vdots & & \ddots & & \vdots \\ \vdots & \vdots & & & \ddots & 0 \\ 0 & 0 & \cdots & \cdots & 0 & V(\mathbf{x}_N) \end{pmatrix}$$

In this case,  $V(\mathbf{x}_i)$  will either have value of 0 or  $V_0$  since the simulated potential barriers will have a constant value  $V_0$ , as indicated in Fig. S3C.

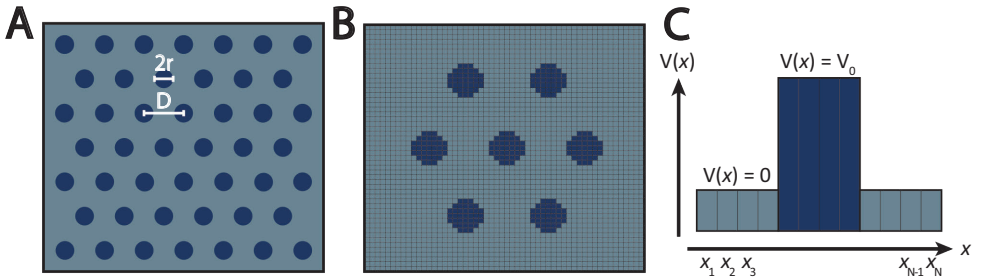


**Figure S3: Numerical muffin-tin model** (A) Simulated triangular lattice with lattice constant  $D$  and diameter  $d$ . (B) A unit cell of the triangular lattice simulated with grid points. In the light-blue grid points, the potential is set to zero, while in the dark-blue grid points, the potential has a value of  $V_0$ , forming a potential landscape with a triangular symmetry. (C) Side-view of the potential landscape in the  $x$ -direction, showing the height of the potential in the dark-blue grid points.

The kinetic part of the Schrödinger equation is more tedious to express in a matrix form, since it contains a second derivative  $\nabla^2$ . An approximation method will be used to write the second derivative into a matrix form, which is called the finite element method. Considering only one dimension, we will start with a wave function  $\psi(x)$  which is assumed to be a solution of the Schrödinger equation. The first derivative of the

wave function between two grid points  $x_{n+1}$  and  $x_n$  with a distance  $\Delta x$  between them is defined as:

$$\left[ \frac{\partial \psi}{\partial x} \right]_{n+1/2} = \frac{\psi(x + \Delta x) - \psi(x)}{\Delta x} = \frac{\psi(x_{n+1}) - \psi(x_n)}{\Delta x}$$

The first derivative between points  $x_n$  and  $x_{n-1}$  can be written in a similar way:

$$\left[ \frac{\partial \psi}{\partial x} \right]_{n-1/2} = \frac{\psi(x_n) - \psi(x_{n-1})}{\Delta x}$$

Using both definitions, the second derivative at grid point  $n$  can now be written in term of the wave function:

$$\left[ \frac{\partial^2 \psi}{\partial x^2} \right]_n = \frac{\left[ \frac{\partial \psi}{\partial x} \right]_{n+1/2} - \left[ \frac{\partial \psi}{\partial x} \right]_{n-1/2}}{\Delta x} = \frac{\psi(x_{n+1}) - 2\psi(x_n) + \psi(x_{n-1}))}{\Delta x^2}$$

Assuming there are  $N$  number of total grid points in the  $x$ -direction, the second derivative of the wave function  $\psi(x)$  at every grid point can now be defined using a column vector representation of the wave function  $\boldsymbol{\psi}(x)$  and a certain  $N \times N$  matrix  $\mathbf{U}_{xx}$ , yielding the following expression:

$$\left[ \frac{\partial^2 \psi}{\partial x^2} \right] = \frac{1}{\Delta x^2} \mathbf{U}_{xx} \boldsymbol{\psi}(x) = \frac{1}{\Delta x^2} \begin{pmatrix} -2 & 1 & 0 & \cdots & \cdots & \cdots & 0 \\ 1 & -2 & 1 & 0 & \cdots & \cdots & \vdots \\ 0 & \ddots & \ddots & \ddots & \ddots & \cdots & \vdots \\ \vdots & \ddots & \ddots & \ddots & \ddots & \ddots & \vdots \\ \vdots & \vdots & \ddots & \ddots & \ddots & \ddots & 0 \\ \vdots & \vdots & \vdots & 0 & 1 & -2 & 1 \\ 0 & \cdots & \cdots & \cdots & 0 & 1 & -2 \end{pmatrix} \begin{bmatrix} \psi(x_1) \\ \psi(x_2) \\ \psi(x_3) \\ \vdots \\ \psi(x_N) \end{bmatrix}$$

Using this matrix format, the second derivatives of the wave function at all grid points can be derived except for the starting grid point ( $n = 1$ ) and the end grid point ( $n = N$ ), where the formula assumes that  $\psi(x_0) = \psi(x_N) = 0$ . This is called the hard-wall boundary condition. Since this is experimentally not feasible, periodic boundary conditions can be implemented, which means that  $\psi(x_0) = \psi(x_N) = 1$ . Implementing this into our matrix will yield:

$$\left[ \frac{\partial^2 \psi}{\partial x^2} \right] = \frac{1}{\Delta x^2} \begin{pmatrix} -2 & 1 & 0 & \cdots & \cdots & \cdots & 1 \\ 1 & -2 & 1 & 0 & \cdots & \cdots & \vdots \\ 0 & \ddots & \ddots & \ddots & \ddots & \cdots & \vdots \\ \vdots & \ddots & \ddots & \ddots & \ddots & \ddots & \vdots \\ \vdots & \vdots & \ddots & \ddots & \ddots & \ddots & 0 \\ \vdots & \vdots & \vdots & 0 & 1 & -2 & 1 \\ 1 & \cdots & \cdots & \cdots & 0 & 1 & -2 \end{pmatrix} \begin{bmatrix} \psi(x_1) \\ \psi(x_2) \\ \psi(x_3) \\ \vdots \\ \psi(x_N) \end{bmatrix}$$

### III Designing honeycomb semiconductors: The muffin-tin model

---

In this way, the boundary of the numerical muffin-tin calculation will have no effect on the electronic structure of the simulated system. To check the differences in electronic structure, both boundary conditions have been simulated using the same lattice, which will be discussed later in this section.

Now that the second derivative has been constructed in matrix format, the matrix needs to be expanded in order to describe a two-dimensional system. Using Cartesian coordinates, the two-dimensional Laplacian operator  $\nabla^2$  is defined as a sum of the second derivatives in both the  $x$ - and  $y$ -direction:

$$\nabla^2 = \frac{\partial^2}{\partial x^2} + \frac{\partial^2}{\partial y^2}$$

For both second derivatives, the same finite-difference equations can be applied, which will result in the second derivative of the wave function at grid position  $(n, m)$ :

$$\begin{aligned} \nabla^2 \psi_{(n,m)} &= \frac{\partial^2 \psi}{\partial x^2} + \frac{\partial^2 \psi}{\partial y^2} \\ &= \frac{\psi(x_{n+1}, y_m) - 2\psi(x_n, y_m) + \psi(x_{n-1}, y_m)}{\Delta x^2} + \frac{\psi(x_n, y_{m+1}) - 2\psi(x_n, y_m) + \psi(x_n, y_{m-1})}{\Delta y^2} \end{aligned}$$

where  $n = 1, 2, \dots, N$  and  $m = 1, 2, \dots, M$  are indices of the grid points in the  $x$ - and  $y$ -direction on a  $N \times M$  grid. To write this equation in a general matrix form, the column  $\psi(x, y)$  needs to be translate into a one-dimensional column of length  $N \times M$ .

$$\psi(x, y) = \begin{bmatrix} \psi(x_1, y_1) \\ \psi(x_2, y_1) \\ \vdots \\ \psi(x_N, y_1) \\ \psi(x_1, y_2) \\ \vdots \\ \psi(x_N, y_M) \end{bmatrix}$$

To obtain a linear system, we introduce global ordering of the grid lattice, explained as in Fig. S4. This will translate into a linear system of equations. Using this method, we need to construct a different matrix using the calculated matrices in finite element method. This matrix can be constructed using the following equation:

$$\nabla^2 = \mathbf{U}_{xx} \otimes \mathbf{I}_{M \times M} + \mathbf{I}_{N \times N} \otimes \mathbf{U}_{yy}$$

where  $\otimes$  stands for the Kronecker product,  $\mathbf{I}_{M \times M}$  and  $\mathbf{I}_{N \times N}$  are  $M \times M$  and  $N \times N$  unity matrices, and  $\mathbf{U}_{xx}$  and  $\mathbf{U}_{yy}$  are the second derivative matrices in the  $x$ - and  $y$ -direction respectively. The Kronecker product between two matrices  $\mathbf{A}$  and  $\mathbf{B}$  of size  $2 \times 2$  can be written as follows:

$$\mathbf{A} \otimes \mathbf{B} = \begin{pmatrix} a_{11}\mathbf{B} & a_{12}\mathbf{B} \\ a_{21}\mathbf{B} & a_{22}\mathbf{B} \end{pmatrix} = \begin{pmatrix} a_{11}b_{11} & a_{11}b_{12} & a_{12}b_{11} & a_{12}b_{12} \\ a_{11}b_{21} & a_{11}b_{22} & a_{12}b_{21} & a_{12}b_{22} \\ a_{21}b_{11} & a_{21}b_{12} & a_{22}b_{11} & a_{22}b_{12} \\ a_{21}b_{21} & a_{21}b_{22} & a_{22}b_{21} & a_{22}b_{22} \end{pmatrix}$$

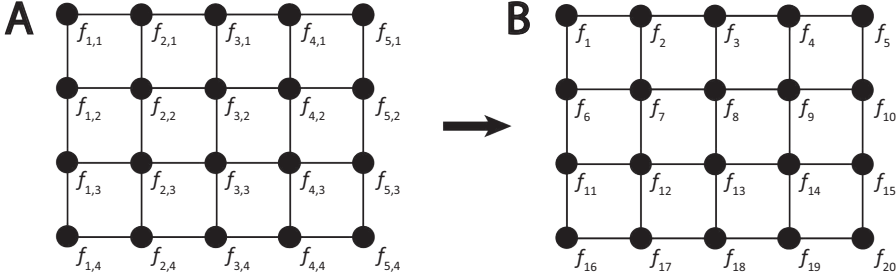


**Figure S4: Rearrangement of grid points to a linear system** (A) Old notation of the grid points in a two-dimensional system. Function  $f_{i,j}$  is the value of the function  $f$  at position  $(i,j)$ . (B) New notation of the grid points.

which will result in a  $4 \times 4$  matrix. Applying the Kronecker product to the second derivative matrices, we end up with a matrix of size  $(N \times M) \times (N \times M)$ . Together with the wave function column of length  $N \times M$ , the Laplacian operator can be written using this matrix format. Also noteworthy is that the matrix is a so-called tridiagonal block matrix, meaning that the matrix can be divided into a collection of smaller matrices which are all tridiagonal. The equation of the two-dimensional Laplacian can easily be extended to three dimensions by adding a third component. We can also easily switch between different boundary conditions by using the different forms of  $\mathbf{U}_{xx}$  and  $\mathbf{U}_{yy}$  as discussed earlier.

Now all the tools are there to completely rewrite the Schrödinger equation into matrix format:

$$\mathbf{H}\psi(\mathbf{x}) = \left[ -\frac{\hbar^2}{2m^*} \nabla^2 + \mathbf{V} \right] \psi(\mathbf{x}) = E\psi(\mathbf{x})$$

where  $\nabla^2$  and  $\mathbf{V}$  are matrices which can be calculated. By constructing a two-dimensional potential landscape and dividing this into grid points, the total Hamiltonian matrix can be formulated and the eigenvalues and eigenvectors of this matrix can be calculated, providing us the energies and wave function at each grid point. From there, the LDOS can be calculated at each grid point, and differential conductance maps can be simulated using the calculated wave functions.

## Local density of states

At each grid point, a list of available energy states is calculated. The local density of states (LDOS) is defined as the total of number of energies  $E$  which can be occupied at grid point  $i$ :

$$\text{LDOS}(i, E) = \sum_{E'} |\psi_{i,E'}|^2 \delta(E - E')$$

where  $\delta(x)$  is the Dirac delta function. Plotting the LDOS will yield a histogram of energy distributions. However, since a histogram is not representable for experimentally obtained results, the Dirac delta function is replaced with a Lorentzian distribution

### III Designing honeycomb semiconductors: The muffin-tin model

---

to take broadening of the energy states into account. The Lorentzian is a continuous probability distribution, which will change the LDOS expression:

$$\text{LDOS}(i, E) = \sum_{E'} |\psi_{i, E'}|^2 \frac{1}{\pi\Gamma} \frac{\Gamma^2}{(E - E')^2 + \Gamma^2}$$

where  $\Gamma$  is the broadening parameter specifying the half-width at half-maximum of each energy state. The broadening  $\Gamma$  was set to 1.0 meV in every numerical muffin-tin calculation performed in this chapter, showing clearly the desired Dirac features. The broadening parameter can be adjusted to more realistic values to fit the simulated LDOS with differential conductance spectra, which will be presented in Chapter IV. Lastly, the offset of the conduction band is not shifted in this model, meaning that the reference energy of the conduction band is equal to 0 eV. This can be shifted when comparing with experimental data.

## Resolution

To check the consistency of the numerical muffin-tin calculation, several parameters of the calculation have been investigated. To start, the total number of grid points is investigated. Upon including more grid points to the model, the calculated energy states will be more stable and precise. However, the size of the Hamiltonian matrix scales linearly with the total number of grid points, meaning that the calculation time increases rapidly. For this reason, a trade-off value needs to be found for the number of total grid points used in the numerical muffin-tin model.

To find this trade-off value, a numerical muffin-tin calculation is performed for a  $7 \times 7$  triangular lattice with lattice parameters of  $D = 40$  nm,  $d = 24$  nm and  $V_0 = 1.0$  eV with different resolution parameters. The resolution of the calculation is expressed as a total number of points per lattice constant. Here, 10, 20 and 30 grid points per lattice constant were used, meaning that size of each grid point is  $4 \times 4$ ,  $2 \times 2$  and  $1.33 \times 1.33$  nm<sup>2</sup>. This will result in simulated  $7 \times 7$  triangular lattice with a total grid sizes of  $81 \times 76$ ,  $161 \times 145$  and  $241 \times 217$  data points.

The LDOS on the lattice site and bridge site of the honeycomb symmetry are calculated and presented in Fig. S5 for the different grid sizes. For the  $81 \times 76$  simulated grid, Dirac features are immediately observed in on the lattice site and bridge such as the two *s*-bands forming a Dirac cone around  $E = 15$  meV. Looking at the *p*-like bands, an intense peak is observed on the lattice site around 30 meV which can be assigned to the flat band, and a second Dirac cone seems to be forming at 45 meV. Comparing with spectra with higher resolution, the intensity of all features are much lower and bit more noisy. In the calculated map, the modulated potential barriers seem not to have a perfect circular shape, and shapes vary between barriers, which is highlighted by the increased electron density on the lattice sites in the middle of the triangular lattice, while on other lattices sites the density is lower. This indicates that the number of grid points for this calculation is too low, and a higher resolution is desired.

Increasing the resolution to  $161 \times 145$  and  $241 \times 217$  will lead to better defined, circular

---

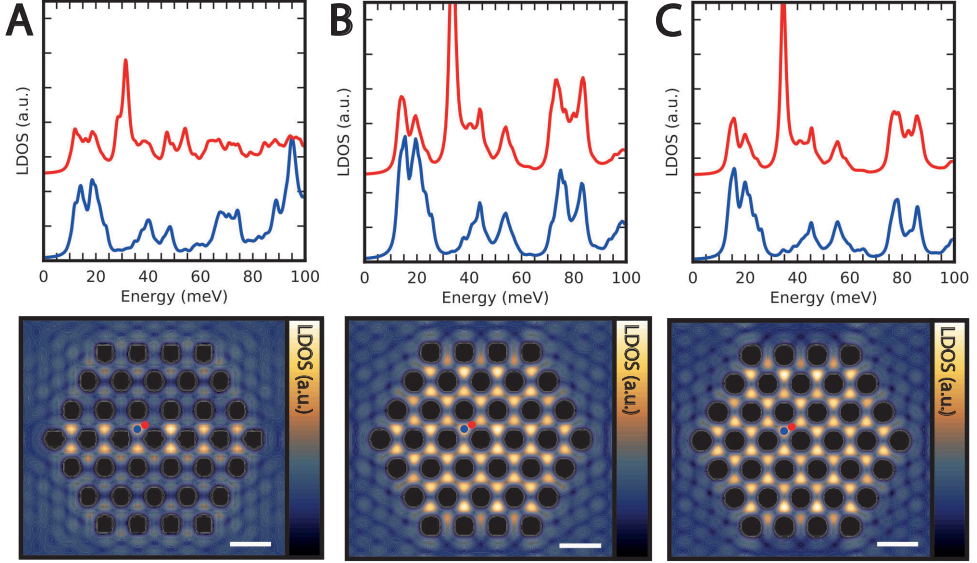


**Figure S5: Resolution effect on the electronic structure.** Calculated LDOS on the lattice (blue) and bridge site (red) for a  $7 \times 7$  triangular lattice with  $81 \times 76$  (A),  $161 \times 145$  (B) and  $241 \times 217$  (C) number of grid points, accompanied with differential conductance maps taken around the energy of the Dirac point ( $E = 20$  meV). Lattice parameters are  $D = 40$  nm,  $d = 24$  nm and  $V_0 = 1.0$  eV. Scalebar denote 50 nm.

potential barriers, improving the consistency of the calculation. Looking at the calculated LDOS, the same features are observed as in the previous calculation, but all features are more clear, and especially higher-order states are more distinct and less noisy. Between the  $161 \times 145$  grid point calculation and the  $241 \times 217$  calculation, no significant differences are detected from the calculated spectra and maps. Therefore, all numerical calculations have been performed with at least 20 grid points per lattice constant. This means that the total grid size of the calculation can still vary, but it is independent of the lattice constant of the unit cell.

## Finite-size effects and boundaries

To investigate the effects of the total size of the triangular lattice onto the local electronic properties, three lattices with different sizes are simulated. The sizes of the triangular lattice are presented Fig. S6. Spectra are calculated as close as possible to the middle of the lattice, showing the LDOS on the lattice site (blue) and bridge site (red). Additionally, differential conductance maps show the change of the LDOS as a function of the lattice size. On top of that, two different boundary conditions are used to define the edge of the simulated area: the hard-wall boundary condition and the periodic boundary condition. For all lattices, lattice parameters of  $D = 40$  nm,  $d = 24$  nm and  $V_0 = 1.0$  eV are used.

First we look at the hard-wall boundary, meaning that the simulated lattice is closed

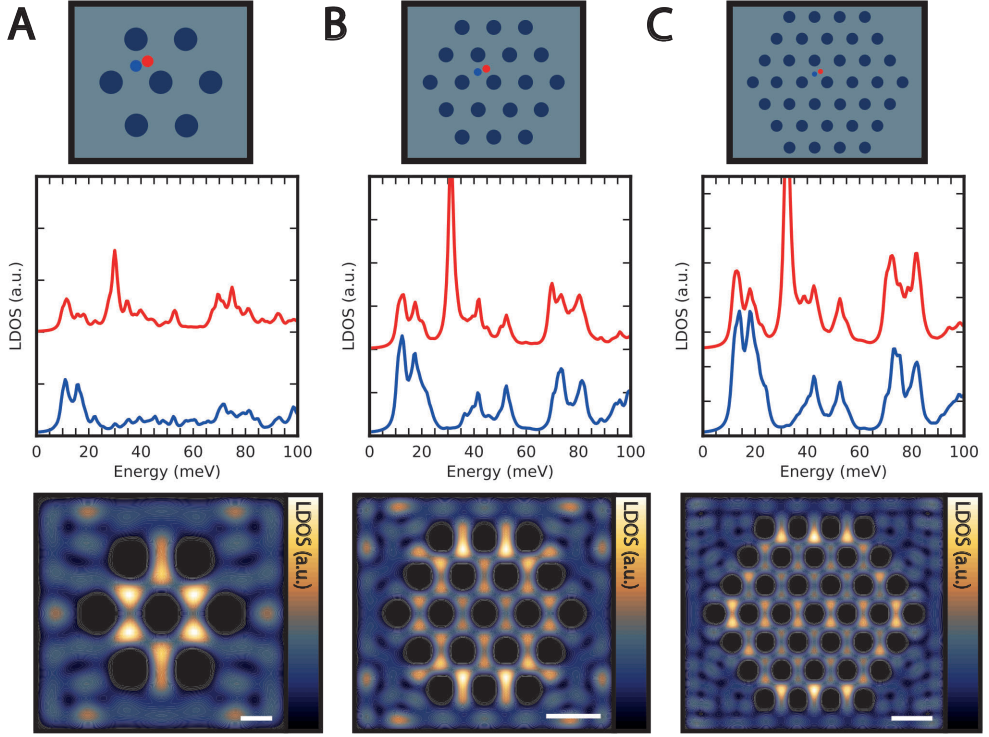


**Figure S6: Finite size effect with hard-wall boundary conditions.** (A) Small simulated  $3 \times 3$  triangular lattice, accompanied with the calculated LDOS on the lattice (blue) and bridge site (red) and a calculated differential conductance map at 15 meV. Scalebar denotes 20 nm. (B) Simulated triangular lattice with one extra ring of potential barriers ( $5 \times 5$  lattice). LDOS are calculated on similar sites, and the map is calculated at 15 meV. Scalebar denotes 50 nm. (C) Large  $7 \times 7$  triangular lattice, accompanied with the calculated LDOS and map at 20 meV. Scalebars denote 50 nm.

by a hard-wall, where the wave function on the edge and beyond the edge is equal to zero ( $\psi(\mathbf{x}) = 0$ ). Looking at the smallest lattice, it is intriguing to see that a  $s$ -Dirac cone and a  $p$ -flat band is already visible on the lattice site and bridge site respectively, while in total only 7 potential barriers are used in this calculation model. This is also visible in the map, showing high intensity on the lattice site and lower intensity at the bridge site around the energy of the first Dirac cone ( $E = 15$  meV), which is similar to the calculated maps in the main chapter. The maps also confirm that the hard-wall boundary conditions is applied correctly, since the electron density reaches zero around the border of the map. However, features higher in energy cannot be observed on the lattice site due to the small lattice size. Increasing to larger lattices will lead to more smooth spectra and maps, Dirac features get better defined and higher order Dirac bands can be recognized. For this reason, triangular lattices of at least  $7 \times 7$  in size are modelled to accurately investigate the electronic properties in other calculation models.

The difference between the hard-wall boundary condition and the periodic boundary

condition can be viewed in Fig. S7, where the LDOS and maps of the different sized lattice are calculated with periodic boundary conditions. Comparing the smallest lattice, large differences can be observed in the calculated LDOS for the hard-wall and no-wall boundary. In the calculated map, a high electron density is found around the border of the map, confirming that a periodic boundary conditions is applied. Increasing to larger lattices, the electronic properties converge into a more stable state, and similar results are obtained with different boundary conditions. This also holds for the calculated maps. Since there is experimentally no hard-wall boundary between electronic states in the honeycomb lattice and the two-dimensional electron gas, the periodic boundary condition is used in all numerical muffin-tin models.

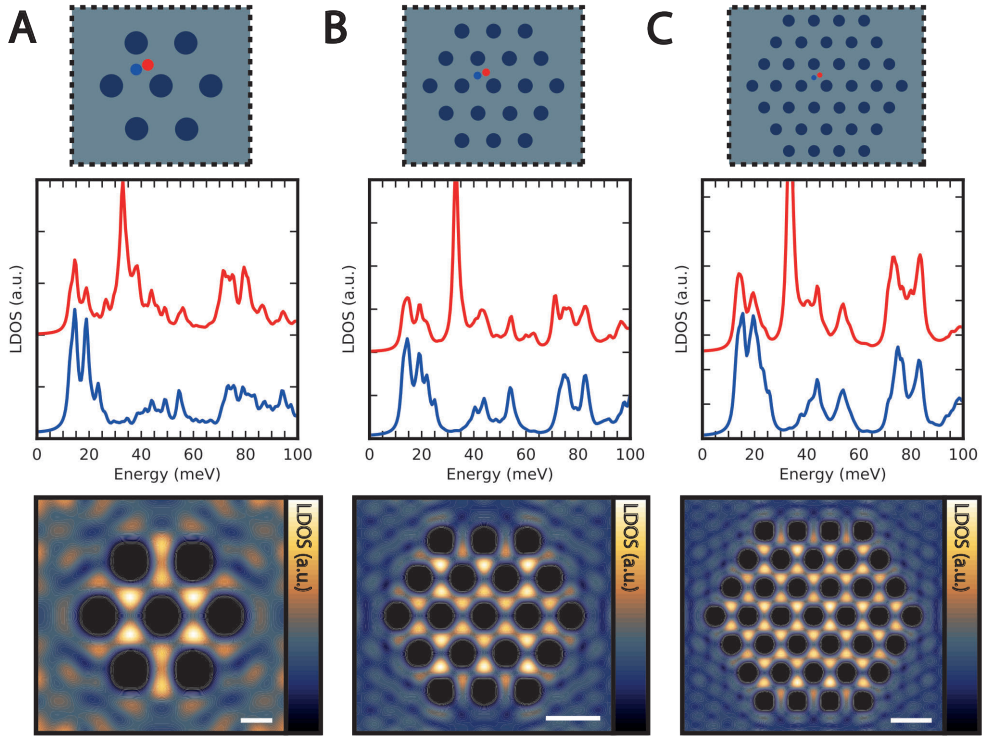


**Figure S7: Finite size effects with periodic boundary conditions.** (A) Small simulated  $3 \times 3$  triangular lattice, accompanied with the calculated LDOS on the lattice (blue) and bridge site (red) and a calculated differential conductance map at  $E = 20$  meV. Scalebar denotes 20 nm. (B) Simulated triangular lattice with one extra ring of potential barriers ( $5 \times 5$  lattice). LDOS are calculated on similar sites, and the map is calculated at  $E = 20$  meV. Scalebars denote 50 nm. (C) Large  $7 \times 7$  triangular lattice, accompanied with the calculated LDOS and map at  $E = 20$  meV. For all lattices, lattice parameters are  $D = 40$  nm,  $d = 24$  nm,  $V_0 = 1.0$  eV. Scalebar denotes 50 nm.

## Unit cell size and radius

To check the validity of the numerical muffin-tin model and to compare it with the analytical model, the size of the unit cell is varied while keeping the ratio between the diameter and unit cell size  $d/D$  constant (Fig. S8A-C). Starting at  $D = 80$  nm, the two peaks of the  $s$ -Dirac cone are merged into one peak, and a quite broad flat-band is observed in a narrow energy window. Decreasing the unit cell size to 40 nm will increase the range of the energy, splitting the Dirac cone in two separate peaks, and higher order Dirac states are visible. The energy range increases similarly as in the analytical model, confirming the exactitude of the model. Upon further decreasing the size of the unit cell ( $D = 20$  nm), the total number of states at the Dirac point of the  $s$ -like Dirac cone are almost vanished, meaning that the full Dirac cone can be observed. Much more noise is also present, which can be attributed to the limit number of calculated eigenvalues, creating more fluctuations in the calculated electron states. All the Dirac features in the lowest unit cell size have also a much higher energy range, meaning that LDOS has a more step-like distribution when the electron states are broadened with  $\Gamma = 1.0$  meV.

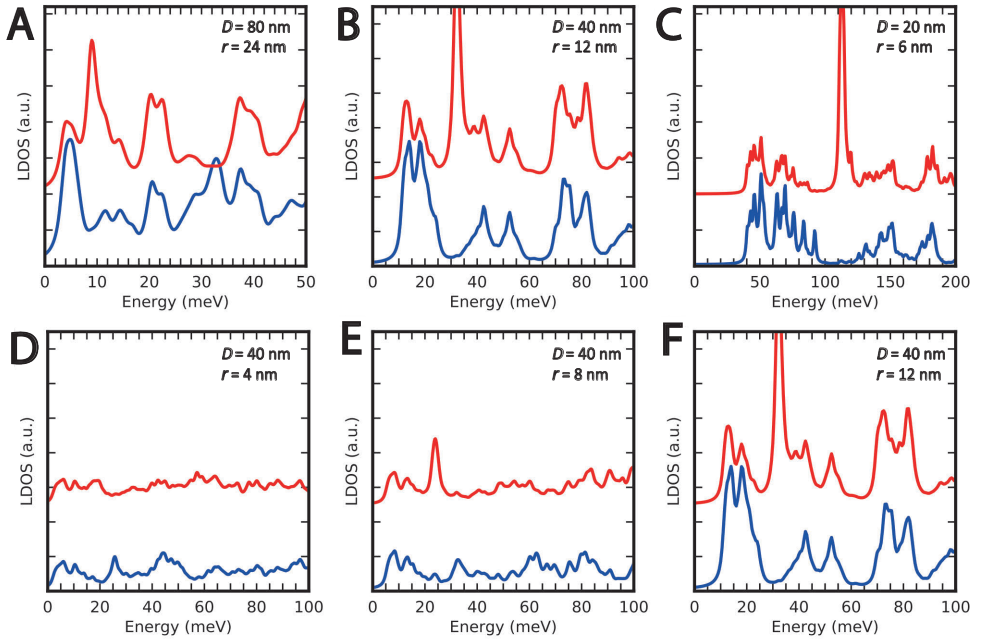


**Figure S8: LDOS with different lattice parameters.** (A-C) Calculated LDOS for a triangular lattice with unit cell sizes  $D = 80$  nm (A), 40 nm (B) and 20 nm (C) with a constant diameter of 0.6 times the lattice constant. (D-F) Calculated LDOS for triangular lattice of  $D = 40$  nm with diameters of  $d = 8.0$  nm (D), 16 nm (E) and 24 nm (F).

Next, the diameter of the electron-repelling potential barriers is also varied (Fig. S8D-F) to verify if the Dirac features change similarly with the observation in the analytical model, as discussed in this chapter. Indeed, when the diameter of the potential barriers

is very small (Fig. S8D), the honeycomb symmetry is not well defined, and almost a flat distribution is obtained on the lattice site (red) and bridge site (blue), similar as for a free two-dimensional electron gas. Upon increasing the diameter (Fig. S8E), Dirac features start to be visible on both sites, especially the  $s$ -like Dirac cone around  $E = 10$  meV and the  $p$ -like flat band around  $E = 25$  meV on the bridge site. Upon further increase of the barrier diameter (Fig. S8F), the Dirac features become even more clear, showing the improved definition of the honeycomb symmetry in the simulated model.

---

## References

- [1] M. Gibertini, A. Singha, V. Pellegrini, M. Polini, G. Vignale, A. Pinczuk, L. N. Pfeiffer, and K. W. West, "Engineering artificial graphene in a two-dimensional electron gas," *Physical Review B*, vol. 79, p. 241406, jun 2009.
- [2] J. Wang, S. Deng, Z. Liu, and Z. Liu, "The rare two-dimensional materials with Dirac cones," 2015.
- [3] C.-H. Park and S. G. Louie, "Making Massless Dirac Fermions from a Patterned Two-Dimensional Electron Gas," *Nano Letters*, vol. 9, pp. 1793–1797, may 2009.
- [4] L. C. Post, T. Xu, N. A. Franchina Vergel, A. Tadjine, Y. Lambert, F. Vaurette, D. Yarekha, L. Desplanque, D. Stiévenard, X. Wallart, B. Grandidier, C. Delerue, and D. Vanmaekelbergh, "Triangular nanoporation and band engineering of InGaAs quantum wells: a lithographic route toward Dirac cones in III–V semiconductors," *Nanotechnology*, vol. 30, p. 155301, apr 2019.
- [5] S. Wang, D. Scarabelli, L. Du, Y. Y. Kuznetsova, L. N. Pfeiffer, K. W. West, G. C. Gardner, M. J. Manfra, V. Pellegrini, S. J. Wind, and A. Pinczuk, "Observation of Dirac bands in artificial graphene in small-period nanopatterned GaAs quantum wells," *Nature Nanotechnology*, vol. 13, pp. 29–33, jan 2018.
- [6] N. A. Franchina Vergel, L. C. Post, D. Sciacca, M. Berthe, F. Vaurette, Y. Lambert, D. Yarekha, D. Troadec, C. Coinon, G. Fleury, G. Patriarche, T. Xu, L. Desplanque, X. Wallart, D. Vanmaekelbergh, C. Delerue, and B. Grandidier, "Engineering a Robust Flat Band in III–V Semiconductor Heterostructures," *Nano Letters*, 2020.
- [7] J. C. Slater, "Wave Functions in a Periodic Potential," *Physical Review*, vol. 51, pp. 846–851, may 1937.
- [8] F. Bloch, "Über die Quantenmechanik der Elektronen in Kristallgittern," *Zeitschrift für physik*, vol. 52, no. 7, pp. 555–600, 1929.
- [9] R. J. Nicholas, J. C. Portal, C. Houlbert, P. Perrier, and T. P. Pearsall, "An experimental determination of the effective masses for Ga x In 1 x As y P 1 y alloys grown on InP," *Applied Physics Letters*, vol. 34, pp. 492–494, apr 1979.
- [10] A. H. Castro Neto, F. Guinea, N. M. R. Peres, K. S. Novoselov, and A. K. Geim, "The electronic properties of graphene," *Reviews of Modern Physics*, vol. 81, pp. 109–162, jan 2009.
- [11] G.-F. Zhang, Y. Li, and C. Wu, "Honeycomb lattice with multiorbital structure: Topological and quantum anomalous Hall insulators with large gaps," *Physical Review B*, vol. 90, p. 075114, aug 2014.
- [12] W. Beugeling, E. Kalesaki, C. Delerue, Y.-m. Niquet, D. Vanmaekelbergh, and C. Morais Smith, "Topological states in multi-orbital HgTe honeycomb lattices," *Nature communications*, vol. 6, p. 6316, 2015.
- [13] C. Wu and S. Das Sarma, " $p_{x,y}$ -orbital counterpart of graphene: Cold atoms in the honeycomb optical lattice," *Physical Review B*, vol. 77, p. 235107, jun 2008.
- [14] E. Tang, J.-W. Mei, and X.-G. Wen, "High-Temperature Fractional Quantum Hall States," *Physical Review Letters*, vol. 106, p. 236802, jun 2011.
- [15] S. A. Parameswaran, R. Roy, and S. L. Sondhi, "Fractional quantum Hall physics in topological flat bands," *Comptes Rendus Physique*, vol. 14, no. 9-10, pp. 816–839, 2013.
- [16] T. Neupert, L. Santos, C. Chamon, and C. Mudry, "Fractional Quantum Hall States at Zero Magnetic Field," *Physical Review Letters*, vol. 106, p. 236804, jun 2011.
- [17] N. B. Kopnin, T. T. Heikkilä, and G. E. Volovik, "High-temperature surface superconductivity in topological flat-band systems," *Physical Review B*, vol. 83, p. 220503, jun 2011.
- [18] C. Delerue, "From semiconductor nanocrystals to artificial solids with dimensionality below two," *Phys. Chem. Chem. Phys.*, vol. 16, no. 47, pp. 25734–25740, 2014.
- [19] C. Delerue and D. Vanmaekelbergh, "Electronic band structure of zinc blende CdSe and rock salt PbSe semiconductors with silicene-type honeycomb geometry," *2D Materials*, vol. 2, p. 034008, jun 2015.
- [20] M. Polini, F. Guinea, M. Lewenstein, H. C. Manoharan, and V. Pellegrini, "Artificial honeycomb lattices for electrons, atoms and photons," *Nature Nanotechnology*, vol. 8, pp. 625–633, sep 2013.
- [21] A. Tadjine, G. Allan, and C. Delerue, "From lattice Hamiltonians to tunable band structures by lithographic design," *Physical Review B*, vol. 94, p. 075441, aug 2016.

- 
- [22] E. Kalesaki, C. Delerue, C. Morais Smith, W. Beugeling, G. Allan, and D. Vanmaekelbergh, “Dirac Cones, Topological Edge States, and Nontrivial Flat Bands in Two-Dimensional Semiconductors with a Honeycomb Nanogeometry,” *Physical Review X*, vol. 4, p. 011010, jan 2014.
- [23] K. K. Gomes, W. Mar, W. Ko, F. Guinea, and H. C. Manoharan, “Designer Dirac fermions and topological phases in molecular graphene,” *Nature*, vol. 483, no. 7389, pp. 306–310, 2012.
- [24] T. S. Gardenier, J. J. van den Broeke, J. R. Moes, I. Swart, C. Delerue, M. R. Slot, C. M. Smith, and D. Vanmaekelbergh, “p Orbital Flat Band and Dirac Cone in the Electronic Honeycomb Lattice,” *ACS Nano*, p. acsnano.0c05747, oct 2020.
- [25] L. Nádovrník, M. Orlita, N. A. Goncharuk, L. Smrčka, V. Novák, V. Jurka, K. Hruška, Z. Výborný, Z. R. Wasilewski, M. Potemski, and K. Výborný, “From laterally modulated two-dimensional electron gas towards artificial graphene,” *New Journal of Physics*, vol. 14, p. 053002, may 2012.
- [26] R. L. Pavelich and F. Marsiglio, “The Kronig-Penney model extended to arbitrary potentials via numerical matrix mechanics,” *American Journal of Physics*, vol. 83, pp. 773–781, sep 2015.
- [27] R. L. Pavelich and F. Marsiglio, “Calculation of 2D electronic band structure using matrix mechanics,” *American Journal of Physics*, vol. 84, pp. 924–935, dec 2016.
- [28] L. Wang, P. M. Asbeck, and Y. Taur, “Self-consistent 1-D Schrödinger-Poisson solver for III-V heterostructures accounting for conduction band non-parabolicity,” *Solid-State Electronics*, vol. 54, no. 11, pp. 1257–1262, 2010.
- [29] Y. Liu, N. Neophytou, G. Klimeck, and M. S. Lundstrom, “Band-structure effects on the performance of III-V ultrathin-body SOI MOSFETs,” *IEEE Transactions on Electron Devices*, vol. 55, no. 5, pp. 1116–1122, 2008.
- [30] G. Zerveas, E. Caruso, G. Baccarani, L. Czornomaz, N. Daix, D. Esseni, E. Gnani, A. Gnudi, R. Grassi, M. Luisier, T. Markussen, P. Osgnach, P. Palestri, A. Schenk, L. Selmi, M. Sousa, K. Stokbro, and M. Visciarelli, “Comprehensive comparison and experimental validation of band-structure calculation methods in III-V semiconductor quantum wells,” *Solid-State Electronics*, vol. 115, pp. 92–102, 2016.
- [31] N. A. Franchina Vergel, A. Tadjine, V. Notot, M. Mohr, A. Kouassi N’Guissan, C. Coinon, M. Berthe, L. Biadala, K. K. Sossoe, M. M. Dzagli, J.-C. Girard, G. Rodary, L. Desplanque, R. Berndt, D. Stiévenard, X. Wallart, C. Delerue, and B. Grandidier, “Influence of doping level and surface states in tunneling spectroscopy of an  $\text{In}_{0.53}\text{Ga}_{0.47}\text{As}$  quantum well grown on p-type doped  $\text{InP}(001)$ ,” *Physical Review Materials*, vol. 3, p. 094604, sep 2019.
- [32] R. Lehoucq, D. Sorensen, and C. Yang, “ARPACK USERS GUIDE: Solution of Large Scale Eigenvalue Problems by Implicitly Restarted Arnoldi Methods,” tech. rep., 1998.
- [33] Z. Liu, J. Wang, and J. Li, “Dirac cones in two-dimensional systems: from hexagonal to square lattices,” *Physical Chemistry Chemical Physics*, vol. 15, no. 43, pp. 18855–18862, 2013.
- [34] C. H. Park, L. Yang, Y. W. Son, M. L. Cohen, and S. G. Louie, “New generation of massless dirac fermions in graphene under external periodic potentials,” *Physical Review Letters*, vol. 101, no. 12, p. 126804, 2008.
- [35] R. W. Robinett, “Visualizing the solutions for the circular infinite well in quantum and classical mechanics,” *American Journal of Physics*, vol. 64, no. 4, pp. 440–446, 1996.
- [36] H. Struve, “Beitrag zur Theorie der Diffraction an Fernröhren,” *Annalen der Physik*, vol. 253, no. 13, pp. 1008–1016, 1882.
-



# Chapter IV

---

## Realizing honeycomb semiconductors: A lithographic route towards nanoperforated InGaAs quantum wells

**Based on:**

L.C. Post, T. Xu, N.A. Franchina Vergel, A. Tadjine, Y. Lambert, F. Vaurette, D. Yarekha, L. Desplanque, D. Stiévenard, X. Wallart, B. Grandidier, C. Delerue, D. Vanmaekelbergh

**Triangular nanoperforation and band engineering of InGaAs quantum wells: a lithographic route toward Dirac cones in III-V semiconductors**

*Nanotechnology* **30**, 15 (155301) 2019

**The design of two-dimensional periodic structures at the nanoscale has renewed the attention for band structure engineering. Here we investigate the nanoporation of an InGaAs quantum well epitaxially grown on InP substrates using high-resolution electron beam lithography and highly anisotropic dry etching. We report on the fabrication of a honeycomb structure with an ultimate resolution down to a periodicity of 40 nm in a 10 nm thick InGaAs quantum well on n-type InP. The quality of the honeycomb structures is discussed in detail, and calculations will show the possibility to measure Dirac physics in these type of samples. Based on the statistical analysis of the fluctuations of the pore size and periodicity, calculations of the band structure are performed to assess the robustness of the Dirac cones with respect to small distortions of the honeycomb lattice.**

## IV.1 Introduction

III-V semiconductor quantum wells have obtained a central place in opto-electronics and advanced logics. In more recent quests for semiconductors with entirely new functions, the effects of a periodic potential on the nanometre scale on the electronic band structure have been theoretically anticipated [1, 2]. In the case that the charge carriers are confined in a honeycomb geometry, the quantum well semiconductor band gap remained, but the highest hole valence and lowest electron conduction bands become Dirac cones with a linear energy-momentum relationship around the K-points in the zone. This means that the beneficial properties of a semiconductor, such as a bandgap and a controllable density of carriers, can be combined with valence and conduction bands with a K-region similar as for graphene. Moreover, the combination of Dirac (mini) bands and spin-orbit coupling may result in topological phases, such as non-trivial flat bands and the quantum spin Hall effect [3–6]. Hence, honeycomb semiconductors form a new material class with unseen electronic functions.

With respect to the question of how to fabricate such honeycomb semiconductors, two possibilities have been put forward, recently. The first route is based on the two-dimensional assembly and attachment of semiconductor nanocrystals providing honeycomb semiconductors of Pb- and Cd-chalcogenides [7, 8] with a periodicity in the 5-10 nm range, supported by calculations [3, 9]. The second route is based on nanopatterning of two-dimensional semiconductors by means of lithography. Importantly, a hexagonal array of pores in a semiconductor quantum well would result in a remaining crystal with a honeycomb geometry.

Such a lithographic nanoporation to form a honeycomb semiconductor has several advantages: (i) it can be applied to families of well-established semiconductor materials with low effective carrier mass and very high electron mobilities, such as several III-V semiconductors; (ii) nanoporation would enable to change the size of the honeycomb unit cell and the size of the pores in an independent way. This allows for a precise tuning of the electronic band structure. (iii) The lithographic procedures can be directly applied to semiconductor quantum wells incorporated in classic transistor de-

vices, allowing for direct investigation of the band structure and transport properties of the honeycomb semiconductor with a controllable position of the Fermi-level. Previous works using a modulation-doped GaAs heterostructure subjected to a lateral attractive potential with honeycomb geometry already showed promising results [10–13], although direct evidence for massless Dirac fermions was not observed yet due to the small width of the Dirac bands [14]. More recently, Wang *et al* realized a honeycomb semiconductor in a nanopatterned GaAs quantum well with a very small lattice constant of 50 nm. Resonant inelastic light-scattering spectra revealed some features of Dirac type bands [15]. However, it was reported that the lattice parameter of a honeycomb semiconductor based on GaAs heterostructures should be as low as 20 nm to directly observe MDFs in standard cryogenic conditions [2].

In the present work, we describe a lithographic nanoporation route towards honeycomb  $\text{In}_{0.53}\text{Ga}_{0.47}\text{As}$  on an InP substrate. We describe how a hexagonal array of pores (antidot lattice) is perforated to force the electrons in a honeycomb geometry. Using this approach, the lattice constant of the honeycomb unit cell can be decreased by a factor  $\sqrt{3}$  compared with previous works, which will significantly increase the width of the Dirac band. The two-dimensional InGaAs layer has a thickness of 10 nm, and is grown on an InP substrate by MBE using well-established routes [16–19], leading to a two-dimensional electron gas with high carrier mobility ( $> 1.3 \cdot 10^5 \text{ cm}^2/\text{Vs}$  at 77 K) [20–23]. Using high-resolution electron beam lithography (EBL) and anisotropic dry etching, a triangular antidot lattice is obtained in the InGaAs quantum well with a unit cell constant as small as 40 nm. We show that the radius of the pores can be tuned in an independent way. Our band structure calculations anticipate that Dirac cones can be obtained with a width of 5.0 meV, allowing for electrical spectroscopy and transport measurements at liquid helium temperature. The morphology of the samples was studied with atomic force microscopy (AFM), energy dispersive electron spectroscopy (EDS) and cross-section transmission electron microscopy (TEM).

The quality of the build-in honeycomb symmetry etched in the QW needs a thorough analysis, since positional disorder in the antidot lattice can greatly affect the symmetry in the lattice, and thus the electronic structure of the system. The disorder in the lattices is quantified on the basis of scanning electron microscopy (SEM) images, which obtained parameters can be used to theoretically investigate the effects of the disorder on the electronic structure using the muffin-tin model. The fabrication of high quality antidot triangular lattices is essential for the observation of Dirac physics in these samples.

## IV.2 Fabrication of a honeycomb semiconductor

The step-by-step fabrication process of the nanoporated InGaAs/InP heterostructure is described in Fig. IV.1. The InP base is placed into a MBE, and a InGaAs quantum well is grown on top of the sample with a typical thickness of 10 nm [24]. Such a quantum well heterostructure with different doping levels inside the InGaAs layer has already been investigated electronically and optically [25–30]. A layer of  $\text{SiO}_2$  is de-

#### IV Realizing honeycomb semiconductors: A lithographic route towards nanoperforated InGaAs quantum wells

posited on top to protect the quantum well layer from contamination during the process (Fig. IV.1A) with a typical thickness of 16 nm. An organic resist layer with a thickness of 50 nm is deposited on top of the sample using a spin coater (Fig. IV.1B), before a triangular pattern of pores is created in the PMMA by electron beam lithography (Fig. IV.1C). The electrons will change the solubility of the exposed resist, which can be removed using a wet etching procedure (Fig. IV.1D). The remaining resist will act as a mask to further etch the pattern into the sample. The hexagonal pattern is first etched into the SiO<sub>2</sub> layer using reactive ion etching (RIE) (Fig. IV.1E), and finally the triangular pattern is transferred into the InGaAs quantum well by BCl<sub>3</sub> based inductive coupled plasma (ICP) etching (Fig. IV.1F). After the lithography process, the sample is cleaned and capped with As, and transferred into an ultra-high vacuum system.

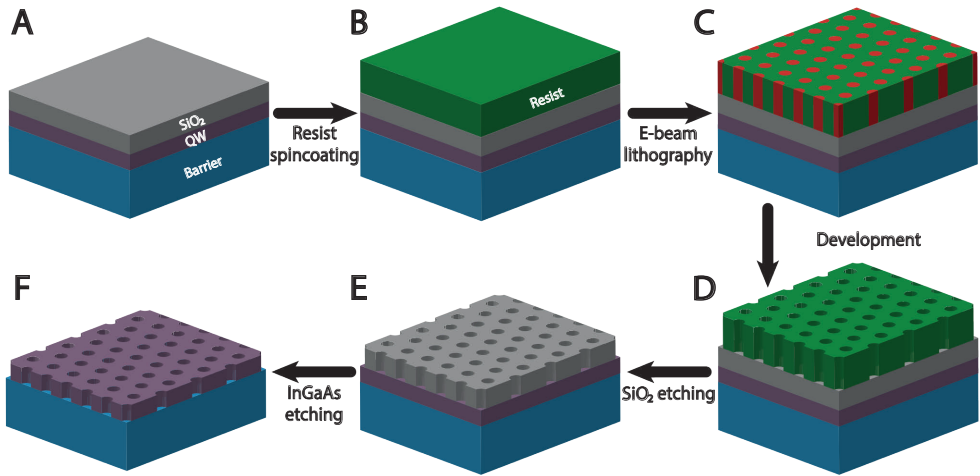


**Figure IV.1: Overview of the fabrication process of the nanoperforated InGaAs/InP heterostructure using electron beam lithography.** (A) The desired heterostructure is grown following well-known growth recipes. (B) Prior to the lithography process, an organic layer is deposited on top of the heterostructure. (C) Electron beam lithography is performed onto the sample, changing the solubility of the exposed resist. By exposing small areas of the resist with a triangular symmetry, the desired symmetry is obtained. (D) The exposed resist is removed using a wet etch step. (E) A dry etch step is applied to etch the triangular pattern into the SiO<sub>2</sub> layer, also (partially) removing the remaining resist. (F) A second, more specific dry etching procedure is applied to etch the pattern in the InGaAs quantum well, (partially) removing the SiO<sub>2</sub> layer.

Scanning electron microscopy (SEM) images of the etched SiO<sub>2</sub> and InGaAs layers are presented in Fig. IV.2. The top three images show a top view of the triangular antidot array of the SiO<sub>2</sub> layer after the first dry etching step in the technological patterning process. The triangular pore arrays have a lattice constant of 60 nm, 50 nm and 40 nm respectively.

The triangular arrays transferred into the InGaAs QW with the same lattice param-

ters are presented in the bottom three SEM images after the ICP etching. Differences in intensity at the edges of the pores can be explained by an accumulation of electrons around the pores. Exact parameters of the fabricated triangular antidot arrays can be found in the method section, and more lithography and etching tests on SiO<sub>2</sub> and III-V semiconductors are presented in the supplementary information (SI).

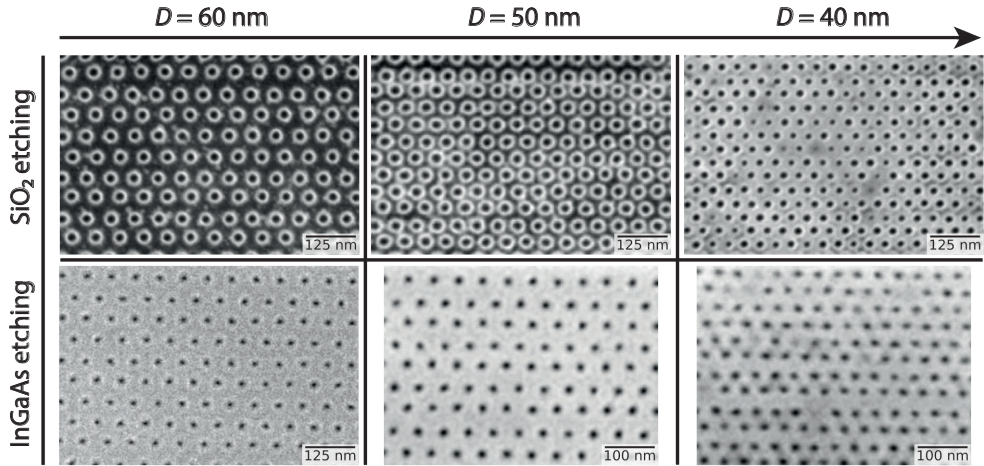


**Figure IV.2: Results of the lithographic patterning in every intermediate stage of the process.** SEM images of the triangular pore pattern in the SiO<sub>2</sub> and InGaAs quantum well layers after the different dry etching procedures. The periodicities of the lattices are 60, 50 and 40 nm in the left, middle, and right image, respectively. The results of the SiO<sub>2</sub> etching is presented in the three top images, the etching of the InGaAs quantum well is presented in the bottom three images.

Over large areas of  $20 \times 5 \mu\text{m}$ , a uniform pore radius and periodicity can be achieved after optimizing the EBL and etching process, with very few pore defects such as missing or misplaced sites. Upon decreasing the unit cell size of the triangular antidot lattice, initial pore defects are starting to be visible. Further decreasing the unit cell size will result in triangular lattices with too many defects, such as missing pores or pores which are merged together into large holes, as can be viewed in the SI. Therefore, the focus of this research was to fabricate these high quality triangular pores with periodicity of at least 40 nm, since it is essential for optimal tuning of the triangular potential that generates the honeycomb geometry inside the QW.

## Structural analysis

To confirm the etched honeycomb geometry in the quantum well, several structural analysis procedures have been carried out. Atomic force microscopy (AFM) measurements were performed on the etched samples to check the height profile of the pores and alignment markers (Fig. IV.3A). On the alignment marker, 15 nm of the substrate sample has been etched, indicating that the pores in the quantum well cross the entire

## IV Realizing honeycomb semiconductors: A lithographic route towards nanoperforated InGaAs quantum wells

10 nm quantum well depth. These results are supported by energy dispersive electron spectroscopy (EDS) measurements (Fig. IV.3C): on the non-etched area (square one of Fig. IV.3A), the chemical elements gallium (Ga) and arsenic (As) are found, consistent with the top InGaAs layer, while on the etched area (square two of Fig. IV.3A), these peaks are absent, demonstrating the complete etching of the InGaAs QW. The spectrum acquired on the QW also shows that the remaining SiO<sub>2</sub> on the QW is removed using the wet etching, since no silicon (Si) peaks are visible and the amplitude of the oxygen (O) peak is similar to the one observed on the InP substrate.

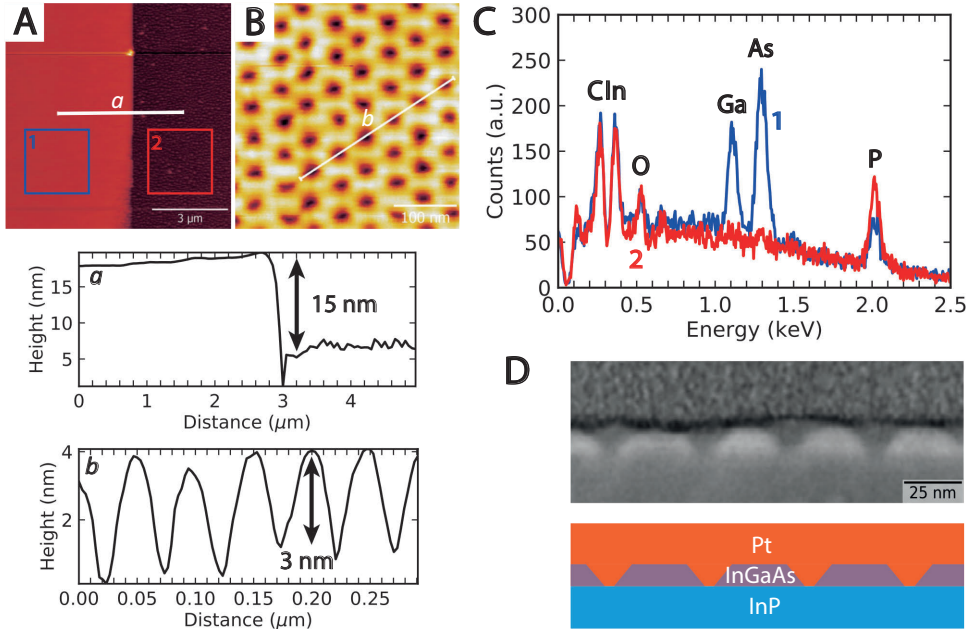


**Figure IV.3: Structural and chemical characterisation of the nanoperforated InGaAs/InP heterostructure.** (A) AFM image and height profile acquired along the horizontal direction. (B) AFM image of the nanoperforated InGaAs QW and height profile acquired along a tilted direction. (C) Chemical EDS analysis of the sample after ICP etching. The spectra were acquired in areas 1 and 2 defined in (a). (D-E) Cross-section scanning TEM image of the nanoperforated InGaAs/InP heterostructure, revealing the formation of conical pores instead of cylindrical pores.

AFM measurements on the large alignment markers only do not prove the complete etching of the QW by the triangular array of pores. When performing AFM measurements directly onto the antidot lattice, a similar uniformity of the lattice parameters is observed, consistent with the SEM results. However, the full depth of the QW cannot be measured directly, due to the broadness of the AFM tip. The AFM tip is too broad to fully enter the pores, making it impossible to measure the full depth of the etched pores (Fig. IV.3B). The shape and depth of the pores was therefore characterized with cross-section transmission electron microscopy (TEM). A cross-section of the InGaAs

sample is obtained by growing a protecting layer of platinum (Pt) on top of the sample, and cut a thin layer out of the sample using a focused ion beam (FIB). The cross-section is placed on the side observed in a TEM.

The scanning TEM image shows the inner shape of the pores directly from a side (Fig. IV.3D). The pores have a conical shape instead of a cylindrical shape due to the non-perfect anisotropic etching process. However, the pores are fully etched down to the InP substrate, meaning that the full width of the QW is also etched inside the pores, confirming the honeycomb geometry in the full QW thickness.

## Band structure calculations

In order to determine the band structure of the nano-perforated heterostructure, calculations were performed based on the geometry of the honeycomb semiconductor material schematized in Fig. IV.4A and IV.4B. The band structure of a 10 nm thick InGaAs with a pore periodicity of  $D = 40$  nm and pore diameter  $d = 19.2$  nm is calculated using an analytical muffin-tin model (Fig. IV.4C). The band structure shows that the lowest two bands form a clear Dirac cone at the K point with an energy width of about 5.0 meV, due to coupling of the  $s$ -type on site envelope functions. The width is much larger with respect to the thermal energy of liquid helium (4.4 T, 0.38 meV), opening up the possibility to measure Dirac physics in lithography patterned heterostructures. At higher energies, we find a quasi flat band and a second Dirac cone due to coupling of the  $p$ -envelope functions. In Fig. IV.4D, the muffin-tin model (black) is compared with a tight-binding calculation (red) for the lowest two bands, showing excellent agreement between the two calculation methods. A detailed description of the muffin-tin calculations can be found in the previous chapter, and more details about the tight-binding calculation can be found in the supplementary Information (SI) section.

The conical shape was taken into account in the tight-binding calculations for a periodicity of 40 nm and a pore diameter of 28.4 nm. The diameter of the pores was reduced from 100% on the top surface of the QW down to 20% at the bottom. The calculated band structure of such type of sample is illustrated in Fig. IV.4E. The band structure shows almost no change in the shape and energy width of the Dirac cone between the conical and cylindrical pores. Although the confinement effect will decrease when lowering the size of the pores further down, the coupling strength will increase. This interplay between the confinement effect and the coupling strength explains why the Dirac cone is only weakly affected by the conical shape of the pores.

## IV.3 Statistical analysis

The previous sections described the fabrication route of a two-dimensional InGaAs semiconductor with a honeycomb geometry, and the interesting electronic properties that the structure potentially holds. Nevertheless, the calculations are only valid for two-dimensional structures with a perfect honeycomb symmetry, without any disorder build inside the lattice. In this section, the exact dimensions of the triangular lattice

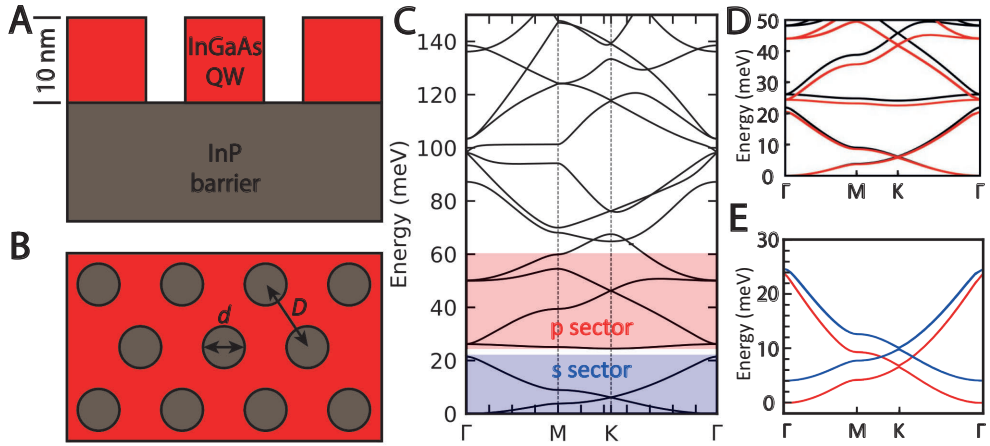


**Figure IV.4: Schematic of the structure used to perform the muffin-tin and tight-binding calculations. (A-B)** Side and top view of an InGaAs single crystal, 10 nm in thickness (red) with a triangular array of etched pores, thus forming a lattice inside the InGaAs/InP heterostructure. Critical structural parameters for the electronic band structure are the thickness of the InGaAs, here 10 nm, the diameter  $d$  of the pores, and the periodicity, i.e. the distance between the centre of two adjacent pores corresponding to the unit cell constant  $D$ . **(C)** Conduction band structure for an InGaAs honeycomb lattice, with a periodicity of  $D = 40$  nm, a pore diameter of  $d = 19.2$  nm and an electron repulsive potential of the pores of 1.0 eV. The sector where the quasi s-orbitals are located are indicated in blue, the p-orbital in red. **(D)** Zoom in of the band structure in the first two sectors. The results of the muffin-tin calculations and tight-binding calculations are presented in black and red respectively. **(E)** Tight binding calculations on conical pores (red) and cylindrical pores (blue) show that the Dirac cones in the band structures are almost unaltered with respect to each other.

are determined, and the disorder on the fabricated structures is analysed using a particle detection script. By calculating the radial distribution function of the measured distances between pores of the triangular lattice and comparing them with two different models, different types of disorder can be differentiated, which can be used to improve the technological process.

There are three potential disorder terms in the lattices which could influence the band structure: a distribution in the distance between the center of the pores, a distribution in the radius of the pores and variation in the shape of the pores. Variation in the shape of the pores can be described by measuring the circularity  $C$ , which describes the roundness of the pores. In principle, disorder in the periodicity should drastically perturb the ideal band structure, while disorder on the shape of the pores has less effect as was illustrated in the previous section.

The nearest distances between the pores can be calculated using a particle detection algorithm, by generating a black-white image and applying a threshold to each individual pixel value. Contours are fitted around all detected pores, obtaining a total surface inside the contour. The center position of each pore is obtained by fitting a circle to the total area inside each contour. The distance  $D$  between two pores is measured using

the obtained center positions of each pore. The radius of each pore is obtained using the total area inside the contour, which is presumed to be a perfect circle. Finally, the circularity is calculated using the total length of the contour of each pore. More information on the exact procedure of the particle detection analysis can be found in the supplementary information. After obtaining complete lists of values for the periodicity, radius and circularity, Gaussian functions are fitted to these distributions, obtaining a mean value and standard deviation value for each distribution.

Using this analysis technique, it is important to note that obtained values might not be fully exact in the absolute sense, since they depend on the used settings in the particle detection algorithm, such as the used threshold. When keeping the settings the same for different images, values can be compared with each other, preserving in this way a relative coherency between the results of different samples. As said, the absolute values might be prone to slight deviations from reality.

The results of the particle detection analysis are presented in Fig. IV.5. For the  $D = 50$  nm triangular antidot lattice (Fig. IV.5A), the measured periodicity is  $D = 49.8 \pm 3.1$  nm with a pore radius of  $r = 7.8 \pm 0.3$  nm and a circularity of  $C = 0.72 \pm 0.06$ .

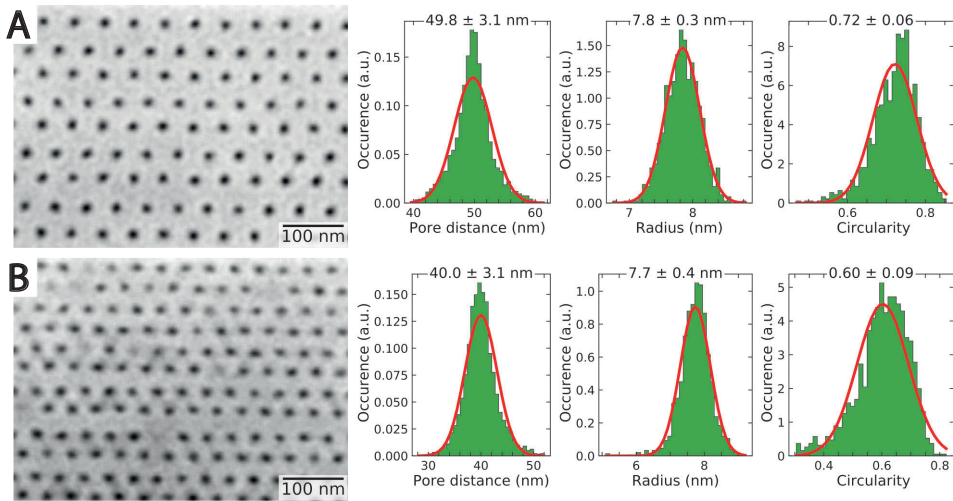


**Figure IV.5: Analysis of the structural disorder parameters.** (A-B) Particle detection analysis on a SEM image of the 50 nm periodicity (A) and 40 nm periodicity (B) triangular lattice. Distributions of the periodicity, pore radius and circularity are plotted next to the SEM images. The distributions are fitted with a standard Gaussian distribution. The mean value and the standard deviation are indicated for each histogram.

For the  $D = 40$  nm lattice (Fig. IV.5B), the calculated periodicity yields  $D = 40.0 \pm 3.1$  nm with a pore radius of  $r = 7.7 \pm 0.5$  nm and a circularity of  $C = 0.60 \pm 0.10$ . Compared with the 50 nm lattice, the standard deviation in the periodicity is the same in absolute value, but relative to the periodicity is larger for the 40 nm lattice. This is not too

surprisingly, since this marks probably the limit of this lithography technique if the disorder is completely random. This can also be observed in the distributions of the pore sizes and shapes: the size of the pore is the same while the standard deviation has increased, and the shape is less circular for the smaller lattice.

## IV.4 Radial distribution function

For an accurate characterization of long-range positional disorder inside the triangular antidot lattice, a two-dimensional radial distribution function of the lattice is calculated to check if the disorder is completely random and independent of the disorder on other positions, or if any structural disorder is present in the lattice. This distribution, also called the pair distribution function of a lattice, can be used to describe the change in the pore density as a function of distance from a reference pore site. More exactly, the pair distribution function  $g(r)$  yields approximately the mean number of lattices sites  $n(r)$  in an annulus with thickness  $dr$  at distance  $r$  from a reference point divided by the area of the annulus  $A_s(r)$  and the mean density of the lattice sites  $\rho$ :

$$g(r) \approx \frac{n(r)}{A_s(r)\rho} \quad (\text{IV.1})$$

Using this formula and a home-build particle detection protocol, the radial distribution function of the total lattice can be calculated from the obtained SEM images.

An uniform disorder is obtained when the pore positions of a perfect lattice are displaced by a random displacement which is sampled from a Gaussian distribution. Conversely, a structural disorder is present when the disorder is not uniform. In order to discriminate whether the disorder is structural or random, the radial distribution function of the lattice can be fitted using two different statistical models: an ideal and a real paracrystal model [31–34].

In an ideal paracrystalline model, the hexagonal lattice sites  $\mathbf{R}_{n,m}^{\text{ideal}}$  are generated by independent vectors  $\mathbf{R}_i^{(1)}$  and  $\mathbf{R}_j^{(2)}$  which will replace the basis vectors  $\mathbf{a}_1$  and  $\mathbf{a}_2$  of a non-disordered lattice.  $\mathbf{R}_i^{(1)}$  and  $\mathbf{R}_j^{(2)}$  are randomly drawn vectors from two-dimensional Gaussian distributions  $\mathbf{G}$  with means  $\mathbf{a}_1$  and  $\mathbf{a}_2$ , and standard deviation  $\Sigma_1$  and  $\Sigma_2$  respectively:

$$\begin{aligned} \mathbf{R}_i^{(1)} &\sim \mathbf{G}(\mathbf{x}; \mathbf{a}_1, \Sigma_1) \\ \mathbf{R}_j^{(2)} &\sim \mathbf{G}(\mathbf{x}; \mathbf{a}_2, \Sigma_2) \end{aligned}$$

For a non-distorted lattice, the  $(n, m)$ 'th lattice site  $\mathbf{R}_{n,m}$  would normally be described as  $\mathbf{R}_{n,m} = n\mathbf{a}_1 + m\mathbf{a}_2$ . Similarly, we can describe the  $(n, m)$ 'th lattice site in the ideal paracrystalline model as:

$$\mathbf{R}_{nm}^{\text{ideal}} = \sum_{i=1}^n \mathbf{R}_i^{(1)} + \sum_{j=1}^m \mathbf{R}_j^{(2)} \quad (\text{IV.2})$$

This means that a two-dimensional ideal paracrystal is generated by first determining all the values for  $\mathbf{R}_i^1$  and  $\mathbf{R}_i^2$  at once for  $(i, j) \in \mathbb{Z}$ , which are used to determine the lattice point  $\mathbf{R}_{nm}^{\text{ideal}}$  at position  $(n, m)$ . This will result in a lattice with a complete network

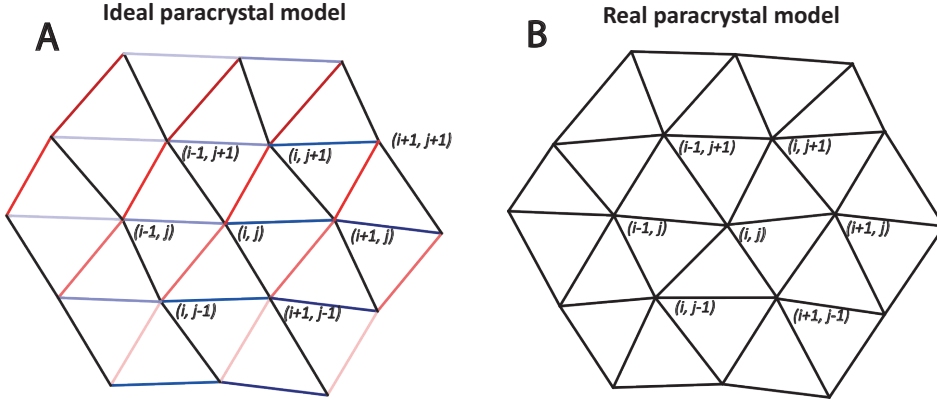


**Figure IV.6: Schematic diagram of the ideal paracrystal model versus the real paracrystal model.** (A) Hexagonal lattice generated using the ideal paracrystal model. The middle lattice site is indicated by position  $(i, j)$ , which is used to indicate all other lattice sites. Lattice vectors indicated with the same color are equivalent, meaning that they have the same length and direction. (B) Hexagonal lattice generated using the real paracrystal model. All lattice vectors have different lengths and directions due to an extra displacement term in the model.

of parallelograms (Fig. IV.6A, indicated in red): starting from the center  $(i, j)$ , lattice site  $(i + 1, j)$  and  $(i, j + 1)$  are distorted, but the lattice site  $(i + 1, j + 1)$  connecting both sites is defined by these two lattice sites according to (Eq. IV.4), forming a parallelogram. Consequently, it is visible that sites within a column (row) are correlated with sites within any other column (row), although they are offset with a single random vector [35, 36]. The disorder introduced in this model is therefore not completely random, which would be expected in a truly disordered lattice, but describes propagating disorder only. Nevertheless, this model will still be used as a comparison with the calculated radial distribution function to check how well the model fits to the experimental data and if the disorder is indeed truly random. Using (Eq. IV.4), the theoretical radial distribution function of the ideal paracrystal model can be calculated and compared with the radial distribution function of the measured hexagonal antidot lattice. The mathematical derivation of the theoretical radial distribution function of this model will be explained in the SI, but the general form can be written as:

$$g(r) = \frac{1}{(2\pi)^{3/2} r \rho} \sum_{n,m} \frac{1}{\sigma_{nm}} \exp\left[-\frac{(r - a_{nm})^2}{2(n+m)\sigma_{\text{ideal}}^2}\right] \quad (\text{IV.3})$$

which is a summation of Gaussian distributions where the mean of each distribution  $a_{nm} \equiv \sqrt{(n + m/2)^2 + (3/4)m^2} a$  changes with  $(n, m)$ , and the standard deviation grows with the lattice site indices  $(n, m)$ .

The other model used for the analysis is the real paracrystal model. This model is generated by adding an uniform disorder term  $\mathbf{R}^{\text{real}}$  to the ideal paracrystal model, which is a random value drawn from a Gaussian distribution  $\mathbf{G}(\mathbf{x}; 0, \Sigma_{\text{real}})$ . This value will shift all individual lattice sites independently from each other (Fig. IV.6B) after

generating the ideal paracrystal model.

Mathematically, the lattice vector of site  $(n, m)$  in this model can be written as a summation of the lattice vectors in the ideal paracrystal model and an uniform disorder term:

$$\mathbf{R}_{nm}^{\text{real}} = \sum_{i=1}^n \mathbf{R}_i^{(1)} + \sum_{j=1}^m \mathbf{R}_j^{(2)} + \mathbf{R}^{\text{real}} \quad (\text{IV.4})$$

which means that this model does not only describe propagating disorder, but also non-propagating disorder indicated with a different standard deviation  $\Sigma_{\text{real}}$ . Again, the theoretical radial distribution function of the real paracrystal model can be calculated, which is more elaborately explained in the SI:

$$g(r) = \frac{1}{(2\pi)^{3/2} r \rho} \sum_{n,m} \frac{1}{\sqrt{(n+m)\sigma_{\text{ideal}}^2 + \sigma_{\text{real}}^2}} \exp\left[-\frac{(r - a_{nm})^2}{2((n+m)\sigma_{\text{ideal}}^2 + \sigma_{\text{real}}^2)}\right] \quad (\text{IV.5})$$

where  $a_{nm} \equiv \sqrt{(n+m/2)^2 + (3/4)m^2} a$  is defined similarly as for the ideal paracrystal model. The pair distribution function is therefore a summation of normal distribution functions with mean  $a_{nm}$  and a two different variances  $\sigma_{\text{ideal}}$  and  $\sigma_{\text{real}}$ .

The radial distribution functions of both models are used to fit the calculated radial distribution function of the measured hexagonal antidot lattice.

In Fig. IV.7A and Fig. IV.7B, SEM images of two lattices with different periodicities are presented which are used for the radial distribution analysis. The calculated radial distribution functions from the 50 nm and 40 nm lattices are presented in Fig. IV.7C-F, indicated in blue. The radial distribution function of the ideal paracrystalline model is fitted in Fig. IV.7C and Fig. IV.7D, yielding a pore-to-pore distance  $a = 49.69$  nm and standard deviation  $\sigma_{\text{ideal}} = 1.64$  nm for the 50 nm lattice, and a pore-to-pore distance  $a = 39.87$  nm and standard deviation  $\sigma_{\text{ideal}} = 1.74$  nm for the 40 nm lattice. Fitting the real paracrystal model to the radial distribution function of the 50 nm lattice, a pore-to-pore distance of  $a = 49.69$  nm, an ideal standard deviation of  $\sigma_{\text{real}} = 1.05$  nm and a real standard deviation of  $\sigma_{\text{real}} = 1.83$  nm are obtained.

When comparing both models with each other, the real paracrystal model is a better fit than the ideal model, showing that random disorder dominates over structural disorder in both lattices. Nevertheless, propagating disorder is clearly present in both the 50 nm and 40 nm lattices when comparing the values of  $\sigma_{\text{ideal}}$  and  $\sigma_{\text{real}}$  with each other. Comparing the disorder between the two differently sized lattices, the disorder remains constant upon decreasing the lattice dimensions, and therefore increases as a percentage of the lattice constant. The effect of propagating disorder is also visible in the SEM images, especially for the 40 nm lattice. This effect is highlighted in both SEM images of Fig. IV.7 using dashed green and red lines: for the 50 nm lattice, the distances between the pores stay visibly the same in the y-direction, while for the 40 nm lattice the distances change alternately, indicating that a structural disorder is present inside the lattice. The origin of the structural disorder is still unknown, but different writing techniques [37] for the electron beam lithography can be investigated to lower the structural disorder in the antidot lattice.

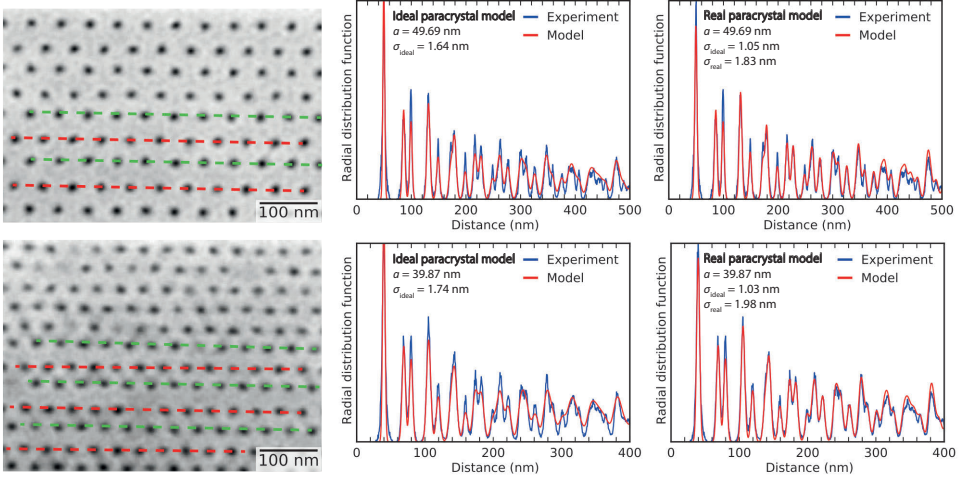


**Figure IV.7: Order-disorder characterization in two InGaAs triangular antidot lattices with periodicity of  $D = 50$  and  $D = 40$  nm.** (A,B) SEM image of the investigated InGaAs triangular antidot lattice with a periodicity of  $D = 50$  nm (A) and  $D = 40$  nm (B). Green and red dashed lines are indicated along the  $x$ -direction of the lattice, showing a clear propagating disorder presence in the  $y$ -direction of the 40 nm periodicity hexagonal lattice. (C,D) Calculated radial distribution function (blue) of the 50 nm periodicity lattice (C) and 40 nm lattice (D) are fitted with the radial distribution functions obtained from the ideal paracrystalline model (red), only describing propagating disorder. (E,F) Calculated radial distribution function (blue) of the 50 nm periodicity lattice (E) and 40 nm lattice (F) are fitted with radial distribution functions obtained from a real paracrystalline model (red), describing both propagating and non-propagating disorder.

## IV.5 Conclusion and outlook

To summarize, a route has been described to create honeycomb semiconductor samples in InGaAs/InP QW heterostructures which are nanoperforated with a two-dimensional triangular lattice of pores using electron beam lithography. Lattices with periodicities of 50 and 40 nm have been demonstrated. The morphology of the samples is thoroughly studied by using various tools, revealing a good degree of control on the lattice parameters. At the smallest periodicity, muffin-tin and tight binding calculations show a clear Dirac cone at the K point with an energy width of several meV. The disorder of the lattice has been thoroughly studied using an effective particle detection protocol and by calculating the radial distribution function of the lattice from the measured SEM images. Two different paracrystalline models have been considered to discriminate between random and structural disorder in the lattice. Although random disorder dominates, structural disorder is clearly present in the fabricated triangular antidot lattices, offering space for further improvement of the fabrication process. Our results provide general guidelines to fabricate honeycomb semiconductors consisting of III-V heterostructures, exhibiting potential Dirac physics such as Dirac cones and non-trivial flat bands.

### Method

**Growth of the InGaAs quantum well.** An InGaAs layer (10 nm) is grown onto the InP substrate using MBE (reference). To protect the surface of the QW layer from carbon contaminations, 16 nm of SiO<sub>2</sub> is grown on top of the QW using plasma-enhanced chemical vapor deposition (PECVD). 150 sccm of 5 % SiH<sub>4</sub>/N<sub>2</sub> and 700 sccm of N<sub>2</sub>O are used as precursors to form the SiO<sub>2</sub>. For the SiO<sub>2</sub> growth, the temperature is 300 °C, the pressure is 1 Torr and the RF power is 20 W. The total deposition time is 13 seconds.

**Electron beam lithography.** The sample is dehydrated by heating the surface to 120 °C for 10 mins, and a diluted polymethylmethacrylate (PMMA) 950K 4% resist is spin coated on top of the sample, followed by an annealing at 80 C for 1 min on a hot plate and a bake out at 180 C for 10 mins. A thickness of 50 nm resist is obtained. E-beam exposure was performed using Raith EBPG 5000Plus equipment, taking advantage of the improved recipes of our previous work [38]. Triangular nanopatterns with different periodicities of 60, 50 and 40 nm were exposed in 20 μm × 5 μm areas with an accelerating voltage of 100 kV, a beam current of 200 pA and an e-beam dose of 10000 μC/cm<sup>2</sup>. The position of the patterns can be located by printing large markers around the patterns, used for localization in the SEM. After the exposure procedure, the resist was developed in a 2:1 methyl-isobutyl ketone:isopropanol (MIBK:IPA) solution for 60 s, removing the exposed resist. The sample is further rinsed in IPA for at least 30 s to stop the development and cleaned under low N<sub>2</sub> flow to remove dust.

**SiO<sub>2</sub> etching.** The triangular pattern is etched inside the SiO<sub>2</sub> layer using reactive ion etching (RIE) in a Plasmalab 80+ (Oxford) system with a mixture of CHF<sub>3</sub> and CF<sub>4</sub> (40/40 sccm). The chamber pressure was set to 50 mTorr, while the RF power was 180 W. The sample was etched for 40 seconds, removing all the SiO<sub>2</sub> inside the pores. The residual PMMA resist on top of the SiO<sub>2</sub> is removed using a gentle O<sub>2</sub> plasma etching procedure. The sample was further rinsed with IPA and low N<sub>2</sub> flow.

**InGaAs etching.** The InGaAs QW was etched for 40 seconds using BCl<sub>3</sub> (30 sccm) based inductively coupled plasma (ICP) etching with power of 200 W and pressure of 2 mTorr, removing the InGaAs inside the pores. The remainder of SiO<sub>2</sub> mask on the sample is removed by wet etching (1% HF for 1 min).

**Atomic force microscopy.** AFM measurements were performed on a JPK Nanowizard II with a Nikon Eclipse Ti-U inverted microscope. The machine was placed on top of an active vibration isolation table together with a Halcyonics Active Vibration Isolation Unit. The whole setup was placed inside a large acoustic vibration box to further isolate the setup from external vibrations. SHR300 ultra sharp AFM probes were used to obtain these measurements, which have a sharp carbon spike attached to a gold coated cantilever. The tips have a typical force constant of 40 N/m, resonance frequency of 300 kHz and a radius curvature of 1 nm.

**Scanning electron microscopy.** Scanning electron microscopy has been performed both at IEMN and at Utrecht University. SEM measurements in Lille are performed on a Zeiss Ultra 55 with a backscattering detector running at 1 kV. Typical settings used for obtaining images are electron accelerating voltages between 3-5 kV, a working distance of 4 mm and a magnification of 100.000-300.000 times. Measurements in Utrecht are performed on a FEI Talos F200X with similar settings

**Energy-dispersive spectroscopy.** High sensitive 2D EDX chemical mapping is performed on the FEI Talos F200X with a electron beam acceleration of 3 kV and 2048 data points between 0 and 10 keV.

**Cross-section TEM.** Cross-section TEM is carried out in a Fei Strata DB 235 Dual-Beam Focus Ion Beam (FIB) system, which was operated at 30 kV equipped with a field emission gun. The spatial resolution was about 2 nm. The TEM foils were prepared by a FIB setup with Ga ions with a resolution of about 7 nm. The sample was protected by growing a layer of Pt on the top of the surface and a thin part of the sample with a thickness of 200 nm is cut out.

**Muffin-tin model.** For the calculation of the band structure, an analytical muffin-tin calculation was performed on a hexagonal lattice by solving the Schrödinger equation analytically. 144 barriers are used for this calculation, solving 144 eigenvalues. Lattice parameters:  $D = 40$  nm, pore diameter  $d = 19.2$  nm, a repulsive potential barrier  $V_0 = 1.0$  eV and an electron effective mass of  $0.041m_e$ . The analytical muffin-tin model was

performed using Python. The mathematical background of the muffin-tin model can be found in Chapter III.



# Supplementary information

## Design of the triangular array

An schematic overview of the general exposed pattern during tests can be viewed in Fig. S1A. Nine squares with pores in a triangular arrangement are designed, with four large markers surrounding the arrays. The large markers will enable to find the arrays when observing the arrays in SEM or AFM, since the arrays cannot be observed with an optical microscope. The distance between two triangular markers is  $200\ \mu\text{m}$ .

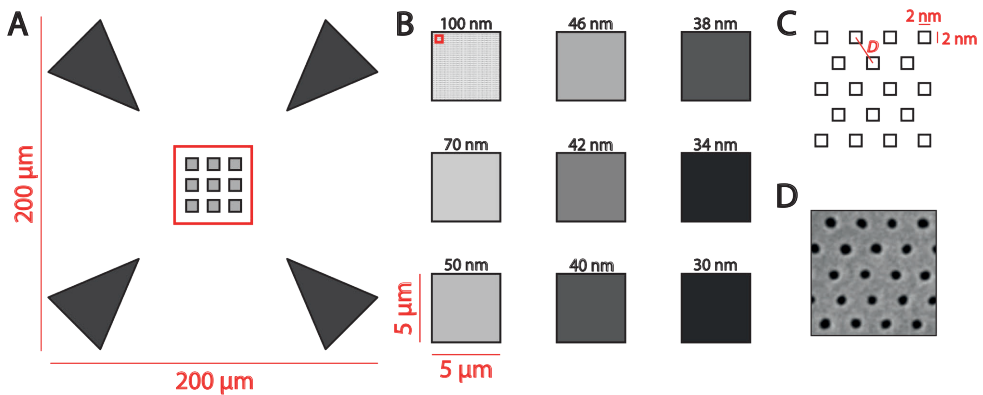


**Figure S1: Design of the triangular antidot lattice.** (A) Schematics of the general design of the triangular lattice with different periodicities. Exposed patterns are indicated in black/grey, sizes of the design are indicated in red. (B) Enlargement (red square in (A)) of the nine triangular lattices with different periodicities. (C) Schematic enlargement (red square in (B)) of a part of the triangular lattice of the 100 nm pore distance. (D) Part of a SEM image of the triangular lattice with a pore-to-pore distance of 50 nm.

Fig. S1B shows an enlargement of the nine squares of Fig. S1A, which the triangular array of pores with pore-to-pore distances of  $D = 100, 70, 50, 46, 42, 40, 38, 34$  and  $30\ \text{nm}$ . The typical dimensions of each square is  $5 \times 5\ \mu\text{m}^2$  in order to obtain long-range lattices. By designing lattices with different periodicities, the optimal distance between pores can be found for the specific lithography settings. The design of each triangular array itself is presented in Fig. S1C. Individual squares with sizes of  $2 \times 2\ \text{nm}^2$  are

designed with varying distance  $D$  for each triangular array. Since the dimensions of the squares are below the resolution limit of the electron beam machine, the squares will be overexposed during the lithography process, resulting in round pores (Fig. S1D). By changing the electron beam doses, the size of the pores can be increased or decreased, which will be demonstrated further down in the supplementary information.

The design files of the triangular array were prepared using a so-called GDS database file format. This also includes patterns which can be designed to be exposed in an electron beam lithography machine. These patterns can be printed repeatedly onto the organic resist layer with different lithography settings and are aligned using standard electron beam lithography markers. Various parameter in the lithography process can be tuned such as different electron beam doses and different apertures of the lenses. This will enable to find the optimal settings for the triangular array with the lowest pore distance and highest quality.

### Preliminary lithography and etching tests

Preliminary lithography and etching tests are performed to obtain the correct lithography settings for high quality, low dimensional triangular arrays, and to transfer the mask with the correct depth into the  $\text{SiO}_2$  and III-V semiconductors layers. For these tests, high-quality commercial GaAs substrates were used, on which a 16 nm thin layer of  $\text{SiO}_2$  was grown using PECVD. Using these test samples, the preliminary lithography and etching results will be discussed in the following sections.

### Electron beam lithography

To start, a GaAs/ $\text{SiO}_2$  substrate is dehydrated by heating the surface to  $120^\circ\text{C}$  for 10 mins and a diluted polymethylmethacrylate (PMMA) 950K 4% resist with a thickness of 50 nm is spin-coated on top of the sample, followed by an annealing at  $80^\circ\text{C}$  for 1 min on a hot plate and a bake out at  $180^\circ\text{C}$  for 10 mins. Triangular nanopatterns with different periodicities of  $D = 100, 70, 50$  and  $40$  nm were exposed in  $50\ \mu\text{m} \times 50\ \mu\text{m}$  areas with an accelerating voltage of 100 kV, a beam current of 200 pA and an e-beam dose ranging between 25000 and 10000  $\mu\text{C}/\text{cm}^2$ . The position of the patterns can be located by printing large markers around the patterns. The resist was developed in a 2:1 methyl-isobutyl ketone:isopropanol (MIBK:IPA) solution for 60 s, removing the exposed resist.

Top view SEM images of the developed resist layer are presented in Fig. S2, showing the triangular array of pores with different periodicities and different electron beam doses. When decreasing the electron beam dose (left to right), the pore size of the triangular array decreases, which is visible in all arrays. Decreasing the electron beam dose too much will result in undeveloped pores, creating vacancies inside the triangular array. When decreasing the periodicity of the pore array, more pores are visible in each which are molten together can be observed when the electron beam dose is too high. In order to obtain high quality arrays with low periodicity, a lower range in electron beam

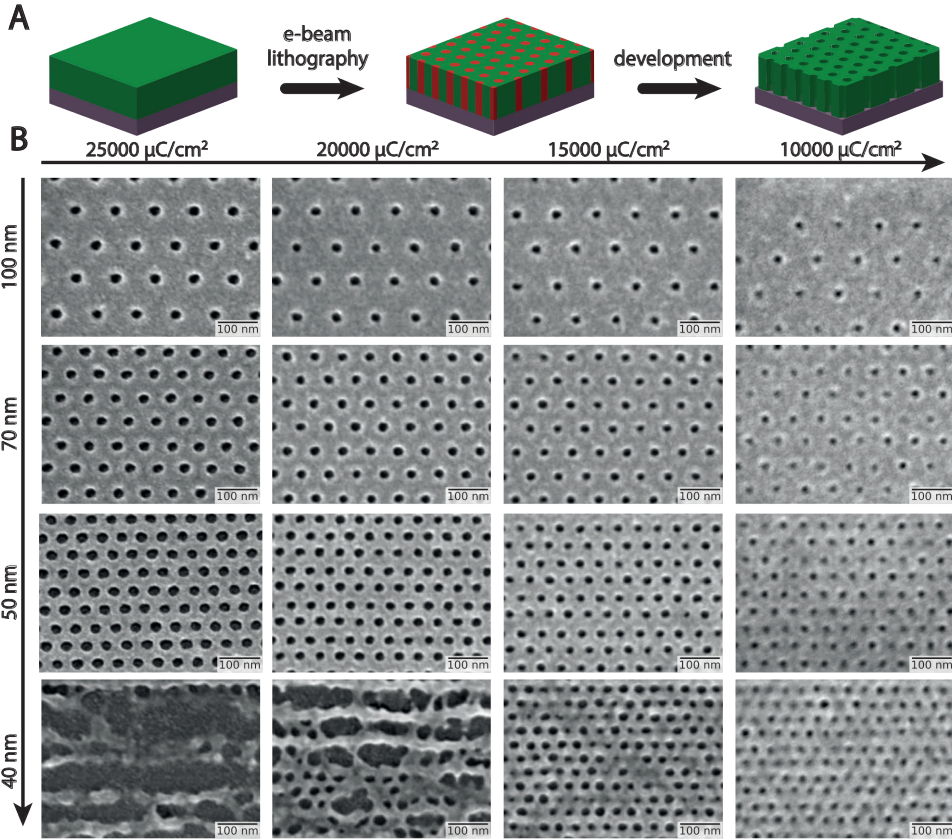


**Figure S2: Electron beam lithography procedure on a GaAs/SiO<sub>2</sub> substrate.** (A) Schematic view of the electron beam lithography procedure. (B) SEM images of triangular arrays patterned with different array periodicities ( $D = 100, 70, 50$  and  $40$  nm) and different electron beam dose values ( $25000, 20000, 15000$  and  $10000$   $\mu\text{C}/\text{cm}^2$ ).

dose needs to be investigated.

## Reactive ion etching of the SiO<sub>2</sub> layer

Etching test on the SiO<sub>2</sub> surface are first performed on a small layer of SiO<sub>2</sub> on top of a commercial GaAs substrate. Etching is performed using a reactive ion etching (RIE) technique with a mixture of CHF<sub>3</sub> and CF<sub>4</sub> gases (40/40 sccm). The chamber pressure was set to 50 mTorr, and a RF power of 180 W is used. The SiO<sub>2</sub> layer is etched for 40 seconds, etching all the SiO<sub>2</sub> inside the pores of the resist. The complete triangular pattern is therefore transferred onto the SiO<sub>2</sub> layer. Residual PMMA resist on top of the SiO<sub>2</sub> surface is removed using a gentle O<sub>2</sub> plasma etching step. The sample was further rinsed and cleaned with IPA under a low N<sub>2</sub> flow.

Results of the etching of the SiO<sub>2</sub> layer can be observed in Fig. S3, which only show

#### IV Realizing honeycomb semiconductors: A lithographic route towards nanoporated InGaAs quantum wells

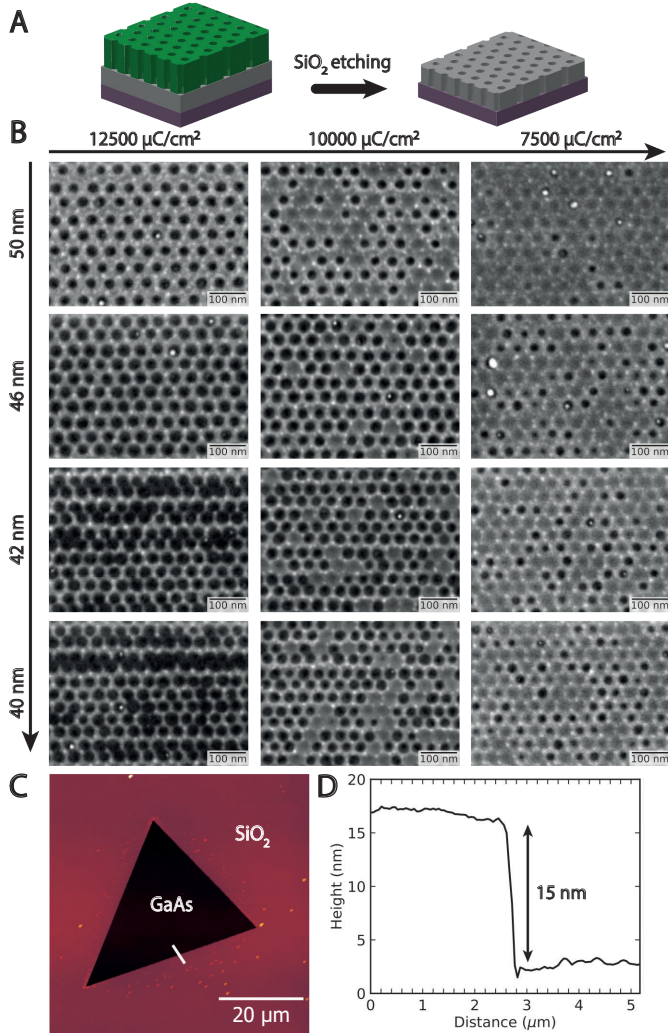


**Figure S3:** SiO<sub>2</sub> etching procedure using reactive ion etching. (A) Schematic view of the etching procedure. (B) SEM images of the SiO<sub>2</sub> etching procedure for different low periodicity arrays ( $D = 50, 46, 42$  and  $40$  nm) and different electron beam dose ( $12500, 10000$  and  $7500 \mu\text{C}/\text{cm}^2$ ). (C) AFM image of the tip of an alignment marker. (D) Height profile acquired along the white line of the AFM image.

lattices with a periodicity between 50 and 40 nm. The SEM images show the difficulty to obtain high-quality array or pores at low periodicities. Increasing the electron beam dose will result in molten structures, and too low electron beam dose values will result in undeveloped pores, which is still mainly an effect of the lithography process. An optimal electron beam dose of  $10000 \mu\text{C}/\text{cm}^2$  is found for the 40 nm periodicity array, which will be used as a guidance for further investigation of the technology process.

---

To confirm that the sample is etched deep enough, atomic force microscopy (AFM) is performed on a large marker surrounding the pores (Fig. S3C). Due to the size of the pores, measuring the depth directly on the array with AFM is not possible. The height profile between the marker and the SiO<sub>2</sub> layer shows a height difference of 15 nm, confirming that the whole 10 nm layer of SiO<sub>2</sub> is etched away.

## Reactive ion etching on III-V semiconductor

The final technological step which is investigated is the etching of the III-V semiconductor layer, which is performed on a GaAs test substrate without the grown SiO<sub>2</sub> layer on top of the sample (Fig. S4A). In this test, PMMA resist is spin-coated on top of the substrate, and electron beam lithography and development of the PMMA resist are performed using similar parameters from the earlier experiments, printing a triangular array of pores in the resist. After the development of the resist, etching is performed using RIE with an argon flow of 12 sccm and a RF power of 350 W, transferring the pattern into the GaAs substrate. The pressure of the RIE chamber was set to 0.2 mTorr. The sample was etched for 35 seconds, removing 22 nm of the PMMA resist and 17 nm of the GaAs inside the pores, which was observed using atomic force microscopy. The remaining PMMA was removed by placing the sample in a ultrasonic bath of Remover PG for 2 minutes, followed by an acetone ultrasonic bath for 2 minutes and finalized by an ultrasonic bath of IPA for two minutes.

Results of the RIE etching procedure are presented in Fig. S4B. Similar to the previous steps in the technology process, decreasing to lower electron beam dose result in smaller, less defined pores which is a direct result from the lithography settings. The depth of the pores is measured using AFM, which is 17 nm measured on a large marker. An increase in height can be observed around the etched area, which is redeposition of material around the contour of the marker. Again, AFM directly onto the triangular array was performed, but the tip of the AFM was too large to fully enter the pores. Nevertheless, the redeposition of material is also visible on the SEM images of the triangular arrays, indicating that extra material is present around the pores. For this reason, other etching techniques were investigated to avoid redeposition of material around the pores.

An other etching technique which is investigated is induced coupled plasma (ICP)-RIE. This etching technique is already extensively studied on various III-V semiconductors, showing the possibility to transfer low-dimensional patterns with a high quality [39]. The advantage of using ICP etching over conventional RIE is the separate control over the generated plasma density and the accelerating ion energy, allowing for a better tuning of the degree of anisotropy of the etching [40].

To accurately investigate the last essential etching step in the fabrication process, electron beam lithography was performed on the designed InGaAs/InP QW heterostructure with an electron beam dose of 10000  $\mu\text{C}/\text{cm}^2$ , and the protecting SiO<sub>2</sub> layer was etched according to previous steps. Lastly, the triangular array was transferred into the InGaAs layer using BCl<sub>3</sub> based ICP-RIE, using the same settings as presented in the

#### IV Realizing honeycomb semiconductors: A lithographic route towards nanoporated InGaAs quantum wells

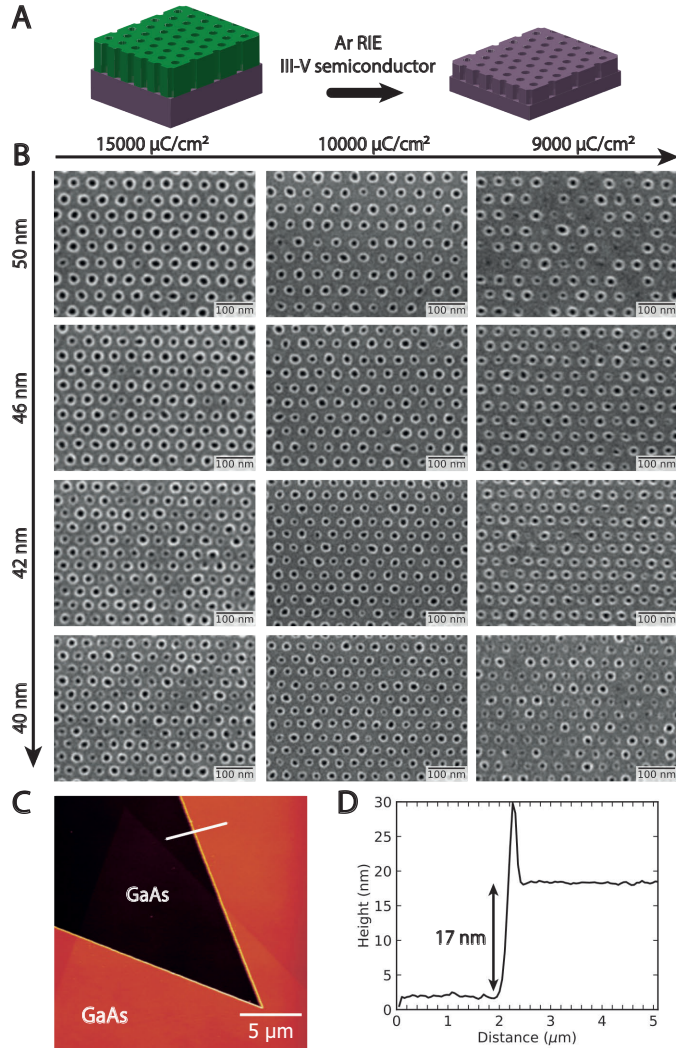


**Figure S4: III-V semiconductor etching procedure using RIE.** (A) Schematic view of the III-V semiconductor etching procedure of the GaAs. (B) SEM images of the III-V semiconductor etching procedure for different low periodicity arrays (50, 46, 42 and 40 nm) and different electron beam dose (15000, 10000 and 9000  $\mu\text{C}/\text{cm}^2$ ). (C) AFM image of an alignment marker. (D) Height profile acquired along the white line of the AFM image

method section of the main body of the chapter (Fig. S5A). After the etching procedure, the remaining  $\text{SiO}_2$  was removed by performing a standard wet etching procedure (1% HF for 1 min).

The results of the  $\text{BCl}_3$  based ICP-RIE procedure are presented in Fig. S5B for a triangular antidot lattice with a periodicity of  $D = 60, 50$  and 40 nm. Next to the SEM images, a full analysis of the lattice is presented, showing the pore distance distribu-

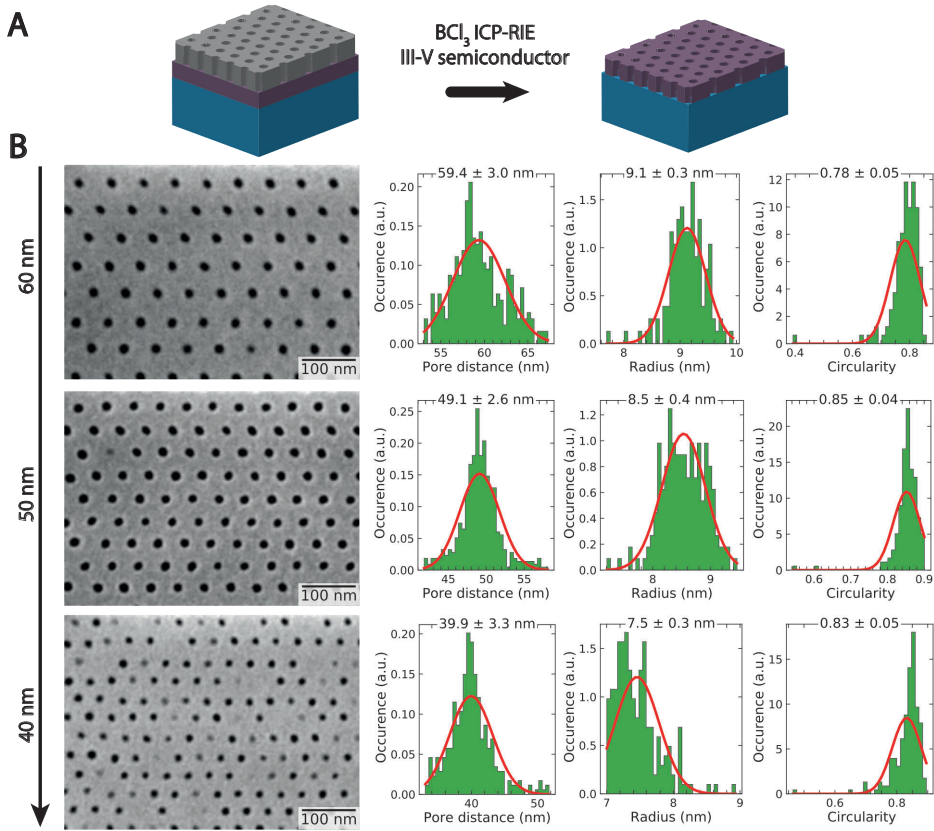


**Figure S5: InGaAs etching using  $\text{BCl}_3$  ICP-RIE** (A) Schematic view of etching process of the InGaAs layer. (B) SEM images of triangular arrays with 60, 50 and 40 nm pore-to-pore distances, including a full statistical analysis.

tions, pore radius distributions and circularity distributions using a particle detection script. The triangular arrays are transferred into the InGaAs layer with a high quality, which can be viewed in the full analysis. When decreasing the pore distance, smaller pores are formed and more vacancies are present which can be observed in the SEM image. The higher uncertainty in the circularity for the 40 nm triangular array also suggests that the 40 nm array is of less quality compared to the other arrays, therefore limiting the size of the triangular lattice to 40 nm.

After imaging of the top-view of the triangular lattice, the heterostructure was further characterized, which results are presented in the main body of this chapter.

## Particle detection algorithm

To accurately investigate the quality of the triangular lattice, a particle detection protocol for SEM images is written, extracting the pore-to-pore distances, pore sizes and

circularity of the pores. By fitting Gaussian distributions to the data sets, average values and standard deviations can be extracted, revealing the amount of positional and radial disorder in the triangular lattice.

First, the full raw SEM image is loaded into the script (Fig. S6A). The image is prepared for particle detection by removing the information bar below the image, and excessive number of pixels ('salt-and-pepper noise') is removed by Gaussian blurring to improve the quality of the SEM image (Fig. S6B). A black-white image of the SEM is obtained using an adaptive Gaussian threshold algorithm (Fig. S6C). The adaptive Gaussian threshold algorithm determines different threshold values for each pixel based on a small area around the pixel, resulting in different threshold values for different areas of the image. These threshold values is Gaussian-weighted sum of the neighborhood values. The adaptive Gaussian threshold algorithm therefore also works for images with varying illumination, which will change when the lattice is imaged with different electron beam doses.

All the pores are labelled, and small grains and hollows which are overlapping with the edge of the image are removed. The total number of pixels in the contour and area of each pore is detected, which is used to find the center coordinates of each pore (Fig. S6D). The radius of each pore is calculated by fitting a circle to every pore, and the circularity of each pore is determined using the equation

$$C = \frac{4\pi A}{P^2}$$

where A is the surface of the pore and P the perimeter of the pore. For a perfect round circle, this equation will yield one. The value C will go down when the pores are less round. Using the center coordinates, all the nearest neighbor distances between the pores are computed. With the obtained data, we obtain three distributions that are plotted in histograms and fitted with a standard Gaussian distribution in order to determine their mean and the standard deviation (Fig. S6E). Using this particle detection script on the obtained SEM images, short range positional disorder and disorder in the shape of the pores can be immediately characterized. Final images are created by cropping the blurred SEM image and by adding a scale bar to the image (Fig. S6F).

## Radial distribution function

As discussed, the radial distribution functions can be calculated from the particle detection algorithm, giving us information of the origin of the disorder. The calculated distribution can be compared with two different models: the ideal paracrystal model and the real paracrystal model. Both models will be further explained here in more detail.

### Ideal paracrystal model

In an two-dimensional ideal paracrystal model, the next neighbor distance between adjacent pores is a variable  $\mathbf{R}^{\text{ideal}}$  which is randomly drawn from a two-dimensional

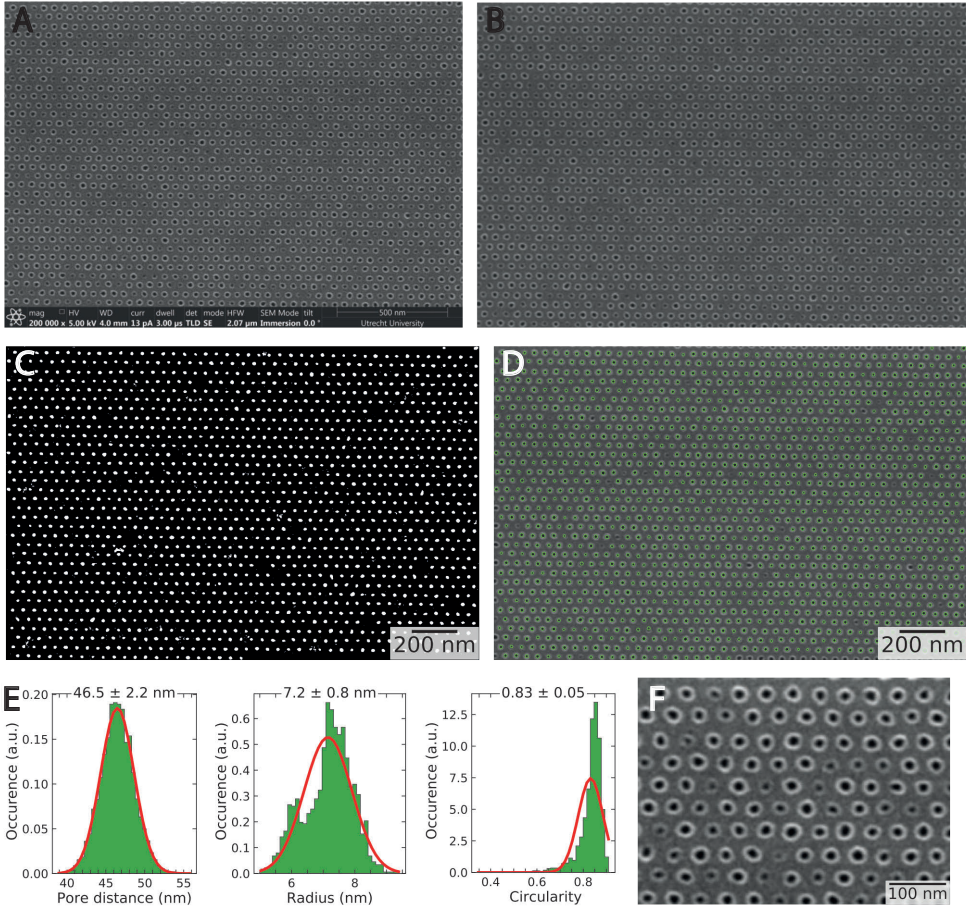


**Figure S6: Schematic overview of the particle detection process.** (A) Full raw SEM image loaded into the particle detection script. (B) Blurred SEM image without the information bar and reduced in pixels to remove 'salt-and-pepper' noise. (C) Binarized image showing the detected triangular array in white. (D) The detected pores are individually fitted with circles (green) with position  $(x,y)$  and radius  $r$ . (E) Distributions of distances between pores, radius of the pores and circularity are calculated and fitted with Gaussian distributions to extract the mean  $\mu$  and standard deviation  $\sigma$  of each distribution. (F) The final blurred SEM is cropped and the correct scalebar is added.

Gaussian distribution  $P^{(d)}(\mathbf{r}) = \mathbf{G}(\mathbf{r}; \mathbf{a}_{(d)}, \Sigma)$  where the length of the  $d$  is equal to the periodicity of the lattice ( $|\langle \mathbf{R}^{\text{ideal}} \rangle| = a$ ) and variance  $\Sigma$ .

As discussed, the  $(n,m)$ 'th lattice site in of an ideal paracrystal lattice is described using the formula:

$$\mathbf{R}_{n,m}^{\text{ideal}} = \sum_{i=1}^n \mathbf{R}_i^{(1)} + \sum_{j=1}^m \mathbf{R}_j^{(2)}$$

Now that an ideal paracrystal can be created, the probability density function  $P_{n,m}(\mathbf{r})$

#### IV Realizing honeycomb semiconductors: A lithographic route towards nanoporated InGaAs quantum wells

can be calculated which is needed to calculate the radial distribution function of the ideal paracrystal. The probability density function of finding lattice site  $(n, m)$  at coordinate  $\mathbf{r}$  can be written as a product of  $n \times m$  Gaussian distributions, which can be simplified in one Gaussian distribution with mean  $\mathbf{R}_{nm}^{\text{ideal}}$  and total variance  $n\boldsymbol{\Sigma}_1 + m\boldsymbol{\Sigma}_2$ :

$$\begin{aligned}
 P_{nm}(\mathbf{r}) &= \underbrace{P^{(1)}(\mathbf{r}) * P^{(1)}(\mathbf{r}) * \dots * P^{(1)}(\mathbf{r})}_{n \text{ times}} * \underbrace{P^{(2)}(\mathbf{r}) * P^{(2)}(\mathbf{r}) * \dots * P^{(2)}(\mathbf{r})}_{m \text{ times}} \\
 &= \underbrace{\mathbf{G}(\mathbf{r}; \mathbf{a}_1, \boldsymbol{\Sigma}_1) * \mathbf{G}(\mathbf{r}; \mathbf{a}_1, \boldsymbol{\Sigma}_1) * \dots * \mathbf{G}(\mathbf{r}; \mathbf{a}_1, \boldsymbol{\Sigma}_1)}_{n \text{ times}} * \underbrace{\mathbf{G}(\mathbf{r}; \mathbf{a}_2, \boldsymbol{\Sigma}_2) * \mathbf{G}(\mathbf{r}; \mathbf{a}_2, \boldsymbol{\Sigma}_2) * \dots * \mathbf{G}(\mathbf{r}; \mathbf{a}_2, \boldsymbol{\Sigma}_2)}_{m \text{ times}} \\
 &= \mathbf{G}(\mathbf{r}; n\mathbf{a}_1, n\boldsymbol{\Sigma}_1) * \mathbf{G}(\mathbf{r}; m\mathbf{a}_2, m\boldsymbol{\Sigma}_2) \\
 &= \mathbf{G}(\mathbf{r}; \mathbf{R}_{nm}, n\boldsymbol{\Sigma}_1 + m\boldsymbol{\Sigma}_2)
 \end{aligned}$$

This shows that the total variance of the probability density function at lattice site  $(n, m)$   $P_{nm}(\mathbf{r})$  grows linearly with the lattice site  $(n, m)$ . For an hexagonal lattice, the unit vectors are defined as  $\mathbf{a}_1 = a\hat{\mathbf{x}}$  and  $\mathbf{a}_2 = \frac{a}{2}\hat{\mathbf{x}} + \frac{\sqrt{3}a}{2}\hat{\mathbf{y}}$ . Assuming that the ideal paracrystal lattice is isotropic, meaning that variance for both lattice vectors is the same ( $\boldsymbol{\Sigma}_1 = \boldsymbol{\Sigma}_2 = \sigma^2\mathbf{I}_2$ , where  $\mathbf{I}_2$  is a two-dimensional identity matrix) the probability density function can be written as:

$$P_{nm}(\mathbf{r}) = \mathbf{G}(\mathbf{r}; (n + m/2)a\hat{\mathbf{x}} + \frac{\sqrt{3}}{2}ma\hat{\mathbf{y}}, (n + m)\sigma^2\mathbf{I}_2)$$

Using this definition of the probability density function, the radial distribution function  $g(r)$  can be calculated, which yields approximately the mean number of lattices sites  $n(r)$  in an annulus with thickness  $dr$  at distance  $r$  from a reference point divided by the area of the annulus  $A_s(r)$  and the mean density of the lattice sites  $\rho$ :

$$g(r) \approx \frac{n(r)}{A_s(r)\rho} \quad (\text{IV.6})$$

The radial distribution function becomes exact when the area of the annulus  $A_s(r) = 2\pi r\Delta r$  becomes smaller and smaller, taking the limit of  $\Delta r$  to zero:

$$g(r) = \lim_{\Delta r \rightarrow 0} \frac{n(r)}{2\pi r\Delta r\rho}$$

A schematic representation of the radial distribution function can be found in Fig. S7.

Next, the mean number of lattice sites in an annulus can be calculated by taking the radial integral over the total probability of finding a lattice site at position  $\mathbf{r}$  in this small annulus. The total probability function  $P(\mathbf{r})$  is simply a summation over all probability density function of every site which was calculated earlier:

$$\begin{aligned}
 n(r) &= \int_r^{r+\Delta r} \int_0^{2\pi} P(\mathbf{r})r d\theta dr \\
 &= \int_r^{r+\Delta r} \int_0^{2\pi} \sum_{n,m} P_{n,m}(\mathbf{r})r d\theta dr
 \end{aligned}$$

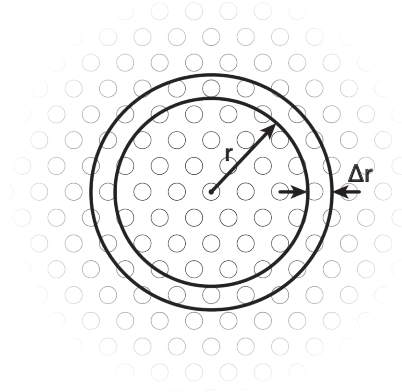


**Figure S7: Geometry for the calculation of the radial distribution function.**

Combining both equations will and applying the fundamental theorem of calculus will yield:

$$\begin{aligned} g(r) &= \frac{1}{2\pi r \rho} \lim_{\Delta r \rightarrow 0} \frac{1}{\Delta r} \int_r^{r+\Delta r} \int_0^{2\pi} \sum_{n,m} P_{n,m}(\mathbf{r}) r d\theta dr \\ &= \frac{1}{2\pi r \rho} \int_0^{2\pi} \sum_{n,m} P_{n,m}(\mathbf{r}) r d\theta \end{aligned}$$

The last step which needs to be performed is to rewrite  $P_{n,m}(\mathbf{r})$  into polar coordinates, since currently it is expressed in cartesian coordinates:

$$\begin{aligned} P_{n,m}(\mathbf{r}) &= \mathbf{G}(\mathbf{r}; (n+m/2)a\hat{\mathbf{x}} + (\sqrt{3}/2)ma\hat{\mathbf{y}}, (n+m)\sigma^2 \mathbf{I}_2) \\ &= \mathbf{G}(x; (n+m/2)a, (n+m)\sigma^2) * \mathbf{G}(y; (\sqrt{3}/2)ma, (n+m)\sigma^2) \\ &= \frac{1}{2\pi(n+m)\sigma^2} \exp\left[-\left(\frac{(x-(n+m/2)a)^2}{2(n+m)\sigma^2} + \frac{(y-(\sqrt{3}/2)ma)^2}{2(n+m)\sigma^2}\right)\right] \end{aligned}$$

Expressing this equation in polar coordinates, and using that the spread of the probability function (that is the standard deviation) is small relative to the distance  $r$  from the reference point ( $r \gg \sqrt{n^2 + m^2}\sigma$ ), an approximation can be made:

$$P_{n,m}(\mathbf{r}) \approx \mathbf{G}(r; \sqrt{(n+m/2)^2 + (3/4)m^2}a, (n+m)\sigma^2) * \mathbf{G}(r\theta; 0, (n+m)\sigma^2) \quad (\text{IV.7})$$

Substituting this equation back into the equation for the radial distribution function, we can further simplify this expression by changing correctly the interval of the integral and approximating this by an integral over the whole space, which is equal to

1:

$$\begin{aligned}
 g(r) &= \frac{1}{2\pi r \rho} \int_0^{2\pi} \sum_{n,m} r d\theta \mathbf{G}(r; \sqrt{(n+m/2)^2 + (3/4)m^2} a, (n+m)\sigma^2) * \mathbf{G}(r\theta; 0, (n+m)\sigma^2) \\
 &= \frac{1}{2\pi r \rho} \sum_{n,m} \mathbf{G}(r; \sqrt{(n+m/2)^2 + (3/4)m^2} a, (n+m)\sigma^2) \int_{-\pi}^{\pi} r d\theta \mathbf{G}(r\theta; 0, (n+m)\sigma^2) \\
 &\approx \frac{1}{2\pi r \rho} \sum_{n,m} \mathbf{G}(r; \sqrt{(n+m/2)^2 + (3/4)m^2} a, (n+m)\sigma^2) \int_{-\infty}^{\infty} r d\theta \mathbf{G}(r\theta; 0, (n+m)\sigma^2) \\
 &= \frac{1}{2\pi r \rho} \sum_{n,m} \mathbf{G}(r; \sqrt{(n+m/2)^2 + (3/4)m^2} a, (n+m)\sigma^2) \\
 &= \frac{1}{2\pi r \rho} \sum_{n,m} \frac{1}{2\pi \sqrt{n+m}\sigma} \exp\left[-\frac{(r - \sqrt{(n+m/2)^2 + (3/4)m^2} a)^2}{2(n+m)\sigma^2}\right]
 \end{aligned}$$

Finally we have obtained the theoretical radial distribution function for an ideal paracrystal, which is a summation of Gaussian distributions where the mean of each distribution  $a_{nm} \equiv \sqrt{(n+m/2)^2 + (3/4)m^2} a$  changes with  $(n, m)$ , and the standard deviation of each Gaussian distribution grows with the lattice site indices  $(n, m)$ :

$$g(r) = \frac{1}{(2\pi)^{3/2} r \rho} \sum_{n,m} \frac{1}{\sigma_{nm}} \exp\left[-\frac{(r - a_{nm})^2}{2(n+m)\sigma_{\text{ideal}}^2}\right] \quad (\text{IV.8})$$

The radial distribution fit of the ideal paracrystal in Fig. IV.7C & D is a least square fit to the experimentally obtained radial distribution function of the SEM image.

## Real paracrystal model

In a real paracrystal model, each lattice site is generated using the ideal paracrystal model and then shifted with an extra random displacement  $\mathbf{R}^{\text{real}}$  which is a random value drawn from a Gaussian distribution  $\mathbf{G}(\mathbf{x}; 0, \mathbf{\Sigma}^{\text{real}})$ . Upon applying this extra shift, a real paracrystal is obtained, which is described in Fig. IV.6B of the main text. With this model, the position of the pore at lattice site  $(n, m)$  can be written as:

$$\begin{aligned}
 \mathbf{R}_{n,m}^{\text{real}} &= \sum_{i=1}^n \mathbf{R}_i^{(1)} + \sum_{j=1}^m \mathbf{R}_j^{(2)} + \mathbf{R}^{\text{real}} \\
 &= \mathbf{R}_{n,m}^{\text{ideal}} + \mathbf{R}^{\text{real}}
 \end{aligned}$$

where  $\mathbf{R}_i^{(1)}$  and  $\mathbf{R}_i^{(2)}$  are defined as in the ideal paracrystal model. To calculate the radial distribution function of the real paracrystal, the probability density function of lattice site  $(n, m)$  needs to be derived. The position of lattice site  $(n, m)$  can be written similar as for the ideal paracrystal model with an addition of an extra variance term in the Gaussian distribution:

$$P_{nm}(\mathbf{r}) = \mathbf{G}(\mathbf{r}; \mathbf{R}_{nm}, n\mathbf{\Sigma}_1^{\text{ideal}} + m\mathbf{\Sigma}_2^{\text{ideal}} + \mathbf{\Sigma}^{\text{real}}) \quad (\text{IV.9})$$

With this probability density function and following the same mathematical steps for a two dimensional hexagonal lattice, a similar pair distribution function can be obtained for the real paracrystal model:

$$g(r) = \frac{1}{(2\pi)^{3/2} r \rho} \sum_{n,m} \frac{1}{\sqrt{(n+m)\sigma_{\text{ideal}}^2 + \sigma_{\text{real}}^2}} \exp\left[-\frac{(r - a_{nm})^2}{2((n+m)\sigma_{\text{ideal}}^2 + \sigma_{\text{real}}^2)}\right] \quad (\text{IV.10})$$

where  $a_{nm} \equiv \sqrt{(n+m/2)^2 + (3/4)m^2} a$  is defined similarly as for the ideal paracrystal model. The pair distribution function is therefore a summation of normal distribution functions with mean  $a_{nm}$  and a total variance  $\sigma_{\text{total}}^2 = (n+m)\sigma_{\text{ideal}}^2 + \sigma_{\text{real}}^2$  which scales with the lattice site  $(n, m)$  similar as for the ideal paracrystal model.

The radial distribution function obtained from the particle particle detection script are both fitted with equation IV.8 and IV.10 using a least square fit.

## Tight-binding model

The atomistic calculations of the electronic structure of the honeycomb lattices made from  $\text{In}_{0.53}\text{Ga}_{0.47}\text{As}/\text{InP}$  heterostructures were performed using a tight-binding approach. The  $\text{In}_{0.53}\text{Ga}_{0.47}\text{As}$  alloy is described as a virtual crystal in which a virtual atom (Va) replaces each In or Ga atom. Each atom in the heterostructures (Va, As, In, P) is described by 20 atomic orbitals,  $sp^3d^5s^*$  for each spin orientation. The  $d$ -orbitals and the second  $s$ -orbital ( $s^*$ ) are required for a good description of conduction bands [42]. The atomic orbitals are considered as orthogonal and the hopping matrix elements are restricted to first nearest neighbors. We used tight-binding parameters (Table S1) which are partly derived from those of Ref. [42]. This model gives an energy gap of 0.8160 eV for  $\text{In}_{0.53}\text{Ga}_{0.47}\text{As}$ , a valence-band offset between  $\text{In}_{0.53}\text{Ga}_{0.47}\text{As}$  and InP of 0.3540 eV, and a conduction-band offset of 0.2536 eV. Spin-orbit coupling is introduced as intra-atomic terms in the  $p$ -sector. Free surfaces are saturated by pseudo-hydrogen atoms described by a single  $s$ -orbital.

#### IV Realizing honeycomb semiconductors: A lithographic route towards nanoporated InGaAs quantum wells

In <sub>0.53</sub> Ga <sub>0.47</sub> As							
$E_s(\text{Va})$	-0.53320	$E_s(\text{As})$	-5.98453	$E_p(\text{Va})$	6.43928	$E_p(\text{As})$	3.57805
$E_d(\text{Va})$	12.61806	$E_d(\text{As})$	12.61806	$E_{s^*}(\text{Va})$	18.58054	$E_{s^*}(\text{As})$	18.58054
$\Delta(\text{Va})$	0.08532	$\Delta(\text{As})$	0.17630				
$V_{ss\sigma}(\text{VaAs})$	-1.54461	$V_{s^*s^*\sigma}(\text{VaAs})$	-3.76901	$V_{ss^*\sigma}(\text{VaAs})$	-2.06653	$V_{ss^*\sigma}(\text{AsVa})$	-1.38306
$V_{sp\sigma}(\text{VaAs})$	2.86527	$V_{sp\sigma}(\text{AsVa})$	2.39829	$V_{s^*p\sigma}(\text{VaAs})$	2.04568	$V_{s^*p\sigma}(\text{AsVa})$	2.42900
$V_{sd\sigma}(\text{VaAs})$	-2.43091	$V_{sd\sigma}(\text{AsVa})$	-2.65354	$V_{s^*d\sigma}(\text{VaAs})$	-0.74850	$V_{s^*d\sigma}(\text{AsVa})$	-0.77492
$V_{pp\sigma}(\text{VaAs})$	4.25538	$V_{pp\pi}(\text{VaAs})$	-1.41030	$V_{pd\sigma}(\text{VaAs})$	-1.93705	$V_{pd\sigma}(\text{AsVa})$	-1.96188
$V_{pd\pi}(\text{VaAs})$	1.87994	$V_{pd\pi}(\text{AsVa})$	1.65707	$V_{dd\sigma}(\text{VaAs})$	-1.17270	$V_{dd\pi}(\text{VaAs})$	2.19187
$V_{dd\delta}(\text{VaAs})$	-1.87195						
InP							
$E_s(\text{In})$	-0.02010	$E_s(\text{P})$	-5.68610	$E_p(\text{In})$	6.14250	$E_p(\text{P})$	2.99070
$E_d(\text{In})$	12.42160	$E_d(\text{P})$	12.42160	$E_{s^*}(\text{In})$	18.51980	$E_{s^*}(\text{P})$	18.51980
$\Delta(\text{In})$	0.11240	$\Delta(\text{P})$	0.02280				
$V_{ss\sigma}(\text{InP})$	-1.40100	$V_{s^*s^*\sigma}(\text{InP})$	-3.68980	$V_{ss^*\sigma}(\text{InP})$	-1.84500	$V_{ss^*\sigma}(\text{PIn})$	-1.28670
$V_{sp\sigma}(\text{InP})$	2.64400	$V_{sp\sigma}(\text{PIn})$	2.16600	$V_{s^*p\sigma}(\text{InP})$	2.05210	$V_{s^*p\sigma}(\text{PIn})$	2.56520
$V_{sd\sigma}(\text{InP})$	-2.21920	$V_{sd\sigma}(\text{PIn})$	-2.55590	$V_{s^*d\sigma}(\text{InP})$	-0.81660	$V_{s^*d\sigma}(\text{PIn})$	-0.79120
$V_{pp\sigma}(\text{InP})$	4.02030	$V_{pp\pi}(\text{InP})$	-1.28070	$V_{pd\sigma}(\text{InP})$	-1.88510	$V_{pd\sigma}(\text{PIn})$	-1.92390
$V_{pd\pi}(\text{InP})$	1.77630	$V_{pd\pi}(\text{PIn})$	1.56790	$V_{dd\sigma}(\text{InP})$	-1.24820	$V_{dd\pi}(\text{InP})$	2.14870
$V_{dd\delta}(\text{InP})$	-1.68570						
Nearest-neighbor hopping terms between In and As							
$V_{ss\sigma}(\text{InAs})$	-1.47890	$V_{s^*s^*\sigma}(\text{InAs})$	-3.85140	$V_{ss^*\sigma}(\text{InAs})$	-2.13200	$V_{ss^*\sigma}(\text{AsIn})$	-1.22190
$V_{sp\sigma}(\text{InAs})$	2.80060	$V_{sp\sigma}(\text{AsIn})$	2.31590	$V_{s^*p\sigma}(\text{InAs})$	1.90120	$V_{s^*p\sigma}(\text{AsIn})$	2.64670
$V_{sd\sigma}(\text{InAs})$	-2.44990	$V_{sd\sigma}(\text{AsIn})$	-2.58280	$V_{s^*d\sigma}(\text{InAs})$	-0.83710	$V_{s^*d\sigma}(\text{AsIn})$	-0.84970
$V_{pp\sigma}(\text{InAs})$	4.11880	$V_{pp\pi}(\text{InAs})$	-1.36870	$V_{pd\sigma}(\text{InAs})$	-2.05840	$V_{pd\sigma}(\text{AsIn})$	-2.12220
$V_{pd\pi}(\text{InAs})$	1.71060	$V_{pd\pi}(\text{AsIn})$	1.54620	$V_{dd\sigma}(\text{InAs})$	-1.20090	$V_{dd\pi}(\text{InAs})$	2.18200
$V_{dd\delta}(\text{InAs})$	-1.77880						
Nearest-neighbor hopping terms between Va and P							
$V_{ss\sigma}(\text{VaP})$	-1.54383	$V_{s^*s^*\sigma}(\text{VaP})$	-3.63368	$V_{ss^*\sigma}(\text{VaP})$	-1.73145	$V_{ss^*\sigma}(\text{PVa})$	-1.45078
$V_{sp\sigma}(\text{VaP})$	2.80192	$V_{sp\sigma}(\text{PVa})$	2.46746	$V_{s^*p\sigma}(\text{VaP})$	2.09727	$V_{s^*p\sigma}(\text{PVa})$	2.48220
$V_{sd\sigma}(\text{VaP})$	-2.26390	$V_{sd\sigma}(\text{PVa})$	-2.66311	$V_{s^*d\sigma}(\text{VaP})$	-0.74248	$V_{s^*d\sigma}(\text{PVa})$	-0.72136
$V_{pp\sigma}(\text{VaP})$	4.10420	$V_{pp\pi}(\text{VaP})$	-1.35275	$V_{pd\sigma}(\text{VaP})$	-1.85008	$V_{pd\sigma}(\text{PVa})$	-1.86148
$V_{pd\pi}(\text{VaP})$	1.94292	$V_{pd\pi}(\text{PVa})$	1.70397	$V_{dd\sigma}(\text{VaP})$	-1.23814	$V_{dd\pi}(\text{VaP})$	2.20816
$V_{dd\delta}(\text{VaP})$	-1.83925						
Parameters for H-Va, H-As, H-In and H-P (eV)							
$E_H$	0.0	$V_{ss\sigma}$	-3.5	$V_{sp\sigma}$	4.5		

**Table S1:** Tight-binding parameters in eV (notations of Slater and Koster [41]) for the In<sub>0.53</sub>Ga<sub>0.47</sub>As/InP system in an orthogonal  $sp^3d^5s^*$  model.  $\Delta$  is the spin-orbit coupling. Va denotes the virtual atom ( $\equiv$  In<sub>0.53</sub>Ga<sub>0.47</sub>). Lattice parameter:  $a = 5.87 \text{ \AA}$ .

---

## References

- [1] A. Tadjine, G. Allan, and C. Delerue, "From lattice Hamiltonians to tunable band structures by lithographic design," *Physical Review B*, vol. 94, p. 075441, aug 2016.
- [2] M. Polini, F. Guinea, M. Lewenstein, H. C. Manoharan, and V. Pellegrini, "Artificial honeycomb lattices for electrons, atoms and photons," *Nature Nanotechnology*, vol. 8, pp. 625–633, sep 2013.
- [3] E. Kalesaki, C. Delerue, C. Morais Smith, W. Beugeling, G. Allan, and D. Vanmaekelbergh, "Dirac Cones, Topological Edge States, and Nontrivial Flat Bands in Two-Dimensional Semiconductors with a Honeycomb Nanogeometry," *Physical Review X*, vol. 4, p. 011010, jan 2014.
- [4] X. Du, I. Skachko, F. Duerr, A. Luican, and E. Y. Andrei, "Fractional quantum Hall effect and insulating phase of Dirac electrons in graphene," *Nature*, vol. 462, pp. 192–195, nov 2009.
- [5] K. I. Bolotin, F. Ghahari, M. D. Shulman, H. L. Stormer, and P. Kim, "Observation of the fractional quantum Hall effect in graphene," *Nature*, vol. 462, pp. 196–199, nov 2009.
- [6] K. S. Novoselov, A. K. Geim, S. V. Morozov, D. Jiang, M. I. Katsnelson, I. V. Grigorieva, S. V. Dubonos, and A. A. Firsov, "Two-dimensional gas of massless Dirac fermions in graphene," *Nature*, vol. 438, no. 7065, pp. 197–200, 2005.
- [7] M. P. Boneschanscher, W. H. Evers, J. J. Geuchies, T. Altantzis, B. Goris, F. T. Rabouw, S. A. P. van Rossum, H. S. J. van der Zant, L. D. A. Siebbeles, G. Van Tendeloo, I. Swart, J. Hilhorst, A. V. Petukhov, S. Bals, and D. Vanmaekelbergh, "Long-range orientation and atomic attachment of nanocrystals in 2D honeycomb superlattices," *Science*, vol. 344, pp. 1377–1380, jun 2014.
- [8] J. J. Geuchies, C. van Overbeek, W. H. Evers, B. Goris, A. de Backer, A. P. Gantapara, F. T. Rabouw, J. Hilhorst, J. L. Peters, O. Konovalov, A. V. Petukhov, M. Dijkstra, L. D. A. Siebbeles, S. van Aert, S. Bals, and D. Vanmaekelbergh, "In situ study of the formation mechanism of two-dimensional superlattices from PbSe nanocrystals," *Nature Materials*, vol. 15, pp. 1248–1254, dec 2016.
- [9] C. Delerue and D. Vanmaekelbergh, "Electronic band structure of zinc blende CdSe and rock salt PbSe semiconductors with silicene-type honeycomb geometry," *2D Materials*, vol. 2, p. 034008, jun 2015.
- [10] M. Gibertini, A. Singha, V. Pellegrini, M. Polini, G. Vignale, A. Pinczuk, L. N. Pfeiffer, and K. W. West, "Engineering artificial graphene in a two-dimensional electron gas," *Physical Review B*, vol. 79, p. 241406, jun 2009.
- [11] C.-H. Park and S. G. Louie, "Making Massless Dirac Fermions from a Patterned Two-Dimensional Electron Gas," *Nano Letters*, vol. 9, pp. 1793–1797, may 2009.
- [12] L. Nádovrník, M. Orlita, N. A. Goncharuk, L. Smrčka, V. Novák, V. Jurka, K. Hruška, Z. Výborný, Z. R. Wasilewski, M. Potemski, and K. Výborný, "From laterally modulated two-dimensional electron gas towards artificial graphene," *New Journal of Physics*, vol. 14, p. 053002, may 2012.
- [13] G. De Simoni, A. Singha, M. Gibertini, B. Karmakar, M. Polini, V. Piazza, L. N. Pfeiffer, K. W. West, F. Beltram, and V. Pellegrini, "Delocalized-localized transition in a semiconductor two-dimensional honeycomb lattice," *Applied Physics Letters*, vol. 97, p. 132113, sep 2010.
- [14] A. Singha, M. Gibertini, B. Karmakar, S. Yuan, M. Polini, G. Vignale, M. I. Katsnelson, A. Pinczuk, L. N. Pfeiffer, K. W. West, and V. Pellegrini, "Two-Dimensional Mott-Hubbard Electrons in an Artificial Honeycomb Lattice," *Science*, vol. 332, pp. 1176–1179, jun 2011.
- [15] S. Wang, D. Scarabelli, L. Du, Y. Y. Kuznetsova, L. N. Pfeiffer, K. W. West, G. C. Gardner, M. J. Manfra, V. Pellegrini, S. J. Wind, and A. Pinczuk, "Observation of Dirac bands in artificial graphene in small-period nanopatterned GaAs quantum wells," *Nature Nanotechnology*, vol. 13, pp. 29–33, jan 2018.
- [16] W. Yeo, R. Dimitrov, W. J. Schaff, and L. F. Eastman, "Material properties of bulk InGaAs and InAlAs/InGaAs heterostructures grown on (111)B and (111)B misoriented by 1° towards 211 InP substrates," *Applied Physics Letters*, vol. 77, pp. 4292–4294, dec 2000.
- [17] I. Watanabe, K. Kanzaki, T. Aoki, T. Kitada, S. Shimomura, and S. Hiyamizu, "Mobility enhancement by reduced remote impurity scattering in a pseudomorphic  $\text{In}_{0.7}\text{Ga}_{0.3}\text{As}/\text{In}_{0.52}\text{Al}_{0.48}\text{As}$  quantum well high electron mobility transistor structure with (411)A super-flat interfaces grown by molecular-beam epitaxy," *Journal of Vacuum Science and Technology B: Microelectronics and Nanometer Structures*, vol. 19, no. 4, p. 1515, 2001.

- 
- [18] S. Perraud, K. Kanisawa, Z.-Z. Wang, and Y. Hirayama, "Unpinning of the Fermi level at (111)A clean surfaces of epitaxially grown n-type  $\text{In}_{0.53}\text{Ga}_{0.47}\text{As}$ ," *Applied Physics Letters*, vol. 89, p. 192110, nov 2006.
- [19] T.-H. Chang, W. Fan, D. Liu, Z. Xia, Z. Ma, S. Liu, L. Menon, H. Yang, W. Zhou, J. Berggren, and M. Hammar, "Selective release of InP heterostructures from InP substrates," *Journal of Vacuum Science and Technology B, Nanotechnology and Microelectronics: Materials, Processing, Measurement, and Phenomena*, vol. 34, p. 041229, jul 2016.
- [20] N. A. Yuzeeva, A. V. Sorokoumova, R. A. Lunin, L. N. Oveshnikov, G. B. Galiev, E. A. Klimov, D. V. Lavruchin, and V. A. Kulbachinskii, "Electron Mobilities and Effective Masses in InGaAs/InAlAs HEMT Structures with High In Content," *Journal of Low Temperature Physics*, vol. 185, pp. 701–706, dec 2016.
- [21] X. Wallart, B. Pinsard, and F. Molloy, "High-mobility InGaAs/InAlAs pseudomorphic heterostructures on InP (001)," *Journal of Applied Physics*, vol. 97, p. 053706, mar 2005.
- [22] J. Millunchick, A. Riposan, B. Dall, C. Pearson, and B. Orr, "Surface reconstructions of InGaAs layers," in *2003 International Symposium on Compound Semiconductors*, pp. 43–44, IEEE, 2003.
- [23] H. Li, J. Wu, Z. Wang, J. Liang, B. Xu, C. Jiang, Q. Gong, F. Liu, and W. Zhou, "Growth and characterization of InGaAs/InAlAs/InP high-electron-mobility transistor structures towards high channel conductivity," *Journal of Crystal Growth*, vol. 186, pp. 309–314, mar 1998.
- [24] M. B. Panish, R. A. Hamm, D. Ritter, H. S. Luftman, and C. M. Cotell, "Redistribution of beryllium in InP and  $\text{Ga}_{0.47}\text{In}_{0.53}\text{As}$  grown by hydride source molecular beam epitaxy and metalorganic molecular beam epitaxy," *Journal of Crystal Growth*, vol. 112, no. 2-3, pp. 343–353, 1991.
- [25] P. E. Smith, S. H. Goss, M. Gao, M. K. Hudait, Y. Lin, S. A. Ringel, and L. J. Brillson, "Atomic diffusion and band lineups at  $\text{In}_{\text{sub}0.53}\text{Ga}_{\text{sub}0.47}\text{As}$ -on-InP heterointerfaces," *Journal of Vacuum Science and Technology B: Microelectronics and Nanometer Structures*, vol. 23, no. 4, p. 1832, 2005.
- [26] M. D. Pashley, K. W. Haberern, R. M. Feenstra, and P. D. Kirchner, "Different Fermi-level pinning behavior on n- and p-type GaAs(001)," *Physical Review B*, vol. 48, pp. 4612–4615, aug 1993.
- [27] J. Shen, D. L. Winn, W. Melitz, J. B. Clemens, and A. C. Kummel, "Real Space Surface Reconstructions of Decapped As-rich  $\text{In}_{0.53}\text{Ga}_{0.47}\text{As}(001)-(2\times4)$ ," *ECS Transactions*, vol. 16, pp. 463–468, dec 2019.
- [28] N. A. Franchina Vergel, A. Tadjine, V. Notot, M. Mohr, A. Kouassi N'Guissan, C. Coinon, M. Berthe, L. Biadala, K. K. Sossoe, M. M. Dzagli, J.-C. Girard, G. Rodary, L. Desplanque, R. Berndt, D. Stiévenard, X. Wallart, C. Delerue, and B. Grandidier, "Influence of doping level and surface states in tunneling spectroscopy of an  $\text{In}_{0.53}\text{Ga}_{0.47}\text{As}$  quantum well grown on p-type doped InP(001)," *Physical Review Materials*, vol. 3, p. 094604, sep 2019.
- [29] K. W. Carey, R. Hull, J. E. Fouquet, F. G. Kellert, and G. R. Trott, "Structural and photoluminescent properties of GaInAs quantum wells with InP barriers grown by organometallic vapor phase epitaxy," *Applied Physics Letters*, vol. 51, no. 12, pp. 910–912, 1987.
- [30] G. Ribordy, N. Gisin, O. Guinnard, D. Stuck, M. Wegmuller, and H. Zbinden, "Photon counting at telecom wavelengths with commercial InGaAs/InP avalanche photodiodes: Current performance," *Journal of Modern Optics*, vol. 51, pp. 1381–1398, jun 2004.
- [31] T. R. Welberry, "Hexagonal paracrystals," *Zeitschrift fur Kristallographie*, vol. 230, no. 1, pp. 69–74, 2015.
- [32] J. L. Eads and R. P. Millane, "Diffraction by the ideal paracrystal," *Acta Crystallographica Section A Foundations of Crystallography*, vol. 57, pp. 507–517, sep 2001.
- [33] R. Hosemann and S. N. Bagchi., "Direct Analysis of Diffraction by Matter," *Science*, vol. 142, pp. 568–569, nov 1963.
- [34] R. Hosemann, W. Vogel, D. Weick, and F. J. Baltá-Calleja, "Novel aspects of the real paracrystal," *Acta Crystallographica Section A*, vol. 37, pp. 85–91, jan 1981.
- [35] B. H. Savitzky, R. Hovden, K. Whitham, J. Yang, F. Wise, T. Hanrath, and L. F. Kourkoutis, "Propagation of Structural Disorder in Epitaxially Connected Quantum Dot Solids from Atomic to Micron Scale," *Nano Letters*, vol. 16, pp. 5714–5718, sep 2016.
-

- 
- [36] K. Whitham, J. Yang, B. H. Savitzky, L. F. Kourkoutis, F. Wise, and T. Hanrath, "Charge transport and localization in atomically coherent quantum dot solids," *Nature Materials*, vol. 15, pp. 557–563, may 2016.
- [37] J. Trasobares, F. Vaurette, M. François, H. Romijn, J.-L. Codron, D. Vuillaume, D. Théron, and N. Clément, "High speed e-beam lithography for gold nanoarray fabrication and use in nanotechnology," *Beilstein Journal of Nanotechnology*, vol. 5, pp. 1918–1925, oct 2014.
- [38] T. Xu, A. Díaz Álvarez, W. Wei, D. Eschimese, S. Eliet, O. Lancry, E. Galopin, F. Vaurette, M. Berthe, D. Desremes, B. Wei, J. Xu, J. F. Lampin, E. Pallecchi, H. Happy, D. Vignaud, and B. Grandidier, "Transport mechanisms in a puckered graphene-on-lattice," *Nanoscale*, vol. 10, no. 16, pp. 7519–7525, 2018.
- [39] T. Maeda, J. Lee, R. Shul, J. Han, J. Hong, E. Lambers, S. Pearton, C. Abernathy, and W. Hobson, "Inductively coupled plasma etching of III–V semiconductors in BCl<sub>3</sub>-based chemistries," *Applied Surface Science*, vol. 143, pp. 174–182, apr 1999.
- [40] T. Maeda, H. Cho, J. Hong, and S. J. Pearton, "New plasma chemistries for etching III–V compound semiconductors: BCl<sub>3</sub> and BBr<sub>3</sub>," *Journal of Electronic Materials*, vol. 28, pp. 118–123, feb 1999.
- [41] J. C. Slater and G. F. Koster, "Simplified LCAO Method for the Periodic Potential Problem," *Physical Review*, vol. 94, pp. 1498–1524, jun 1954.
- [42] J.-M. Jancu, R. Scholz, F. Beltram, and F. Bassani, "Empirical *spds*\* tight-binding calculation for cubic semiconductors: General method and material parameters," *Physical Review B*, vol. 57, pp. 6493–6507, mar 1998.



# Chapter V

---

## Investigating honeycomb semiconductors: Structural and electronic investigation of an engineered InGaAs honeycomb semiconductor

**Based on:**

N.A. Franchina Vergel\*, L.C. Post\*, D. Sciacca, M. Berthe, F. Vaurette, Y. Lambert, D. Yarekha, D. Troadec, C. Coinon, G. Fleury, G. Patriarche, T. Xu, L. Desplanque, X. Wallart, D. Vanmaekelbergh, C. Delerue, B. Grandidier

**Engineering a Robust Flat Band in III-V Semiconductor Heterostructures**

*Nano Letters* **21**, 1 (680-685) 2021

\*Both authors contributed equally

**Electron state energies in solids can be modified by quantum confinement which has been exhaustively exploited with III-V semiconductor heterostructures to investigate intriguing physical phenomena with tremendous consequences in our everyday life [1]. Adding the concept of geometric lattices to these systems [2,3] offers the prospect to reach further freedom and flexibility in the design of electronic bands. An interesting situation arises with the creation of highly correlated and non-trivial eigenstates, which involves the engineering of flat bands [4]. However, this scheme is very challenging, because it requires the construction of specific two-dimensional lattices with periodicities at the limit of high-throughput lithography and a strong immunity against geometrical fluctuations [5–7]. In this chapter, we describe the design of a multi-orbital honeycomb lattice, obtained by block copolymer (BCP) lithography, in an  $\text{In}_{0.53}\text{Ga}_{0.47}\text{As}/\text{InP}$  heterostructure quantum well with a lattice constant of 21 nm. Despite the nanoporation of the well for enhanced confinement, optimization of the surface quality enables a scanning tunneling spectroscopy of the local density of states exhibiting salient *s*- and *p*-orbital bands. We show that the *p*-orbital flat band is protected against the disorder induced by imperfections of the nanopatterning, making this industry-standard technology a powerful tool for studying exotic phases of matter.**

## V.1 Introduction

The propagation of waves interacting with a periodic potential landscape leads to the formation of energy bands for wavelengths on the order of the lattice constant. This concept has played an essential role in the development of solid-state physics and thus of the semiconductor industry. It is also universal [8] and has been successfully applied to the controlled propagation of photons, plasmons, exciton polaritons and phonons, by designing suitable periodic structures using lithographic methods borrowed from the semiconductor process technology [9, 10].

Further breakthroughs in band engineering derive from the physics of graphene [3] and consist in confining the waves in one direction and applying a nanoscale periodic potential in the lateral directions [11–13]. For electrons in two-dimensional (2D) crystals, such a small potential strongly affects their energy dispersion. This concept of band engineering was nicely validated with scanning tunneling microscopy (STM) for a two-dimensional electron gas localized at the surface of a metal by building disorder-free honeycomb and Lieb lattices with periodicities in the nanometer range [14–16]. Transposing this approach to semiconductor heterostructures, in which the Fermi level and the carrier density can be easily tuned, is particularly attractive as it would open new research fields in which geometric lattice concepts can be combined with spin-orbit coupling or with electronic or magnetic interactions for the study of new electronic phases and band structure topology. However, this is very challenging because engineering bands and bandgaps with widths in the 10 meV range or above, compatible with applications in information technologies, requires the construction of lattices

with periodicities below 50 nm, down to 10 nm [5, 17, 18].

Although the honeycomb patterning of a semiconductor heterostructure with potential periodicities around 100 nm showed the faint signature of band features imposed by the patterning [6, 19], progress in this field has been slow, impeded by immature technologies for nanoscale patterning. Moreover, the fate of the band structure with respect to the ubiquitous disorder introduced by the patterning processes is still unknown, despite numerous theoretical predictions of the influence of disorder on specific energy-momentum dispersions, such as conical intersections and nondispersive bands [7, 20, 21].

Here, we present a solid-state electronic platform in which the honeycomb lattice is obtained by patterning a triangular array of antidots (pores) in an  $\text{In}_{0.53}\text{Ga}_{0.47}\text{As}/\text{InP}$  (hereafter,  $\text{InGaAs}/\text{InP}$ ) heterostructure quantum well (QW) using block copolymer (BCP) lithography. Aiming at engineering electronic bands with widths up to 10 meV, our approach takes advantages of the following properties: 1) the small effective mass of  $\text{InGaAs}$  to enhance quantum confinement effects; 2) a low cost and large scale self-assembled BCP enabling the creation of a honeycomb lattice with a lattice constant  $a \approx 21$  nm; 3) a complete perforation of the QW leading to the maximum periodic potential achievable for lateral confinement. Moreover, the doped heterostructure overcomes the limited effective screening in semiconductor materials, while dedicated technology results in a clean, reconstructed top surface, keeping the density of surface states low despite manifold technological processes.

## V.2 Engineering of a Dirac-type band structure by lithographic design

As shown in Fig. V.1A, band theory predicts that the step-like two-dimensional density of states (DOS) of a 10 nm-thick  $\text{InGaAs}$  QW grown by molecular beam epitaxy (MBE) on an  $\text{InP}$  (001) substrate gets featured upon its perforation with tiny pores arranged in a triangular lattice with a periodicity  $D$  of 36 nm. This arises from the interplay between band folding in the Brillouin zone of the super-lattice and the gap opening at the edges or at the centre of the Brillouin zone due to scattering of the electronic waves by the periodic potential of the pores (Fig. V.1B). As the pore size increases, these features get more pronounced and separate in energy due to a stronger lateral confinement, which is further explained in the supplementary information (SI). At a pore diameter  $d$  of 20 nm, the DOS consists of well separated mini-bands (Fig. V.1C), including, in the lowest part of the spectrum, two Dirac cones (DC) and a flat band (FB), the latter giving rise to an intense peak in the DOS. As each lattice site in the honeycomb lattice can be considered as a quantum dot characterized by  $s$ - and  $p$ -orbitals, the two lowest bands in Fig. V.1C have a pronounced  $s$ -like character, while the next four bands are mainly  $p$ -like. A ratio  $d/D$  of 0.56 is predicted to maximize the  $s$ -DC bandwidth (7 meV between the M points of the Brillouin zone) and to ensure the absence of hybridization between the  $s$ - and  $p$ -bands (see SI), leading to the formation of a distinct FB, 22 meV above the  $s$ -DC. Due to the  $p$ -character of the FB, the corresponding peak in the LDOS

## V Investigating honeycomb semiconductors: Structural and electronic investigation of an engineered InGaAs honeycomb semiconductor

vanishes at lattice sites where  $p$ -orbitals have a node, and presents a maximum at the bridge sites connecting two lattice sites (Fig. V.1A) [22].

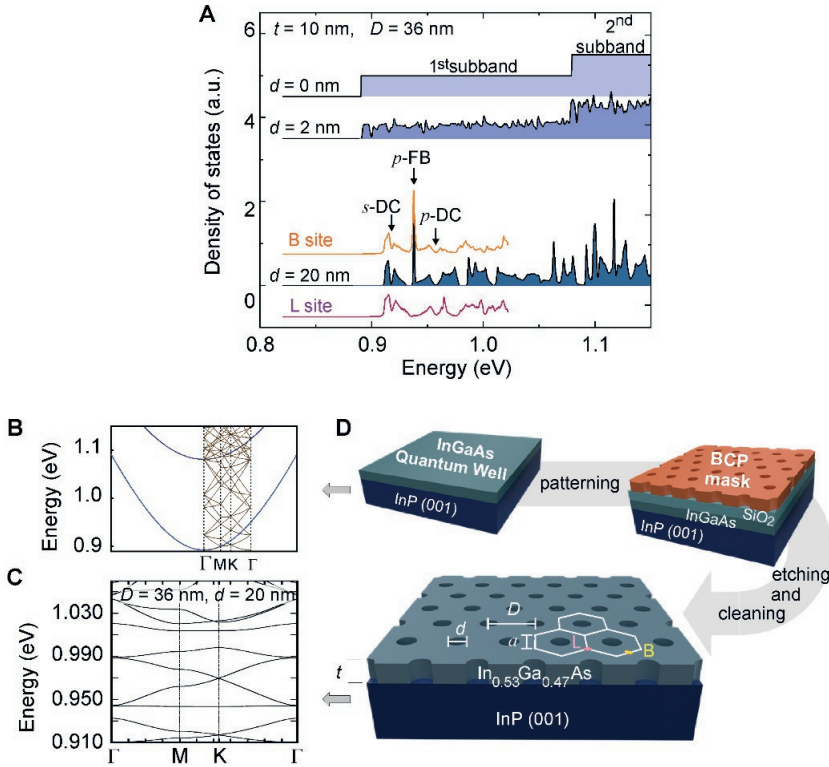


**Figure V.1: Band structure engineering upon the periodic nanoporation of a quantum well.** (A) Variation of the conduction-band density of states of an InGaAs quantum well grown on a InP (001) substrate, which is nanoporated with increasing pore sizes. The thickness  $t$  of the quantum well, the periodicity  $D$  of the lattice and the diameter  $d$  of the pores are indicated. The local density of states at the lattice (L) and bridge (B) sites are superimposed to the density of states for a pore diameter of 20 nm. Vertical arrows point to key features of the density of states, such as Dirac cones (DC) and a flat band (FB). The energy reference is the top of the bulk valence band. (B) Band structure of the quantum well in the first Brillouin zone and in the reduced zone scheme obtained for a periodicity of 36 nm in the real space. (C) Band structure of the triangular nanoporated quantum well with  $D = 36$  nm,  $d = 20$  nm. (D) Illustration of the fabrication process using a self-assembled block copolymer (BCP) thin film as a mask to obtain a honeycomb lattice with a lattice constant  $a = D/\sqrt{3}$ .

The top-down patterning methodology using a self-assembled BCP thin film is illustrated in Fig. V.1D [23]. The plasma-enhanced chemical vapour deposition of a 16 nm-thick  $\text{SiO}_2$  layer on the QW, prior to the spin coating of the BCP thin film, warrants a successful pattern transfer to the InGaAs QW. As seen in Fig. V.2A, after the removal of this protective layer, the QW shows periodic pores, arranged into the micro-domain

structure of the BCP mask, which is also illustrated in the SI. The generated antidot lattice has a periodicity of  $36.0 \pm 2.8$  nm and a pore size of  $20.0 \pm 1.4$  nm (Fig. V.2B, C), calculated using an in-home build particle detection script. In comparison with other lithographic techniques, the BCP lithography approach offers the advantage to create a honeycomb pattern over arbitrarily large areas, which makes its observation with STM straightforward. As the deposition of the  $\text{SiO}_2$  layer leads to the oxidation of the QW surface, which is further altered by the etching of the  $\text{SiO}_2$  mask at the end of the whole workflow, a cleaning of the surface with atomic hydrogen and  $\text{As}_4$  flux was performed in the MBE chamber [24]. It was followed by a thin amorphous As capping [25], which is key to recover a clean and well-ordered InGaAs (001) surface [26], as demonstrated in the STM image of Fig. V.2D. Based on the height profile of Fig. V.2E, the surface structure is consistent with an As-rich ( $2 \times 4$ ) surface [27]. Although the STM tip is not sharp enough to reach the bottom of the pore, cross-sectional scanning transmission electron microscopy (STEM) of the heterostructure indicates the full perforation of the QW (Fig. V.2F). The conical shape of the pores does not significantly affect the electronic properties of the structure [28].

To further investigate the QW surface, a topographic STM image is presented in Fig. V.3, showing the fabricated honeycomb lattice from a three-dimensional view point. Since the STM image is scanned in feedback settings, the image is purely topographic. The honeycomb symmetry is well-defined, but clear non-uniformities are present in the shape of the pores and surface roughness. Observing more closely, the thickness of the QW is thinner on the bridge sites compared with the lattice sites of the honeycomb lattice on multiple areas of the honeycomb lattice. Since bridge sites are located more closely to the pores than the lattice sites, less QW material is present than on the lattice sites due to anisotropic etching of the pores [29], which becomes more problematic upon decreasing the size of the honeycomb unit cell. The possible electronic effects will be discussed further in this chapter.

### V.3 Electronic characterization of the honeycomb semiconductor

To investigate if major changes occur in the electronic structure of the nanoporated InGaAs quantum well, differential conductance spectroscopy is performed on the nanoporated sample over the full energy range of the band gap, and compared with spectra of the atomically resolved InGaAs quantum well (Fig. V.4). In order to resolve the DOS in the conduction band using scanning tunneling spectroscopy (STS), the QW was doped with Be atoms at a concentration higher than  $10^{19} \text{ cm}^{-3}$ . The degenerate holes in the QW ensure the efficient recombination of the tunneling electrons, avoiding any charging of the QW. More importantly, it minimizes the potential fluctuations caused by the random distribution of the charged impurities and defects. This screening efficiency is kept intact after the nanoporation of the QW, as the pinning of the Fermi level at the surface remains close to the top of the valence band. Even though it can shift between remote regions of the samples, at most by 85 meV (Fig. V.4B), a mean position of  $160 \pm 11$  meV above the valence band edge indicates a low density of

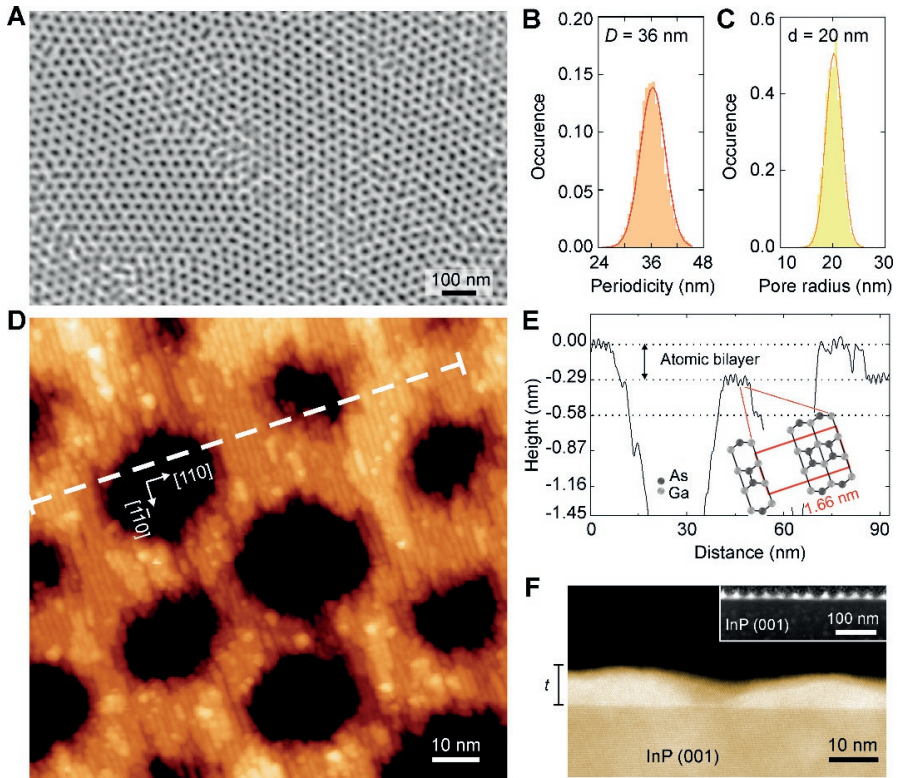


**Figure V.2: Structural properties of the nanoporated InGaAs quantum well** (A) SEM image showing the successful pattern transfer. (B) and (C) Distributions of the pore periodicity and pore diameter measured from SEM images. (D) Atomically-resolved STM image of the nanoporated InGaAs (001) surface, showing variability in the pore size and height of the lattice sites. (E) Height profile measured along the dash segment of the STM image. The corrugation seen on the atomic terraces arises from the As-rich ( $2 \times 4$ ) reconstruction, which is highlighted in the graph. (F) High resolution cross-sectional high angle annular dark field STEM image of the nanoporated heterostructure. Inset: Larger cross-sectional view.

defects [30], which is remarkable in view of the large number of technological processes undergone by the sample. The spectra of the atomically resolved InGaAs quantum well (indicated in black) shows a clear band gap of about 1.0 eV, and three quantized states are visible in the conduction band, labelled by  $E_1$ ,  $E_2$  and  $E_3$ . These quantized states are characteristic for the DOS of a two-dimensional material.

After the nanoporation of the quantum well, the Fermi level is still pinned close to the top of the valence band, which ensures an efficient recombination of the tunneling electrons (red). Also, the size of the band gap remains unaltered after performing the technological processes. Upon shifting to a different area on the nanoporated material, similar spectra are obtained (dark-red), indicating that the general electronic properties do not change over large distances.

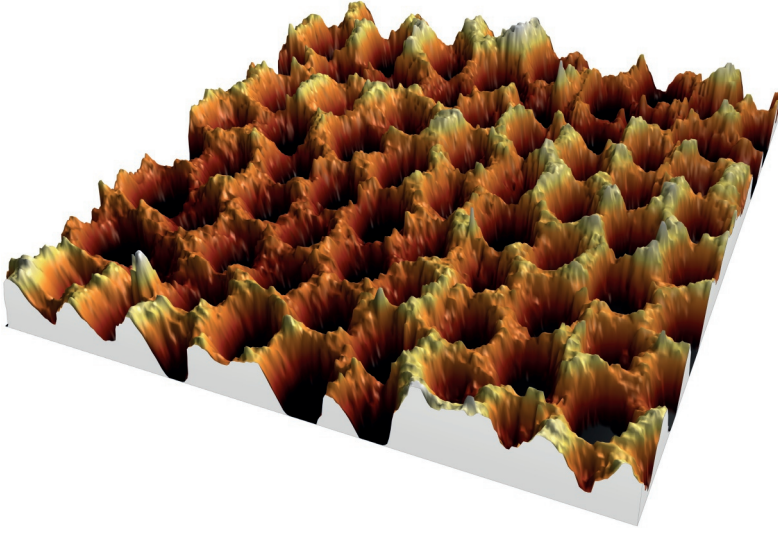


**Figure V.3:** Three-dimensional topographic STM image of the triangular antidot lattice showing a stronger etching at the bridge sites in comparison with the lattice sites. Image size:  $300 \times 300 \text{ nm}^2$ . Feedback parameters:  $V_s = +3.00 \text{ V} / I_{\text{setpoint}} = 20 \text{ pA}$ .

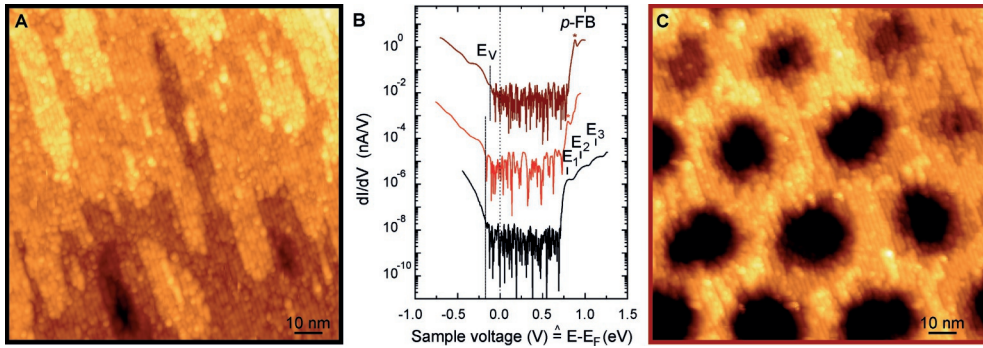


**Figure V.4: Comparison of the tunneling spectra before and after nanoporation.** (A) Atomically resolved STM image of the surface of the InGaAs (001) quantum well. (B) Tunneling spectra measured on the InGaAs quantum well (bottom) and on the bridge sites of a nanoporated InGaAs quantum well in two different regions separated by hundreds of micro meters (intermediate and top). The spectra were vertically shifted for clarity. The top of the valence band, the three quantized states in the quantum well and the flat band in the nanoporated quantum well are labelled  $E_V$ ,  $E_1$ ,  $E_2$ ,  $E_3$ , and FB respectively. Feedback parameters, in order from bottom to top:  $V_s = +1.30 \text{ V}$ ,  $I_{\text{setpoint}} = 400 \text{ pA}$  (bottom),  $V_s = +1.10 \text{ V}$ ,  $I_{\text{setpoint}} = 50 \text{ pA}$  (intermediate),  $V_s = +1.00 \text{ V} / I_{\text{setpoint}} = 100 \text{ pA}$  (top). (C) Atomically resolved STM image of the surface of the nanoporated InGaAs (001) quantum well. The upper right area of the STM image shows a partial mask transfer from the BCP thin film.

To investigate the electronic properties of the nanoporated quantum well more closely, a zoomed-in spectra is performed on the conduction band. Spatially-resolved tunneling spectra were first acquired across two lattice sites (Fig. V.5A). Right at the bridge

## V Investigating honeycomb semiconductors: Structural and electronic investigation of an engineered InGaAs honeycomb semiconductor

site  $B$  (blue), the differential conductance spectrum reveals a distinct peak centered at  $788 \pm 3$  meV, with two tiny shoulders pointed by arrows at smaller bias (770 meV and 753 meV) and another one at higher bias (780 meV) (Fig. V.5B). The peak fades 2 nm away from the bridge site, whereas the shoulders turn into distinct peaks. Remarkably, these features are observed to be symmetric with respect to the bridge site. On the honeycomb lattice site  $L_2$ , the peak doublet is still visible, while the third peak becomes blurred. The doublet is absent in the opposite lattice site ( $L_1$ ); as shown in Fig. V.5C, a height difference of two bilayers between lattice sites  $L_1$  and  $L_2$  strongly decreases the transmission probability, preventing the detection of the conduction band edge at position  $L_1$  for similar STS feedback parameters (see SI).

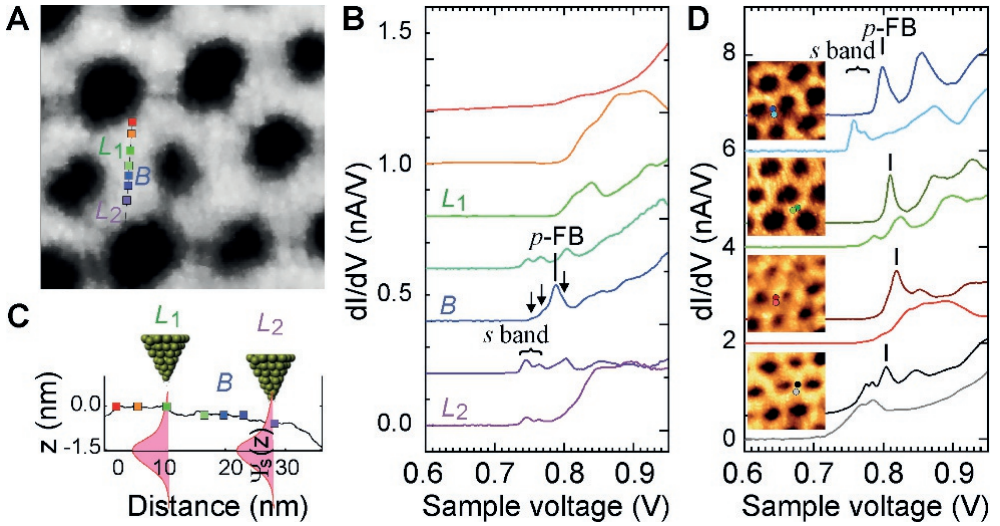


**Figure V.5: Spatially-resolved scanning tunneling spectroscopy of the honeycomb lattice.** (A) topographic and (B) spectroscopic measurements at varying positions across two adjacent lattices via a bridge site, labelled  $L_1$ ,  $L_2$  and  $B$  respectively. The vertical segment indicates the position of the  $p$ -flat band, whereas the arrows point to spectral features of the  $s$ - and  $p$ -dispersive bands. (C) Contour followed by the STM tip scanning at constant height between the acquisition of the spectra. The electronic coupling of the tip states with the wave function  $\Psi_s$  of the antidot lattice depends on the thickness of the lattice sites  $L_1$  or  $L_2$ . (D) Check of the occurrence of the  $p$ -orbital FB peak on the bridge site concomitant with its absence on the adjacent lattice site in four regions of the sample. Insets: STM images of the corresponding regions, which shows various degrees of patterning disorder.

A careful analysis of the surface corrugation (Fig. V.2D, V.3 and Fig. V.4C) reveals that the etching of the QW is usually more pronounced at the bridge sites, allowing a stronger coupling of the tip states to the electronic states of the honeycomb lattice. This generally means that the measured electronic states are more pronounced on the bridge sites due to the vicinity of the STM tip to the QW surface. Focussing the STS measurements in the vicinity of bridge sites for many other areas of the sample, some of them being separated by hundreds of micrometers from each other, we consistently measured the same spatial dependence of the most intense peak within 2 to 3 nm from

the bridge site (Fig. V.5D and SI). In line with the theoretical predictions of Fig. V.1A, which need to be shifted in energy as the experimental reference is given by the position of the Fermi level, we assign this peak to the  $p$ -FB. We identify the peak doublet and the third peak measured at smaller and higher bias to the dispersive  $s$ - and  $p$ -bands respectively. The peak doublet at the lowest energy reflects the maximum LDOS at the M point of the Brillouin zone for a  $s$ -orbital DC. We, however, observe a strong variation in the shape and peak separation of this feature. For instance, the energy difference between the two maxima is often substantially larger than the 7 meV expected for an ideal honeycomb lattice. This can be explained by a stronger local coupling between the lattice sites, as the energy differences between the two maxima is given by the nearest neighbour hopping between the  $s$ -orbitals on the lattice sites [31].

## V.4 Conclusions and outlook

Using the honeycomb lattice as a prominent example, we presented the basis of a future technological platform for two-dimensional semiconductors in which the band structure can be engineered by nano-perforation with lattice constants  $< 50$  nm. The intrinsic honeycomb resonances are still perturbed by nanoscale disorder, but remain visible over the entire honeycomb structure. Especially the  $p$ -orbital flat-band, arising from the interference of in-plane  $p$ -orbitals, is an intrinsic lattice resonance that is strongly resilient against the disorder induced by imperfect nanoporation. Further investigation of the influence of the disorder onto the electronic structure will be performed in the next chapter. Strengthening the intrinsic band features in this lattice, or any other lattice of interest, by smaller lattice vectors and reduced disorder is now within reach.

## Method

**Growth of the InGaAs/InP heterostructure** The  $\text{In}_{0.53}\text{Ga}_{0.47}\text{As}/\text{InP}$  heterostructures were grown by molecular beam epitaxy (MBE) on a Zn p-type doped InP (001) substrate with a concentration of  $4 \times 10^{18} \text{ cm}^{-3}$ , following well-known growth routines [32]. The samples consist of a top 10 nm-thick  $\text{In}_{0.53}\text{Ga}_{0.47}\text{As}$  quantum well, a 10 nm-thick InP spacer layer and a 100 nm-thick p-doped InP buffer layer. The buffer layer was doped with Be acceptors at a concentration of  $7 \times 10^{18} \text{ cm}^{-3}$ . The whole structure was grown at  $525^\circ\text{C}$  in order to favor the diffusion of Be in the quantum well [26, 32, 33]. To protect the surface of the QW from carbon contaminations, 16 nm of  $\text{SiO}_2$  was grown on top of the QW using plasma-enhanced chemical vapour deposition (PECVD).

**Block copolymer lithography** Poly(styrene)-block- (poly)methylmethacrylate (PS-*b*-PMMA) copolymers were synthesized the sequential anionic polymerization of styrene and methyl methacrylate leading to well-defined BCP architectures with low dispersity. The resulting BCP was dissolved in toluene (2 wt%) and spin-coated onto chemically-modified  $\text{SiO}_2$  surface. The self-assembly of the BCP layer was further promoted by thermal annealing at  $220^\circ\text{C}$  leading to out-of-plane PMMA cylinders packed into a triangular lattice. By selectively removing the PMMA domains using plasma chemistry, this process results in the formation of a PS honeycomb mask.

**Dry etching process** After the formation of the mask, the triangular pattern was first etched inside the  $\text{SiO}_2$  layer using reactive ion etching (RIE) in a Plasmalab 80+ (Oxford) system with a mixture of  $\text{CHF}_3$  and  $\text{CF}_4$ . The chamber pressure was set to 10 mTorr, while the power was 300 W. The sample was etched for 40 s, making pores inside the whole thickness of the  $\text{SiO}_2$  layer. The remaining resist on top of the nanoporated

## V Investigating honeycomb semiconductors: Structural and electronic investigation of an engineered InGaAs honeycomb semiconductor

---

SiO<sub>2</sub> layer was subsequently removed. The triangular pattern was then etched inside the In<sub>0.53</sub>Ga<sub>0.47</sub>As QW using BCl<sub>3</sub> based inductively coupled plasma (ICP) etching with a ICP power of 200 W and a RIE power of 50 W. The pressure inside the chamber was set to 2 mTorr and the samples were etched for 40 s. The nanoporated SiO<sub>2</sub> mask was removed by a wet etching in diluted HF at 1% for 30 s.

**Surface cleaning and capping** The final step of the nanofabrication consisted in the cleaning and protection against oxidation. For this purpose, after the wet HF etching of the SiO<sub>2</sub> layer, the samples were loaded back to the MBE chamber. They were annealed at 430°C and bombarded with H plasma for the deoxidization of the surface. The H plasma was performed under an As flux to compensate the As desorption caused by the high temperature. At the end of the deoxidization, the samples were cooled down to room temperature and their surface was capped with 10 nm of amorphous As. This protective layer preserved the surface to become contaminated during the transfer of the samples in air between the MBE chamber and the STM setup. In the preparation chamber of the STM setup, the thin As layer was desorbed at 350°C for 2 hours to recover the As-rich (001) surface of the nanoporated In<sub>0.53</sub>Ga<sub>0.47</sub>As QW.

# Supplementary information

## Electronic structure calculations

In this work, the electronic structure of the honeycomb superlattices of InGaAs (described in Figure S1) was calculated using three different methodologies of decreasing computational requirements:

1. Atomistic tight-binding method
2. Effective-mass approximation plus non-parabolic corrections
3. Effective tight-binding model

Using these models, results obtain from spatially-resolved scanning tunneling spectroscopy can be compared with each other to fully understand the calculated electronic structure.

### Atomistic tight-binding method

Following Refs. [18,28], we used a fully atomistic tight-binding method to calculate the electronic structure of the superlattices. The InGaAs alloy is described as a virtual zinc-blende crystal in which a virtual atom (Va) represents each In or Ga atom. Each atom (Va, As) in a superlattice is described by 20 atomic orbitals,  $sp^3d^5s^*$  for each spin orientation ( $s^*$  is a second  $s$ -orbital). The tight-binding parameters, restricted to nearest-neighbor hopping, are written in the two-center approximation and are given in the Supplementary Information of Ref. [18]. The simulated surfaces are passivated by pseudo-hydrogen atoms such that they form a very high potential barrier for the electrons.

We have investigated systems containing up to  $\sim 10^5$  atoms and  $\sim 2 \times 10^6$  atomic orbitals. Because of these large numbers, only the lowest conduction minibands are calculated using the numerical methods described in Ref. [34]. These methods are based on the Jacobi-Davidson algorithm, which allows us to compute only few eigenvalues (and corresponding eigenstates) near a given energy  $\sigma$ . In this work,  $\sigma$  is set in the

V Investigating honeycomb semiconductors: Structural and electronic investigation of an engineered InGaAs honeycomb semiconductor

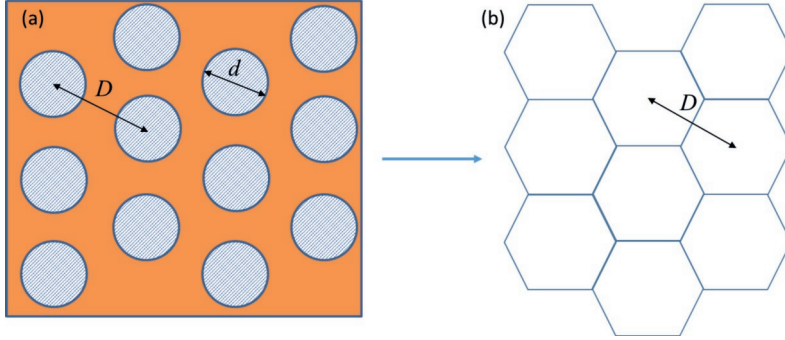


**Figure S1: Schematic view of the simulated superlattice.** (A) Schematic top view of a honeycomb superlattice realized by perforating a thin film of  $\text{In}_{0.53}\text{Ga}_{0.47}\text{As}$  (hereafter, InGaAs) with a periodic (triangular) array of cylindrical holes (blue disks). The electrons are confined in the remaining semiconductor material that forms a honeycomb superlattice. (B) Effective honeycomb lattice seen by the electrons in the system. The lowest conduction bands can be described by an effective tight-binding model characterized by one  $s$ -orbital and three  $p$ -orbitals on each node (site) of the lattice.

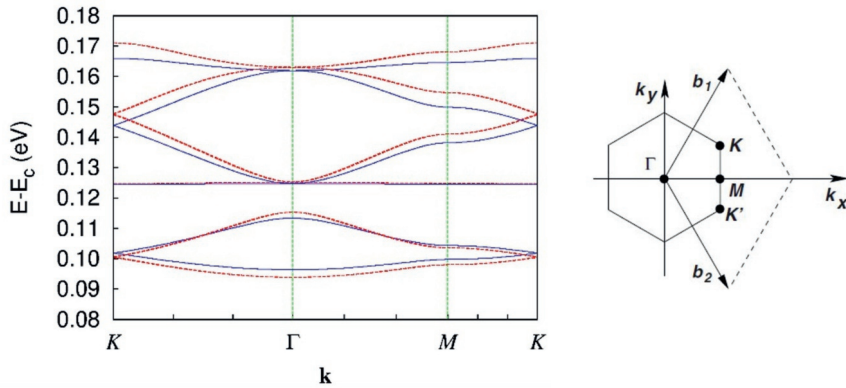


**Figure S2:** Band structure of a honeycomb superlattice realized in a 9.8 nm thick  $\text{In}_{0.53}\text{Ga}_{0.47}\text{As}$  film ( $D = 35.2$  nm,  $d = 20.6$  nm). Lowest conduction bands along the  $K$ - $\Gamma$ - $M$ - $K$  path in the Brillouin zone of the honeycomb lattice calculated using the atomistic tight-binding method (red dotted line) or the effective-mass method including non-parabolic corrections (blue solid lines). The reference of energy is the conduction-band minimum  $E_c$  of bulk InGaAs.

bulk gap. Figure S2 presents the conduction band structure for a honeycomb superlattice close to the one experimentally studied in the present work. As already discussed in Refs. [18, 28], the behaviour of these minibands can also be understood by considering each vertex of the superlattice as a quantum dot characterized by  $s$ - and  $p$ -orbital states, like artificial atoms. Due to the honeycomb geometry, the  $s$ -like states (of the artificial atoms) give rise to the lowest minibands (“the  $s$ -bands”) which behave like  $\pi$ -bands in graphene, with a Dirac cone at  $K$  points. Higher in energy, the in-plane  $p_{x,y}$ -states ( $z$  being the vertical direction) also form a Dirac cone in addition to non-

trivial flat bands induced by the frustration of the  $p_{x,y}$ -orbitals under the hexagonal symmetry resulting in destructive quantum interferences.

## Muffin-tin model plus non-parabolic corrections

The atomistic tight-binding calculations are numerically very heavy, and only the lowest conduction bands can be computed. To be able to compute more bands at a lower cost, we have performed calculations in the muffin-tin (MT) model in which we solve the Schrödinger equation:

$$\left(\frac{\hbar^2}{2m^*}\Delta + V(\mathbf{r})\right)\Psi(\mathbf{r}) = \epsilon\Psi(\mathbf{r}) \quad (\text{V.1})$$

where  $m^* = 0.041m_0$  and  $V(\mathbf{r})$  is the height of the confining potential. By placing repelling potential barriers in a triangular arrangement (Fig. S1), a honeycomb lattice can be obtained. In the case of cylindrical barriers and the effective mass being isotropic, the Schrödinger equation can be separated in two equations: the first one along the  $z$ -direction and the second one in the  $x$ - $y$  plane. The eigenstates and eigenvalues are written as:

$$\begin{aligned} \Psi(\mathbf{r}) &= \chi_n(z)\phi_m(x, y) \\ \epsilon &= \epsilon_n^\perp + \epsilon_m^\parallel \end{aligned} \quad (\text{V.2})$$

Along the  $z$ -direction, we are left with the problem of a simple quantum well problem which can be solved analytically:

$$\epsilon_n^\perp = \frac{\hbar^2}{2m^*} \left(\frac{n\pi}{t}\right)^2 \quad (\text{V.3})$$

where  $t$  is the film thickness and  $n$  is an integer.

Along  $x$ - $y$ , the Schrödinger equation must be solved numerically. We used two numerical methods, either a muffin-tin approach or a simple  $s$ -band tight-binding description, but we checked that they provide identical results. In the muffin-tin approach, the wave functions  $\psi_m(x, y)$  are decomposed into plane waves and the potential  $V(x, y)$  is written as Fourier series. Details on the methodology can be found in the Supplementary Information of Ref. [28] and in Chapter 3 of the thesis.

We have found that this model provides a good description of the bands but tends to overestimates quantum confinement effects compared to the atomistic tight-binding method. This is due to the fact that the conduction band of bulk InGaAs is actually non parabolic away from the band edge. This leads to an overestimation of confinement effects that increases with energy. In order to improve the accuracy, a simple solution is to apply non-parabolic (NP) corrections. Following Refs. [35, 36], an eigenvalue  $\epsilon$  obtained in MT becomes, in NP-MT, the energy  $E$  given by:

$$E = \frac{1}{2\alpha} \left[ -1 + \sqrt{1 + 4\alpha\epsilon} \right] \quad (\text{V.4})$$

where  $\alpha = 1.3\text{eV}^{-1}$  for InGaAs.

Figure S2 shows the comparison between atomistic tight-binding calculations and NP muffin-tin calculations for the lowest conduction bands ( $n=1$ ). The agreement between both models is excellent, in spite of the considerable reduction in computation effort. Similar agreement was found for other dimensions of the superlattices ( $D,d$ ). As a consequence, all other theoretical results presented in the present work were calculated using the NP-EMA approach.

## Evolution of the bands with geometrical dimensions

Figure S3 shows the evolution of the DOS for a triangular arrangement of repulsive potential barriers with a constant periodicity of  $D = 36$  nm and an increasing pore diameter. The DOS is plotted for several geometrical ratio values  $d/D$ . At very low ratio ( $d/D = 0.01$ ), the structure reaches the electronic properties of a two-dimensional free electron gas, which can be observed in the quintessential steps in the DOS. Upon increasing the ratio, small peaks are starting to emerge in each step. At a  $d/D$  ratio of 0.39, the lowest  $p$ -flat band starts to emerge from the density of states, indicated by a sharp peak around 0.12 eV. A  $s$ -type Dirac cone is also viewed lower in energy, which is not entirely splitted from the flat band due to relative strong  $s$ - $p$  hybridization. With increasing pore diameter and thus lateral confinement, the mini-bands shift apart and a second  $p$ -flat band emerges at the highest energy side of the  $p$ -dispersive band at 0.18 eV. In between both  $p$ -states, a broad  $p$ -type Dirac cone is visible.

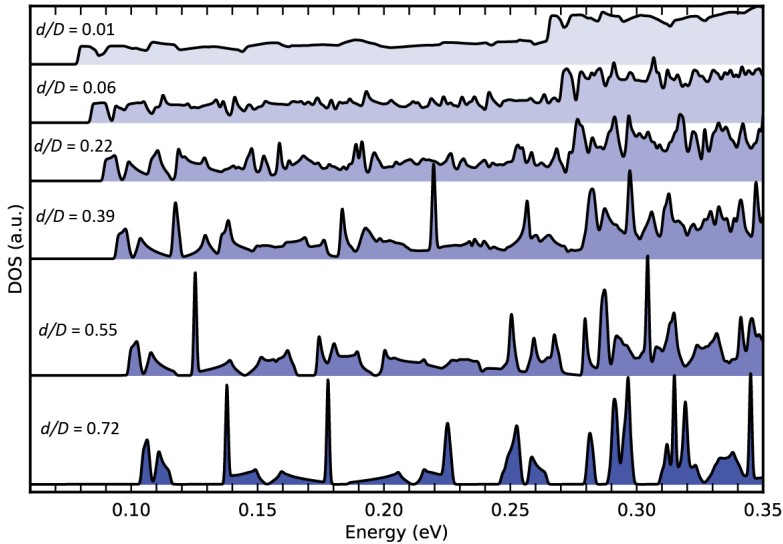


**Figure S3: Evolution of the density of states** Evolution of the density of states as a function of the pore diameter for a triangular lattice with a periodicity  $D = 36.0$  nm. The density of states was obtained from muffin-tin calculations, including non-parabolicity effect. A 0.5 meV broadening was added to the spectra. The reference of energy is the conduction-band minimum  $E_c$  of bulk InGaAs.

Looking at the second quantization step of the DOS starting from 0.27 eV, more distinct peaks can be observed. Comparing the peaks with the DOS at the first quantization step, somewhat of a similarity can be observed, and the intensity of the peaks change similarly with the geometrical ratio  $d/D$ . Therefore, we believe that at higher energies we observe a mixture of states from a higher order state in the lateral direction  $z$  and the lowest states from the  $x$ - $y$  plane. This is quite logical since the calculated electron energy states in the  $x$ - $y$  plane and  $z$ -direction can be solved separately. Especially the  $s$ -like Dirac cone around 0.29 eV and a  $p$ -like Dirac cone at 0.33 eV can be recognized from the calculated DOS.

Figure S4 presents the evolution of several energy features of the  $s$ - and  $p$ -like bands with the geometrical ratio  $d/D$ , which is used to better understand the formation of the Dirac bands. In the case where we wish to study the orbital degrees of freedom and the physics of in-plane  $p$ -orbitals in the honeycomb lattice, we wish to have separated  $s$ - and  $p$ -bands. Also, a well-defined flat band is desired, which is the case when the lowest  $p$ -band is very flat. Lastly, a relatively large width between the two  $s$ -bands at the  $M$  point is aspired, which would mean that we would obtain an  $s$ -type Dirac cone with a maximal broadness at periodicity  $D$ . These plots shows us the ideal geometric pore ratio to meet all these demands, which is universal for all periodicities for the triangular lattice. An optimal geometric ratio of  $d/D \sim 0.6$  is appropriate for this purpose.

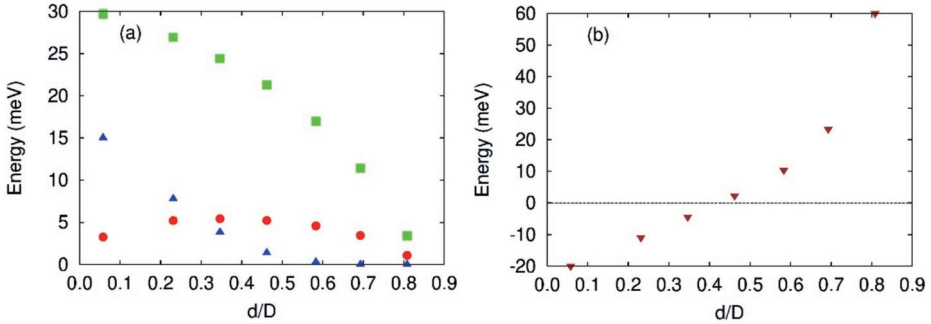


**Figure S4: Evolution of the band structure (including non-parabolic corrections) for honeycomb superlattices.** (A) Energy distance between different bands as function of the ratio  $d/D$ , where  $d$  is the diameter of the holes and  $D$  the distance between two consecutive holes ( $D = 35.2$  nm). Green squares (■): Width of the  $s$ -band at the  $\Gamma$  point. Red dots (●): Same but at the  $M$  point. Blue triangles (▲): Width of the "flat" band. (B) Energy gap between the top of the  $s$  band (at  $\Gamma$ ) and the bottom of the "flat"  $p$ -band (at  $K$ ) indicated by brown triangles (▼). A negative value means that the two bands overlap but in different regions of the  $k$ -space.

The numerical muffin-tin approach was further used to investigate the local electronic properties of the honeycomb lattice by calculating the local density of states (LDOS) along connecting lattice site (Fig. S5), which is used to directly compare spatially-resolved STS measurements. On the bridge site of the honeycomb lattice (red), a sharp peak is visible (0.124 eV) which can be assigned to the  $p$ -flat band. Moving toward the lattice site, the flat band slowly vanishes, while the clear  $s$ -type Dirac cone remains

## V Investigating honeycomb semiconductors: Structural and electronic investigation of an engineered InGaAs honeycomb semiconductor

visible (0.106 eV). To underline, differential conductance maps are calculated in the energy region of the  $s$ -band and  $p$ -bands, showing the electron density at different sites. The electron probability pattern at the  $p$ -type flat band energy (0.124 eV) is remarkable, with a very high electron probability at the bridge sites that decreases towards the lattice site and vanishes at the lattice site. Although differential conductance maps measurements are not stable enough for these samples due to disorder in the structure and unit cell size, the calculated maps can be useful to compare with more disordered lattice, and to predict the effect onto the electronic structure.

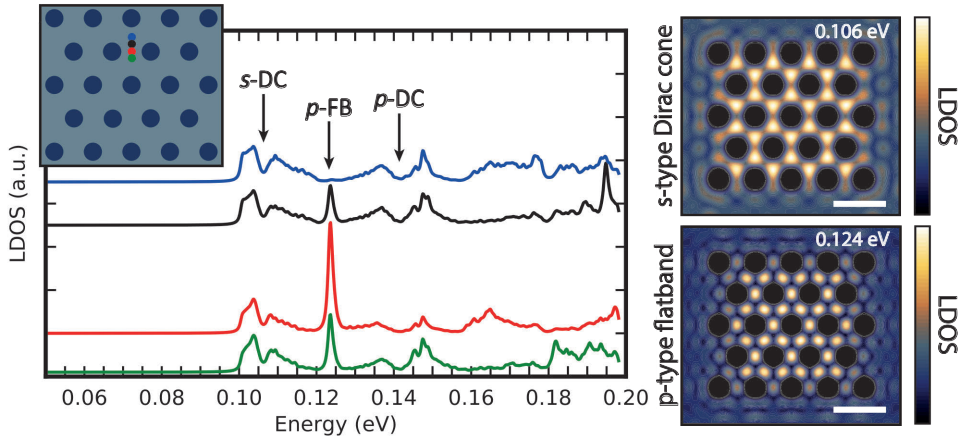


**Figure S5: Local electronic properties of a honeycomb semiconductor.** The LDOS was obtained using a numerical muffin-tin model for a triangular lattice of  $D = 36.0$  nm,  $d = 20.0$  nm and cylindrical potential barriers (dark blue). The local density of states was calculated on the lattice site of the honeycomb lattice (blue), bridge site (red) and intermediate sites (black and green). A 0.5 meV broadening has been taken into account. The reference of energy is the conduction-band minimum  $E_c$  of bulk InGaAs. On the right side, the distribution of the electron density was calculated for the lattice shown in the inset at energies corresponding to  $s$ -Dirac cone (0.106 eV) and the  $p$ -flat band (0.124 eV).

## Effective tight-binding model

An effective tight-binding model was also considered, giving us a tool to investigate which atomic site orbitals are involved in the formation of the electronic bands, and the influence of the coupling strength between orbitals on the electronic structure.

The lowest conduction mini-bands can be described using an effective tight-binding model in which each site of the honeycomb lattice formed by the triangular antidot lattice is described by one  $s$ - and three  $p$ -orbitals (see Fig. S6A). The Hamiltonian in this model is defined by six parameters: two on-site parameters  $E_s$  and  $E_p$ , and four hopping parameters  $V_{ss\sigma}$ ,  $V_{sp\sigma}$ ,  $V_{pp\sigma}$ ,  $V_{pp\pi}$ , notated similarly as in Ref. [37].  $V_{ss\sigma}$  denotes the interaction energy between the  $s$ -orbitals of two adjacent sites, the interaction energy between the  $s$ -orbital and the in-plane  $p_x$ - and  $p_y$ -orbital is denoted by  $V_{sp\sigma}$ , the interaction between both in-plane  $p$ -orbitals on neighboring sites is denoted by  $V_{pp\sigma}$ , and finally  $V_{pp\pi}$  denotes the interaction between the  $p_z$ -orbitals of adjacent sites. On-site orbitals at higher energies are neglected in this model, and only nearest-neighbor coupling is taken into account. Using these descriptions, the general tight-binding Hamiltonian can be written as:

$$\mathbf{H} = \begin{pmatrix} \mathbf{H}_1 & \mathbf{H}_2 \\ \mathbf{H}_2^\dagger & \mathbf{H}_1 \end{pmatrix} \quad (\text{V.5})$$

where  $\mathbf{H}_1$  and  $\mathbf{H}_2$  are defined as:

$$\mathbf{H}_1 = \begin{pmatrix} E_s & 0 & 0 \\ 0 & E_p & 0 \\ 0 & 0 & E_p \end{pmatrix}$$

$$\mathbf{H}_2 = \begin{pmatrix} V_{ss\sigma} \left( e^{\frac{ik_x}{\sqrt{3}}} + 2e^{-\frac{ik_x}{2\sqrt{3}}} \cos\left(\frac{k_y}{2}\right) \right) & V_{sp\sigma} \left( -e^{\frac{ik_x}{\sqrt{3}}} + e^{-\frac{ik_x}{2\sqrt{3}}} \cos\left(\frac{k_y}{2}\right) \right) & V_{sp\sigma} i\sqrt{3} e^{-\frac{ik_x}{2\sqrt{3}}} \sin\left(\frac{k_y}{2}\right) \\ V_{sp\sigma} \left( e^{\frac{ik_x}{\sqrt{3}}} - e^{-\frac{ik_x}{2\sqrt{3}}} \cos\left(\frac{k_y}{2}\right) \right) & -V_{pp\sigma} e^{\frac{ik_x}{\sqrt{3}}} - \left( \frac{V_{pp\sigma}}{2} - \frac{3V_{pp\pi}}{2} \right) e^{-\frac{ik_x}{2\sqrt{3}}} \cos\left(\frac{k_y}{2}\right) & -\left( V_{pp\sigma} + V_{pp\pi} \right) \frac{i\sqrt{3}}{2} e^{-\frac{ik_x}{2\sqrt{3}}} \sin\left(\frac{k_y}{2}\right) \\ -V_{sp\sigma} i\sqrt{3} e^{-\frac{ik_x}{2\sqrt{3}}} \sin\left(\frac{k_y}{2}\right) & -\left( V_{pp\sigma} + V_{pp\pi} \right) \frac{i\sqrt{3}}{2} e^{-\frac{ik_x}{2\sqrt{3}}} \sin\left(\frac{k_y}{2}\right) & V_{pp\pi} e^{\frac{ik_x}{\sqrt{3}}} - \left( \frac{3V_{pp\sigma}}{2} - \frac{V_{pp\pi}}{2} \right) e^{-\frac{ik_x}{2\sqrt{3}}} \cos\left(\frac{k_y}{2}\right) \end{pmatrix}$$

The tight-binding Hamiltonian can be calculated for different  $k_x$  and  $k_y$  values along the high-symmetry lines of the Brillouin zone of the honeycomb lattice. The energies can be obtained by calculating the eigenvalues of the obtained matrices and plotted along the high-symmetry lines.

The parameters of the effective tight-binding model are derived using numerical fits of the band structures calculated from the NP-MT model. Figure S6B-E presents band structure for the NP-MT model (blue) and the effective tight-binding model (red) for a triangular lattice with  $D = 36.0$  nm and varying geometrical ratios  $d/D$ . The following tight-binding parameter values were used for fitting the tight-binding model with the NP-MT model (the on-site parameters are in eV, the hopping parameters in meV):  $E_s = 0.10$ ,  $E_p = 0.13$ ,  $V_{ss\sigma} = -3.5$ ,  $V_{sp\sigma} = 6.1$ ,  $V_{pp\sigma} = 10.7$ ,  $V_{pp\pi} = -1.1$  when  $d/D = 0.46$ . For  $d/D = 0.58$ :  $E_s = 0.11$ ,  $E_p = 0.14$ ,  $V_{ss\sigma} = -2.8$ ,  $V_{sp\sigma} = 3.0$ ,  $V_{pp\sigma} = 13.1$ ,

## V Investigating honeycomb semiconductors: Structural and electronic investigation of an engineered InGaAs honeycomb semiconductor

$V_{pp\pi} = -0.3$ . For  $d/D = 0.69$ :  $E_s = 0.12$ ,  $E_p = 0.16$ ,  $V_{ss\sigma} = -1.9$ ,  $V_{sp\sigma} = 0.1$ ,  $V_{pp\sigma} = 13.1$ ,  $V_{pp\pi} = 0.1$ . The effective tight-binding model cannot address situations where  $d/D \rightarrow 0$  (e.g.,  $d/D = 0.06$ ), because the tight-binding method is on principle unsuitable for describing a two-dimensional free electron gas. The band structures show that the effective tight-binding model gives a very good description of the lowest bands in the  $s$ - and  $p$ -sectors for different values of  $d/D$ , indicated by the matching bands of both models. This is especially true for high  $d/D$  values. This can be explained by the fact that orbitals higher than the  $p$ -orbital are not included in the tight-binding model, but they are included in the NP-MT model. These orbitals still play an important role at low geometric ratios, but their effect on the  $s$ - and  $p$ -orbitals will diminish when the on-site energy separation between the  $s$ -orbital and  $p$ -orbital increases, when more pure  $s$ - and  $p$ -bands are obtained.

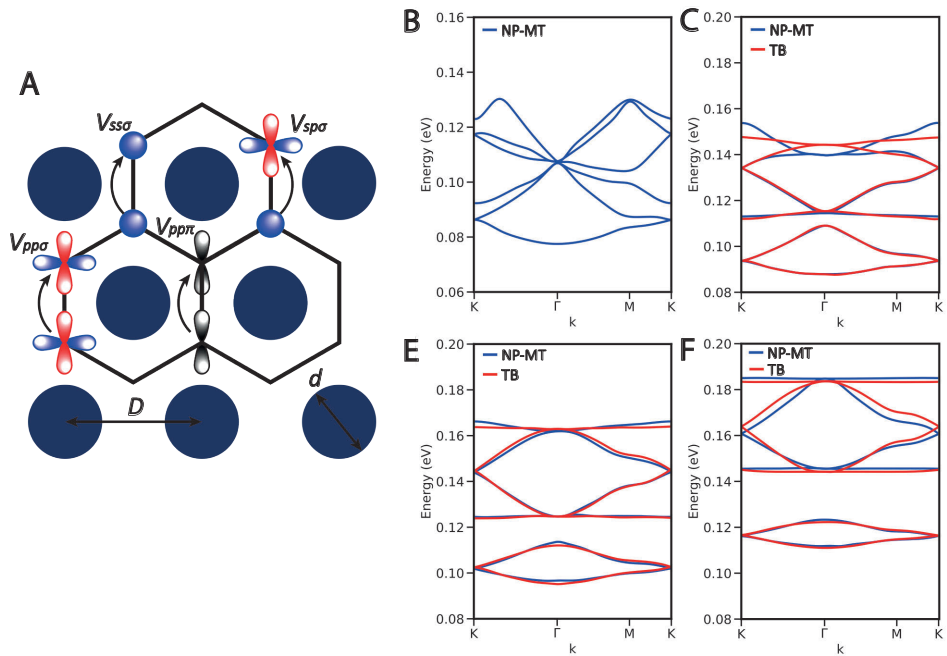


**Figure S6: Band structures comparing the effective tight-binding model and NP-EMA.** (A) Schematic presentation of the tight-binding model, showing how the honeycomb symmetry is formed which can be electronically described using a tight-binding model. (B-E) Calculated band structures with relative pore sizes of (B)  $d/D = 0.06$ , (C)  $d/D = 0.46$ , (D)  $d/D = 0.58$  and (E)  $d/D = 0.69$ . The blue curves show the bands calculated using NP-MT, red curves show calculated bands using the effective tight-binding model with one  $s$ - and three  $p$ -orbitals per site. The  $p_z$  orbital, placed at high energy, is not involved in the visible bands. The reference of energy is the conduction-band minimum  $E_c$  of bulk InGaAs.

The corresponding parameter values are presented in Fig. S7, showing how the tight-binding parameter change when increasing the geometric ratio. When  $d/D$  is large, the  $s$ - and  $p$ -sectors are well separated, since the  $s$ - $p$  hybridization is weak ( $V_{sp\sigma} \rightarrow 0$ ).

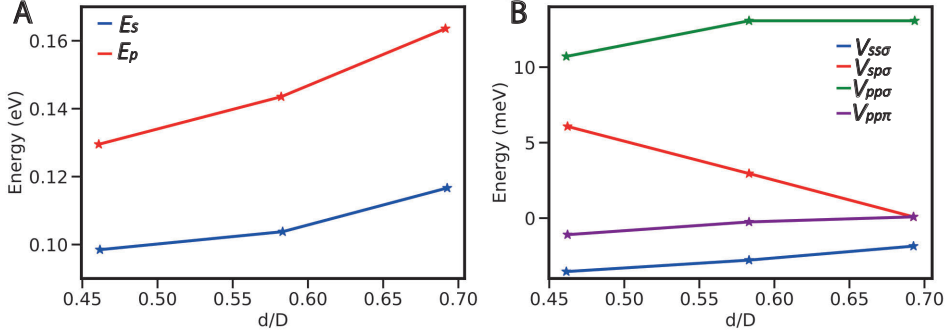


**Figure S7: Parameters of the effective tight-binding model.** (A) Obtained on-site parameters  $E_s$  and  $E_p$  by fitting the model to the NP-MT model, the reference of energy being the conduction-band minimum  $E_c$  of bulk InGaAs. (B) Obtained hopping parameters  $V_{ss\sigma}$  (+),  $V_{sp\sigma}$  (\*),  $V_{pp\sigma}$  (\*),  $V_{pp\pi}$  (□) from the fitting procedure.

On the opposite situation ( $d/D \rightarrow 0$ ),  $s$ - $p$  hybridization is strong, and we recover the situation of the free-electron gas. The gaps at  $\Gamma$  and  $M$  in the  $s$ -sector are of different nature. The gap at  $\Gamma$  increases when  $d/D \rightarrow 0$  because it comes from the folding of the free-electron parabola at the zone center [38]. On the contrary, the gap at  $M$  closes both when  $d/D \rightarrow 0$  and  $d/D \rightarrow 1$ , and presents a maximum in between. This results from opposite effects of  $V_{ss\sigma}$  and  $V_{sp\sigma}$  terms on the gap.

## Experimental conductance spectroscopy

To validate the experimental data in the main body of the chapter, more conductance measurements are presented on two different scanning tunneling microscopy machines with different settings. Results on both machines will be discussed here.

### High voltage sweeps differential-conductance spectra

At Utrecht University, STM experiments were performed in a low temperature, UHV ( $5 \times 10^{-11}$  Torr) Polar SPM system (Sigma Surface Science). STM measurements were performed at 5K with a Pt-Ir tip, which was prepared by cutting a Pt-Ir wire. Topographic STM images were usually acquired at feedback conditions of +1.3 V for the sample voltage and 100 pA for the setpoint current. Spatially-resolved tunneling spectroscopy were performed by starting with a feedback voltage of +1.3 V, and the voltage sweep limited between +1.3 and +0.7 V. The differential conductance was acquired with a lock-in amplifier using a bias modulation of 2 – 3 mV peak to peak at a frequency of 973 Hz. Tens of spectra were recorded, with a typical number of 801 data points per sweep with an acquisition time of 500 ms and a delay time of 100 ms, yielding a total sweep time of 8 min. During the data processing, spectra were averaged, and no background subtraction was performed.

Differential conductance spectra are presented in Fig. S8. Measurements were performed on different bridge sites  $B$  (green) and lattice sites  $L$  (red) of the honeycomb lattice. Measured area have micrometer distances between them. Desirable spots for measurements are marked which have the least amount of deformed and/or vacancy pores nearby. Prior to every differential conductance measurement, the tip is approach to the surface and stabilized for at least one hour.

Inspecting all the differential conductance spectra, two quantized states of the quantum well are clearly visible which are indicated by  $E_1$  and  $E_2$  in Fig. S8. These states were not visible in earlier measurements due to the lower bias voltage range. When looking more closely onto the first quantized state on both sites, Dirac features are more difficult to recognize compared to the measurements performed in Lille, which can also be assigned to the larger voltage sweep. Comparing differential conductance spectra with each other, some reassembles between bridge sites can be observed: a clear distinctive peak around 820 mV is observed on the bridge site at the start of the conduction band, which is absent on all lattice sites. Therefore, we attribute this peak to the dispersion less  $p$ -flat band, which is also located in a similar bias range measured in Lille (Fig. V.3 and Fig. S9). Changes in shape and position of the peak can be explained by disorder in the honeycomb symmetry or by defects in the surface.

Comparing the lattice sites with each other on the other hand, we do not observe any distinct Dirac features. Especially the  $s$ -bands, which should be located lower in energy compared to the  $p$ -like flat band, is not visible in the spectra on both sites. This can be explained by the lower sensitivity of the measured differential conductance spectra compared to the measurements performed in Lille, which is due to the larger bias

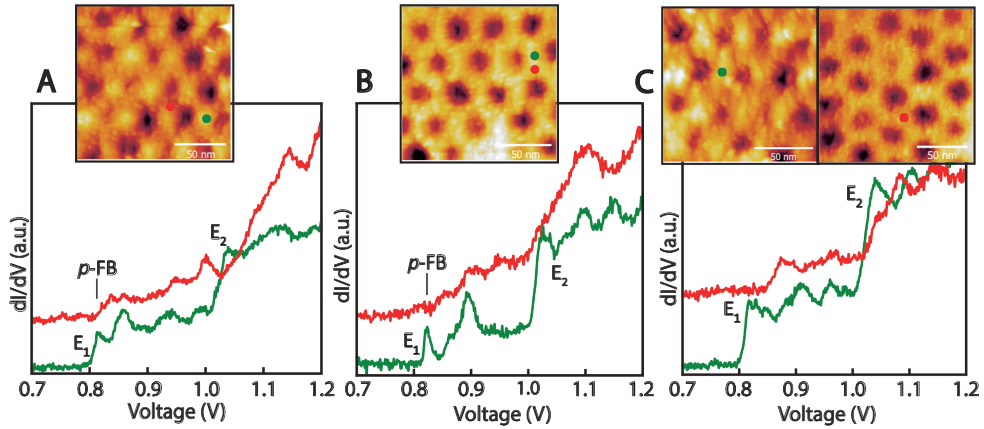


**Figure S8: Differential conductance spectroscopy performed in Utrecht.** Topographic and spectroscopic measurements at different lattice sites (red) and bridge sites (green) measured at the university of Utrecht. Feedback settings:  $V_s = +1.30$  V and  $I_{\text{setpoint}} = 100$  pA. The peak corresponding to the flat band and the individual quantized states of the QW are indicated by FB,  $E_1$  and  $E_2$  respectively.

voltage sweeping range. Also a longer acquisition time was needed for each individual spectra due to the larger bias voltage range, resulting in less spectra which could be used for averaging. We also note that the etching of the quantum well is more pronounced at the bridge site of the honeycomb lattice, increasing the transmission probability compared with lattice sites. This could also explain the more pronounced features on the bridge sites compared to the measurements of the lattice sites.

Looking at the second quantization step of all the bridge sites, we note that features can be observed which are somewhat symmetrical with the features on the first quantization step. This would be in agreement with calculations from the muffin-tin model presented in Chapter II and Fig. S4, showing a repetition of Dirac features in the second quantized state combined with higher-orbital physics from the first quantization step. Although we cannot assign features at higher bias directly to potential Dirac physics, the symmetrical agreement between the two quantized states is already remarkable.

## Low voltage sweep differential-conductance spectra

For the high-resolution differential-conductance measurements, STM experiments were performed in a low temperature (4.4 K), UHV ( $5 \times 10^{-11}$  Torr) STM (Omicron) at IEMN, Lille. STM measurements were performed at 5K with a tungsten tips prepared by an electrochemical etching and then cleaned by direct contact heating in UHV. Topographic STM images were usually acquired at feedback conditions of +2.0 V for the sample voltage and 20 pA for the setpoint current. Spatially-resolved tunneling spectroscopy were first acquired by reducing the sample bias to +1.3 V and by increasing the setpoint current to 100 pA. The position of the Fermi level with respect to the valence band was then determined by disabling the feedback and measuring sequences of I-V curves. For such measurements, a voltage ramp from positive to negative voltages and then a reverse ramp both with a total duration of 10 s were applied. In order to increase the energy resolution in the spectral range corresponding to the conduction band, the feedback voltage was reduced to +1.0 V or less and the voltage sweep limited between +0.5 and +1.0 V. The differential conductance was acquired with a lock-in amplifier, using a bias modulation of 2-3 mV peak to peak at a frequency of 490 Hz. Hundreds of spectra were recorded when the sweep time was limited to 20 s, averaging all spectra during the data processing. No background was subtracted from the spectra.

In Fig. S9, differential-conductance spectra obtained in Lille are presented. Zoomed-in spectra with high sensitivity and transmission probability are obtained, revealing low bias features in the electronic structure. First, spectroscopy is performed along two lattice ( $L$ ) sites, showing a distinctive peak at the bridge site ( $B$ ) at 810 mV (light blue) (Fig. S9B). The distinctive peak fades away when measuring away from the bridge site, and smaller peaks become more visible at lower bias voltages (785 mV). These features are very similar compared with the differential conductance spectra presented in the main body. It is also clear that the QW thickness at the bridge site  $B$  is much thinner compared to the thickness at the lattice site  $L$ . The spectra on the bridge and lattice site are also plotted in Fig. S9C, including spectra with increased sensitivity, enhancing the transmission probability. These spectra show two small peaks indicated by arrow, which can be attributed to the maximum LDOS at the  $M$  point for a  $s$ -orbital Dirac cone.

Differential conductance spectra across the bridge site  $B$  between two adjacent pores show how that the  $p$ -flat band peak slowly disappears when moving away from the bridge site towards a pore (Fig. S9D). On the edge of the pore (red), hardly any signal is observed, showing a low electron density. Finally, many different bridge site spectra were obtained over multiple unit cells of the honeycomb lattice, which are presented in Fig. S9F and G. Although shape and position of the  $p$ -flat band may vary between sites, the same distinct peak is observed, showing the resilience of the dispersion less band in the honeycomb lattice, while disorder in the honeycomb symmetry is clearly present. This will be further investigated in the following chapter.

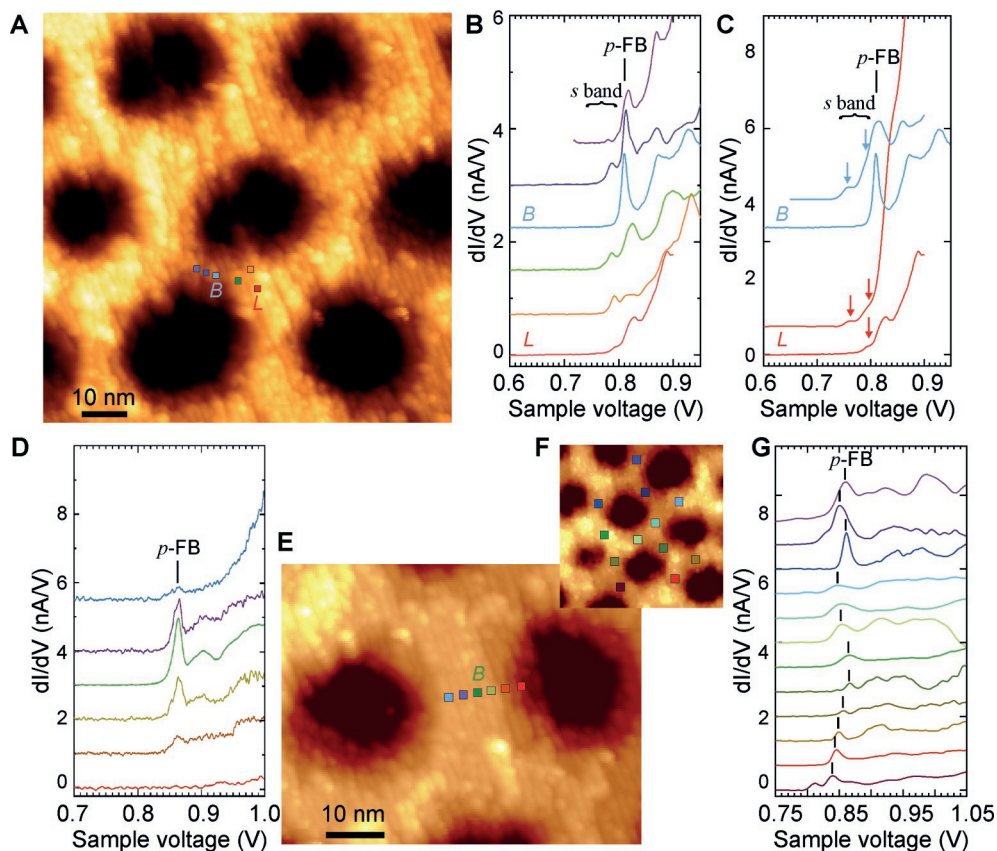


**Figure S9: Differential conductance spectroscopy performed at IEMN, Lille.** (A) Topographic and (B) spectroscopic measurements at varying positions along the connection bridging two lattice sites. The lattice site and bridge site are labelled *L* and *B* respectively. The vertical segment indicates the position of the *p*-flat band, whereas the bracket indicates the extent of the *s*-dispersive bands. All the spectra were acquired with a setpoint current of 250 pA and a duration of 7.3 s per voltage ramp. The feedback voltage was +1.0 V, except at the lattice site, where it was reduced to +0.9 V in order to slightly improve the sensitivity of the measurement. Indeed, based on the STM contrast, the lattice site is higher than the other locations. (C) In order to further increase the sensitivity of the measurements by enhancing the transmission probability across the tunneling barrier, the setpoint current was increased to 300 pA at the lattice site (upper red curve) or the sample bias was reduced to +0.9 V at the bridge site (upper blue curve). As a result, small peaks pointed by vertical arrow appear. (D) Spectroscopic and (E) topographic measurements at varying positions across a bridge site that separates two adjacent pores. The differential conductance spectra correspond to single *dI*-*dV* measurements, except for the spectrum acquired at the bridge site, which was obtained after averaging 250 traces. (F) Topographic and (G) spectroscopic measurements at different neighboring bridge sites. Feedback parameters for the spectroscopic measurements: Sample bias of +1.1 V and setpoint current of 150 pA. Spectroscopic measurements are obtained by averaging 250 spectra.

---

## References

- [1] Z. I. Alferov, “Nobel lecture: The double heterostructure concept and its applications in physics, electronics, and technology,” *International Journal of Modern Physics B*, vol. 16, pp. 647–675, feb 2002.
- [2] B. Sutherland, “Localization of electronic wave functions due to local topology,” *Physical Review B*, vol. 34, pp. 5208–5211, oct 1986.
- [3] M. Polini, F. Guinea, M. Lewenstein, H. C. Manoharan, and V. Pellegrini, “Artificial honeycomb lattices for electrons, atoms and photons,” *Nature Nanotechnology*, vol. 8, pp. 625–633, sep 2013.
- [4] D. Leykam, A. Andreanov, and S. Flach, “Artificial flat band systems: from lattice models to experiments,” *Advances in Physics: X*, vol. 3, p. 1473052, jan 2018.
- [5] E. Kalesaki, C. Delerue, C. Morais Smith, W. Beugeling, G. Allan, and D. Vanmaekelbergh, “Dirac cones, topological edge states, and nontrivial flat bands in two-dimensional semiconductors with a honeycomb nanogeometry,” *Physical Review X*, vol. 4, no. 1, pp. 1–12, 2014.
- [6] S. Wang, D. Scarabelli, L. Du, Y. Y. Kuznetsova, L. N. Pfeiffer, K. W. West, G. C. Gardner, M. J. Manfra, V. Pellegrini, S. J. Wind, and A. Pinczuk, “Observation of Dirac bands in artificial graphene in small-period nanopatterned GaAs quantum wells,” *Nature Nanotechnology*, vol. 13, pp. 29–33, jan 2018.
- [7] J. D. Bodyfelt, D. Leykam, C. Danieli, X. Yu, and S. Flach, “Flatbands under Correlated Perturbations,” *Physical Review Letters*, vol. 113, p. 236403, dec 2014.
- [8] E. Yablonoitch, “Inhibited Spontaneous Emission in Solid-State Physics and Electronics,” *Physical Review Letters*, vol. 58, pp. 2059–2062, may 1987.
- [9] S. Noda, “Full Three-Dimensional Photonic Bandgap Crystals at Near-Infrared Wavelengths,” *Science*, vol. 289, pp. 604–606, jul 2000.
- [10] M. Eichenfield, J. Chan, R. M. Camacho, K. J. Vahala, and O. Painter, “Optomechanical crystals,” *Nature*, vol. 462, no. 7269, pp. 78–82, 2009.
- [11] L. Tarruell, D. Greif, T. Uehlinger, G. Jotzu, and T. Esslinger, “Creating, moving and merging Dirac points with a Fermi gas in a tunable honeycomb lattice,” *Nature*, vol. 483, pp. 302–305, mar 2012.
- [12] D. Torrent and J. Sánchez-Dehesa, “Acoustic analogue of graphene: Observation of dirac cones in acoustic surface waves,” *Physical Review Letters*, vol. 108, no. 17, pp. 1–5, 2012.
- [13] T. Jacqmin, I. Carusotto, I. Sagnes, M. Abbarchi, D. D. Solnyshkov, G. Malpuech, E. Galopin, A. Lemaître, J. Bloch, and A. Amo, “Direct Observation of Dirac Cones and a Flatband in a Honeycomb Lattice for Polaritons,” *Physical Review Letters*, vol. 112, p. 116402, mar 2014.
- [14] K. K. Gomes, W. Mar, W. Ko, F. Guinea, and H. C. Manoharan, “Designer Dirac fermions and topological phases in molecular graphene,” *Nature*, vol. 483, pp. 306–310, mar 2012.
- [15] R. Drost, T. Ojanen, A. Harju, and P. Liljeroth, “Topological states in engineered atomic lattices,” *Nature Physics*, vol. 13, no. 7, pp. 668–671, 2017.
- [16] M. R. Slot, T. S. Gardenier, P. H. Jacobse, G. C. P. van Miert, S. N. Kempkes, S. J. M. Zevenhuizen, C. M. Smith, D. Vanmaekelbergh, and I. Swart, “Experimental realization and characterization of an electronic Lieb lattice,” *Nature Physics*, vol. 13, pp. 672–676, jul 2017.
- [17] M. Gibertini, A. Singha, V. Pellegrini, M. Polini, G. Vignale, A. Pinczuk, L. N. Pfeiffer, and K. W. West, “Engineering artificial graphene in a two-dimensional electron gas,” *Physical Review B - Condensed Matter and Materials Physics*, vol. 79, no. 24, pp. 8–11, 2009.
- [18] A. Tadjine, G. Allan, and C. Delerue, “From lattice Hamiltonians to tunable band structures by lithographic design,” *Physical Review B*, vol. 94, p. 075441, aug 2016.
- [19] L. Du, S. Wang, D. Scarabelli, L. N. Pfeiffer, K. W. West, S. Fallahi, G. C. Gardner, M. J. Manfra, V. Pellegrini, S. J. Wind, and A. Pinczuk, “Emerging many-body effects in semiconductor artificial graphene with low disorder,” *Nature Communications*, vol. 9, p. 3299, dec 2018.
- [20] D. Soriano, F. Ortman, and S. Roche, “Three-dimensional models of topological insulators: Engineering of Dirac cones and robustness of the spin texture,” *Physical Review Letters*, vol. 109, no. 26, pp. 1–5, 2012.
- [21] T. Bilitewski and R. Moessner, “Disordered flat bands on the kagome lattice,” *Physical Review B*, vol. 98, no. 23, pp. 1–6, 2018.

- 
- [22] C. Wu, D. Bergman, L. Balents, and S. Das Sarma, "Flat bands and wigner crystallization in the honeycomb optical lattice," *Physical Review Letters*, vol. 99, no. 7, pp. 1–4, 2007.
- [23] H. S. Suh, D. H. Kim, P. Moni, S. Xiong, L. E. Ocola, N. J. Zaluzec, K. K. Gleason, and P. F. Nealey, "Sub-10-nm patterning via directed self-assembly of block copolymer films with a vapour-phase deposited topcoat," *Nature Nanotechnology*, vol. 12, no. 6, pp. 575–581, 2017.
- [24] M. Fahed, L. Desplanque, D. Troadec, G. Patriarche, and X. Wallart, "Selective area heteroepitaxy of GaSb on GaAs (001) for in-plane InAs nanowire achievement," *Nanotechnology*, vol. 27, p. 505301, dec 2016.
- [25] T. Xu, K. A. Dick, S. Plissard, T. H. Nguyen, Y. Makoudi, M. Berthe, J. P. Nys, X. Wallart, B. Grandidier, and P. Caroff, "Faceting, composition and crystal phase evolution in IIIIV antimonide nanowire heterostructures revealed by combining microscopy techniques," *Nanotechnology*, vol. 23, no. 9, 2012.
- [26] N. A. Franchina Vergel, A. Tadjine, V. Notot, M. Mohr, A. Kouassi N'Guissan, C. Coinon, M. Berthe, L. Biadala, K. K. Sossoe, M. M. Dzaghi, J.-C. Girard, G. Rodary, L. Desplanque, R. Berndt, D. Stiévenard, X. Wallart, C. Delerue, and B. Grandidier, "Influence of doping level and surface states in tunneling spectroscopy of an  $\text{In}_{0.53}\text{Ga}_{0.47}\text{As}$  quantum well grown on p-type doped  $\text{InP}(001)$ ," *Physical Review Materials*, vol. 3, p. 094604, sep 2019.
- [27] J. Shen, D. L. Winn, W. Melitz, J. B. Clemens, and A. C. Kummel, "Real Space Surface Reconstructions of Decapped As-rich  $\text{In}_{0.53}\text{Ga}_{0.47}\text{As}(001)-(2\times 4)$ ," *ECS Transactions*, vol. 16, pp. 463–468, dec 2019.
- [28] L. C. Post, T. Xu, N. A. Franchina Vergel, A. Tadjine, Y. Lambert, F. Vaurette, D. Yarekha, L. Desplanque, D. Stiévenard, X. Wallart, B. Grandidier, C. Delerue, and D. Vanmaekelbergh, "Triangular nanoporation and band engineering of InGaAs quantum wells: a lithographic route toward Dirac cones in III–V semiconductors," *Nanotechnology*, vol. 30, p. 155301, apr 2019.
- [29] S. J. Pearton and F. Ren, "Science of dry etching of III-V materials," *Journal of Materials Science: Materials in Electronics*, vol. 5, pp. 1–12, feb 1994.
- [30] M. D. Pashley, K. W. Haberern, R. M. Feenstra, and P. D. Kirchner, "Different Fermi-level pinning behavior on n - and p -type GaAs(001)," *Physical Review B*, vol. 48, pp. 4612–4615, aug 1993.
- [31] T. S. Gardenier, J. J. van den Broeke, J. R. Moes, I. Swart, C. Delerue, M. R. Slot, C. M. Smith, and D. Vanmaekelbergh, "p Orbital Flat Band and Dirac Cone in the Electronic Honeycomb Lattice," *ACS Nano*, p. acsnano.0c05747, oct 2020.
- [32] M. B. Panish, R. A. Hamm, D. Ritter, H. S. Luftman, and C. M. Cotell, "Redistribution of beryllium in InP and  $\text{Ga}_{0.47}\text{In}_{0.53}\text{As}$  grown by hydride source molecular beam epitaxy and metalorganic molecular beam epitaxy," *Journal of Crystal Growth*, vol. 112, no. 2-3, pp. 343–353, 1991.
- [33] S. Koumetz, J. Marcon, K. Ketata, M. Ketata, C. Dubon-Chevallier, P. Launay, and J. L. Benchimol, "Be diffusion mechanisms in InGaAs during post-growth annealing," *Applied Physics Letters*, vol. 67, no. 1995, p. 2161, 1995.
- [34] Y. Niquet, C. Delerue, G. Allan, and M. Lannoo, "Method for tight-binding parametrization: Application to silicon nanostructures," *Physical Review B*, vol. 62, no. 8, pp. 5109–5116, 2000.
- [35] H. Ehrenreich, "Band structure and electron transport of GaAs," *Physical Review*, vol. 120, no. 6, pp. 1951–1963, 1960.
- [36] L. Wang, P. M. Asbeck, and Y. Taur, "Self-consistent 1-D Schrödinger-Poisson solver for III-V heterostructures accounting for conduction band non-parabolicity," *Solid-State Electronics*, vol. 54, no. 11, pp. 1257–1262, 2010.
- [37] J. C. Slater and G. F. Koster, "Simplified LCAO Method for the Periodic Potential Problem," *Physical Review*, vol. 94, pp. 1498–1524, jun 1954.
- [38] C. Delerue, "From semiconductor nanocrystals to artificial solids with dimensionality below two," *Phys. Chem. Chem. Phys.*, vol. 16, no. 47, pp. 25734–25740, 2014.
-



# Chapter VI

---

Investigation of the electronic effects of geometric disorder in a honeycomb semiconductor: from a local defect to a glassy system

**Based on:**

L.C. Post, C. Delerue, B. Grandidier, D. Vanmaekelbergh  
**Electronic investigation of geometric disorder in a honeycomb semiconductor: from a local defect to a glassy system**

*In preparation*

**In contrast to a perfect lattice, the structural analysis of the nanoporated QW reveals obvious modulations in the honeycomb geometry and semiconductor thickness. While a conical shape of the pores does not significantly affect the band structure [1], small changes in the dimensions of the patterned structure alter the vertical and lateral confinement of each lattice site and thus the  $s$ - and  $p$ -orbital on-site energies as well as the coupling between two adjacent sites [2, 3]. In this chapter, the electronic effects of the lateral- and vertical disorder will be investigated using two different models, namely a numerical muffin-tin model and an effective tight-binding model. First, the muffin-tin model is used to implement local perturbation to the lattice geometry, resulting in energy shifts and perturbation of the local density of states, but only to a distance of a few unit cells around the perturbations. Hence, we simulate a localised electronic defect. By analyzing STM images, lattices that are disordered over larger areas are investigated, showing that the density of states is more perturbed, although often with some resemblance of the density of states of the ideal lattice. Finally, an effective tight-binding model is used to approach the disorder problem by investigating the effect of spatial variation in the on-site energies and the coupling between two neighbouring lattice sites. Both models provide a density of states landscape that shows only qualitative agreement with the measurements. The disordered structure can be considered as a glassy version of a honeycomb semiconductor.**

## VI.1 Introduction

When disorder is implemented into a perfectly defined lattice, the electronic properties of the lattice will change. Imposing disorder onto a lattice can result in localization of the electronic wave functions, which is also called Anderson localization [4]. This can be understood by the interference of multiple wave paths of the electrons [5]. An other effect is the smoothening of Van Hove singularities [6] in the density of states of the disordered lattice, smearing out the electronic states over the energy [7]. Upon increasing the total number of defects and the randomness of the disorder, more complex effects can be observed, eventually resulting in complete localization of the electronic wave functions.

Disorder has also been studied in lattices of particles different from electrons, for instance in lattices of ultra-cold atoms [8, 9] and in photonic arrays [10]. It is especially interesting to investigate the effect of lattice disorder on the flat band of the system. Theoretical predictions argue that dispersionless bands are persistent to disorder and fluctuations in for example magnetic systems [11], and can even lead to new exciting physics phenomena such as flat band splitting [12, 13], leading to flat band ferromagnetism.

In this chapter, the electronic structure of a disordered honeycomb semiconductor will be investigated by distorting the triangular antidot lattice. For this, two different theoretical models will be used. First, a numerical muffin-tin model will be used to cal-

culate the electronic properties of a triangular array of pores with one perturbed pore. For reference, an unperturbed triangular antidot lattice is used (Fig. VI.1A), similar to the muffin-tin calculations in previous chapters. Two different types of disorder will be considered in the triangular lattice: a positional shift of the middle pore and a variation in the size of the middle pore. The direct effect on the honeycomb symmetry can be viewed in Fig. VI.1B-C.

Upon increasing the size of the middle pore (Fig. VI.1B) with a value  $\Delta_d$  to a new value  $d' = d + \Delta_d$ , the size of the red hexagon of the honeycomb lattice will increase. This makes the six lattice sites around the pore smaller, hence the on-site  $s$ - and  $p$ -orbitals increase in energy. Second, the increased radius also affects the interaction between these sites, and between these sites and nearest neighbour sites in a second shell.

An other method to distort the honeycomb lattice is to shift the position of the middle pore with a value  $\Delta_D$  (Fig. VI.1C), which will result in a distortion of the central (red) hexagon, affecting on-site energies of a number of lattice sites and coupling parameters. This will break the symmetry in the honeycomb lattice, affecting on-site energies, and the electronic coupling between the sites.

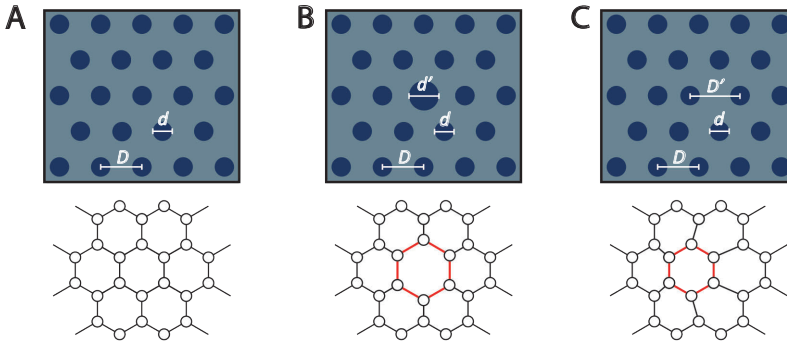


**Figure VI.1: Disordered honeycomb lattice using the muffin-tin model.** (A) Schematic view of the triangular antidot lattice (top) with pore-to-pore distance  $D$  and diameter  $d$ . This will result in an honeycomb lattice (bottom) without any disorder. (B) Schematic view of the triangular antidot lattice where the size of the middle pore is increased with a value  $\Delta_d$ , resulting in a local perturbed honeycomb lattice. (C) Schematic view of the triangular antidot lattice where the position of the middle pore is shifted to the left with a value  $\Delta_D$ , resulting in a local perturbed honeycomb lattice.

A more experimental approach to the numerical muffin-tin model can be achieved by converting a scanning tunneling microscopy (STM) topograph image into a two-dimensional potential landscape using a particle detection algorithm (Fig. VI.2). By assigning a repulsive potential to individual pixels inside the detected pores of the STM image, a potential landscape can be defined which can be implemented into the muffin-tin model. This will give us the opportunity to calculate directly the theoretical LDOS from a STM image for comparison with experimental observations. On top of

that, the local electronic properties of a disordered lattice can be investigated by calculating the LDOS on different sites and presenting the LDOS as a map of the squared wave-function. Experimentally, other forms of disorder in the honeycomb semiconductor could potentially arise from fluctuations in the quality of the semiconductor quantum well, such as variation in the surface chemistry due to the technological processes, disorder in the different layers of the quantum well or potential fluctuations caused by a random distribution of charged impurities and defects [14–17]. Although the main focus will be on the lattice disorder, imperfections in the quality of the honeycomb semiconductor will have a large effect on the local density of states. Also the shape of the pores in the antidot lattice can have an effect on the electronic structure, although it was already discussed in Chapter III that this effect is only minor [1].

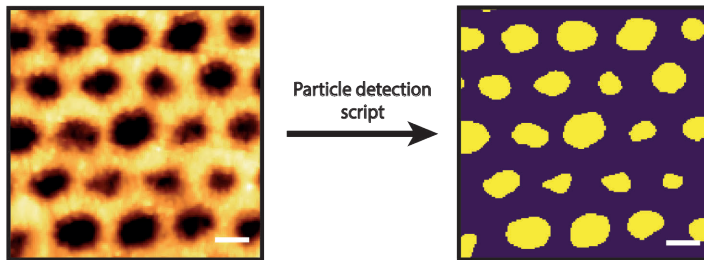


**Figure VI.2: Particle detection protocol onto a STM topograph image.** A STM topograph image is loaded in the script, detecting the pixels located inside the pores, creating a black-white image. This image is used as a potential landscape in the numerical muffin-tin model, being able to calculate its electronic structure. Scale bars in both images denote 30 nm.

---

Finally, a completely different approach will be used to interpret the disorder by using an effective tight-binding model. In this model, each site of the honeycomb lattice is described by one  $s$ - and three  $p$ -orbitals. By applying small energy fluctuations to the on-site energies of the honeycomb lattice, the disorder in the lattice can be mimicked. With this model, we obtained effects on the local density of states very similar as with the muffin-tin model.

### VI.2 Investigation of the electronic effects of a single local distortion of the honeycomb lattice

The effect onto the electronic structure when varying a single pore size of the triangular antidot lattice is presented in Fig. VI.3A. For the theoretical triangular antidot lattice, a pore-to-pore distance  $D = 36.0$  nm and a pore diameter of  $d = 20.0$  nm is used. The diameter  $d'$  is slowly increased in size by adding small values  $\Delta_d$  to the diameter of the middle pore. The LDOS is calculated on the lattice site and bridge site on multiple positions, starting adjacent to the distorted pore (red) and moving one period away (blue) and two periods away (green) from the distorted pore. The positions are also indicated in Fig. VI.3A. When the pore is not distorted ( $\Delta_d = 0$  nm), a clear  $s$ -like Dirac

cone (*s*-DC) is obtained on both the lattice site and bridge site on all positions, and a distinct *p*-like dispersion less band (*p*-FB) on the bridge site only, similar to earlier results. Upon adding a small distortion ( $\Delta_d = 2$  nm), no significant differences can be spotted in the LDOS of the lattice site and bridge site, independent of the position from the distorted pore. Further increase of the pore size will change the LDOS around the defect, disturbing the band structure and thus creating electronic defects with energy levels detached from the electronic band. On both the lattice and bridge site adjacent to the pore defect (Fig. VI.3B), features of a *s*-orbital Dirac cone are still visible with an increase of the peak intensity of the right M point. The energy width of the two M points decreases with increasing pore size, which can be explained by the increasing distance between the two adjacent lattice sites. It is also notable that the features of the original Dirac band structure seem to shift to higher energies, which can be explained by the direct increase of the pore size, increasing the confinement effect in the antidot lattice. Interestingly to note is that the peak dedicated to the *p*-like flat band remains visible even at relative high pore sizes, up to an increment of 8 nm. Above this value, the flat-band resonance splits into two separate peaks.

It is important to note that band structures only hold for periodic, non-perturbed lattices: this means that a local disturbance of the periodicity creates an electronic defect smeared out over different lattice and bridge sites. The calculated energy levels detach from the original band structure and localization, especially if the resulting energy is lower than that of the periodic ideal band structure. Locally, there are no *s*- and *p*-bands any more, but we end up with a collection of local *s*-like and *p*-like energy levels with similar features as for the ideal honeycomb band structure. However, if the energy deviations are very small, the energy levels can still more or less be seen as an element of the original band.

On the blue sites (Fig. VI.3C), an increase of the left peak (0.12 eV) at the M point of the Brillouin zone can be observed on the lattice site when increasing the pore size. The calculated LDOS on the blue lattice site also shows an increase between the two *s*-like states, extending the energy width to almost 20 meV. This effect occurs when two adjacent lattice sites get closer to each other, strengthening the coupling between both sites [18]. On the bridge site, the two M points of the *s*-like Dirac cone merge together into one broad *s*-like state, and the distinct peak of the *p*-like flat band decreases.

In general, the increase in pore size has less effect on the LDOS of the two green sites (Fig. VI.3D), which are the two sites furthest away from the distorted pore. This shows that the effect of the disorder on the electronic structure is very local. At the site of the distortion and just around it, energy levels are (slightly) detached from the bands, and thus form defect levels. Two lattice sites away from the distortion, the LDOS reflects the normal periodic dispersion of the bands, protected by the regular honeycomb structure.

LDOS wave-function maps are presented in Fig. VI.3E-F, which are calculated at the energy of the *s*-DC (0.124 eV) and *p*-FB (0.138 eV) of the unperturbed lattice. For the original honeycomb lattice, the maps show a high intensity on the lattice site and bridge around the *s*-like Dirac cone energy point, and high intensity on the bridge

VI Investigation of the electronic effects of geometric disorder in a honeycomb semiconductor: from a local defect to a glassy system

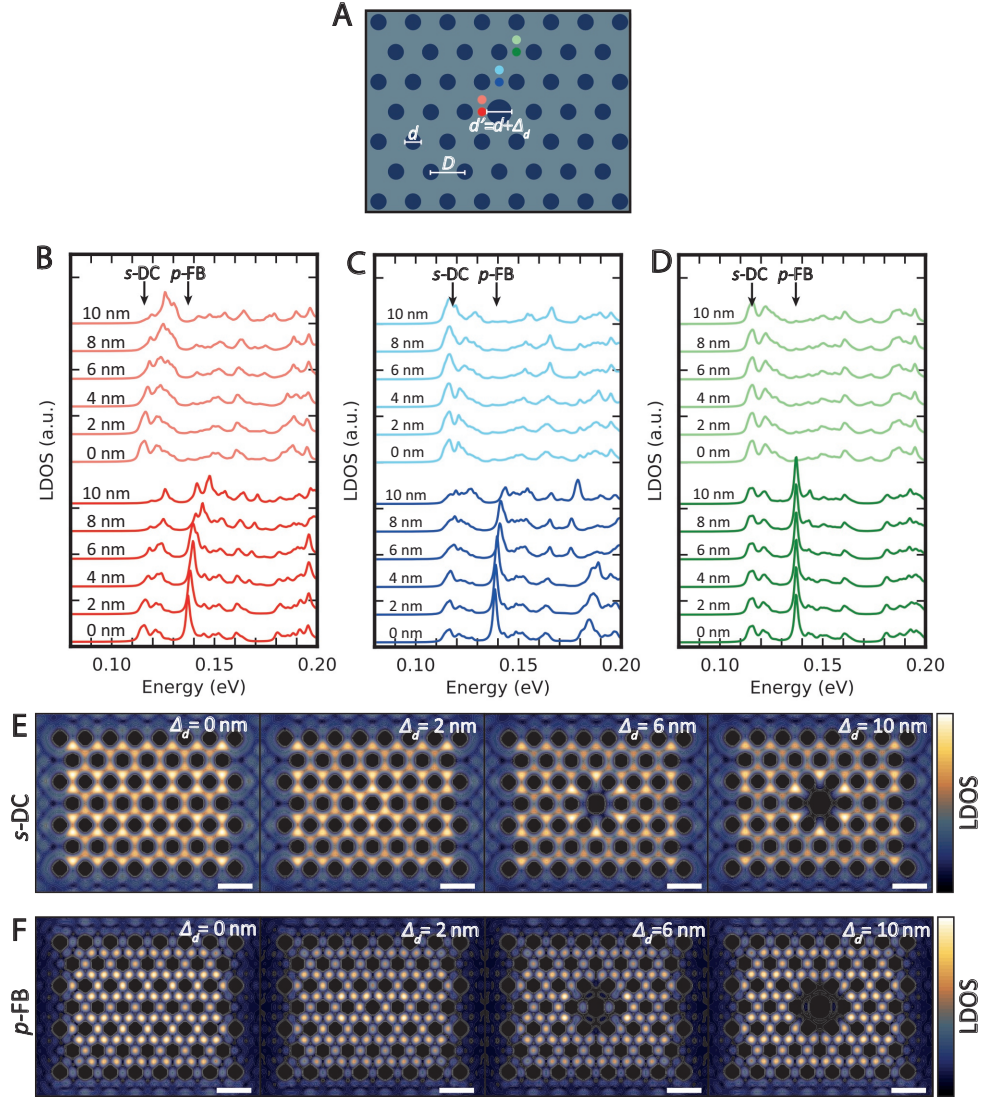


**Figure VI.3: Electronic properties of a triangular antidot lattice with an increased pore size.** (A) Schematic view of the disordered triangular antidot lattice. The diameter is slowly shifted from 0 to 10 nm with steps of 2 nm. (B-D) Simulated differential conductance spectra taken at the lattice site and bridge site on three different locations, ranging from more close to further away from the disordered pore. The locations of the  $s$ -like Dirac cone ( $s$ -DC) and  $p$ -like flat band ( $p$ -FB) of the unperturbed lattice are denoted in the spectra. For all calculated LDOS spectra, A Lorentzian broadening of 1 meV, and the reference of energy is the conduction-band minimum  $E_c$  of bulk InGaAs. (E-F) Simulated LDOS wave-function maps calculated around the original  $s$ -DC energy (0.117 eV) and  $p$ -like flat band energy (0.138 eV). The dark area highlight the extension of the local defect. Scale bars denote 50 nm.

site around the energy of the  $p$ -like flat band. Upon increasing the size of the middle pore, the electron density in the vicinity of the pore lowers at the normal band energy, because of the detachment of the energy level as a defect and the shift to higher energy, but remains in the rest of the lattice. This shows that disorder in the pore size only affects the electronic structure locally around the pore. Although the  $s$ - and  $p$ -levels shift in energy with respect to the original map, most features remain recognizable. These results indicate a similar local density of states, though locally shifted in energy, of the Dirac bands of the ideal system.

Next, the honeycomb lattice is distorted by shifting the position of the middle pore slowly to the left with step values  $\Delta_D$ , illustrated in Fig. VI.4. Again, the local electronic properties are calculated on multiple lattice and bridge sites of the honeycomb lattice with varying distances from the shifted pore. The LDOS on these sites are presented in Fig. VI.4B-D. Since the calculated spectra on the red sites are much closer when the middle pore is shifted, large changes to the electronic structure can be observed. On the bridge site, the  $p$ -like flat band located at 0.138 eV diminishes when moving the pore position more to the left. When the pore is shifted too much, the LDOS is calculated directly inside the shifted potential barrier, and no states can be observed at all. Looking at the red lattice site, features of the  $s$ -type Dirac cone shifts to higher energies due to the increase of confinement, and changes to one large distinct peak on the lattice site.

On the other side of the shifted pore (brown), less confinement is present, shifting the  $s$ -levels to lower energy. This is significantly visible for the bridge site. The original flat band features remain visible on the bridge site, showing a remarkable resilience toward the imposed disorder. Looking at positions further away from the shifted pore (blue and green), less impact is spotted when shifting the pore position, meaning that the effect on the electronic structure is again locally, roughly one or two periodicities away from the shifted pore. This is also observed in the LDOS wave-function maps, which are simulated with increasing shift in the pore position.

These calculations show that a local perturbation of the honeycomb symmetry has a local effect only on the electronic structure of the system. Features of the original, unperturbed density of states can shift in energy and shape, but are still recognizable as  $s$ - and  $p$ -states. The numerical muffin-tin model shows that shifting the periodicity of the lattice has more impact on the local density of states compared with an increase of the pore size. However, both types of disorder show that the feature originating from the  $p$ -like flat band remains present at large amount of disorder.

### VI.3 Fully disordered antidot lattices: a glassy version of the honeycomb semiconductor

Now that we understand how local disorder, i.e. by forming a defect state, in the honeycomb geometry will change the local electronic properties of the honeycomb semiconductor, more disordered and complex honeycomb lattices need to be simulated to

VI Investigation of the electronic effects of geometric disorder in a honeycomb semiconductor: from a local defect to a glassy system

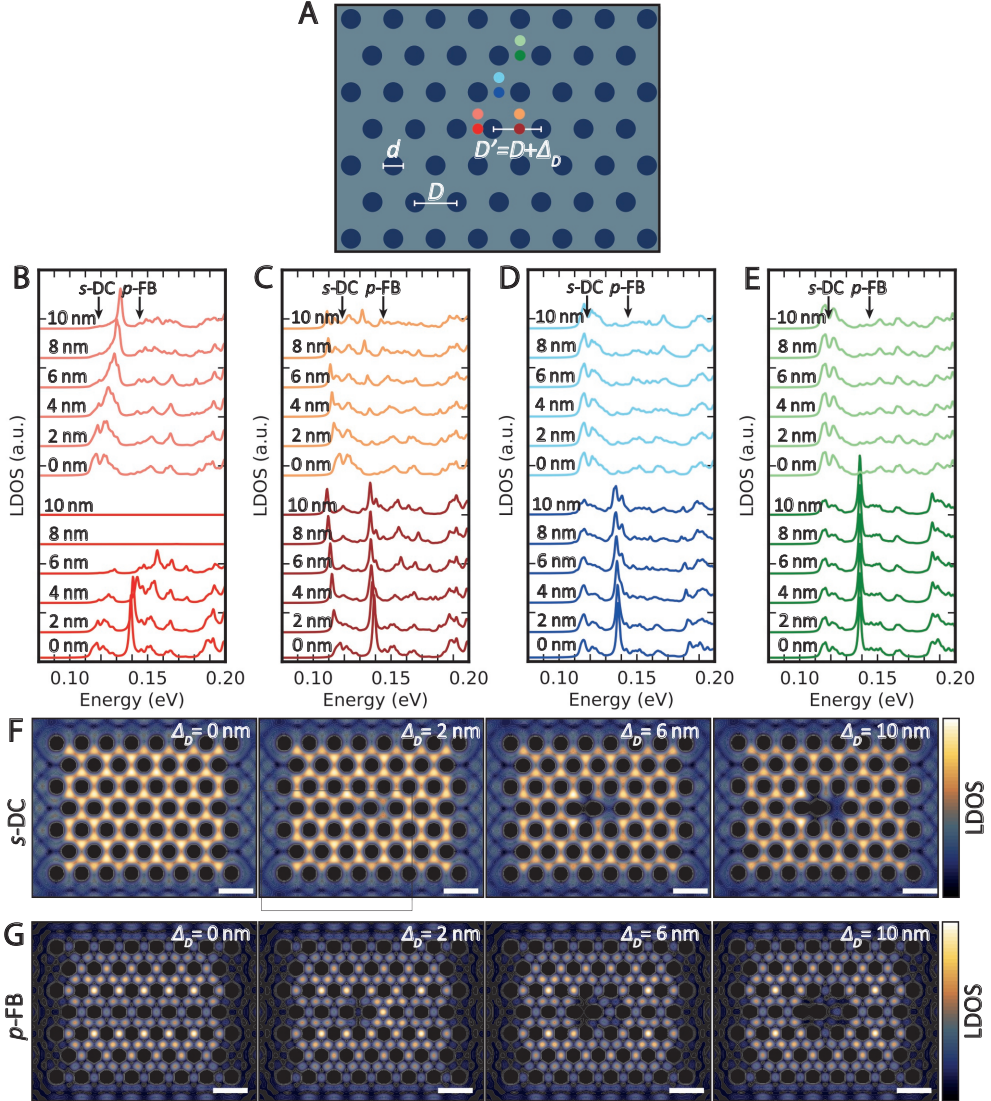


**Figure VI.4: Electronic properties of a triangular antidot lattice with a shifted pore position.** (A) Schematic view of the disordered simulated antidot lattice. Lattice parameters:  $D = 36.0$  nm,  $d = 20$  nm. The middle pore position is slowly shifted from 0 to 10 nm to the left with steps of 2 nm. (B-E) Simulated differential conductance spectra taken at the lattice site and bridge site of three different unit cells, ranging from more close to further away from the disordered pore. The suggested locations of the  $s$ -DC and  $p$ -FB are denoted in the spectra. For all calculated LDOS spectra, A Lorentzian broadening of 1 meV, and the reference of energy is the conduction-band minimum  $E_c$  of bulk InGaAs. (F-G) Simulated LDOS wave-function maps calculated around the  $s$ -like DC (0.117 eV) and  $p$ -like flat band (0.138 eV). The dark area highlight the extension of the local defect. Scale bars denotes 50 nm.

investigate the electronic properties, and argue if the features originating from the Dirac-like band structure survive the present disorder. For this, a scanning tunneling microscope (STM) topographic image of a lithographic designed InGaAs honeycomb semiconductor is analyzed using a particle detection script, which can be used to define the potential  $V(x, y)$  in the numerical muffin-tin model. Using this method, a direct comparison between experimental differential conductance spectra and simulated LDOS spectra can be made, and the validity of the model can be reviewed.

A STM image of an InGaAs honeycomb semiconductor is presented in Fig. VI.5A, accompanied with experimental differential conductance spectra on the lattice site (green), bridge site (black) and two intermediate sites (dark-red and red). Features of the local density of states of  $s$ - and  $p$ -bands are visible, with a distinct peak around 0.79 V on the bridge site which we can designate to the  $p$ -like flat band, indicated by  $p$ -FB. At lower energies, two small peaks are visible on the lattice site and intermediate sites, which indicated the presence of the  $s$ -bands, possible a Dirac cone. Also on the bridge sites, faint features can be observed since the left side of the distinct peak holds two tiny shoulders. However, these peaks are much weaker compared with the other sites. Also note that the energy width between the doublet peaks of the  $s$ -bands is about 20 meV, which is larger than the theoretically predicted value of 7 meV [1] for an ideal honeycomb lattice with a comparable dimension. This can be explained by a stronger  $s$ - $s$  nearest-neighbour coupling locally due to the present disorder in the honeycomb symmetry.

The calculated LDOS of the simulated lattice are presented in Fig. VI.5B, showing the lowest bands of the conduction band. The LDOS is computed on the indicated sites similar as the positions measured in the STM image, and the LDOS on the lattice and bridge sites of an ideal lattice is also shown for comparison. Looking at the calculated local density of states, features of  $s$ -states can be observed on the different sites, which is indicated by the position of a possible  $s$ -type Dirac cone ( $s$ -DC). Comparing with the LDOS of the ideal honeycomb lattice with a lower broadening, the overall energy position and shape are in agreement. Looking at the bridge site, the two possible  $s$ -states merge into one distinct peak, which is not visible in the experimental results.

When looking at possible higher energy states for the ideal lattice, a clear  $p$ -like flat band state is expected on the bridge site around 0.78 eV. This is also observed in the experimental results, but is not clear in the calculated local density of states, where the feature is much more broad. This broad feature is completely absent on the lattice site, which suggest that this feature is indeed a feature originating from the  $p$ -like flat band state. However, too many variation is present in the spectra to proof the real presence of Dirac-like states. Although resemblances between the calculated and experimental results can be observed, we conclude that it is hard to get a full grip on the measured electronic resonances from these spectra; this is very different from the control of a single defect in an otherwise periodic lattice environment. The calculated LDOS does show qualitative agreement with the experimental measurements.

LDOS wave-function maps are calculated using the electron wave functions at the  $s$ -DC energy and  $p$ -FB energy (Fig. VI.5C). Here, a drastic impact of disorder onto the local

## VI Investigation of the electronic effects of geometric disorder in a honeycomb semiconductor: from a local defect to a glassy system

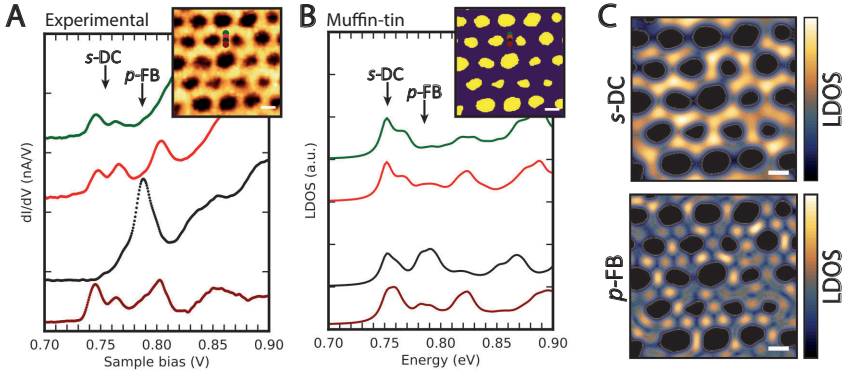


**Figure VI.5: Experimental and theoretical electronic structure of a disordered honeycomb semiconductor.** (A) Experimental conductance spectra acquired on the bridge site (black), lattice site (green) and two intermediate sites below (dark-red) and above (red) the bridge site of the nanoporated InGaAs honeycomb semiconductor. The exact locations of the acquired spectra are indicated in the STM image. The suggested locations of the *s*-like Dirac cone (*s*-DC) and *p*-like flat band (*p*-FB) are also denoted in the spectra. Imaging settings:  $I_{\text{setpoint}} = 20$  pA,  $V_s = 2.0$  V. Scale bar denotes 20 nm. (B) Local density of states calculations using the numerical muffin-tin model using the STM image acquired in (A). The sites of the calculated LDOS are indicated on the acquired image from the particle detection protocol. The calculated LDOS spectra are broadened using a Lorentzian broadening of 6 meV, matching the broadness of the peaks in the spectra with the broadness of the features observed experimentally. The LDOS of an ideal honeycomb lattice ( $D = 36.0$  nm,  $d = 20.0$  nm) on the bridge site (B-site) and lattice site (L-site) are also presented for direct comparison, using a broadening of 1 meV. The reference in energy for the calculated LDOS of both the disordered and ideal honeycomb lattice has been aligned with respect to the experimental Fermi level pinning, 160 meV above the top of the valence band. Scale bar in the simulated lattice denotes 20 nm. (C) LDOS wave-function maps simulated around the *s*-type Dirac cone and the *p*-type flatband energy using the acquired STM image. Scale bars denote 20 nm.

electronic structure can be observed over the whole simulated honeycomb lattice. Although strong fluctuation occur in the lattice, electron states are more present on most lattice sites around the ideal *s*-DC energy, while around the ideal *p*-FB energy, states are more distinct present on the bridge sites. This is again in qualitative agreement with the calculated wave-function maps for the ideal honeycomb lattice. Instead of an electronic lattice, the electronic states of an electronic glass are obtained, with some features present of possible Dirac-like states. Unfortunately, experimental differential conductance maps cannot be measured accurately on these samples due to the large number of defects still present in the surface of the QW, causing instability in the STM tip.

The variance of the local electronic structure of the honeycomb semiconductor is confirmed by performing the same analysis on different STM topograph images. In Fig. VI.6A, a STM image of the InGaAs honeycomb semiconductor is studied on a different area using the same particle detection method, and spectra on different lattice sites (Fig. VI.6C) and bridge sites (Fig. VI.6D) are simulated. A similar energy offset is used

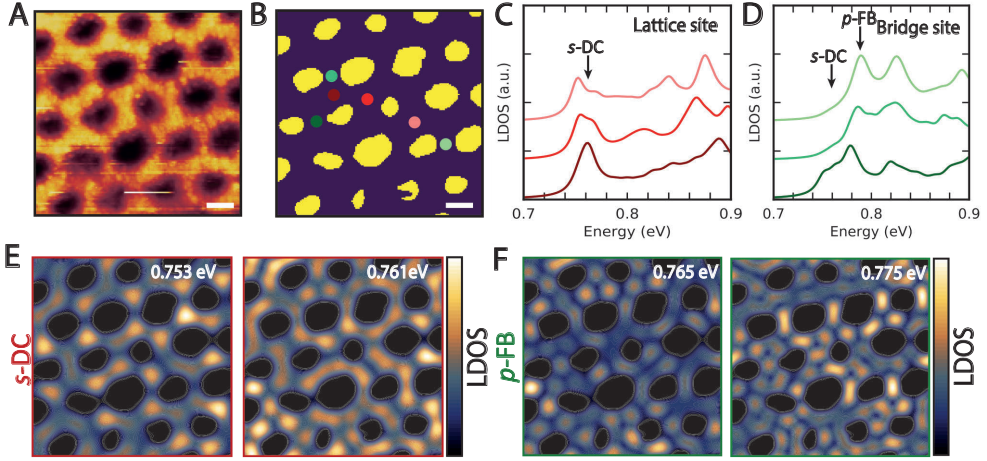


**Figure VI.6: Electronic structure of a fully disordered triangular antidot lattice.** (A) STM image of the honeycomb InGaAs heterostructure created using BCP lithography. Imaging settings:  $I_{\text{setpoint}} = 20$  pA,  $V_s = 2.0$  V. Scale bar denotes 20 nm. (B) Analyzed STM image using a particle detection script, detecting the pixel inside the pores (yellow) and outside the pores (purple). Scale bar denotes 20 nm. (C-D) Simulated local density of states calculated on various lattice sites (C) and bridge sites (D). The locations of the calculated spectra are indicated in (B). The calculated LDOS spectra are broadened using a Lorentzian broadening of 6 meV, matching the broadness of the peaks in the spectra with the broadness of the features observed experimentally. The reference in energy has been aligned with respect to the experimental Fermi level pinning, 160 meV above the top of the valence band. (E) Simulated LDOS wave-function maps calculated around the  $s$ -like DC, showing the variation of the  $s$ -bands. (F) Simulated LDOS wave-function maps calculated around the  $p$ -like FB, showing the variation of the  $p$ -bands on the bridge site in different unit cells.

as in the previous calculated LDOS, and a similar broadening parameter is used.

When looking at different lattice sites (red), a distinct peak is visible around 0.760 eV, which can be attributed to the  $s$ -type Dirac cone. The two peaks which signature the Dirac cone are broadened into one peak due to disorder and broadening. In all peaks, shoulders are still visible, which can vary in energy. Looking at higher energies, peaks show similar features, but are shifted due to the disorder. Looking at the different bridge sites (green), a distinct peak is visible at 0.780 eV, which is higher in energy than the  $s$ -like states. Therefore, this peak is assigned to the  $p$ -like flat band, which again can fluctuate in energy. Around the energy of the  $s$ -like states, small peaks are visible which are signatures of the  $s$ -like states.

Wave-function maps are calculated around the energies of the  $s$ -like states and  $p$ -like states. Although the visible states are not symmetrical in the lattice, again similar features are observed compared with wave-function maps of perfectly-ordered lattices. Around the  $s$ -like Dirac cone, higher intensity is normally observed on the lattice sites, while at energies of the  $p$ -like flat band, states at the bridge sites are encountered. Interesting to see is that  $s$ -states and  $p$ -states can be found at different energies on

different positions inside the honeycomb lattice, which can vary over energies of 10 meV. This especially shows that the effect of disorder is really local. In the framework of solid state physics, we can conclude that the geometrical disorder results in localised wave-functions and an energy distribution of the resonances comparable with that in an electronic glass.

## VI.4 Disordered tight-binding model

To support the results from the muffin-tin model, a like-wise disorder study is performed using a tight-binding model. Since the model is based on the interaction of individual electron wave functions, small energy fluctuations can be introduced directly into the model, simulating disorder in the system.

First, the tight-binding Hamiltonian of a honeycomb lattice is constructed. A Hamiltonian is constructed by using one  $s$ - and two  $p$ -orbitals for each honeycomb lattice site using periodic wave functions [19]. By solving the eigenvalues of this matrix, six bands of the band structure can be calculated for different  $k_x$  and  $k_y$  values along the high-symmetry lines of the Brillouin zone of the honeycomb lattice. The energies can be obtained by calculating the eigenvalues of the obtained matrices and plotted along the high-symmetry lines. The values of the parameters of the tight-binding Hamiltonian, defined by two on-site energies  $E_s$  and  $E_p$  and four nearest-neighbor hopping parameters  $V_{ss\sigma}$ ,  $V_{sp\sigma}$ ,  $V_{pp\sigma}$  and  $V_{pp\pi}$  [20] were derived by fitting band structures calculated from the muffin-tin model with varying geometric ratios  $d/D$  using the non-parabolic correction [21–23]. Using this procedure, values of the tight-binding parameters can be plotted as function of the geometric ratio  $d/D$  of the triangular antidot lattice, which is presented in Fig. VI.7. The tight-binding parameters are derived for a triangular antidot lattice with lattice parameters  $D = 35.2$  nm and varying diameters  $d$ .

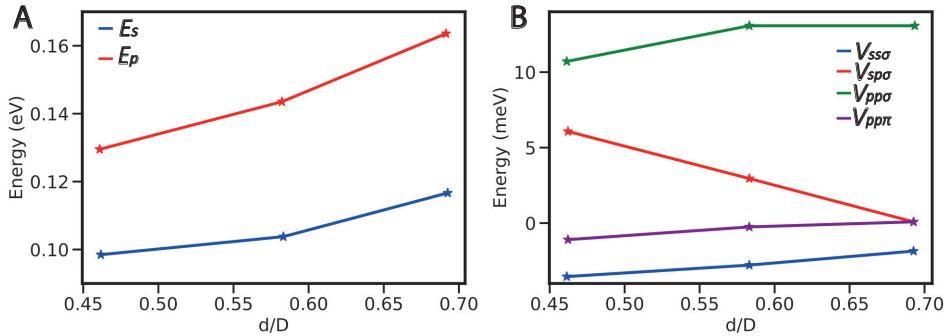


**Figure VI.7: Parameters of the honeycomb tight-binding model.** (A) Obtained on-site parameters  $E_s$  and  $E_p$  by fitting the tight-binding model to the non-parabolic muffin-tin model. (B) Obtained hopping parameters  $V_{ss\sigma}$  (+),  $V_{sp\sigma}$  (\*),  $V_{pp\sigma}$  (\*),  $V_{pp\pi}$  (□) from the fitting procedure with the muffin-tin model.

To introduce disorder to the tight-binding model, the tight-binding parameters of each

site can be slowly varied, resulting in different coupling strengths between sites of the honeycomb lattice. Using the diagrams presented in Fig. VI.7, an estimate of the energy perturbation can be derived in each parameter upon increasing or decreasing the size of the pore or the pore-to-pore distance. For example, an increase in the ratio  $d/D$  from 0.55 to 0.60 increases the  $s$  on-site energies by approximately 3 meV and reduces the hopping integral between the  $s$ - and  $p$ -orbitals by 1 meV. This shows that the on-site terms are much more sensitive to fluctuations in the ratio  $d/D$  than the hopping terms. The diagrams also show that the energy variations of the on-site terms are slightly smaller but comparable to the peak separation in the first doublet which is two times the interaction energy between adjacent  $s$ -orbitals. This means that the disorder is serious but will not completely cloud the intrinsic band features of the lattice.

Now that the amount of lattice disorder is linked to the energy fluctuation in the on-site and hopping parameters, it can be applied into the tight-binding model. As the on-site energies are more affected by the lattice disorder than the hopping terms, a random energy perturbation was added to the initial on-site parameters  $E_s^0$  and  $E_p^0$  of different sites  $i$ , while the hopping terms were kept constant:

$$\begin{aligned} E_s^i &= E_s^0 + \delta E \\ E_p^i &= E_p^0 + \delta E \end{aligned}$$

where  $\delta E$  are randomly drawn values between a certain amplitude. Here, an amplitude of 5 meV is used. All on-site parameters  $E_s^i$  and  $E_p^i$  of different sites  $i$  will have different values. By performing this procedure correctly, a truly disordered honeycomb lattice will be obtained, demonstrated in Fig. VI.8A.

Using an amplitude of  $\pm 5$  meV, a disordered lattice is simulated, and the LDOS spectra are calculated between two particular lattice sites presented in Fig. VI.8B. The spectra show that the applied disorder has only minor effects on the  $p$ -orbital flat band, while it has a more drastic effect on the peak doublet of the  $s$ -orbital Dirac cone. The on-site fluctuations pull the peaks in the first doublet (M-points of the  $s$ -band) further apart, adding 4 meV to their natural separation. The spectra also show the possibility of an increased intensity of the left peak, or the right peak, while a similar peak height is expected for a non-disordered honeycomb lattice, as can be shown in the black spectra indicated below the bridge site. Although the flat band is robust, splitting of the flat band is observed on the bridge site and intermediate site (red). All these effects on the  $p$ -orbital flat band and the  $s$ -orbital band are in line with the previous results obtained from the numerical muffin-tin model.

To check the consistency of these results, calculations for tens of different bridge sites were performed (Fig. VI.8C) on honeycomb lattices with different configurations. Eight random bridge site spectra are presented in Fig. VI.8C. The results show a substantial variation in the doublet peak shapes and peak separation for the dispersive bands, whereas the  $p$ -orbital flat band is generally preserved. Moreover, the simulated disorder shifts states of the dispersive  $p$ -band towards the  $p$ -FB. A spatial variation of 8 meV is observed in the energy position of the  $p$ -like flat band using this model, while the experimental fluctuation is around 19 meV which was discussed in Chapter V. We

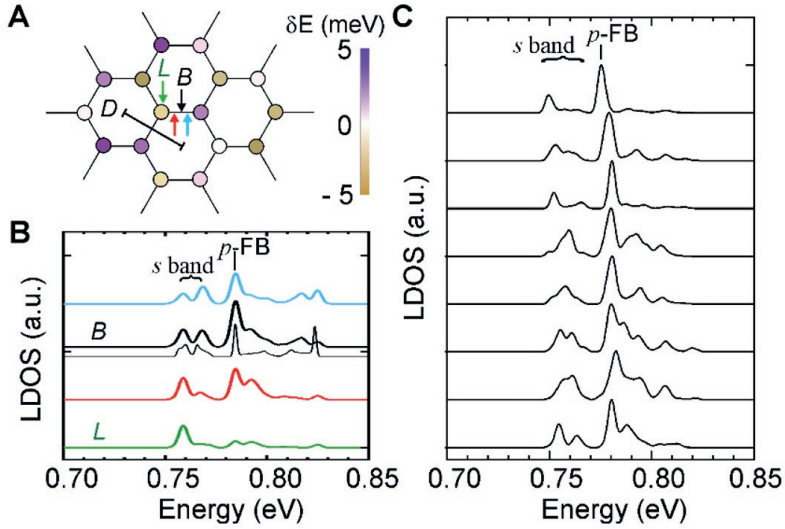


**Figure VI.8: Disorder study using the tight-binding model.** (A) Effective tight-binding model where each site of the lattice is described by one  $s$ - and two  $p$ -orbitals. On each site, a random potential perturbation  $\delta E$  is applied to the on-site energies  $E_s$  and  $E_p$ . (B) Local density of states calculated along the connection bridging two lattice sites at the positions marked with arrows in (A). The black thin curve, calculated at the bridge site in the absence of disorder, is used as a reference. The reference of energy is tuned to the measured value in the differential conductance spectra, which is the conduction-band minimum  $E_c$  of the InGaAs QW. (C) Representative LDOS calculated for eight different bridge sites among 422 sites, which show the robustness of the  $p$ -FB peak and the variability of the dispersive  $s$ -bands. In (B) and (C), the amplitude of  $\delta E$  is  $\pm 5$  meV. The reference in energy has been aligned with respect to the experimental Fermi level pinning, 160 meV above the top of the valence band. All the curves, except the reference one in (B), were convoluted with a Gaussian function to account for the bias modulation of 3 meV.

attribute this difference between simulations and experiment to small variations of the Fermi level pinning. Indeed, a variation in the position of the Fermi level induces a long-range potential shift, which is not included in the calculations.

Looking at the lower  $s$ -bands, a wide variation of shapes is observed. In some spectra, the first doublet gets further diverged from their original splitting. Other spectra show also merging of the two M-points of the Dirac cone, showing one broad peak. Lastly, some spectra show a more intense first peak, other spectra an increase second peak, breaking the symmetrical shape of the Dirac cone. Most critical is that the  $s$ -bands and  $p$ -bands remain separated from each other, meaning that the  $s$ -orbital Dirac cone remains isolated and is not mixed with higher-order states.

Further results on the consistency of the model and using different amplitude values can be found in the supplementary information. Also the effect on the local electronic structure from variation in the quantum well thickness can be found in the supplementary information.

## VI.5 Conclusions and outlook

To conclude, the effect of disorder onto the electronic structure of an honeycomb semiconductor has been studied using two different models. The numerical muffin-tin model was utilized to investigate the effect of a local defect in a periodic honeycomb lattice. On top of that, the model was adapted to directly analyze STM topograph images and to calculate the LDOS of fully disordered honeycomb lattices at various lattice sites, showing the resilience of the  $p$ -like flat band peak despite the fluctuation in shape and position of the  $s$ - and  $p$ -bands. A tight-binding model was introduced to explore the disorder effects as an analogy with the muffin-tin model. Comparing both the effective tight-binding model and the muffin-tin model, clear similarities can be observed in the calculated LDOS. Both calculations show the resilience of flat band despite the addition of the disorder, and a variation in shape and position the  $s$ -bands and  $p$ -bands is observed, which is in agreement with experimental results.



# Supplementary information

## Numerical muffin-tin model

The muffin-tin calculation is performed in Python. The model is solved numerically in the  $x$ - $y$  plane, and analytically in the  $z$  plane as explained in Chapter III. A non-parabolic correction was applied to the model to obtain more realistic energy values. In all muffin-tin models, a potential barrier height of  $V_0 = 5.0$  eV is incorporated in the calculation, using a sufficient height potential barrier to correctly simulate the empty pores. In all calculations, periodic boundary conditions were assumed in all simulated lattices to obtain realistic electron states around the edges of the simulated lattice.

## From STM topograph towards potential landscape

STM images were analyzed using an effective particle detection script, similar as described in chapter 3. Raw STM images were levelled using the three point leveling tool, and scars in the image were corrected using Gwyddion [24]. The obtained image is loaded in the particle detection script, which is performed in Python. The image are resized, and a threshold is applied to the image using the OpenCV package, detecting the pixels inside the pores. The same threshold value is used for all STM images. The obtained mask image is directly used as a two-dimensional potential landscape in the numerical muffin-tin model.

To all honeycomb lattice analyzed using the particle detection script, a potential barrier height of  $V_0 = 5.0$  eV is assigned to each detected yellow pixel inside the pores. A thin edge with no pores is simulated along the border the image in order to correctly apply periodic boundary conditions. Again, the model is solved numerically in the  $x$ - $y$  plane, and analytically in the  $z$  plane. A non-parabolic correction was applied to the model.

## Tight-binding model

In the tight-binding model, we have considered a finite sample of 477 sites in the form of a disk built from the honeycomb lattice (Fig. S1A). A Hamiltonian will be considered where each site of the honeycomb lattice is described by one  $s$ - and two  $p$ -orbitals

## VI Investigation of the electronic effects of geometric disorder in a honeycomb semiconductor: from a local defect to a glassy system

using periodic wave functions [19]. Using these descriptions, the general tight-binding Hamiltonian can be calculated and written as:

$$\mathbf{H} = \begin{pmatrix} \mathbf{H}_1 & \mathbf{H}_2 \\ \mathbf{H}_2^\dagger & \mathbf{H}_1 \end{pmatrix} \quad (\text{VI.1})$$

where  $\mathbf{H}_1$  and  $\mathbf{H}_2$  are defined as:

$$\mathbf{H}_1 = \begin{pmatrix} E_s & 0 & 0 \\ 0 & E_p & 0 \\ 0 & 0 & E_p \end{pmatrix}$$

$$\mathbf{H}_2 = \begin{pmatrix} V_{ss\sigma} \left( e^{\frac{ik_x}{\sqrt{3}}} + 2e^{-\frac{ik_x}{2\sqrt{3}}} \cos\left(\frac{k_y}{2}\right) \right) & V_{sp\sigma} \left( -e^{\frac{ik_x}{\sqrt{3}}} + e^{-\frac{ik_x}{2\sqrt{3}}} \cos\left(\frac{k_y}{2}\right) \right) & V_{sp\sigma} i\sqrt{3} e^{-\frac{ik_x}{2\sqrt{3}}} \sin\left(\frac{k_y}{2}\right) \\ V_{sp\sigma} \left( e^{\frac{ik_x}{\sqrt{3}}} - e^{-\frac{ik_x}{2\sqrt{3}}} \cos\left(\frac{k_y}{2}\right) \right) & -V_{pp\sigma} e^{\frac{ik_x}{\sqrt{3}}} - \left( \frac{V_{pp\sigma}}{2} - \frac{3V_{pp\pi}}{2} \right) e^{-\frac{ik_x}{2\sqrt{3}}} \cos\left(\frac{k_y}{2}\right) & -\left( V_{pp\sigma} + V_{pp\pi} \right) e^{\frac{ik_x}{\sqrt{3}}} e^{-\frac{ik_x}{2\sqrt{3}}} \sin\left(\frac{k_y}{2}\right) \\ -V_{sp\sigma} i\sqrt{3} e^{-\frac{ik_x}{2\sqrt{3}}} \sin\left(\frac{k_y}{2}\right) & -\left( V_{pp\sigma} + V_{pp\pi} \right) e^{\frac{ik_x}{\sqrt{3}}} e^{-\frac{ik_x}{2\sqrt{3}}} \sin\left(\frac{k_y}{2}\right) & V_{pp\pi} e^{\frac{ik_x}{\sqrt{3}}} - \left( \frac{3V_{pp\sigma}}{2} - \frac{V_{pp\pi}}{2} \right) e^{-\frac{ik_x}{2\sqrt{3}}} \cos\left(\frac{k_y}{2}\right) \end{pmatrix}$$

The parameters of the tight-binding Hamiltonian, defined by two on-site energies  $E_s$  and  $E_p$  and four nearest-neighbor hopping parameters  $V_{ss\sigma}$ ,  $V_{sp\sigma}$ ,  $V_{pp\sigma}$  and  $V_{pp\pi}$  [20] were derived by fitting band structures calculated from the muffin-tin model as discussed in the main body of the chapter. Higher order hopping terms, such as next-nearest-neighbor hopping, are neglected in the model.

### Adding disorder to the model

To introduce disorder in the honeycomb lattice, both on-site terms  $E_s$  and  $E_p$  for each lattice site are shifted with an energy shift  $\delta E$  in the intervals  $\left[ -\frac{\Delta E}{2}, \frac{\Delta E}{2} \right]$  (Fig. S1B). We consider a uniform distribution of the random variables in these intervals. Upon performing this procedure correctly, we end up with different on-site terms ( $E_s^1$ ,  $E_s^2$ ,  $E_p^1$  etc.) for each individual lattice site.

To estimate the amount of energy shift for each parameter due to lattice disorder, the tight-binding parameters are plotted as function of  $d/D$  of the triangular antidot lattice. Since the hopping parameters of the model hardly alter upon changing the ratio between the diameter of the pores, the nearest-neighbor hopping parameters  $V_{ss\sigma}$ ,  $V_{sp\sigma}$ ,  $V_{pp\sigma}$  and  $V_{pp\pi}$  were remain constant.

Using this estimation method, energy perturbations can also be derived when investigation variation in the quantum well thickness. Based on height profiles acquired from STM images from Chapter V, various thickness in the quantum well can be observed, which also can cause energy perturbations in the electronic structure. Since the  $z$ -direction can be solved analytically, the energy perturbation can be directly calculated by changing the thickness  $t$  of the quantum well with a value of  $\delta t$ :

$$\Delta E_v = E_t - E_{t-\delta t} = \frac{\hbar^2 \pi^2}{2m^*} \left( \frac{1}{t^2} - \frac{1}{(t-\delta t)^2} \right) \approx \frac{\hbar^2 \pi^2}{m^*} \left( \frac{\delta t}{t(t-\delta t)^2} \right) \quad (\text{VI.2})$$

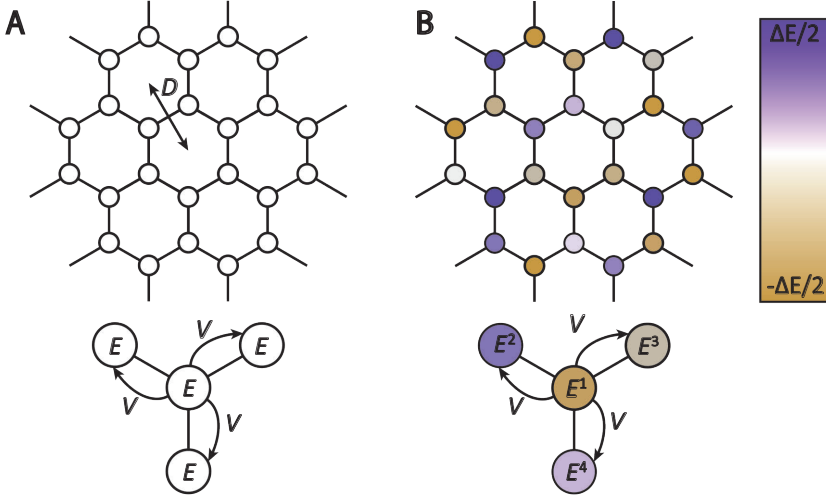


**Figure S1: Tight-binding model for the disordered honeycomb lattice.** (A) General model of the honeycomb lattice used for the tight-binding model (top), which is described by the general on-site parameters  $E$  ( $E_s$  and  $E_p$  for the  $s$ -orbital and  $p$ -orbital respectively) and the hopping parameters  $V$  ( $V_{ss\sigma}$ ,  $V_{sp\sigma}$ ,  $V_{pp\sigma}$  and  $V_{pp\pi}$ ). (B) General model of the disordered honeycomb lattice used for the tight-binding model (top), where all individual on-site parameters are shifted with a random value, ending up with different on-site terms  $E_s^1$ ,  $E_s^2$ ,  $E_p^1$  etc.

which holds for small values of  $\delta t$  and was evaluated for the lowest  $s$ -state ( $n = 1$ ). As an example, a thickness reduction of one bilayer ( $\delta t = 0.29$  nm) from an InGaAs quantum well with thickness  $t = 10$  nm yields an increase of the confinement of  $\Delta E_v = 5.6$  meV. This value will only increase further when increasing to higher states for the vertical confinement.

## Disordered tight-binding model

Now that the size of the energy perturbation is roughly estimated for both the lattice disorder as the in-plane disorder, both parameters can be implemented in the tight-binding model. As an extension of the previous model, we now choose on-site energy shifts  $\delta E_v$  and  $\delta E_h$  in the intervals  $\left[-\frac{\Delta E_v}{2}, \frac{\Delta E_v}{2}\right]$  and  $\left[-\frac{\Delta E_h}{2}, \frac{\Delta E_h}{2}\right]$ , respectively. We consider a uniform distribution of the random variables in these intervals. Using this method, the model does not show differences electronically between lattice disorder and in-plane disorder, but solely the amount of disorder expressed in an energy fluctuation. Again, since the hopping terms of the model are significantly less affected than the on-site terms, only disorder effects induced by the variations of  $E_s$  and  $E_p$  is investigated. The on-site energies are re-written as

$$\begin{aligned} E_s &= E_s^0 + \delta E_v + \delta E_h \\ E_p &= E_p^0 + \delta E_v + 2\delta E_h \end{aligned}$$

where  $\delta E_v$  ( $\delta E_h$ ) is a random energy shift due to vertical (horizontal, or in-plane) disorder. In the equation, we also take into account that  $E_p$  varies two times faster

with the geometrical factor  $d/D$  compared with  $E_s$ , observed from the diagram in Fig. VI.7A. This will result in an additional factor two. The vertical disorder  $\delta E_v$  comes from variations in thickness of the semiconductor film that results from the etching process. Keep in mind that the on-site energy terms  $E_s$  and  $E_p$  describe the lowest states of the honeycomb geometry, which is combined with the  $s$ -state of the in-plane confinement only. Since the disorder investigation is only performed at the lowest energy states, higher-order states in the in-plane confinement is not taken into account

With this model, a finite honeycomb lattice is simulated with varying on-site energy terms. Typical spectra of the LDOS are presented in Fig. S2 on ten random bridge sites of the lattice with varying amount of energy fluctuations. In each diagram, the red spectra shows the LDOS for the unperturbed honeycomb lattice. As reference energy, the conduction-band minimum  $E_c$  of bulk InGaAs is used. A broadening function with an energy broadening of 1 meV is used for this model.

For  $\Delta E_v = \Delta E_h = 1$  meV (Fig. S2A), the LDOS on all bridge sites do not differ substantially from the LDOS calculated in absence of disorder since the energy fluctuations is still low. The lowest peaks between 0.09 and 0.11 eV correspond to the  $\pi$ -like  $s$ -bands. The LDOS is vanishing at the Dirac point and has a V shape in its vicinity. The most visible peak, higher in energy (0.123 eV), is attributed to the  $p$ -like flat band. Above, the less visible and broader peaks are attributed to the  $\pi$ -like  $p$ -bands characterized by a second Dirac cone (0.144 eV).

By increasing the disorder all the way up to  $\Delta E_v = \Delta E_h = 6$  meV, the broad peaks related to the  $\pi$ -like  $s$ - and  $p$ -bands deform, new peaks appear and there are increasing variations of the spectra from site-to-site, similar as observed in measured differential conductance spectra. Remarkably, the main peak coming from the  $p$ -type flat band is very resilient to the disorder compared to the other peaks. For example, for  $\Delta E_v = \Delta E_h = 4$  meV, the flat band peak remains visible on the 10 sites that we have selected, whereas the peaks arising from  $s$ -bands exhibit important variations.

The resilience of the flat-band peak to disorder can be understood as follows:

- First, the flat band is relatively well separated from the other band in energy. For moderate disorder, the coupling and mixing to other bands remains weak.
- Second, the flat band is composed of a large number of degenerate states which can be as linear superposition of Wannier-like localized states. There exists one localized state per hexagonal plaquette and its configuration in terms of  $p$ -orbitals is shown in Fig. S3A [25]. Coupling between localized states induced by disorder is only possible between states that share a common bond, on neighbor hexagons.
- Third, any asymmetry between the two sub-lattices that form the honeycomb lattice deforms the dispersive  $\pi$ -like  $s$ - and  $p$ -bands but has no effect on the flat  $p$ -bands. The honeycomb lattice is characterized by two sites (A and B) per unit cell. The sites of sub-lattice A are only connected to sites of sub-lattice B (chiral

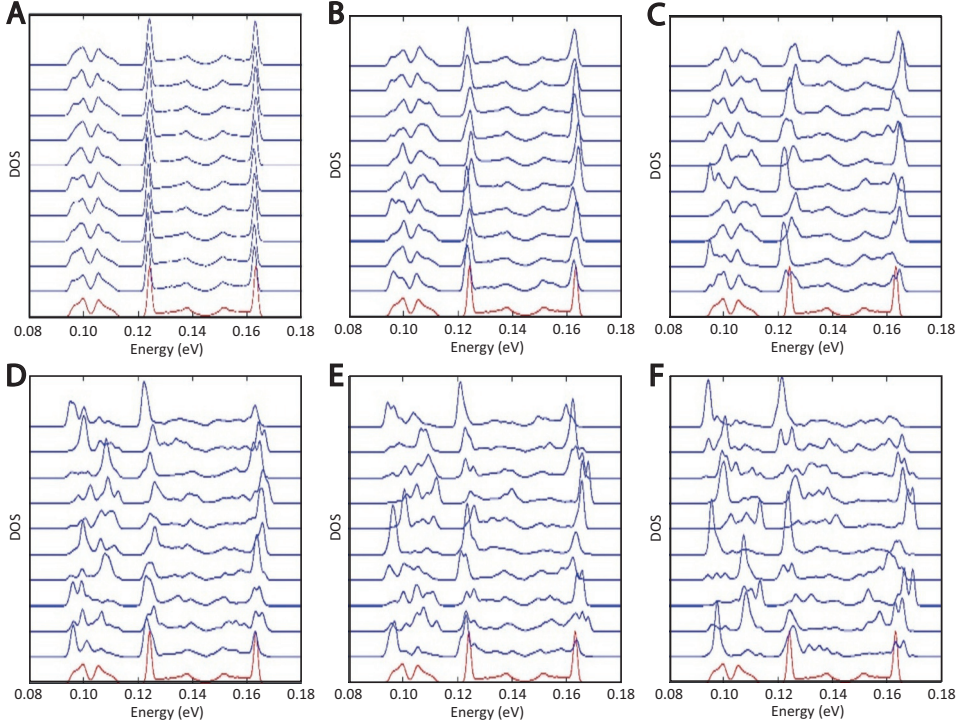


**Figure S2: DOS of disordered honeycomb lattices.** LDOS on 10 different bridge sites of the disordered honeycomb lattice sample. From top-left to bottom-right, an energy fluctuation of  $\Delta E_v = \Delta E_h = 1, 2, 3, 4, 5, 6$  meV. The red curve is the LDOS in absence of disorder, shown as reference. The reference of energy is the conduction-band minimum  $E_c$  of bulk InGaAs.

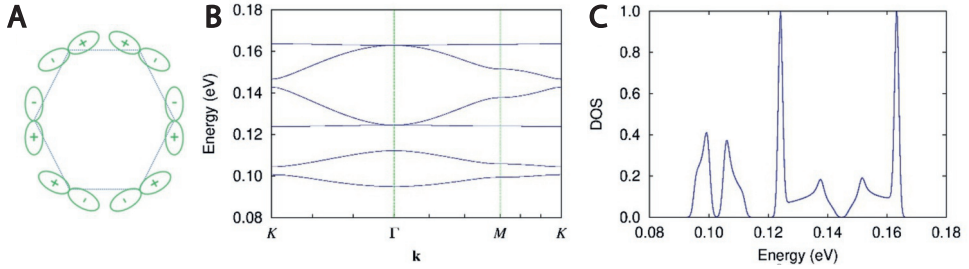


**Figure S3: DOS of disordered honeycomb lattices.** (A) Eigenstate for the lowest flat band localized on one hexagon of the honeycomb lattice. (B) Band structure of the asymmetric honeycomb lattice. (C) DOS corresponding to this band structure. The reference of energy is the conduction-band minimum  $E_c$  of bulk InGaAs.

symmetry) but they are equivalent in graphene-like lattices :  $E_s^A = E_s^B, E_p^A = E_p^B$ . It is interesting to consider the case where sub-lattices A and B are not equivalent (asymmetric lattice). We have calculated the band structure using the effective tight-binding model in which we set:  $E_s^A \rightarrow E_s^A + \Delta, E_s^B \rightarrow E_s^B - \Delta, E_p^A \rightarrow E_p^A +$

## VI Investigation of the electronic effects of geometric disorder in a honeycomb semiconductor: from a local defect to a glassy system

---

$\Delta, E_p^B \rightarrow E_p^B - \Delta$ . Fig. S3B shows this band structure for  $\Delta = 2$  meV. Gaps open at Dirac cones but flat bands remain flat (maintaining a weak  $s$ - $p$  hybridization). In other words, flat bands are resilient to sub-lattice asymmetry.

To investigate the direct effect of disorder onto individual lattice site, modulated LDOS spectra are presented in Fig. S4 on different sites of the honeycomb lattice with increasing energy perturbation. All spectra are calculated using the same pattern of disorder as indicated in Fig. S4A, but its amplitude is tuned by a uniform factor on the whole sample. On every site, the lowest plot shows the unperturbed LDOS, which is multiplied up to seven times towards the highest plot. Site 1 to 10, as indicated in Fig. S4A, is plotted in Fig. S4B-K. In this way, the effect of the disorder can be followed on each individual site.

Looking first at the lower  $s$ -orbitals, drastic changes can be observed in the height of both M peaks, around 0.10 eV. A few sites show an increase in peak height of the left M peak (e.g. on sites 1, 4 or 7), other sites show an increase of the right M peak (sites 2, 8 or 10). Some sites even show splitting of the M peaks, completely destroying the Dirac point of the lattice. In many cases, the flat-band peak is more robust to disorder than the other peaks. Even if at high disorder potential, it tends to split in two peaks [12]. When the on-site potential (energy) is strongly positive (e.g., on sites 2, 3 or 6), the flat-band peak tends to shift to higher energy at increasing potential strength. Other interesting point is the robustness of the  $p$ -like Dirac cone (0.145 eV) and the higher  $p$ -like flat band (0.16 eV), showing that all  $p$ -bands in the honeycomb lattice are more resilient to disorder in the lattice.

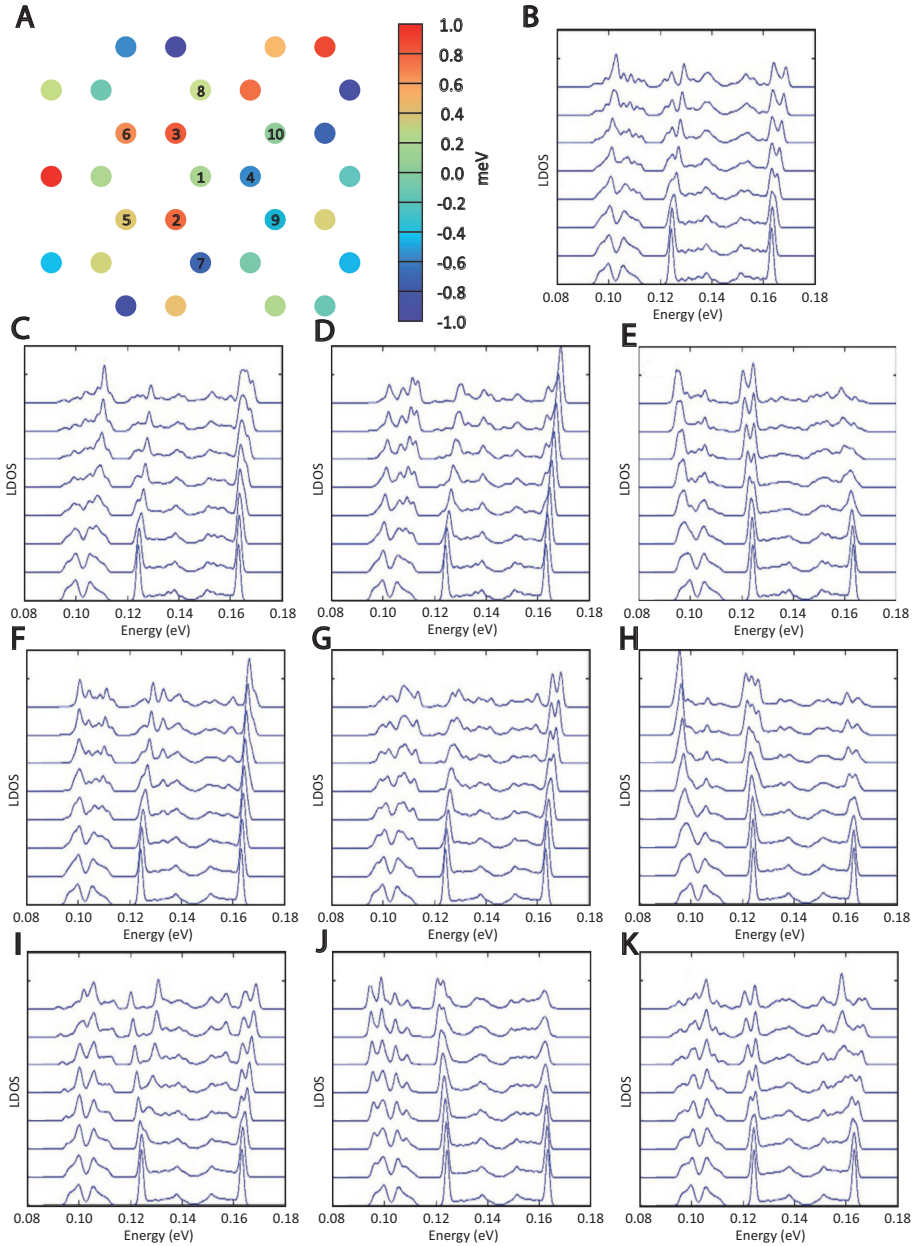


**Figure S4: LDOS of locally disordered honeycomb lattices** (A) Top, left: Region of a disordered honeycomb lattice. On each site, the potential  $\delta E_v + \delta E_h$  chosen at random ( $\Delta E_v = \Delta E_h = 1$  meV) is visualized by its color (color scale from -1 to +1 meV). (B-K) The LDOS on sites from 1 to 10 as illustrated in (A). In each figure, the LDOS is always calculated using the same disorder potential landscape but its amplitude is tuned uniformly by an integer factor varying from 0 (no disorder) to 7 (strong disorder).

---

## References

- [1] L. C. Post, T. Xu, N. A. Franchina Vergel, A. Tadjine, Y. Lambert, F. Vaurette, D. Yarekha, L. Desplanque, D. Stiévenard, X. Wallart, B. Grandidier, C. Delerue, and D. Vanmaekelbergh, "Triangular nanoporation and band engineering of InGaAs quantum wells: a lithographic route toward Dirac cones in III–V semiconductors," *Nanotechnology*, vol. 30, p. 155301, apr 2019.
- [2] C. Delerue, "From semiconductor nanocrystals to artificial solids with dimensionality below two," *Phys. Chem. Chem. Phys.*, vol. 16, no. 47, pp. 25734–25740, 2014.
- [3] A. Tadjine, G. Allan, and C. Delerue, "From lattice Hamiltonians to tunable band structures by lithographic design," *Physical Review B*, vol. 94, p. 075441, aug 2016.
- [4] P. W. Anderson, "Absence of diffusion in certain random lattices," *Physical Review*, vol. 109, no. 5, pp. 1492–1505, 1958.
- [5] J. Billy, V. Josse, Z. Zuo, A. Bernard, B. Hambrecht, P. Lugan, D. Clément, L. Sanchez-Palencia, P. Bouyer, and A. Aspect, "Direct observation of Anderson localization of matter waves in a controlled disorder," *Nature*, vol. 453, no. 7197, pp. 891–894, 2008.
- [6] L. Van Hove, "The occurrence of singularities in the elastic frequency distribution of a crystal," *Physical Review*, vol. 89, no. 6, pp. 1189–1193, 1953.
- [7] K. L. Lee, B. Grémaud, C. Miniatura, and D. Delande, "Analytical and numerical study of uncorrelated disorder on a honeycomb lattice," *Physical Review B*, vol. 87, p. 144202, apr 2013.
- [8] C. Wu, D. Bergman, L. Balents, and S. Das Sarma, "Flat bands and wigner crystallization in the honeycomb optical lattice," *Physical Review Letters*, vol. 99, no. 7, pp. 1–4, 2007.
- [9] L. Sanchez-Palencia and M. Lewenstein, "Disordered quantum gases under control," *Nature Physics*, vol. 6, no. 2, pp. 87–95, 2010.
- [10] U. Kuhl, F. M. Izrailev, A. A. Krokhin, and H. J. Stöckmann, "Experimental observation of the mobility edge in a waveguide with correlated disorder," *Applied Physics Letters*, vol. 77, no. 5, pp. 633–635, 2000.
- [11] M. Maksymenko, R. Moessner, and K. Shtengel, "Persistence of the flat band in a kagome magnet with dipolar interactions," *Physical Review B*, vol. 96, no. 13, pp. 1–11, 2017.
- [12] T. Bilitewski and R. Moessner, "Disordered flat bands on the kagome lattice," *Physical Review B*, vol. 98, no. 23, pp. 1–6, 2018.
- [13] S. Flach, D. Leykam, J. D. Bodyfelt, P. Matthies, and A. S. Desyatnikov, "Detangling flat bands into Fano lattices," *EPL (Europhysics Letters)*, vol. 105, p. 30001, feb 2014.
- [14] D. G. Deppe and N. Holonyak, "Atom diffusion and impurity-induced layer disordering in quantum well III-V semiconductor heterostructures," *Journal of Applied Physics*, vol. 64, no. 12, 1988.
- [15] M. Morgenstern, J. Klijn, C. Meyer, M. Getzlaff, R. Adlung, R. A. Römer, K. Rosnagel, L. Kipp, M. Skibowski, and R. Wiesendanger, "Direct Comparison between Potential Landscape and Local Density of States in a Disordered Two-Dimensional Electron System," *Physical Review Letters*, vol. 89, p. 136806, sep 2002.
- [16] M. Morgenstern, A. Georgi, C. Straßer, C. Ast, S. Becker, and M. Liebmann, "Scanning tunneling microscopy of two-dimensional semiconductors: Spin properties and disorder," *Physica E: Low-dimensional Systems and Nanostructures*, vol. 44, pp. 1795–1814, jun 2012.
- [17] N. A. Franchina Vergel, A. Tadjine, V. Notot, M. Mohr, A. Kouassi N'Guissan, C. Coinon, M. Berthe, L. Biadala, K. K. Sossoe, M. M. Dzagli, J.-C. Girard, G. Rodary, L. Desplanque, R. Berndt, D. Stiévenard, X. Wallart, C. Delerue, and B. Grandidier, "Influence of doping level and surface states in tunneling spectroscopy of an  $\text{In}_{0.53}\text{Ga}_{0.47}\text{As}$  quantum well grown on p-type doped  $\text{InP}(001)$ ," *Physical Review Materials*, vol. 3, p. 094604, sep 2019.
- [18] T. S. Gardenier, J. J. van den Broeke, J. R. Moes, I. Swart, C. Delerue, M. R. Slot, C. M. Smith, and D. Vanmaekelbergh, "p Orbital Flat Band and Dirac Cone in the Electronic Honeycomb Lattice," *ACS Nano*, p. acsnano.0c05747, oct 2020.
- [19] J. C. Slater, "Wave Functions in a Periodic Potential," *Physical Review*, vol. 51, pp. 846–851, may 1937.
- [20] J. C. Slater and G. F. Koster, "Simplified LCAO Method for the Periodic Potential Problem," *Physical Review*, vol. 94, pp. 1498–1524, jun 1954.

- 
- [21] G. Zerveas, E. Caruso, G. Bacarani, L. Czornomaz, N. Daix, D. Esseni, E. Gnani, A. Gnudi, R. Grassi, M. Luisier, T. Markussen, P. Osgnach, P. Palestri, A. Schenk, L. Selmi, M. Sousa, K. Stokbro, and M. Visciarelli, “Comprehensive comparison and experimental validation of band-structure calculation methods in III-V semiconductor quantum wells,” *Solid-State Electronics*, vol. 115, pp. 92–102, 2016.
  - [22] L. Wang, P. M. Asbeck, and Y. Taur, “Self-consistent 1-D Schrödinger-Poisson solver for III-V heterostructures accounting for conduction band non-parabolicity,” *Solid-State Electronics*, vol. 54, no. 11, pp. 1257–1262, 2010.
  - [23] Y. Liu, N. Neophytou, G. Klimeck, and M. S. Lundstrom, “Band-structure effects on the performance of III-V ultrathin-body SOI MOSFETs,” *IEEE Transactions on Electron Devices*, vol. 55, no. 5, pp. 1116–1122, 2008.
  - [24] D. Nečas and P. Klapetek, “Gwyddion: An open-source software for SPM data analysis,” *Central European Journal of Physics*, vol. 10, no. 1, pp. 181–188, 2012.
  - [25] C. Wu and S. Das Sarma, “ $p_{x,y}$ -orbital counterpart of graphene: Cold atoms in the honeycomb optical lattice,” *Physical Review B*, vol. 77, p. 235107, jun 2008.



# Chapter VII

---

Application of honeycomb semiconductors:  
Outlook & future prospects

**Based on:**  
*This chapter was written for this thesis*

**The research performed in this thesis shows that honeycomb semiconductors can be created using techniques already well-mastered by the semiconductor industry. Although the first signs of Dirac physics has been observed in these samples, we are still far away from implementing these electronic properties into real semiconductor devices. This last chapter of the thesis will discuss first how we can optimize the fabrication process, to obtain better-defined honeycomb nano symmetries with a smaller period, thus making the Dirac physics more robust. We will not only look into improvement of the used lithography techniques, but also investigate other lithography techniques. Second, a proposed work-flow will be presented how to implement honeycomb semiconductors into electronic devices. Lastly, lattice symmetries different from the honeycomb symmetry will be considered which will hold other interesting electronic properties. By using lithography, we have the freedom to create any symmetry that we want, and thus to tune the electronic structure of materials indefinitely, creating truly designer materials.**

### VII.1 Process optimization

Honeycomb semiconductors are a special type of material which can be fabricated using lithography techniques. Although this research has showed the possibilities to build these, improvement of the quality and size of the honeycomb geometry is still desired to render more robust Dirac bands. Several parameters in the electron beam lithography procedure contribute to the resolution of the pores, such as instrument limitations, interactions between electrons and the resist, the development of the resist and finally the pattern transfer into the semiconductor layer. Further developments in this field have already shown the possibilities to create very small pores with sizes of sub-5 nm using aberration-corrected electron beam lithography [1]. Also new developments regarding the electron beam resist show the possibility to reduce the dimensions of the pores [2]. The quality of the honeycomb pattern is mainly determined by the pattern transfer into the semiconductor layer, which still faces challenges to meet the resolution requirements. For silicon based materials, etching experiments have shown the possibility to fabricate sub-10 nm devices using induced coupled plasma etching procedures [3].

Lithography techniques other than electron beam lithography (EBL) and block copolymer lithography (BCPL) can also be considered and exploited. A third lithography technique investigated in this research is thermal scanning probe lithography (t-SPL), which is part of the broad scanning probe lithography (SPL) family [4]. This technique makes use of a heated conical tip, which is used to directly pattern an organic layer consisting of polyphthalaldehyde (PPA). By optimizing the parameters of this technique, such as applied force and tip temperature, sub-10 nm features can be obtained in silicon based semiconductor materials [5,6]. Not only offers this technique the possibility to remove material, but also to change the functionality of a material by performing deprotection of functional surface groups [7], precursor conversion [8], amorphization [9], crystallization [10] or magnetic polarization [11].

Major strengths of t-SPL are that no charged particles are used to create features, which is important for creating low-dimensional devices while avoiding unwanted formation of covalent bonds, lattice defects, vacancies or trapped charges, which could influence the electronic properties of the nano device [12]. This technique also paves the way to create three-dimensional nanostructures [13, 14], extending even further the vast amount of possibilities with this technique. Further advantages of this technique are the robust but compact setup of the machine, the possibility to perform t-SPL under ambient conditions and *in-situ* atomic force microscopy (AFM) can be performed to image the surface topography before, during and after the lithography process with the same probe. Challenges in t-SPL are mainly the patterning speed, which is similar as for electron beam lithography. This can be solved by performing t-SPL with multiple probes in parallel [15].

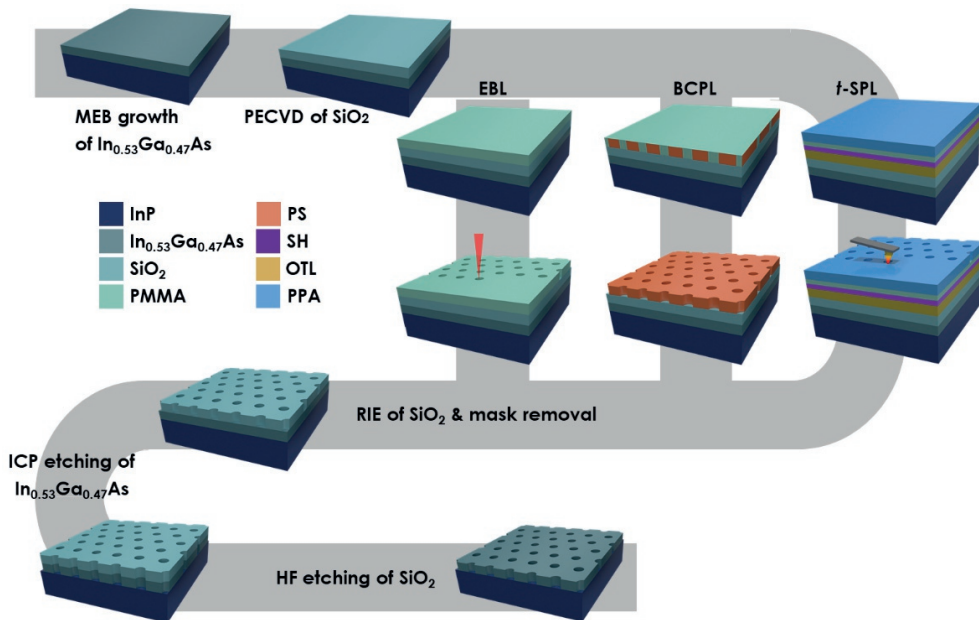


**Figure VII.1:** Schematic workflow diagram for lithographic fabrication of a triangular antidot lattice in an  $\text{In}_{0.53}\text{Ga}_{0.47}\text{As}$  quantum well grown on a  $\text{InP}$  (001) substrate by molecular beam epitaxy (MBE). Three techniques were used: e-beam lithography (EBL), block copolymer lithography (BCPL) and thermal scanning probe lithography (t-SPL).

A general work-flow diagram is presented in Fig. VII.1 to fabricate honeycomb semiconductors using different lithography techniques. The procedure for EBL and BCPL can be found in Chapter IV and V respectively. The thermal scanning probe lithography procedure uses a four-layer pattern transfer stack, consisting of a 8 nm thick polyphthalaldehyde (PPA) thermal resist layer, a 2 nm thick polymethylmethacrylate (PMMA) buffer layer, a 1.5 nm thick spincoated silicon hard mask (SH 113, PiBond Oy) and lastly a 40 nm thick organic transfer layer (OTL 405, PiBond Oy), which was all spin-coated on top of the  $\text{SiO}_2$  protective layer. A commercial t-SPL system (NanoFra-

zor Explore, Heidelberg Instruments Nano) was used to pattern the PPA layer with a tip heater temperature of 700 °C. Followed by a brief O<sub>2</sub>/N<sub>2</sub> reactive ion etching descum step to remove the PMMA buffer layer at the bottom of the pattern, the PPA pattern was first transferred into the silicon hard mask in a CHF<sub>3</sub> reactive ion etching (RIE) step and further into the OTL in another O<sub>2</sub> RIE step.

A comparison of the nanopatterning between the lithography techniques is presented in Fig. VII.2 using scanning electron microscopy (SEM) images. Optimization of the EBL parameters has let to an optimal periodicity of 39 nm between the pores. Further adjustments of the parameters has let to overlap of the pores due to proximity effects, making it unable to lower the dimensions of the honeycomb symmetry. Using the BCPL and the t-SPL technique, the periodicity was further lowered to 36 nm and 30 nm respectively, while the sizes of the pores are for all techniques roughly the same, about 20 nm. Based on a statistical analysis of the pore sizes [16], smaller disorder was measured in the t-SPL mask compared with the EBL and BCPL masks. The full width at half maximum of the pore size distribution was calculated, yielding values of 1.6 nm, 1.4 nm and 1.0 nm of EBL, BCPL and t-SPL respectively. For both BCPL and t-SPL, lower dimensions of the honeycomb symmetry are still possible, which will increase the present disorder in the lattice. This will need further investigation to reduce the periodicity without loss of quality. Also other lithography techniques, such as helium ion beam lithography (HIBL) [17–19], can be exploited to reduce the periodicity of the lattice.

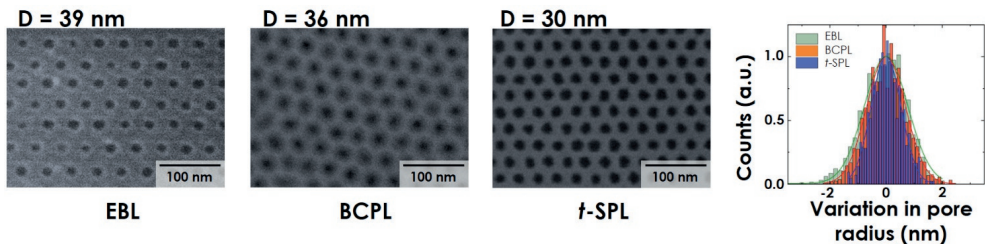


**Figure VII.2:** SEM images of the masks prepared with EBL, BCPL and t-SPL. The periodicity of the triangular lattice is indicated for each mask. Comparison between the pore sizes for the three different masks is plotted in the histogram.

## VII.2 Transport measurements

This research explored the local electronic properties of a honeycomb semiconductor by performing low-temperature scanning tunneling spectroscopy. For a more general characterization, electronic magneto-transport measurements can be performed on honeycomb semiconductors shaped and connected to a Hall bar symmetry [20, 21]. This will allow direct access to both the longitudinal resistance  $R_L$  and transverse resistance  $R_H$  by measuring the voltages  $V_L$  and  $V_H$  as a function of the current  $I$ . Physical parameters such as the mobility and mean free path of the charge carriers can be studied as a function of the temperature, charge density and magnetic field in the semiconductor

quantum well.

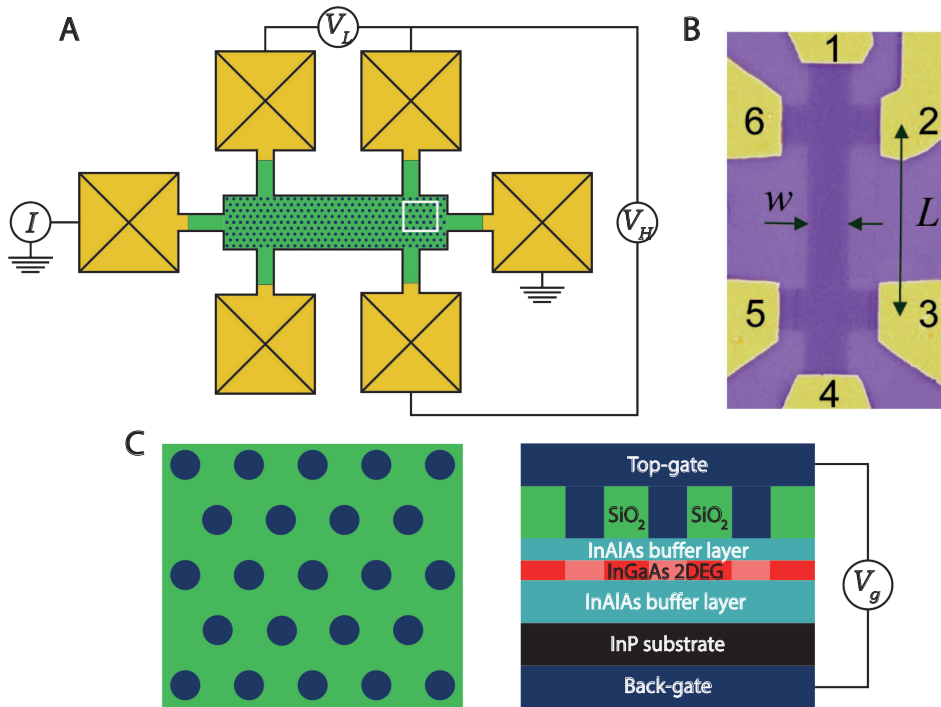


**Figure VII.3: Hall bar design for an InGaAs based honeycomb semiconductor.**(A) Schematic overview of the Hall bar device for the honeycomb semiconductor. (B) SEM image of a graphene Hall bar device, adapted from Ref. [22]. False colours are chosen to indicate the ohmic contacts of the device. (C) Top-view (left) and cross-section view (right) of the proposed III-V semiconductor heterostructure with a honeycomb nanogeometry. The heterostructure is sandwiched between two gates, allowing for remote potential modulation.

A proposed design for electronic magneto-transport measurements in an InGaAs honeycomb semiconductor is presented in Fig. VII.3A. The general design is similar as for electronic devices in graphene (Fig. VII.3B) [22–25] and in other III-V semiconductor materials [26–28]. First, the III-V semiconductor heterostructure is grown using molecular beam epitaxy, following well-known growth procedures [29–31]. The heterostructure is protected by a layer of  $\text{SiO}_2$  grown by plasma-enhanced chemical vapor deposition (PECVD) (Fig. VII.3C). Then, the honeycomb pattern is defined in the  $\text{SiO}_2$  layer over an typical area of 1 micron in width and 5 micron in length, preferably using EBL or t-SPL. Metal gate deposition is performed to create the top-gate above the honeycomb lattice and to define the Hall bar geometry. By growing a top-gate and back-gate on the heterostructure, remote potential modulation can be performed on the honeycomb semiconductor. Not only can Dirac physics be investigated as function of the potential inside the barriers, but it will also be easier to carry out electronic measurements on the pristine InGaAs quantum well, i.e. in absence of a potential

modulation.

For the further Hall bar fabrication itself, we rely on standard processing which is already developed for III-V based heterostructures. Finally, we end up with a micron scale honeycomb semiconductor device with six ohmic contacts (Fig. VII.3A), where two current contacts are attached on the ends of the device, and four voltage contacts are attached on the top and bottom of the device. The longitudinal and horizontal resistances  $R_L$  and  $R_H$  can be derived, which is used to calculate the conductivity of the honeycomb semiconductor. This can be performed in presence of a magnetic field, meaning that Shubnikov-de Haas oscillations [24] can be studied. Another evidence for the presence of Dirac fermions would be to measure the half-integer quantum Hall effect similar to what is observed in graphene [23, 32]. Next, it would be interesting to study the magneto-electronic properties when the Fermi level is positioned in the flat band, looking beyond the properties of graphene. Since the electrons in the flat band have no kinetic energy, interactions dominate the Hamiltonian. Several new physical phenomena, such as Wigner crystallization [33] and unusual magnetism, have been predicted in this regime. Also, direct access to the density of states (and thus the band structure) of the device is possible when using a capacitance spectroscopy setup. This technique already revealed the electronic properties of several two-dimensional systems [34–36].

### VII.3 Beyond InGaAs-based honeycomb semiconductors

The researched conducted in this thesis is focused on InGaAs-based honeycomb semiconductors. However, the idea behind designer materials is to be able to create different symmetries with different materials, obtaining different electronic properties. In this last part of this chapter, the wide possibilities to create designer materials is discussed by looking into different compounds, different symmetries and different dimensions.

#### Materials

With regard to the type of semiconductor compound, there are many more materials that can be used for band engineering and geometrical patterning. The choice to focus on III-V heterostructures in this research is justified as the charge carriers have a low effective mass in these type of materials, the growth process can be controlled to individual atomic layer precision thanks to molecular beam epitaxy, and the processing of III-V semiconductors is well-mastered. Technically, every semiconductor can be used for this research as long as it can be grown two-dimensionally, meaning that barrier materials have to be found with suitable band gaps, without large lattice mismatch at the surfaces, and uncontrollable doping effects in both the quantum well and barrier materials. Patterning also needs investigation of the etching procedures at the nano-scale.

A first improvement to consider is to use an InAs-based quantum well material. It has

---

a lower effective mass compared with InGaAs [37], it can be grown two-dimensionally between suitable barrier materials [38–40] and similar etching profiles are expected. Generally, this semiconductor would enhance the energy width of the Dirac cone and separation between the bands, a much desired property. In general, other III-V and even II-VI semiconductor based quantum wells yield similar band structures [41], but the band gap and band offset are different for each compound. Using heavy metal semiconductors such as InSb-based quantum wells, it is also possible to implement spin-orbit coupling. Intrinsic spin-orbit coupling results in topological band-openings at the Dirac point between the flat band and the other  $p$ -bands, giving rise to helical quantum channels, i.e. the quantum spin Hall effect [42]. In addition, there is a Rashba effect [43] resulting in a lift of the spin-degeneracy of the bands. Eventually, the ultimate goal would be to implement Dirac physics in silicon-based devices. However, this is not feasible yet due to the large effective electron mass compared to III-V semiconductor, and the limited research in the fabrication process of silicon in the quantum limit in general.

## Lattice symmetries

This research has focused on the honeycomb symmetry only, but other symmetries can also be considered when the fabrication process is mastered. Some symmetries, such as the square lattice, are still straightforward to fabricate, but also more complex symmetries are possible to design. Of prime interest are the Lieb lattice and the kagome lattice as they show Dirac physics and eventually topological corner and end states [44, 45]. For each symmetry, the correct antidot lattice has to be derived, and the difficulties have to be considered. Figure VII.4 presents a few different symmetries with corresponding antidot lattices [41]. Figure VII.4A shows the honeycomb symmetry and its antidot lattice, which was used as template in the lithographic procedure. Other symmetries and their representative antidot lattices are the square lattice (B), Lieb lattice (C) and kagome lattice (D). The parameters of each antidot lattice is indicated in the images.

The square lattice itself is electronically not too interesting, but this symmetry could still be used to confirm the calculated electronic properties experimentally, which has been used in various models [46]. Things get more interesting in the kagome and Lieb lattice. Both in the kagome [47–50] and the Lieb [51, 52] lattices, Dirac cones and non-trivial flat bands are predicted. In the Lieb lattice, the nondispersive band lies between the two Dirac bands, while in the kagome lattice the flat band is located directly below/above the Dirac cone. Since both lattices share the same structural configuration in the unit cell, similar electronic features are observed in the theoretical models [53].

It has been shown that both lattices can be built artificially on metal surfaces [54, 55] by manipulating CO molecules on a Cu(111) substrate [44, 56]. A major obstacle to implement these symmetries into an electronic device is to nanopattern pores with different sizes in the semiconductor quantum well. This is limited by the resolution of the desired antidot lattice. Upon further improvement of the resolution of the lithography

process, Lieb and kagome lattices will become within reach. The number of possible symmetries is endless, which will help to reach our goal to create designer materials using lithography.

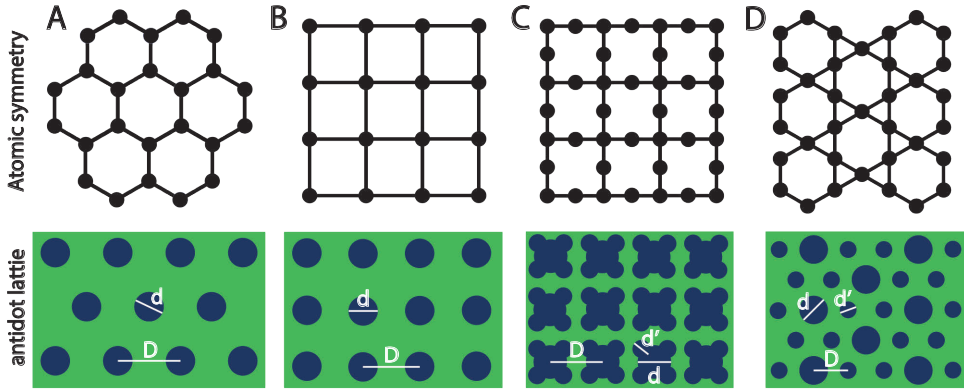


**Figure VII.4: Geometries of different lattices.** Atomic lattices (top) and the corresponding antidot lattices (bottom) for the honeycomb lattice (A), square lattice (B), Lieb lattice (C) and kagome lattice (D). The tunable parameters of the antidot lattices are indicated in the figures.

## Dimensionality

Lastly, lithographic-based techniques give the opportunity to fabricate semiconductor materials with different dimensionalities. Both quantum dots [57, 58] and nanowires [59, 60] have already been extensively studied, exhibiting fascinating electronic and/or optical properties [61–64]. Recent research even showed the possibility to confine electrons in a planar fractal with dimension between 1 and 2 [45]. Lithography additionally provides the freedom to combine electron systems into one single device. One special case highlighted here is a double honeycomb semiconductor device, basically designing artificial bilayer graphene.

Bilayer graphene consist of two graphene layers stacked on top of each other. It can exist in different modifications: AA, AB or twisted bilayer graphene [65]. AA stacked bilayer graphene is a configuration in which the carbon atoms of the second layer are placed exactly on top of the first layer. However, AA stacked bilayer graphene is difficult to fabricate since it is likely to be metastable. In the AB stacked configuration, half of the carbon atoms of the second layer are place on top of carbon atoms of the first layer, and the other half are placed in the center of the hexagons. This will result in a more stable configuration, and different experimental studies have been performed on this configuration [66–69]. In the twisted bilayer configuration, the second layer is twisted with a certain angle compared with the first layer.

Electronically, significant differences will occur for the different modifications. Looking at the  $s$ -bands, four Dirac bands are observed for the AA stacked bilayer graphene,

which are two copies of the single layer graphene band structure. Two Dirac bands touch each other higher in energy than the Fermi level, and two Dirac bands touch each other lower in energy [70–72]. For the AB configuration, again four Dirac bands are observed around the Fermi level, but here two bands form a Dirac cone with an energy splitting, and the other two bands form a second Dirac cone with the Dirac point at zero energy [65, 73], effectively changing the band structure of the bilayer graphene.

A bilayer honeycomb semiconductor can be designed by alternating barrier and quantum well materials. An AA configuration bilayer honeycomb semiconductor can be fabricated by direct nanopatterning or by etching the top layer and apply a top and bottom gate to the device. An AB configuration bilayer honeycomb semiconductor will be more challenging to fabricate using lithography: the lower quantum well needs to be etched and the pores need to be filled with barrier material before the second quantum well can be grown and etched.

Once it is possible to fabricate bilayer honeycomb semiconductors, the electronic structure can be tuned exactly: not only can the unit cell size of the honeycomb lattice be varied, but also the distance between the two quantum wells can be altered. For the AA configuration, it is discussed that the splitting between the two Dirac cones is linear with the interlayer coupling, and therefore exponential dependent on the the distance between the two quantum wells [41]. Therefore, splitting between the Dirac cones can be controlled exactly.

## Conclusions and outlook

This chapter showed the possibilities in the field of lithography. Progress in this field will allow to optimize the engineering of honeycomb semiconductors and incorporate them in state-of-the-art devices. A general template was presented to implement honeycomb semiconductors into Hall bars, which can be used to directly access the electronic properties and reveal the exotic physics predicted by theory.

This chapter also presents future designs with different lattice symmetries: heterostructures using different compounds, different symmetries with their own unique electronic structure and different dimensionalities. The possibilities are truly endless. By optimizing our power to manipulate materials at the nanoscale, true designer materials can be constructed with full control over their electronic properties.

---

## References

- [1] V. R. Manfrinato, A. Stein, L. Zhang, C.-Y. Nam, K. G. Yager, E. A. Stach, and C. T. Black, “Aberration-Corrected Electron Beam Lithography at the One Nanometer Length Scale,” *Nano Letters*, vol. 17, pp. 4562–4567, aug 2017.
- [2] A. S. Gangnaik, Y. M. Georgiev, and J. D. Holmes, “New Generation Electron Beam Resists: A Review,” *Chemistry of Materials*, vol. 29, pp. 1898–1917, mar 2017.
- [3] M. M. Mirza, H. Zhou, P. Velha, X. Li, K. E. Docherty, A. Samarelli, G. Ternent, and D. J. Paul, “Nanofabrication of high aspect ratio (50:1) sub-10 nm silicon nanowires using inductively coupled plasma etching,” *Journal of Vacuum Science & Technology B*, vol. 30, p. 06FF02, nov 2012.
- [4] R. Garcia, A. W. Knoll, and E. Riedo, “Advanced scanning probe lithography,” *Nature Nanotechnology*, vol. 9, pp. 577–587, aug 2014.
- [5] Y. K. Ryu Cho, C. D. Rawlings, H. Wolf, M. Spieser, S. Bisig, S. Reidt, M. Sousa, S. R. Khanal, T. D. Jacobs, and A. W. Knoll, “Sub-10 Nanometer Feature Size in Silicon Using Thermal Scanning Probe Lithography,” *ACS Nano*, vol. 11, no. 12, pp. 11890–11897, 2017.
- [6] H. Wolf, C. Rawlings, P. Mensch, J. L. Hedrick, D. J. Coady, U. Duerig, and A. W. Knoll, “Sub-20 nm silicon patterning and metal lift-off using thermal scanning probe lithography,” *Journal of Vacuum Science & Technology B*, vol. 33, no. 2, p. 02B102, 2015.
- [7] J. Duvigneau, H. Schönherr, and G. J. Vancso, “Nanoscale thermal AFM of polymers: Transient heat flow effects,” *ACS Nano*, vol. 4, no. 11, pp. 6932–6940, 2010.
- [8] Z. Wei, D. Wang, S.-y. Kim, S.-Y. Kim, Y. Hu, M. K. Yakes, A. R. Laracuente, Z. Dai, S. R. Marder, C. Berger, W. P. King, W. A. de Heer, P. E. Sheehan, and E. Riedo, “Nanoscale Tunable Reduction of Graphene Oxide for Graphene Electronics,” *Science*, vol. 328, pp. 1373–1376, jun 2010.
- [9] S. T. Zimmermann, D. W. Balkenende, A. Lavrenova, C. Weder, and J. Brugger, “Nanopatterning of a Stimuli-Responsive Fluorescent Supramolecular Polymer by Thermal Scanning Probe Lithography,” *ACS Applied Materials and Interfaces*, vol. 9, no. 47, pp. 41454–41461, 2017.
- [10] A. Podpirka, W. K. Lee, J. I. Ziegler, T. H. Brintlinger, J. R. Felts, B. S. Simpkins, N. D. Bassim, A. R. Laracuente, P. E. Sheehan, and L. B. Ruppalt, “Nanopatterning of GeTe phase change films via heated-probe lithography,” *Nanoscale*, vol. 9, no. 25, pp. 8815–8824, 2017.
- [11] E. Albisetti, D. Petti, M. Pancaldi, M. Madami, S. Tacchi, J. Curtis, W. P. King, A. Papp, G. Csaba, W. Porod, P. Vavassori, E. Riedo, and R. Bertacco, “Nanopatterning reconfigurable magnetic landscapes via thermally assisted scanning probe lithography,” *Nature Nanotechnology*, vol. 11, no. 6, pp. 545–551, 2016.
- [12] D. Teweldebrhan and A. A. Balandin, “Modification of graphene properties due to electron-beam irradiation,” *Applied Physics Letters*, vol. 94, no. 1, pp. 94–97, 2009.
- [13] S. T. Howell, A. Grushina, F. Holzner, and J. Brugger, “Thermal scanning probe lithography—a review,” *Microsystems and Nanoengineering*, vol. 6, no. 1, pp. 1–24, 2020.
- [14] D. Pires, J. L. Hedrick, A. De Silva, J. Frommer, B. Gotsmann, H. Wolf, M. Despont, U. Duerig, and A. W. Knoll, “Nanoscale Three-Dimensional Patterning of Molecular Resists by Scanning Probes,” *Science*, vol. 328, pp. 732–735, may 2010.
- [15] K. M. Carroll, X. Lu, S. Kim, Y. Gao, H. J. Kim, S. Somnath, L. Polloni, R. Sordan, W. P. King, J. E. Curtis, and E. Riedo, “Parallelization of thermochemical nanolithography,” *Nanoscale*, vol. 6, no. 3, pp. 1299–1304, 2014.
- [16] L. C. Post, T. Xu, N. A. Franchina Vergel, A. Tadjine, Y. Lambert, F. Vaurette, D. Yarekha, L. Desplanque, D. Stiévenard, X. Wallart, B. Grandidier, C. Delerue, and D. Vanmaekelbergh, “Triangular nanoporation and band engineering of InGaAs quantum wells: a lithographic route toward Dirac cones in III–V semiconductors,” *Nanotechnology*, vol. 30, p. 155301, apr 2019.
- [17] A. N. Abbas, G. Liu, B. Liu, L. Zhang, H. Liu, D. Ohlberg, W. Wu, and C. Zhou, “Patterning, characterization, and chemical sensing applications of graphene nanoribbon arrays down to 5 nm using helium ion beam lithography,” *ACS Nano*, vol. 8, no. 2, pp. 1538–1546, 2014.

- 
- [18] D. Winston, B. M. Cord, B. Ming, D. C. Bell, W. F. DiNatale, L. A. Stern, A. E. Vladar, M. T. Postek, M. K. Mondol, J. K. W. Yang, and K. K. Berggren, "Scanning-helium-ion-beam lithography with hydrogen silsesquioxane resist," *Journal of Vacuum Science & Technology B*, vol. 27, no. 6, p. 2702, 2009.
- [19] X. Shi and S. A. Boden, "Scanning helium ion beam lithography," in *Frontiers of Nanoscience*, vol. 11, pp. 563–594, 2016.
- [20] L. J. van der Pauw, "A method of measuring the resistivity and hall coefficient on lamellae of arbitrary shape," *Philips Technical Review*, vol. 20, pp. 220–224, 1958.
- [21] L. J. van der Pauw, "A method of measuring the resistivity and hall coefficient of discs of arbitrary shape," *Philips Research Reports*, vol. 13, no. 1, pp. 1–9, 1958.
- [22] D. A. Abanin, S. V. Morozov, L. A. Ponomarenko, R. V. Gorbachev, A. S. Mayorov, M. I. Katsnelson, K. Watanabe, T. Taniguchi, K. S. Novoselov, L. S. Levitov, and A. K. Geim, "Giant nonlocality near the dirac point in graphene," *Science*, vol. 332, no. 6027, pp. 328–330, 2011.
- [23] X. Du, I. Skachko, F. Duerr, A. Luican, and E. Y. Andrei, "Fractional quantum Hall effect and insulating phase of Dirac electrons in graphene," *Nature*, vol. 462, pp. 192–195, nov 2009.
- [24] K. S. Novoselov, A. K. Geim, S. V. Morozov, D. Jiang, M. I. Katsnelson, I. V. Grigorieva, S. V. Dubonos, and A. A. Firsov, "Two-dimensional gas of massless Dirac fermions in graphene," *Nature*, vol. 438, pp. 197–200, nov 2005.
- [25] V. Miseikis, F. Bianco, J. David, M. Gemmi, V. Pellegrini, M. Romagnoli, and C. Coletti, "Deterministic patterned growth of high-mobility large-crystal graphene: A path towards wafer scale integration," *2D Materials*, vol. 4, no. 2, 2017.
- [26] H. E. Ruda and N. Matsuura, *Springer Handbook of Electronic and Photonic Materials*. Cham: Springer International Publishing, 2017.
- [27] A. Nainani, B. R. Bennett, J. Brad Boos, M. G. Ancona, and K. C. Saraswat, "Enhancing hole mobility in III-V semiconductors," *Journal of Applied Physics*, vol. 111, no. 10, 2012.
- [28] B. R. Bennett, J. B. Boos, M. G. Ancona, N. A. Papanicolaou, G. A. Cooke, and H. Kheyrandish, "In-AlSb/InAs/AlGaSb Quantum Well Heterostructures for High-Electron-Mobility Transistors," *Journal of Electronic Materials*, vol. 36, pp. 99–104, feb 2007.
- [29] W. Yeo, R. Dimitrov, W. J. Schaff, and L. F. Eastman, "Material properties of bulk InGaAs and InAlAs/InGaAs heterostructures grown on (111)B and (111)B misoriented by 1° towards 211 InP substrates," *Applied Physics Letters*, vol. 77, pp. 4292–4294, dec 2000.
- [30] X. Wallart, B. Pinsard, and F. Mollot, "High-mobility InGaAsInAlAs pseudomorphic heterostructures on InP (001)," *Journal of Applied Physics*, vol. 97, p. 053706, mar 2005.
- [31] I. Watanabe, K. Kanzaki, T. Aoki, T. Kitada, S. Shimomura, and S. Hiyamizu, "Mobility enhancement by reduced remote impurity scattering in a pseudomorphic  $\text{In}_{0.7}\text{Ga}_{0.3}\text{As}/\text{In}_{0.52}\text{Al}_{0.48}\text{As}$  quantum well high electron mobility transistor structure with (411)A super-flat interfaces grown by molecular-beam epitaxy," *Journal of Vacuum Science & Technology B: Microelectronics and Nanometer Structures*, vol. 19, no. 4, p. 1515, 2001.
- [32] Y. Zhang, Y.-W. Tan, H. L. Stormer, and P. Kim, "Experimental observation of the quantum Hall effect and Berry's phase in graphene," *Nature*, vol. 438, pp. 201–204, nov 2005.
- [33] C. Wu and S. Das Sarma, " $p_{x,y}$ -orbital counterpart of graphene: Cold atoms in the honeycomb optical lattice," *Physical Review B*, vol. 77, p. 235107, jun 2008.
- [34] B. Hunt, J. D. Sanchez-Yamagishi, A. F. Young, M. Yankowitz, B. J. LeRoy, K. Watanabe, T. Taniguchi, P. Moon, M. Koshino, P. Jarillo-Herrero, and R. C. Ashoori, "Massive Dirac Fermions and Hofstadter Butterfly in a van der Waals Heterostructure," *Science*, vol. 340, pp. 1427–1430, jun 2013.
- [35] E. A. Henriksen and J. P. Eisenstein, "Measurement of the electronic compressibility of bilayer graphene," *Physical Review B*, vol. 82, p. 041412, jul 2010.
- [36] C. R. Dean, L. Wang, P. Maher, C. Forsythe, F. Ghahari, Y. Gao, J. Katoch, M. Ishigami, P. Moon, M. Koshino, T. Taniguchi, K. Watanabe, K. L. Shepard, J. Hone, and P. Kim, "Hofstadter's butterfly and the fractal quantum Hall effect in moiré superlattices," *Nature*, vol. 497, no. 7451, pp. 598–602, 2013.
- [37] N. Bouarissa and H. Aourag, "Effective masses of electrons and heavy holes in InAs, InSb, GaSb, GaAs and some of their ternary compounds," *Infrared Physics Technology*, vol. 40, pp. 343–349, aug 1999.
-

- 
- [38] Y. Lin, J. A. Carlin, A. R. Arehart, A. M. Carlin, and S. A. Ringel, "High-mobility two-dimensional electron gas in InAlAsInAs heterostructures grown on virtual InAs substrates by molecular-beam epitaxy," *Applied Physics Letters*, vol. 90, p. 012115, jan 2007.
- [39] S. Ishida, A. Fujimoto, M. Araki, K. Oto, A. Okamoto, and I. Shibusaki, "Low-temperature transport properties in  $\text{Al}_x\text{Ga}_{1-x}\text{As}_y\text{Sb}_{1-y}/\text{InAs}$  quantum wells: Well-width dependence," *Journal of Crystal Growth*, vol. 301-302, pp. 199–202, apr 2007.
- [40] A. A. Podpirka, J. Shabani, M. B. Katz, M. E. Twigg, S. Mack, C. J. Palmstrøm, and B. R. Bennett, "Growth and characterization of (110) InAs quantum well metamorphic heterostructures," *Journal of Applied Physics*, vol. 117, p. 245313, jun 2015.
- [41] A. Tadjine, G. Allan, and C. Delerue, "From lattice Hamiltonians to tunable band structures by lithographic design," *Physical Review B*, vol. 94, p. 075441, aug 2016.
- [42] E. Kalesaki, C. Delerue, C. Morais Smith, W. Beugeling, G. Allan, and D. Vanmaekelbergh, "Dirac Cones, Topological Edge States, and Nontrivial Flat Bands in Two-Dimensional Semiconductors with a Honeycomb Nanogeometry," *Physical Review X*, vol. 4, p. 011010, jan 2014.
- [43] G. A. Khodaparast, R. E. Doezema, S. J. Chung, K. J. Goldammer, and M. B. Santos, "Spectroscopy of Rashba spin splitting in InSb quantum wells," *Physical Review B - Condensed Matter and Materials Physics*, vol. 70, no. 15, pp. 1–6, 2004.
- [44] M. R. Slot, T. S. Gardenier, P. H. Jacobse, G. C. P. van Miert, S. N. Kempkes, S. J. M. Zevenhuizen, C. M. Smith, D. Vanmaekelbergh, and I. Swart, "Experimental realization and characterization of an electronic Lieb lattice," *Nature Physics*, vol. 13, pp. 672–676, apr 2017.
- [45] S. N. Kempkes, M. R. Slot, S. E. Freney, S. J. Zevenhuizen, D. Vanmaekelbergh, I. Swart, and C. M. Smith, "Design and characterization of electrons in a fractal geometry," *Nature Physics*, vol. 15, no. 2, pp. 127–131, 2019.
- [46] C. Delerue, "From semiconductor nanocrystals to artificial solids with dimensionality below two," *Phys. Chem. Chem. Phys.*, vol. 16, no. 47, pp. 25734–25740, 2014.
- [47] H. M. Guo and M. Franz, "Topological insulator on the kagome lattice," *Physical Review B - Condensed Matter and Materials Physics*, vol. 80, no. 11, pp. 20–23, 2009.
- [48] D. Guterding, H. O. Jeschke, and R. Valentí, "Prospect of quantum anomalous Hall and quantum spin Hall effect in doped kagome lattice Mott insulators," *Scientific Reports*, vol. 6, p. 25988, sep 2016.
- [49] J. Li, Y.-F. Wang, and C.-D. Gong, "Tight-binding electrons on triangular and kagomé lattices under staggered modulated magnetic fields: quantum Hall effects and Hofstadter butterflies," *Journal of Physics: Condensed Matter*, vol. 23, p. 156002, apr 2011.
- [50] D. L. Bergman, C. Wu, and L. Balents, "Band touching from real-space topology in frustrated hopping models," *Physical Review B*, vol. 78, p. 125104, sep 2008.
- [51] M. Niță, B. Ostahie, and A. Aldea, "Spectral and transport properties of the two-dimensional Lieb lattice," *Physical Review B - Condensed Matter and Materials Physics*, vol. 87, no. 12, p. 125428, 2013.
- [52] R. A. Vicencio, C. Cantillano, L. Morales-Inostroza, B. Real, C. Mejía-Cortés, S. Weimann, A. Szameit, and M. I. Molina, "Observation of Localized States in Lieb Photonic Lattices," *Physical Review Letters*, vol. 114, p. 245503, jun 2015.
- [53] W. Jiang, M. Kang, H. Huang, H. Xu, T. Low, and F. Liu, "Topological band evolution between Lieb and kagome lattices," *Physical Review B*, vol. 99, p. 125131, mar 2019.
- [54] S. Li, W.-X. Qiu, and J.-H. Gao, "Designing artificial two dimensional electron lattice on metal surface: a Kagome-like lattice as an example," *Nanoscale*, vol. 8, no. 25, pp. 12747–12754, 2016.
- [55] W.-X. Qiu, S. Li, J.-H. Gao, Y. Zhou, and F.-C. Zhang, "Designing an artificial Lieb lattice on a metal surface," *Physical Review B*, vol. 94, p. 241409, dec 2016.
- [56] S. N. Kempkes, M. R. Slot, J. J. van den Broeke, P. Capiod, W. A. Benalcazar, D. Vanmaekelbergh, D. Bercioux, I. Swart, and C. Morais Smith, "Robust zero-energy modes in an electronic higher-order topological insulator," *Nature Materials*, vol. 18, no. 12, pp. 1292–1297, 2019.
- [57] S. Lüscher, A. Fuhrer, R. Held, T. Heinzel, K. Ensslin, M. Bichler, and W. Wegscheider, "Quantum wires and quantum dots defined by lithography with an atomic force microscope," *Microelectronics Journal*, vol. 33, pp. 319–321, apr 2002.
-

- 
- [58] J.-S. Park, J. Kyhm, H. H. Kim, S. Jeong, J. Kang, S.-e. Lee, K.-T. Lee, K. Park, N. Barange, J. Han, J. D. Song, W. K. Choi, and I. K. Han, "Alternative Patterning Process for Realization of Large-Area, Full-Color, Active Quantum Dot Display," *Nano Letters*, vol. 16, pp. 6946–6953, nov 2016.
- [59] M. Tchernycheva, A. Messanvi, A. de Luna Bugallo, G. Jacopin, P. Lavenus, L. Rigutti, H. Zhang, Y. Halioua, F. H. Julien, J. Eymery, and C. Durand, "Integrated Photonic Platform Based on InGaN/GaN Nanowire Emitters and Detectors," *Nano Letters*, vol. 14, pp. 3515–3520, jun 2014.
- [60] J. Vukajlovic-Plestina, W. Kim, V. G. Dubrovski, G. Tütüncüoğlu, M. Lagier, H. Potts, M. Friedl, and A. Fontcuberta i Morral, "Engineering the Size Distributions of Ordered GaAs Nanowires on Silicon," *Nano Letters*, vol. 17, pp. 4101–4108, jul 2017.
- [61] L. N. Tripathi, T. Kang, Y.-M. Bahk, S. Han, G. Choi, J. Rhie, J. Jeong, and D.-S. Kim, "Quantum dots-nanogap metamaterials fabrication by self-assembly lithography and photoluminescence studies," *Optics Express*, vol. 23, p. 14937, jun 2015.
- [62] S. Gazibegovic, D. Car, H. Zhang, S. C. Balk, J. A. Logan, M. W. A. de Moor, M. C. Cassidy, R. Schmits, D. Xu, G. Wang, P. Krogstrup, R. L. M. Op het Veld, K. Zuo, Y. Vos, J. Shen, D. Bouman, B. Shojaei, D. Pennachio, J. S. Lee, P. J. van Veldhoven, S. Koelling, M. A. Verheijen, L. P. Kouwenhoven, C. J. Palmstrøm, and E. P. A. M. Bakkers, "Epitaxy of advanced nanowire quantum devices," *Nature*, vol. 548, pp. 434–438, aug 2017.
- [63] V. Mourik, K. Zuo, S. M. Frolov, S. R. Plissard, E. P. A. M. Bakkers, and L. P. Kouwenhoven, "Signatures of Majorana Fermions in Hybrid Superconductor-Semiconductor Nanowire Devices," *Science*, vol. 336, pp. 1003–1007, may 2012.
- [64] K. Kishino, A. Kikuchi, H. Sekiguchi, and S. Ishizawa, "InGaN/GaN nanocolumn LEDs emitting from blue to red," p. 64730T, feb 2007.
- [65] A. Rozhkov, A. Sboychakov, A. Rakhmanov, and F. Nori, "Electronic properties of graphene-based bilayer systems," *Physics Reports*, vol. 648, pp. 1–104, aug 2016.
- [66] M. T. Allen, J. Martin, and A. Yacoby, "Gate-defined quantum confinement in suspended bilayer graphene," *Nature Communications*, vol. 3, p. 934, jan 2012.
- [67] H. Overweg, P. Rickhaus, M. Eich, Y. Lee, R. Pisoni, K. Watanabe, T. Taniguchi, T. Ihn, and K. Ensslin, "Edge channel confinement in a bilayer graphene n–p–n quantum dot," *New Journal of Physics*, vol. 20, p. 013013, jan 2018.
- [68] M. Eich, R. Pisoni, A. Pally, H. Overweg, A. Kurzmann, Y. Lee, P. Rickhaus, K. Watanabe, T. Taniguchi, K. Ensslin, and T. Ihn, "Coupled Quantum Dots in Bilayer Graphene," *Nano Letters*, vol. 18, pp. 5042–5048, aug 2018.
- [69] M. Sui, G. Chen, L. Ma, W.-Y. Shan, D. Tian, K. Watanabe, T. Taniguchi, X. Jin, W. Yao, D. Xiao, and Y. Zhang, "Gate-tunable topological valley transport in bilayer graphene," *Nature Physics*, vol. 11, pp. 1027–1031, dec 2015.
- [70] R. Roldán and L. Brey, "Dielectric screening and plasmons in AA-stacked bilayer graphene," *Physical Review B - Condensed Matter and Materials Physics*, vol. 88, no. 11, p. 115420, 2013.
- [71] C. J. Tabert and E. J. Nicol, "Dynamical conductivity of AA-stacked bilayer graphene," *Physical Review B*, vol. 86, p. 075439, aug 2012.
- [72] M. Sanderson, Y. S. Ang, and C. Zhang, "Klein tunneling and cone transport in AA-stacked bilayer graphene," *Physical Review B*, vol. 88, p. 245404, dec 2013.
- [73] E. McCann and M. Koshino, "The electronic properties of bilayer graphene," *Reports on Progress in Physics*, vol. 76, p. 056503, may 2013.



# Chapter VIII

---

## Samenvatting in het Nederlands

In dit proefschrift wordt de mogelijkheid onderzocht om materialen te maken die de elektronische eigenschappen van halfgeleidermaterialen en grafeen combineren: zogenaamde honingraat halfgeleiders. Deze materialen worden gemaakt door middel van nanolithografie, een fabricatiemethode die periodieke structuren kan construeren met een periode van enkele tientallen nanometers. Ter vergelijking, 1 nanometer staat gelijk aan 0.000000001 meter, wat ook wel gelijk staat aan de verhouding tussen de aarde en een knikker: stel dus dat de aarde een diameter heeft van 1 meter, dan heeft een knikker een diameter van een nanometer.

Dit hoofdstuk zal eerst een korte uitleg geven over halfgeleiders en grafeen, en waarom deze materialen zo interessant zijn. Vervolgens zal worden uitgelegd hoe de elektronische eigenschappen van deze twee materialen gecombineerd kunnen worden, en waarom daarvoor specifiek nanolithografie gebruikt wordt. Vervolgens zullen de hoofdstukken in dit proefschrift kort worden samengevat.

## Halfgeleiders

Allereerst, wat wordt er precies bedoeld met halfgeleiders? Halfgeleidermaterialen zijn materialen die in zuivere toestand niet geleiden, maar die makkelijk geleidend kunnen worden gemaakt door bepaalde 'verontreinigingen' toe te voegen aan het niet geleidende materiaal. Een klassiek voorbeeld hiervan is silicium (Si), dat men eerst ontdekte als isolator (Figuur VIII.1A). Door kleine hoeveelheden fosfor (P) of boor (B) toe te voegen kan dit materiaal geleidend worden gemaakt. Door deze eigenschap is de halfgeleider een basiscomponent voor diodes, transistoren en chips, ook vooral omdat de elektronische eigenschappen van dit materiaal makkelijk veranderd kunnen worden.

We willen graag weten wat er elektronisch gezien precies gebeurt met de ladingsdragers (elektronen) in een halfgeleider. Dit kan worden omschreven door middel van een zogenaamde bandenstructuur, die aangeeft welke elektronische toestanden, beschreven door een koppel van energie en momentum, toegestaan zijn. De bandenstructuur is een theoretisch model die voor elk materiaal uniek is, en kan gebruikt worden om veel fysieke eigenschappen van een materiaal af te leiden, zoals de geleiding en de optische absorptie.

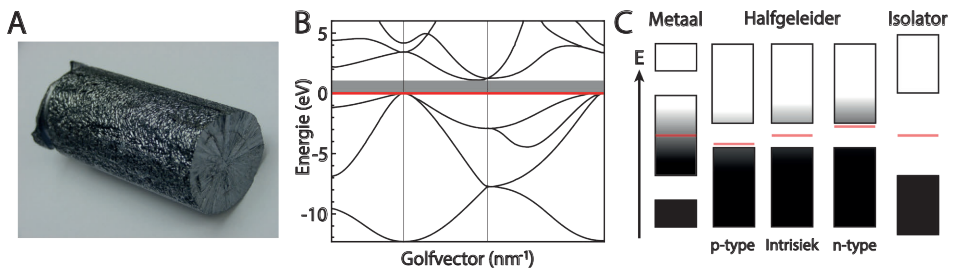


**Figure VIII.1:** (A) Een stuk silicium, een zeer bekende halfgeleider die als hoofdcomponent gebruikt wordt in computerchips. (B) Bandenstructuur van silicium, waarbij de bandkloof is aangegeven met grijs, en het Fermi-energie is aangegeven met een rode lijn. (C) Schematische weergaven van de laagste band die nog gevuld is met elektronen (valentieband) en de eerstvolgende lege band (geleidingsband) voor een metaal, halfgeleider en een isolator.

De bandenstructuur van silicium is weergegeven in Figuur VIII.1B. De toegestane energietoestanden zijn aangegeven met zwarte lijnen, die ook wel banden worden genoemd. We kunnen deze energietoestanden van beneden naar boven vullen met elektronen: elektronen zullen daarbij als eerst de vrije toestand van een zo laag mogelijke energie bezetten tot een bepaald energiepunt waar alle elektronen gevuld zijn. Dit energiepunt wordt ook wel de Fermi-energie genoemd, vernoemd naar de Italiaanse natuurkundige Enrico Fermi. De Fermi-energie is dus de energie van het hoogst gevulde energieniveau in de grondtoestand van de elektronen. In de bandenstructuur voor intrinsiek silicium is dit punt aangegeven met een rode lijn.

De bandenstructuur laat zien dat de Fermi-energie voor intrinsiek silicium precies in

---

een gebied ligt waar geen banden zijn (grijs gebied). Dit gat wordt ook wel een bandkloof genoemd. De verschillende elektronische eigenschappen van isolatoren, geleiders en halfgeleiders kunnen verklaard worden door de positie van het Fermi-niveau ten opzichte van de bandkloof. Een vereenvoudigende schematische weergave van de bandenstructuur van verschillende materialen is te zien in Figuur VIII.1C, waarin de energietoestanden en bandkloof zijn te zien voor metalen, halfgeleiders en isolatoren. De laatst gevulde band onder de Fermi-energie wordt ook wel de valentieband genoemd, en de eerstvolgende lege band wordt de geleidingsband genoemd.

Als het Fermi-energie (aangegeven met een rode lijn) halverwege een band ligt, zijn er dus hoger gelegen energietoestanden die bezet kunnen worden door elektronen. Door toevoeging van energie kunnen elektronen deze toestanden bezetten, vrijkomen uit het atoomrooster en vrij bewegen door het materiaal: dit zorgt voor elektrische geleiding. Dit materiaal wordt ook wel een metaal genoemd.

Het Fermi-niveau kan ook midden in een energiekloof liggen, wat dus ook geldt voor silicium. Als deze kloof heel groot is, dan is er geen enkele manier mogelijk om elektronen over te brengen van die valentieband naar de geleidingsband: het materiaal wordt dan een isolator genoemd, en geleiding is niet mogelijk in z'n materiaal. Bij een halfgeleider ligt de Fermi-energie ook midden in een bandkloof, maar is deze kloof relatief klein: elektronen kunnen dan nog wel in de valentieband gebracht worden. De elektronen kunnen de bandkloof overbruggen door er veel energie aan mee te geven waardoor ze de geleidingsband kunnen bezetten, en zodoende de halfgeleider geleidend maken. Een gemakkelijkere manier is echter om 'verontreinigingen' in te brengen. Door Si te doperen met P of As kunnen we de positie van het Fermi-niveau verhogen tot dicht bij de conductieband, waardoor er vrije elektronen zijn in de conductieband (n-type halfgeleider). Omgekeerd kunnen we B doping toebrengen die het Fermi-niveau tot juist boven de gevulde valentieband brengt. Hierdoor ontstaan lege niveaus in de valentieband, 'gaten' die als positieve quasi-deeltjes ook voor geleiding zorgen. Dit is schematisch aangegeven in Figuur VIII.1C. Het verschil tussen isolatoren en halfgeleiders is dat voor isolatoren de energiegrootte van de bandkloof tussen de valentieband en de geleidingsband groter is dan 5 elektronvolt (eV), waarbij conventionele halfgeleiders een bandkloof hebben tussen de 1 en 1.5 eV.

## Honingraat-geometrie

Het belangrijkste kernwoord in dit onderzoek is de honingraat-geometrie, maar wat maakt deze zeshoekige symmetrie zo interessant? De interesse in de honingraat-geometrie is ontstaan vanuit grafeen (Figuur VIII.2A), een materiaal wat is opgebouwd uit een enkele laag koolstofatomen die in een honingraatstructuur zitten. Grafeen is een geleidend materiaal, wat betekent dat de elektronen in een honingraatstructuur door het grafeen bewegen. Deze combinatie geeft grafeen bijzondere elektronische eigenschappen, die we kunnen begrijpen door naar de bandenstructuur te kijken. De bandenstructuur van grafeen (Figuur VIII.2B) laat zien dat rond de Fermi-energie de elektronen een lineair verband hebben tussen de kinetische energie en hun impulsmo-

ment in plaats van een kwadratisch verband, wat normaal is voor deeltjes met massa. In de natuurkunde is een lineair verband tussen de energie en golfvector kenmerkend voor massaloze lichtdeeltjes, die fotonen worden genoemd. Fotonen zijn de snelste deeltjes die we kennen, die in vacuüm bewegen met een snelheid van 300.000 km/s. Dit betekent dus dat elektronen, normaal gezien deeltjes met een bepaalde massa, bij deze energietoestanden zich gedragen als massaloze lichtdeeltjes.

Alhoewel de elektronen in grafen niet de snelheid van het licht bereiken, is het experimenteel aangetoond dat ze slecht 300 keer langzamer bewegen dan de snelheid van het licht: effectief betekent dit dat grafen honderd keer beter elektrisch geleidt dan silicium. Het lineaire verband in de bandenstructuur komt overeen met een Dirac-kegel in het energie-momentum schema  $E(p_x, p_y)$  (elk impuls moment in het grafen vlak is een vector combinatie van de  $x$ - en  $y$ -component). Dit is schematisch weergegeven in Figuur VIII.2C. Hierbij laten we alleen de valentieband en de geleidingsband zien. We zien dat kegels in het energie schema de energietoestanden beschrijven waarbij de elektronen zich gedragen als massaloze lichtdeeltjes.

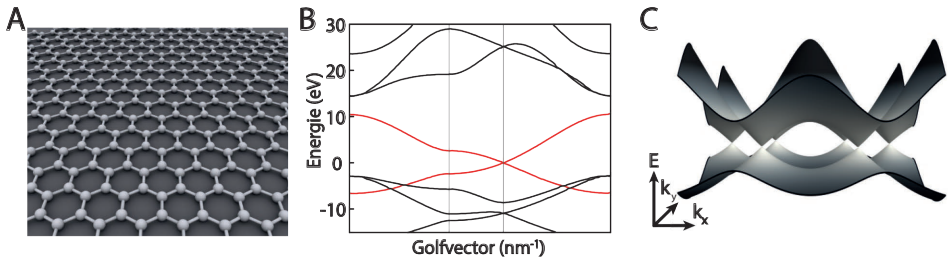


**Figure VIII.2:** (A) Schematische weergave van het materiaal grafen, wat is opgebouwd uit een enkele laag koolstofatomen in een honingraatstructuur. (B) De bandenstructuur van grafen. Op de plek waar de energie nul is raken twee banden aangegeven in rood elkaar precies zonder dat ze overlappen. Rondom dit punt is een lineair verband te zien. (C) Een tweedimensionale weergave van de twee banden waar ze elkaar raken. Als gevolg van het lineaire verband vormen de banden kegels, die ook wel Dirac kegels genoemd worden.

## Honingraat halfgeleiders

Het doel van dit onderzoek is om de elektronische eigenschappen van grafen te combineren met de elektronische eigenschappen van halfgeleiders. Maar waarom willen we dit eigenlijk onderzoeken, aangezien grafen op zichzelf al zo interessant is? De voornaamste reden hiervoor is dat grafen geen halfgeleider is, maar een zogenaamde halfmetaal: de valentieband en geleidingsband raken elkaar perfect op de Fermi-energie. Dit betekent dat grafen geen bandkloof heeft dicht bij het Fermi-niveau, wat het moeilijk maakt om het materiaal elektrisch te switchen van een toestand met veel ladingsdragers naar een toestand zonder ladingsdragers. Dit elektrisch switchen in een transistor is noodzakelijk bij logische operaties die plaatsvinden in grote circuits van transistoren in een computer. Hiervoor wordt gedopeerd Si gebruikt.

---

De interessante elektronische eigenschappen van grafeen, bijvoorbeeld de hoge snelheid van de elektronen, zijn gerelateerd aan de intrinsieke honingraat symmetrie. Tweedimensionale halfgeleiders met dezelfde honingraat geometrie behouden hun normale band kloof, maar de structuur van de conductie- en valentiebanden wordt mede bepaald door de honingraat geometrie, en lijkt dus op de Dirac kegels van grafeen. De periodiciteit van de honingraat is tientallen nanometers, veel groter dan bij grafeen. Daardoor is de energie breedte van de Dirac banden veel kleiner dan bij grafeen, en zijn de eigenschappen alleen goed te bestuderen bij voldoende lage temperatuur. Tweedimensionale halfgeleidermaterialen met een honingraat nanogeometrie worden in dit onderzoek honingraat halfgeleiders genoemd.

De methode om honingraat halfgeleiders te maken in dit onderzoek is een zogenaamde top-down benadering. Eerst wordt een tweedimensionaal halfgeleidermateriaal gegroeid van enkele atoomlagen dik op een ander materiaal. Daarbij wordt gebruik gemaakt van groeiprocessen die goed bekend zijn in de halfgeleiderindustrie. In die dunne, tweedimensionale halfgeleider zitten de elektronen gevangen in de verticale  $z$ -richting, maar ze kunnen vrij bewegen in de  $x$ - en  $y$ -richting in het vlak. Vervolgens wordt een periodiek hexagonaal rooster van kleine gaten aangebracht in de dunne halfgeleider. Een schematische weergave hiervan is te zien in Figuur VIII.3A. Door de gaten (weergegeven in blauw) in een hexagonale configuratie te plaatsen, worden de vrije elektronen in de halfgeleider gedwongen om in een honingraat symmetrie te bewegen, dus zoals in grafeen. De honingraat halfgeleider kan in perspectief worden gezien in Figuur VIII.3B. De technologische uitdaging bestaat erin de gaten zo klein mogelijk te maken en zo dicht mogelijk bij elkaar te zetten, en tegelijkertijd de hexagonale orde zo goed mogelijk te handhaven. Hoe kleiner de rooster periodiciteit, hoe breder de banden, en hoe robuster de elektronische Dirac structuur. Een dergelijk rooster van gaten wordt gemaakt met behulp van een techniek die veelgebruikt wordt door de halfgeleiderindustrie: lithografie.

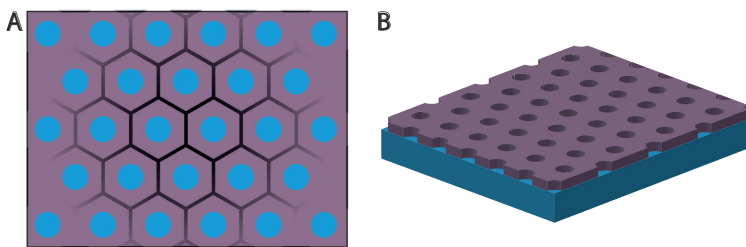


**Figure VIII.3:** (A) Bovenaanzicht en (B) zijaanzicht van een honingraat halfgeleider.

---

## Lithografie

Het woord lithografie is afgeleid van de Oudgriekse woorden *lithos* (steen) en *graphein* (tekenen/schrijven), wat dus letterlijk vertaald naar steendruk. Het is een druktechniek wat is ontwikkeld tussen 1794 en 1798 door Alois Senefelder. Vroeger werd

## VIII Samenvatting in het Nederlands

---

lithografie gebruikt voor het drukken van tekeningen en teksten door deze aan te brengen in een bepaald soort kalksteen. Door deze vochtig te houden en het tekenmateriaal te vervangen voor drukinkt kan de afbeelding worden overgebracht op papier. Later kon door een meer ingewikkelde procedure ook meerkleurdrukken gemaakt worden met deze techniek, wat uiteindelijk vooral z'n toepassing vond in het maken van tekeningen. Een mooi voorbeeld hiervan is een litho van *De Aardappeleters*, een wereldberoemd schilderij van Vincent van Gogh (Figuur VIII.4).

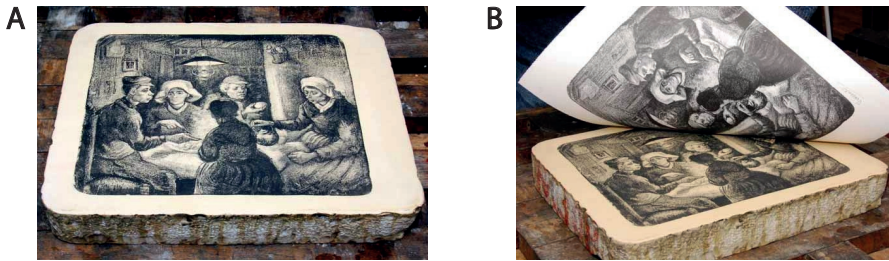


**Figure VIII.4:** (A) Een tekening van *De Aardappeleters* (1885), origineel geschilderd door Vincent van Gogh. Deze tekening is gemaakt in kalksteen, wat gebruikt kan worden voor lithografie. (B) De tekening is direct gedrukt op papier door middel van een steindruk.

---

De hedendaagse lithografie techniek die gebruikt wordt om elektronische schakelingen te maken ziet er iets anders uit. Deze lithografie techniek wordt fotolithografie genoemd, en stelt ons in staat om zeer kleine structuren te 'printen' met een grootte tussen enkele micrometers en honderden nanometers groot. Het lithografieproces is schematisch weergegeven in Figuur VIII.5A. De techniek maakt gebruik van een fotogevoelig masker, die als eerst aangebracht wordt op het materiaal. Tijdens het lithografieproces zelf wordt er licht op het masker beschenen, die de oplosbaarheid van het fotogevoelige masker verandert. Dit is in Figuur VIII.5A aangegeven met rode gebieden. Tijdens de ontwikkelstap waarbij het belichte materiaal in een chemisch bad wordt geplaatst wordt de belichte of juist onbelichte deel van de fotogevoelige laag verwijderd. We eindigen dus met een chemisch masker met een bepaald patroon in deze laag. Het patroon wordt dan in de halfgeleider geprint door de rest van de fotogevoelige laag te bombarderen met ionen en/of moleculen. Het voordeel van deze lithografie techniek is dat het uitermate geschikt is voor massafabricatie van elektronische schakelingen in bijv. computerchips. In Figuur VIII.5B is een foto te zien van een silicium schijf die is bewerkt met fotolithografie, waarin honderden microchips geprint zijn. Elk van deze microchips bestaat weer uit miljarden transistoren

In dit proefschrift wordt geen gebruik gemaakt van fotolithografie, maar zijn andere, vergelijkbare lithografie technieken gebruikt voor het fabriceren van honingraat halfgeleiders. De direct reden hiervoor is omdat conventionele fotolithografie niet verfijnd genoeg is om roosters te maken met voldoende kleine periodiciteit ( $< 50$  nm).

De eerste lithografietechniek die is gebruikt is elektronenbundellithografie. De principes zijn precies hetzelfde als bij gewone fotolithografie, alleen wordt het fotogevoelige masker

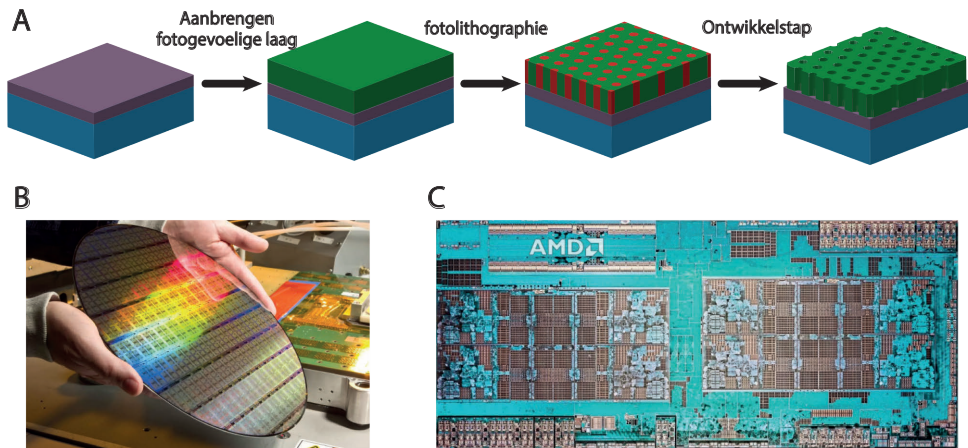


**Figure VIII.5:** (A) Schematische weergaven van het fotolithografieproces. (B) Een silicium wafer waarin honderden computerchips zijn gemaakt door middel van fotolithografie. (C) Een foto van een processor, die opgebouwd is vanuit miljarden transistoren. Deze zijn allemaal gemaakt met behulp van fotolithografie.

niet beschenen met licht, maar met elektronen (Figuur VIII.6A). Hiermee kunnen structuren geprint worden ter grootte van enkele tientallen nanometers, wat ongeveer 100 keer kleiner is vergeleken met conventionele fotolithografie. Een elektronmicroscop afbeelding van het hexagonale patroon gemaakt met elektronenbundellithografie is te zien in Figuur. VIII.6B. Een groot nadeel van deze techniek is dat het nog niet geschikt is voor massafabricatie, omdat structuren individueel moeten worden beschenen. Dit kost ontzettend veel tijd. Zo heeft deze techniek ongeveer 12 dagen nodig om een oppervlakte van een kubieke centimeter te printen. Om deze reden wordt er veel onderzoek gedaan in elektronenbundellithografie om het proces te optimaliseren, en laat deze techniek ook vooral zien dat het mogelijk is om nog kleinere structuren te printen vergeleken met fotolithografie.

De andere lithografie techniek die is gebruikt in dit onderzoek heet blokcopolymerlithografie. Dit is een lithografie techniek die gebruik maakt van twee verschillende chemische verbindingen die bestaan uit zeer grote moleculen. Deze zogenaamde polymeren kunnen op het halfgeleidermateriaal worden aangebracht, waar ze een zelfassemblage proces ondergaan door het masker te verwarmen (Figuur. VIII.6C). Tijdens dit proces ordenen de polymeren zich in een bepaalde symmetrie, zoals bijvoorbeeld vierkant of hexagonale structuren. De symmetrie en grootte kan gecontroleerd worden door de compositie van de polymeer en de lengte van de polymeerketting te veranderen. Doordat het zelfassemblage proces verschillend loopt per gebied, zullen de gaten niet zo mooi gerangschikt zijn als bij het andere lithografieproces. Dit is goed te zien op de elektronmicroscop afbeelding van Figuur. VIII.6D. Het voordeel van dit proces is dat nog kleinere structuren gemaakt kunnen worden, en dat het proces snel uitgevoerd kan worden over grote oppervlaktes.

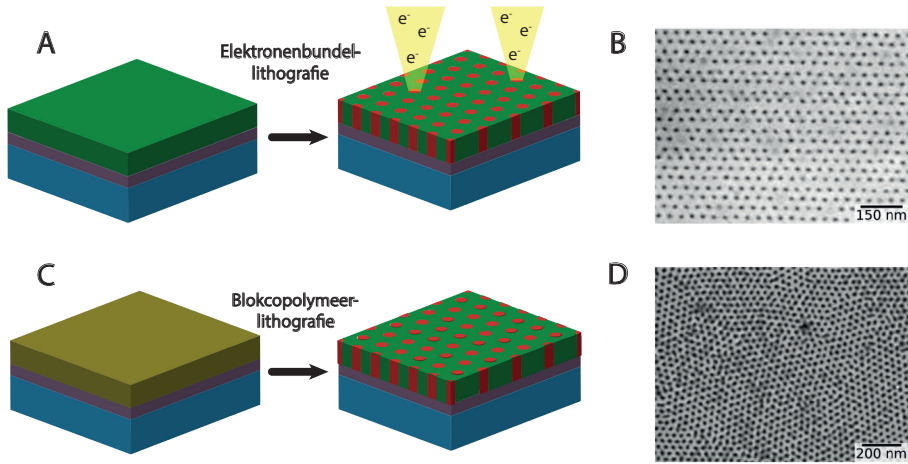


**Figure VIII.6:** (A) Schematische weergave van elektronenbundellithografie, met daarbij een raster elektronenmicroop afbeelding van de gemaakte honingraat halfgeleider met behulp van deze techniek. (B) Schematische weergave van blokcopolymeerlithografie, met daarbij een raster elektronenmicroop afbeelding van de gemaakte honingraat halfgeleider.

## Wat staat er in dit proefschrift?

In dit proefschrift wordt onderzoek gedaan naar de elektronische eigenschappen van tweedimensionale InGaAs halfgeleiders met een honingraat nanostructuur. Dit proefschrift kan worden onderverdeeld in drie delen: modelleren, maken en meten. Eerst wordt de honingraat halfgeleider gemodelleerd door middel van het zogenaamde *muffin-tin* model, waaruit de elektronische eigenschappen kunnen worden berekend. Vanuit hier kunnen we de elektronische eigenschappen veranderen en optimaliseren door de posities en grootte van de putten te veranderen (Hoofdstuk III). Vervolgens worden de honingraat halfgeleiders gefabriceerd, zowel door middel van elektronenbundellithografie als met behulp van blokcopolymeerlithografie (Hoofdstuk IV en V). De elektronische structuur van de gefabriceerde honingraat halfgeleiders wordt gemeten door middel van rastertunnelmicroscopie, waarmee de lokale elektronische eigenschappen van het rooster nauwkeurig onderzocht kan worden (Hoofdstuk V). De resultaten worden vergeleken met het theoretische *muffin-tin* model, en het effect van wanorde in het honingraatrooster wordt zo kwantitatief mogelijk bepaald (Hoofdstuk VI).

**Hoofdstuk II** beschrijft de theorie en methodologie om het onderzoek in dit proefschrift te begrijpen. Eerst worden de algemene elektronische eigenschappen van bulk en tweedimensionale halfgeleiders uitgelegd. Door gebruik te maken van een *tight-binding model* worden de interessante elektronische eigenschappen van grafen onderstreept. Door deze twee theorieën te combineren voorspellen we de elektronische structuur van een honingraat halfgeleider. Verder wordt in dit hoofdstuk de fabricatiemethodologie van de honingraat halfgeleiders besproken, inclusief de apparatuur die daarvoor nodig is. Als laatste leggen we in meer detail uit hoe we de elektronische structuur van honingraat halfgeleiders kunnen meten met rastertunnelingmicroscopie en

---

spectroscopie.

**Hoofdstuk III** behandelt twee verschillende *muffin-tin* modellen die de elektronische structuur van de honingraat halfgeleider omschrijven. In een analytische aanpak van het model kunnen we de bandenstructuur modelleren door een tweedimensionaal elektrongas op te sluiten in een periodiek hexagonaal rooster van gaten. De gaten worden beschreven als hoge-energie gebieden waar elektronen dus niet kunnen komen (een hexagonaal 'anti-rooster'). We kunnen de elektronische eigenschappen optimaliseren door de parameters van het antirooster aan te passen. Daarbij zullen bijkomende effecten meegenomen worden in de berekening om meer realistische resultaten te verkrijgen. Aansluitend wordt de Schrodinger vergelijking voor het *muffin-tin model* numeriek opgelost. De berekende energieniveaus, die banden vormen, kunnen we dan vergelijken met de toestandsdichtheid gemeten met rastertunnelingspectroscopie.

**Hoofdstuk IV** beschrijft het werkschema om honingraat halfgeleiders te maken met behulp van elektronenbundellithografie. Door een dunne laag van het halfgeleider materiaal InGaAs te groeien op een andere halfgeleidermateriaal kunnen we een kwantumput creëren waarin we een tweedimensionaal elektrongas verkrijgen. Een hexagonaal antirooster in het InGaAs materiaal wordt verkregen door middel van elektronenbundellithografie en verschillende ets procedures. De structurele kwaliteit van het gemaakte honingraat halfgeleider, dus de vorm en de periodiciteit van de gaten rooster, wordt gekwantificeerd met verschillende methodieken.

**Hoofdstuk V** presenteert de elektronische eigenschappen van een honingraat halfgeleider gemeten met rastertunnelingmicroscopie en spectroscopie. Door middel van blok-copolymeerlithografie verbeteren we de kwaliteit en de dimensies van de honingraat halfgeleider. Aan de hand van de  $dI/dV$ -spectra (toestandsdichtheid) observeren we een robuuste "vlakke band" op specifieke symmetrie punten van het honingraatrooster. Een elektronische vlakke band is een band waarbij de energie van de elektronen constant is, dus onafhankelijk van hun impuls of hun golflengte. Een vlakke band is een generieke eigenschap van de honingraat halfgeleider op voorwaarde dat er geen hybridisatie plaatsvindt tussen de on-site orbitalen. De vlakke band verdween niet als gevolg van de structurele wanorde in het honingraatrooster. Dit resultaat is een aansprekend voorbeeld van hoe rooster-geometrie kan resulteren in zeer speciale elektronische eigenschappen.

**Hoofdstuk VI** laat met behulp van twee theoretische modellen, namelijk het *muffin-tin* model en de *tight-binding* model, zien wat het effect is van wanorde in een honingraatrooster op de elektronische eigenschappen van het honingraat halfgeleider. Hierbij worden verschillende types van wanorde meegenomen in het model en laten we zien dat de verwachten effecten terug te zien zijn in de experimentele metingen. Het model laat zien dat de berekende vlakke band in het model bestand is tegen de energieverbreding wat veroorzaakt wordt door de roosterwanorde.

**Hoofdstuk VII** behandelt de verdere optimalisatie, toepassingen en mogelijkheden van het onderzoek in dit proefschrift. Verdere verbeteringen van de orde en verlagening van de periodiciteit in de honingraat halfgeleider is nu al mogelijk door middel

van nieuwe lithografie technieken zoals rasteraaldlithografie. Door een meetcircuit te maken in de honingraat halfgeleider kunnen elektrische transport metingen uitgevoerd worden. De resultaten zijn van groot belang in de natuurkunde, en zullen wellicht ook duidelijk maken of het voordelig is om honingraat halfgeleiders te gebruiken in transistoren, bijvoorbeeld om gebruik te maken van de grote elektronenmobilititeit. Als laatste laten we zien er ook andere geometrieën leiden tot een interessante bandenstructuur. "Rooster engineering" laat toe om halfgeleiders te fabriceren met elektronische banden die interessant zijn voor de wetenschap, maar ook voor specifieke toepassingen.

# Acknowledgements

After four and a half years, this scientific adventure has come to an end. In this period I have been supported by many professional colleagues, musical colleagues, friends and family. I would like to thank everyone who has supported and/or contributed to my work in these years.

Allereerst wil ik graag mijn promotor **Daniel Vanmaekelbergh** bedanken, die mij niet alleen heeft begeleidt tijdens mijn promotieonderzoek, maar ook tijdens mijn masteronderzoek. Daniel, door de jaren heen heb ik veel van jou geleerd: hoe je gecompliceerde problemen, theorieën en resultaten kan terug brengen naar een simpele oplossing, en er niet alleen naar kan kijken met een natuurkundige blik, maar om deze problemen ook te bekijken door een scheikundige bril. Ook je enthousiasme over het onderzoek heeft me zeer geïnspireerd. Onze interesse in klassieke muziek hebben we ook samen kunnen delen, wat resulteerde dat je regelmatig bent komen luisteren naar een van mijn concerten.

I performed much of my research in Lille, where I met many new colleagues who worked together with me on this project. **Bruno Grandidier** and **Christophe Delerue**, I want to thank you both for your excellent supervision on the project, and for your hospitality when I was in Lille. Although I do not have any copromotors, I always had the feeling that both of you were my copromotors. You helped me tremendously on both the theoretical side as on the experimental side of the project. Also I want to thank you for organizing the summerschool on Corsica!

**Nathali Vergel**, you helped me a lot with the sample fabrication during the entire project, especially when I couldn't be in Lille. It was also nice that you could come and visit Utrecht for STM measurements, I really enjoyed those days where we could actually perform measurements on our work! **Yannick Lambert**, you were the first guy in Lille who helped me during my first year of my research, which I am really grateful for. Not only we could get along in our passion for science, but also in our passion for football! **Tao Xu**, I want to thank you for your help during the writing of our first paper, and your critical view on the paper. **Athmane Tadjine**, although we did not work together for a long time, you helped me enormously with your theoretical paper which started this whole project, and which also inspired me to investigate the theoretical side of the project. I really enjoyed your PhD defence, I was glad I could be there! There are also many engineers in the Dirac III-V project who helped in

the fabrication process of the samples. I want to thank **Xavier Wallart**, **Ludovic Desplanque**, **Francois Vaurette** and **Dimitri Yarekha** who helped and/or assisted me during the growth process, lithography process or etching process of the samples. I also want to thank all the colleagues from the other French institutes in which we worked together in this project.

Part of the research that I performed in Utrecht was achieved in the basement of the Ornstein building, together with the members of 'Team Kelder' and multiple scanning probe microscopes. I have worked in CMI with Team Kelder for approximately 6 years, and I have seen the group grow with the addition of multiple microscopes, scientists and students! I had a great time working together with my colleagues, and therefore I would like to thank Ingmar, all PhDs, postdocs and students.

**Ingmar Swart**, van deze groep ongeregelde onderzoekers heb je een hele mooie onderzoeksgroep gemaakt, die nog steeds flink aan het uitbreiden is! Alhoewel je niet direct betrokken was bij mijn project, stond je wel altijd klaar als ik tegen problemen aan liep, en was je altijd zeer betrokken en hulpvaardig bij m'n project. Naast het onderzoek ben je ook altijd zeer betrokken bij de collega's met wie je samenwerkt, en heb je me ook het belang laten zien van een groep die altijd voor elkaar klaar staat. Ook heb ik zeer genoten van onze tijd buiten CMI, met als hoogtepunt toch wel de voetbaldag die je had georganiseerd in Ankeveen!

**Marlou Slot**, met jou als mijn begeleider tijdens m'n masteronderzoek heb ik toch de knoop doorgehakt om een promotieonderzoek te gaan doen bij CMI, wat erin resulteerde dat we ook nog als collega's konden samenwerken! Jij hebt me geleerd dat onderzoek doen ook een kwestie is van precies en concencieus werken, wat toch niet mijn sterkste kant bleek te zijn. Buiten het onderzoek om was het ook altijd heel gezellig en konden we elkaar altijd vinden in de muziek. Ze boffen maar in Washington dat je daar een postdoc bent gaan doen, ze hebben daar een zeer goede onderzoeker erbij gekregen!

**Tomas Meerwijk**, ik heb de eer gehad om jou te mogen begeleiden tijdens je bachelor en masteronderzoek, eerst op de AFM en daarna op de STM. Je hebt me ontzettend geholpen met de STM metingen in Utrecht, en de meettijd een stuk aangenamer gemaakt met je foute muzieksmaak die je aan mij hebt overgedragen. Ik mis onze broodjes saliccia op bij de lunch op vrijdag!

**Jesper Moes**, een zeer gewaardeerde collega die altijd paraat staat voor mij en andere, en die me ontzettend heeft geholpen met de STM metingen in Utrecht. Buiten de werkvloer zijn we vaak samen aan het squashen, klaverjassen, gamen of hebben we leuke snooker/pool avondjes. Bedankt voor alle leuke momenten, ik hoop dat er nog vele zullen volgen! **Peter Jacobse**, jouw toewijding aan de wetenschap en de voetbaltafel heeft me altijd geïnspireerd. Je staat altijd helemaal open voor alles en iedereen, dit waardeer ik enorm aan jou. Ik hoop je snel te mogen opzoeken in Berkeley! **Saoirsé Freeney**, you were an amazing office mate, and although you had some hiccups during your research, you never lost your happiness! I always loved to share our cooking and baking experiences with each other, your Bombay potatoes are still fre-

---

quently cooked! **Thomas Gardenier**, een collega aan wie je altijd vragen kan stellen en met wie je altijd kan babbelen, zowel over wetenschap als over muziek! Gelukkig heeft de vete tussen het USC en het USKO ons nooit in de weg gezeten. Ontzettend bedankt voor je hulp tijdens m'n metingen in Utrecht! **Pierre Capiod**, we directly hit it off! You helped me tremendously with my research, with the connection you have with Lille, and we had an amazing time at the summerschool in Corsica. I will always remember you as the guy that when you make a picture of him, that the picture will be something special! I'm happy for you that you started working together with Bruno in Lille again, and I hope to visit you there soon! **Pascal Vermeeren**, je passie voor organische chemie heeft mij, als natuurkundige, altijd verbaasd. Ondanks deze mismatch konden we elkaar altijd vinden in onze liefde voor Ajax, maar ook vooral in die ene karaokebar in Amsterdam (ik zal ons duet daar nooit vergeten)! **Jette van den Broeke**, bedankt voor alle goede theoretische discussies! **Jan Cupe-rus** en **Rian Ligthart**, ik heb jullie hele traject door de universiteit meegemaakt, en nu zijn jullie zeer gewaardeerde collega's geworden! Ik wens jullie veel succes met jullie onderzoek (pas goed op m'n AFM **Jan**), hopelijk gaan jullie veel mooie metingen doen met de nieuwe microscoop! Als laatste wil ik **Jos Mulkens** bedanken! Jos, je nieuwsgierigheid en doorzettingsvermogen in de wetenschap heb ik zeer gewaardeerd: als je een vraag had, ging je pas weg als het hele verhaal duidelijk is! Ik wil je ook vooral speciaal bedanken dat je me hebt geïntroduceerd in jouw brassband, waar we nu samen in spelen!

I also want to thank all the bachelor and master students of 'Team Kelder' who I worked with, without who all our research and great atmosphere would not have been possible! Thank you **Sam Bormann**, **Jan Jurre Harsveld van der Veen**, **Mark Mangnus**, **Jaap Hartevelde**, **Thomas Mercadier**, **Leon Arends**, **Auke Vlasblom** and **Lisanne Knijff**!

Team Kelder is onderdeel van de groep Condensed Matter and Interfaces (CMI), waar ik ook een aantal mensen wil bedanken! Ik wil allereerst beginnen met de organisatie binnen onze groep! **Andries Meijerink**, **Celso de Mello Donega** and **Zeila Zanolli**, thank you very much for leading this open and warm research group, for your interest during the group meetings and for organizing all of the activities! Daarnaast wil ik ook graag **Harold de Wijn** bedanken voor de interesse in m'n werk en voor z'n leerzame college's! Uiteraard mag de technische ondersteuning niet ontbreken, en daarom wil ik ook **Peter van den Beld** en **Hans Ligthart** bedanken! Jullie staan altijd klaar om een oplossing te vinden voor de technische miserie waar we tegenaan liepen, en zorgen voor een goede en leuke sfeer in de groep! Ook gaat er grote dank uit naar **Stephan Zevenhuizen** voor de geleverde IT support! **Linda Kummeling** en **Silvia Benschop**, veel dank voor jullie hulp in de organisatie, en jullie persoonlijke interesse in iedereen die in onze groep werkt! Ook al werken jullie meer achter de schermen, zullen hebben een grote toegevoegde waarde in het werk wat we doen!

Nu wil ik graag m'n directe collega's bedanken! **Tim Prins**, wij gaan werkelijk all the way sinds we waren begonnen aan onze masteronderzoek in CMI! Je bent een zeer gewaardeerde collega en vriend, en ik ben zeer blij dat je m'n paranimf wilt zijn op

m'n verdediging! Je bent altijd zeer meegaand met mensen wat ik zeer in je waardeer! Niet alleen op de werkvloer ben je vaak de last man standing, maar ook vaak samen in de bar zijn we nog tot laat te vinden! Ik hoop dat we nog veel squash potjes mogen spelen, dat we nog veel voetbal mogen spelen/kijken en dat we nog veel biertjes mogen brouwen en drinken! **Annalisa Brodu**, as my very appreciated officemate you were always the last one who entered our office, but also the last one who went home! I had a great time with you in our office, and sorry that Tim and I gave you a hard time now and then. **Bas Salzmänn**, je nuchtere blik op de wereld kon ik altijd zeer waarderen, en er was altijd tijd voor een praatje over werk of daarbuiten. Vooral op de zomerschool op Corsica hebben we elkaar echt leren kennen! Bedankt voor alle leuke en gezellige momenten! **Jur de Wit**, ik heb je meegemaakt tijdens de werkcolleges, en nu ben je een zeer goede collega op werk! Ook al heb je een aantal pogingen ondernomen om mij fysiek wat aan te doen, hoop ik dat we snel weer wat squash potjes kunnen spelen! **Ian Pompermayer**, my good Brazilian friend! You were a great colleague in our group, where you shared your love for science and beer with everyone! **Jaco Geuchies**, jouw enthousiasme en interesse in de wetenschap heb ik altijd zeer gewaardeerd, en ik ben blij dat we niet alleen samen hebben mogen werken op CMI, maar dat we daarnaast elkaar ook hebben gevonden als hardloophuddy, waar we samen grote afstanden overbruggen. Ik hoop dat onze marathon in Rotterdam dit jaar doorgaat! **Naud van Bunningen**, met jou erbij is de vrijmibo nooit saai! Ook onze voorliefde voor koffie konden we delen! **Maryam Alimoradi Jazi**, thank you for the nice conversations that we had, and especially your addicting laugh! **Annelies van der Bok**, bedankt voor je aanwezigheid en gezelligheid in de groep, de bordspelletjes vrijmibo's waren altijd gezellig! **Federico Montanarella**, in exchange for some Mathematica advice you gave me a great time in the group, I especially remember the great time we had in Torremolinos! **Serena Busatto**, I really enjoyed your enthusiasm for everything, especially for online escape rooms. **Joep Peters**, met jou is het niet alleen goed praten over werk, maar je bezorgt ook iedereen een goede tijd, bedankt hiervoor! Ook wil je nog graag bedanken voor het versieren van mijn bureau!

Lastly, I want to thank all my colleagues for the great atmosphere in our group, not only for being there to discuss research and the good conversations, but also for the nice time we had off the workfloor, such as in 'groepsuitjes', national and international conferences, defence parties, the Christmas events where we displayed our 'sjoelen' and 'klaverjas' talents and all the Debye events. Thanks to all of you, **Anne Berends**, **Carlo van Overbeek**, **Sophia Buhbut-Sinai**, **Jara Vliem**, **Pradip Chakraborty**, **Liudmyla Chepyga**, **Jeppe Christiansen**, **Robin Geitenbeek**, **Onno Gijzeman**, **Per-Anders Hansen**, **Elleke van Harten**, **Jacobine van Hest**, **Mathijs de Jong**, **John Kelly**, **Vasilii Khanin**, **Chun Che Lin**, **Marie van de Haar**, **Christa van Oversteeg**, **Freddy Rabouw**, **Tim Senden**, **Maaïke van der Sluijs**, **Giuseppe Soligno**, **Atul Sontakke**, **Sadakzu Wakui**, **Kelly Sowers**, **Ward van der Stam**, **Markus Suta**, **Pedro Villanueva-Delgado**, **Dick de Boer**, **Zijun Wang**, **Weiwei Wu**, **Chenghui Xia**, **Kunyuan Xu**, **Wenjin Xu**, **Dechao Yu**, **Ting Yi**, **Li Huaiyong** and all students who performed their research in our group!

Buiten het werk wil ik uiteraard ook een hoop vrienden bedanken die mij hebben

---

gemaakt tot wie ik nu ben. Met vrijwel iedere persoon heb ik samen mooie muziek mogen maken in verschillende symfonie orkesten, wat me niet alleen een uitlaatklep bood, maar wat me ook verrijkt heeft als persoon.

**Daniel**, jij kwam in 2016 voor een jaar meespelen met het Utrechtsch Studenten Concert (USC), en binnen dit jaar hebben we een geweldige band opgebouwd! Ondanks dat je weer terug bent in Duitsland, zoeken we je nog steeds ieder half jaar op in Heidelberg, en kom jij ook vaak naar Utrecht. Je bent een ontzettend eerlijk en zeer betrokken persoon, en ik ben dan ook zeer blij dat je m'n paranimf wil zijn op mijn verdediging! Ik hoop dat we nog vele jaren huttentochten gaan doen in de Alpen, een van de vele passies die wij delen! **Martijn** en **Daphne**, ook jullie hebben een zeer speciaal plekje in mijn hart. Vijf jaar lang vast aandeel in de kopersectie in het USC, en ik ben zeer blij dat we elkaar nog steeds vaak zien om te gaan hardlopen, eten, goed gesprekken te hebben en wijntjes te drinken! Ik kijk er weer naar uit om samen in de bergen te gaan lopen met jullie! **Joachim**, wij gaan echt lang terug, helemaal tot in 2011 bij ons eerste project in het USC. Daarna hebben we overal in Nederland en Europa samen muziek gemaakt in verschillende symfonieorkesten. Je eerlijkheid, oprechtheid en betrokkenheid waardeer ik zeer! Ondanks dat je nu in Duitsland woont ben ik zeer blij dat we nog steeds contact hebben! **Jurgen**, niet alleen ben ik blij dat we elkaar hebben gevonden tijdens het Nederlands Studenten Orkest in 2016, ook ben ik zeer blij dat ik je mijn huisgenoot mag noemen in onze geweldige TaK casa! Eigenlijk ben ik vooral blij dat ik je vooral niet zie als huisgenoot, maar gewoon als een hele goede vriend!

Een zeer bijzondere vriendengroep die ik heb overgehouden uit mijn tijd in het USC is de '**Ladies who lunch**', waarmee we iedere dinsdag gingen lunchen na de maandagavond borrel met het USC. Alhoewel deze traditie helaas (voorlopig) verloren is gegaan, is de vriendengroep nog steeds gebleven. **Beatrix**, een spontaner persoon dan jij ken ik niet in mijn kringen! Voor goede gesprekken, liefst met een wijntje of biertje erbij, kan ik altijd bij jou terecht, wat je dan altijd weer terugbetaald in de vorm van gezelligheid en een avond vol verrassingen. **Floor**, jij hebt me laten zien dat het niet uitmaakt wat je doet, als je het maar doet voor 100%. Dit geldt niet alleen voor muziek maken, maar ook voor borrels. **Nienke**, niet alleen kunnen wij samen lekker borrelen, maar ook hebben we elkaar gevonden in het hardlopen! **Rachel**, jou moet ik vooral bedanken voor de gezellige wijnavondjes die we hebben gehad! Last but certainly not least wil ik ook graag de rest van deze vriendengroep bedanken de geweldige tijd die ik heb gehad in het USC: **Quentin, Dauwe, Laura, Lucas, Niels** en uiteraard **Myrthe**.

**Jasper, Leon, Siebren** en **Mark**, onze voorliefde voor bier en mooie muziek (vooral de Alpensymfonie) heeft ons samengebracht, en ik kijk er naar uit om dit snel weer op te pakken! **Hanna** en **Remco**, als onderdeel van de 'Instrumetare Rumori' verzorgen wij voor musicaal vuurwerk bij het Bach Ensemble van Amsterdam. Het liefst doen we dit uiteraard in de grote kathedraal van Vezelay, waarna we op de camping weer snel aan de Bourgondische wijn mogen! Snel maar weer doen? **Marlies**, ook jou wil ik nog apart bedanken voor de leuke tijd die we hebben bij Bellitoni, en daarbuiten met de leuke etentjes samen met Jurgen! **Gerben**, ook wij gaan al lange tijd mee samen,

## Acknowledgements

---

helemaal vanaf die tournee naar Marokko! Ik hoop snel dat we weer samen muziek mogen maken in een kopersectie!

**Meron, Floris en Peter-Jan**, ik kijk altijd er weer naar uit als ons whiskyclubje weer bij elkaar komt, om nieuwe whiskies uit te proberen en (vooral moderne) klassieke muziek te gaan luisteren!

Tijdens m'n laatste jaar onderzoek was het schrijven thuis een serieuze uitdaging, maar dat is gelukkig een stuk makkelijker gemaakt toen **Tomas** mij uitnodigde in zijn vriendengroep waarmee we samen games spelen: **Vivian, Amber, Sander, Ralph, Cris, Sebas, Edo, Eline** en **Katelijne**, ontzettend bedankt voor de leuke tijd die we hebben!

Lieve **Anouk**, ook al kennen we elkaar nog niet zo heel lang, ik ben blij dat we elkaar hebben ontmoet in dat koude Amsterdam! Ik hoop dat we samen nog veel leuke dingen gaan meemaken!

Lieve **Corine, Bart, Kees** en **Ellen**! Ontzettend bedankt voor de vele support en steun die jullie mij hebben gegeven, vooral in het afgelopen jaar! Niet alleen stonden jullie mij bij tijdens m'n onderzoek, maar komen jullie ook trouw luisteren naar al mijn concerten! Het is fijn om te weten dat jullie altijd voor mij klaar staan!

# Publications and conference contributions

## Publications

This thesis is based on the following publications:

- L.C. Post, T. Xu, N.A. Franchina Vergel, A. Tadjine, Y. Lambert, F. Vaurette, D. Yarekha, L. Desplanque, D. Stiévenard, X. Wallart, B. Grandidier, C. Delerue, D. Vanmaekelbergh, "Triangular nanoporation and band engineering of InGaAs quantum wells: a lithographic route toward Dirac cones in III–V semiconductors". *Nanotechnology* 30 (15), pp. 155301 (2019). (Chapter III & IV)
- N.A. Franchina Vergel, L.C. Post, D. Sciacca, M. Berthe, F. Vaurette, Y. Lambert, D. Yarekha, D. Troadec, C. Coinon, G. Fleury, G. Patriarche, T. Xu, L. Desplanque, X. Wallart, D. Vanmaekelbergh, C. Delerue, B. Grandidier, "Engineering a Robust Flat Band in III–V Semiconductor Heterostructures". *Nano Letters* 21 (1), pp 680-685 (2021). (Chapter V)
- L.C. Post, C. Delerue, B. Grandidier, D. Vanmaekelbergh. "Electronic investigation of geometric disorder in a honeycomb semiconductor: from a local defect to a glassy system". *In preparation*. (Chapter VI)

## Other publications by the author:

- J.E. Schmidt, F.C. Hendriks, M. Lutz, L.C. Post, D. Fu, B.M. Weckhuysen, "Diagnosing the Internal Architecture of Zeolite Ferrierite". *ChemPhysChem* 19 (4), pp. 367-372 (2017).
- D.S. Gavhane, H. van Gog, B. Thombare, G. Lole, L.C. Post, M.A. More, M.A. van Huis, "In situ electron microscopy study of structural transformations in 2D CoSe<sub>2</sub>". *npj 2D Materials and Applications* 5 (24), (2021).

- B. Salzmann, J. Vliem, N. Maaskant, L.C. Post, C. Li, S. Bals, D. Vanmaekelbergh, "From CdSe nanoplatelets to quantum rings by thermochemical edge re-configuration". *In preparation*.

## Conference contributions

- Fabrication of honeycomb semiconductors using electron beam lithography (oral presentation). *nanoGe September Meeting, Barcelona, Spain, September 2017*.
- Fabrication of honeycomb semiconductors using electron beam lithography (poster). *Physics@FOM, Veldhoven, the Netherlands, January 2018*.
- Nanoperforation of InGaAs quantum wells: a lithographic route towards III-V semiconductors with a honeycomb nanogeometry (poster). *nanoGe Fall Meeting, Torremolinos, Spain, October 2018*.
- Nanoperforation of InGaAs quantum wells: a lithographic route towards III-V semiconductors with a honeycomb nanogeometry (poster). *Physics@FOM, Veldhoven, the Netherlands, January 2019*.
- Graphene physics in III-V semiconductors (poster). *DPG Spring Meeting, Regensburg, Germany, April 2019*.
- Fabrication and characterization of triangular nanoperforated InGaAs honeycomb semiconductors (poster). *1D2DNanomat summer school, La Marana (Corsica), France, July 2019*.
- Graphene physics in III-V semiconductors (poster). *Symposium Dutch Scanning Probe Microscopy, Amsterdam, the Netherlands, November 2019*.
- Triangular nanoperforation and band engineering of InGaAs quantum wells (poster). *Physics@FOM, Veldhoven, the Netherlands, January 2020*.
- Graphene physics in III-V honeycomb semiconductors (oral) (cancelled). *DPG Spring Meeting, Dresden, Germany, April 2020*.

## About the author

Christiaan Post was born on the 6th of February, 1991 in Hilversum. He attended the gymnasium at the 'Gemeentelijk Gymnasium Hilversum' in Hilversum. In 2009, he started his undergraduate studies in physics and astronomy at Utrecht University. He performed his bachelor thesis in 2012 at the Institute of Subatomic Physics group under supervision of Alessandro Grelli and André Mischke, and wrote his bachelor thesis entitled "Study of the systematic uncertainty in the measurement of  $D^{*+}$  production versus multiplicity in proton-proton collisions at  $\sqrt{s} = 7$  TeV at ALICE".



In 2013, he started his masters in 'Nanomaterials: Chemistry and Physics', focusing on experimental physics. He performed his master research in the Condensed Matter and Interfaces group, investigating the coverage of semiconductor nanoplatelets onto various substrates using ambient atomic force microscopy. He performed his research under the supervision of Marlou Slot, Ingmar Swart and Daniel Vanmaekelbergh, and obtained his master degree in 2016.

Christiaan started his PhD research in April 2016. The project he worked on was part of the NWO project 'Superfacial superstructures', focussing on the fabrication and characterization of honeycomb semiconductors designed by various lithography techniques, which was carried out in collaboration with the 'Institut d'Electronique de Microélectronique et de Nanotechnologie' in Lille, the 'Laboratoire de Chimie des Polyèmeres Organiques' in Bordeaux and the 'Institute Néel' in Grenoble. The main results from this research collaboration are presented in this thesis, were published in various papers and presented at national and international conferences. Besides his research, Christiaan was a teaching assistant for several years in the courses 'Quantum Chemistry' and 'Solids and Surfaces', and guided two students in the 'Experimental Design' course. He supervised one student during both his bachelor and master research, Tomas Meerwijk.

Besides his PhD research, Christiaan plays trumpet on a semi-professional level. He played for several years in the 'Utrechtsch Studenten Concert', and also played in several other orchestras and ensembles in and around the area of Utrecht, Amsterdam, Den Haag and Nijmegen. In his spare time, he enjoys running, squash, cooking, brewing beer and hikes in the mountains together with his friends.





